ABSTRACT

PREPARATION AND FIRST RESULT OF BNL EXPERIMENT E821
"A NEW PRECISION MEASUREMENT OF THE MUON (G – 2)
VALUE"



Sergei Ivanovich Redin
Yale University
May 1999



The new muon (g–2) experiment had been prepared at the Brookhaven National Laboratory (BNL) to push experimental uncertainty in $a_\mu = \frac{1}{2}(g_\mu - 2)$ down by a factor of 20. That would allow to measure the weak interaction contribution to $a_\mu$ at the level of 4 standard deviations and probe the physics beyond the Standard Model.

The first ("engineering") run with pion injection was successfully made in 1997. The result obtained from this run is:

$$a_{\mu^+} = 116\,592\,500(1520) \times 10^{-11}\ (13.0\,ppm),$$

which is comparable in precision and in agreement with previous most precise measurements at CERN:

$$a_{\mu^+} = 116\,591\,000(1100) \times 10^{-11}\ (9.4\,ppm),$$

$$a_\mu = 116\,592\,300(840) \times 10^{-11}\ (7.2\,ppm).$$

Both CERN and BNL results are in agreement with current theoretical value:

$$a_\mu = 116\,591\,628(77) \times 10^{-11}\ (0.66\,ppm).$$

Further improvements in accuracy of $a_\mu(experiment)$ is expected from 1998 and 1999 runs with direct muon injection, which would provide higher number of stored muons and less systematic error. Further improvements in accuracy of $a_\mu(theory)$ is also expected in one or two years, mostly from more precise measurement of hadron vacuum polarization contribution at CMD–2 experiment, Novosibirsk, Russia.

# PREPARATION AND FIRST RESULT OF BNL EXPERIMENT E821 “A NEW PRECISION MEASUREMENT OF THE MUON (G – 2) VALUE”

A Dissertation
Presented to the Faculty of the Graduate School
of
Yale University
in Candidacy for the Degree of
Doctor of Philosophy

By
Sergei Ivanovich Redin

Dissertation Director: Vernon Hughes

May 1999

# Acknowledgments

This work is a part of coherent efforts of large group of people and I would like to thank all and each member of BNL (g–2) collaboration for extremely fruitful team work. I especially want to thank those physicists who worked close to me and shared with me their rich experiences and right attitudes : Gerry Bunce, Bill Morse, Ralf Prigl, Yannis Semertzidis, Wuzheng Meng from Brookhaven National Laboratory, Satish Dhawan, Dave Kawall, Matthias Grosse–Perdekamp and Axel Steinmetz from Yale University, Lee Roberts, Stratos Efstathiadis and Ofer Rind from Boston University, Priscilla Cushman, Joel Kindem, Steve Giron and Dave Zimmerman from University of Minnesota, Yuri Orlov from Cornell University and Sergei Sedykh from University of Illinois. With special warm feeling I would like to thank Nikolay Ryskulov, Boris Khazin, Yuri Shatunov, Evgeny Solodov, Sergei Serednyakov, Gennady Fedotovich, Vladimir Druzhinin and Ivan Logashenko from Budker Institute of Nuclear Physics (BINP) for work with me, and also for their support and encouragement.

The most important part of this work was done in collaboration with Nikolay Ryskulov from BINP. This is designing of Hall Probe Device, which enable us to measure radial component of magnetic field with unprecedental for Hall probes accuracy of better than $10^{-5}$. With Hall probes we also monitored position of the superconducting coils during the magnet commissioning, which turned out to be the most valuable single piece of information in understanding and fixing coils' stability.

This work would not be possible without high quality job done by BNL (g–2) engineers, designers and technicians. I would like to thank all of them and especially those who were in touch with me: Lou Snydstrup, Chen Pai, John Benante, Don Von Lintig, Steve Kochis.

I would like to honor my friend and colleague in both (g–2) and CMD–2 experiments Yury Merzlyakov, AGS expert Sanki Tanaka and AGS secretary Paula Hughes, who passed away last year.

I am very grateful to my dissertation director and cospokesman of the experiment Vernon W. Hughes for his support, help and leadership. I should note here that my participation in this experiment was initiated by collaboration agreement between (g–2) collaboration and CMD–2 group, established by Professor V. W. Hughes and academician L. M. Barkov from Budker Institute. Also I want to thank Vernon and his wife

Miriam for their hospitality given to me and my family.

I would like to thank Rob Carey and Doug Brown from Boston University, Vanya Logashenko from Budker Institute, Irving Polk from BNL and Vernon Hughes for their help in writing this dissertation.

Finally, I am deeply grateful to my wife Olga and my family for their love, understanding and patience.

# Contents

# List of Tables

# List of Figures

# Chapter 1

# Introduction

The muon (g–2) value is of central importance to particle physics. Comparison of experimental and theoretical values has provided an important test of QED and of the behavior of the muon as a heavy electron. The current experimental value

$$a_\mu(exp) = \frac{1}{2}(g-2)_\mu = 116\ 592\ 300\ (840) \times 10^{-11}\ (7.2\ ppm)\ \ [1,\ 2,\ 3]$$

has been measured at CERN. The theoretical value for $a_\mu$ can be expressed as a sum

$$a_\mu(th) = a_\mu(QED) + a_\mu(hadronic) + a_\mu(weak).$$

Current values are :

$$a_\mu(QED) = 116\ 584\ 706\ (2) \times 10^{-11}\ [4,\ 5],$$

$$a_\mu(hadronic) = 6771\ (77) \times 10^{-11}\ [5,\ 6,\ 7,\ 8],$$

$$a_\mu(weak) = 151\ (4) \times 10^{-11}\ [9].$$

The total theoretical value of $a_\mu$ is

$$a_\mu(th) = 116\ 591\ 628\ (77) \times 10^{-11}\ (0.66\ ppm)$$

and

$$a_\mu(exp) - a_\mu(th) = 670\ (840) \times 10^{-11}.$$

$a_\mu(exp)$ and $a_\mu(th)$ are in good agreement, but the uncertainty in $a_\mu(exp)$ is much larger than that in $a_\mu(th)$. We note that the uncertainty in $a_\mu(th)$ is dominated by lack of knowledge of $a_\mu(hadronic)$.

The goal of the BNL E821 experiment is a precision measurement of $a_\mu$ to 0.35 ppm, a factor of 20 better than the CERN value. The motivations for this precise measurement are to provide
(1) a very sensitive and crucial test of the standard theory;
(2) measurement of the weak interaction contribution to $a_\mu$ as a critical test of the

renormalizability of the electroweak theory;
(3) a powerful probe of physics beyond the standard theory.

The principle of the BNL experiment is based on the spin motion of polarized muons in a storage ring and is the same as that for the most recent CERN experiment [1]. In a uniform magnetic field B the spin precesses with an angular frequency $\omega_s$ which is greater than the orbital cyclotron frequency $\omega_c$ by $\omega_a$, which is the (g–2) precession frequency:

$$\omega_a = \omega_s - \omega_c = \frac{e}{mc} a_\mu B. \tag{1.1}$$

In order to retain muons in the storage ring vertical focusing is provided by electrostatic quadrupoles. With both magnetic and electric fields present, the expression for $\omega_a$ becomes

$$\vec{\omega}_a = \frac{e}{mc} [a_\mu \vec{B} - (a_\mu - \frac{1}{\gamma^2 - 1}) \vec{\beta} \times \vec{E}]. \tag{1.2}$$

For a special value of muon energy $E_\mu = 3.096$ GeV and $\gamma = 29.3$, the electric field does not contribute to $\vec{\omega}_a$. Choosing this "magic energy" allows us to separate the functions of the fields: the homogeneous magnetic field B determines the muon spin precession and electrostatic quadrupoles provide vertical focusing of the muon beam.

The (g–2) frequency $\omega_a$ appears as a modulation of the muon decay electron spectrum. Electrons from muon decay are detected with calorimeters and their times of arrival are accurately measured. An accurate determination of $a_\mu$ requires an accurate measurement of $\omega_a$ and of B.

The increased precision in our experiment is possible principally because of the high proton beam intensity of the AGS, which is about 200 times that available at CERN, where the dominant error was statistical. Our secondary beam line will provide either $\pi$ or $\mu$ beams for injection into the storage ring. With $\pi$ injection a fraction of the muons from $\pi$ decays are captured in the storage ring; with $\mu$ injection a fast kicker is required to capture muons and a higher intensity of stored muons is expected.

The principal equipment for the experiment is the superferric storage ring with B = 1.45 T and a diameter of 14.22 m. To achieve the desired precision we must know B averaged over the muon storage volume at the 0.1 ppm level. Hence the requirements on the field homogeneity and stability are very stringent. The magnetic field B will be measured by proton NMR. The electron detectors are to be located on the inside of the ring. They must handle high rates and provide precise time measurements with systematic errors less than 20 ps. The detailed description of the BNL E821 experiment set–up can be found in our most recent design report [10] and in [11, 12].

The author was deeply involved with the commissioning of the superferric magnet and with precision field measurement and shimming. Multipole analysis of the NMR data was his responsibility as well as various measurements with Hall probes, which have less precision than NMR probes, but are needed to measure the direction of the field and can work in a highly inhomogeneous magnetic field.

Probably the most important application of Hall probes in our muon (g–2) experiment is measuring the radial component of the field. To limit the vertical excursions of the muon beam and for the measurement of the muon electric dipole moment, the radial magnetic field averaged over the storage volume should be smaller than 50 ppm with respect to the vertical field. A Hall probe device which measures the radial component of the field with a precision of about 10 ppm was designed and built by the author in cooperation with Novosibirsk members of our collaboration. It is currently being used.

This dissertation reports in detail the preparation and results of the BNL E821 experiment based on the first run in April–July 1997.

In Chapter 2 we briefly discuss the current status of theoretical calculations of the muon (g–2) value and the ability of the BNL experiment to test the Standard Model and to search for physics beyond it. We also discuss the hadronic vacuum polarization contribution to $a_\mu$ and the Novosibirsk experiments which measure it. The author was deeply involved in the Novosibirsk experiments before joining the BNL (g–2) experiment.

Chapter 3 gives a brief review of the three previous CERN muon (g–2) experiments.

Chapter 4 contains a technical description of the present BNL experiment.

Chapter 5 describes the commissioning of the superferric magnet and the shimming of the magnetic field prior to the first run.

Chapter 6 describes the first run in April–July 1997, including its milestones, problems and solutions.

Chapter 7 describes the offline analysis of the data, and the evaluation of the muon (g–2) value including statistical and systematical errors.

Chapter 8 contains a discussion of the results. Plans for upgrade of the apparatus are also described.

Appendix I contains a paper with the result of the 1997 run of the experiment, submitted to *Physical Review Letters*.

An article from *Soviet Journal Nuclear Physics* which was prepared for publication by the author and which contains in part results of the Novosibirsk CMD experiment is reprinted in Appendix II.

# Chapter 2

# Muon (g–2) in Theory

## 2.1 Standard Model

The gyromagnetic ratio g of a particle is defined as the dimensionless ratio

$$g = \frac{magnetic\ moment}{e\hbar/2mc} \Big/ \frac{angular\ momentum}{\hbar}.$$

For a lepton the Dirac theory predicts g = 2. A deviation from g = 2, $a = \frac{1}{2}$(g–2) arises from radiative corrections. The electron $a_e$ value has been measured to 3.7 parts per billion (ppb):

$$a_e = \frac{1}{2}(g-2) = 11\ 596\ 521\ 884(43)\ \times\ 10^{-13}\ [13],$$

which is one of the most precise measurements in physics. The experimental value agrees with the theoretical value calculated in QED including $O(\alpha/\pi)^4$ term if we take $\alpha$ from the Quantum Hall effect measurements,

$$\alpha^{-1}(Hall) = 137.036\ 003\ 7(33)\ [14].$$

Alternatively, the most accurate value for $\alpha$ is obtained by equating $a_e(exp)$ and $a_e(theory)$:

$$\alpha^{-1}(a_e) = 137.035\ 999\ 58(52)\ [15].$$

This number is used in the calculation of the (g–2) value for the muon.

Pure QED calculations for the muon (g–2) value were done to very high order in the same fashion as for the electron [16]:

$$a_\mu(QED) = C_1\frac{\alpha}{\pi} + C_2\left(\frac{\alpha}{\pi}\right)^2 + C_3\left(\frac{\alpha}{\pi}\right)^3 + C_4\left(\frac{\alpha}{\pi}\right)^4 + C_5\left(\frac{\alpha}{\pi}\right)^5 = 116\ 584\ 706(2)\times 10^{-11},$$

where $C_1 = 0.5$, $C_2 = 0.765\ 857\ 381(51)$, $C_3 = 24.050\ 531(40)$, $C_4 = 126.02(42)$ and $C_5 = 930(170)$. Note that $C_n/C_{n-1} \sim ln(m_\mu/m_e) = 5.3$ due to extra $e^+\,e^-$ loop, the effect which is absent for $a_e(QED)$.

Another important difference is that because the mass of the muon is much greater than that of electron, the relative contribution of heavier particles to $a_\mu$ goes as $\sim (m_\mu/m_e)^2 = 4.3 \times 10^4$ and diagrams with quark loops or even weak bosons contribute significantly to the final result and hence

$$a_\mu(th) = a_\mu(QED) + a_\mu(hadronic) + a_\mu(weak).$$

### 2.1.1 Hadronic Contribution

The leading strong interaction correction to $a_\mu$ arises from hadronic vacuum polarization in the order of $(\alpha/\pi)^2$, see Figure 2.1. This contribution can be evaluated from a dispersion relation using $e^+ e^- \longrightarrow hadrons$ and hadronic $\tau$–decay data and from perturbative QCD calculations for higher energy. Recent analysis gives

$$a_\mu(hadronic\ vacuum\ polarization, O(\alpha/\pi)^2) = 6951(75)\ \times\ 10^{-11}[6,\ 7,\ 17].$$

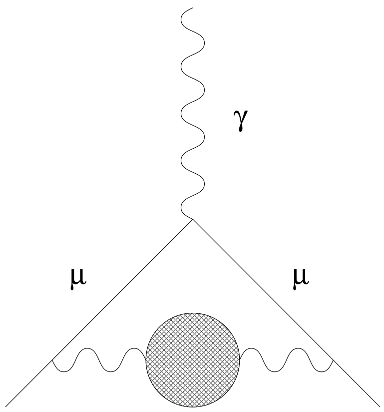


**Figure 2.1**: Lowest order of hadronic vacuum polarization contribution to $a_\mu$.

The next order hadron vacuum polarization terms, shown in Figure 2.2, also can be found using experimental data, though calculations are far more elaborate. That was done in [8] with a precision much better than the anticipated precision of BNL (g–2) experiment:

$$a_\mu(h.v.p,\ O(\alpha/\pi)^3) = -101(6) \times 10^{-11}.$$

Another $O(\alpha/\pi)^3$ term, hadronic light–by–light scattering diagram shown in Figure 2.3, has been difficult to express in terms of experimentally accesible observables,

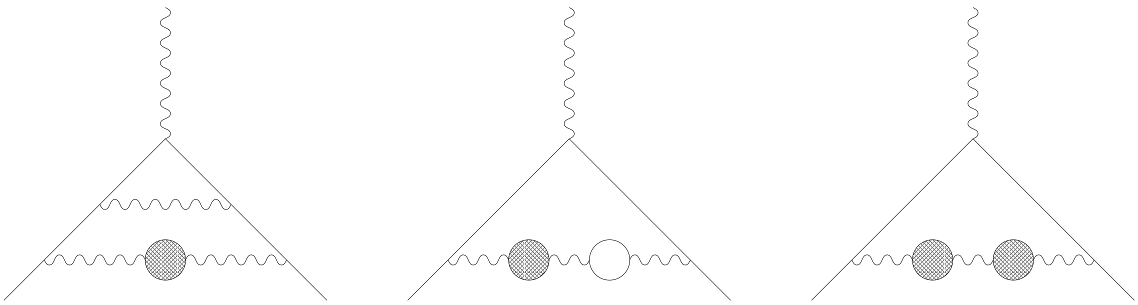

**Figure 2.2**: Hadron vacuum polarization contribution to $a_\mu$ at the order of $(\alpha/\pi)^3$. Sum over all possible permutations is assumed.

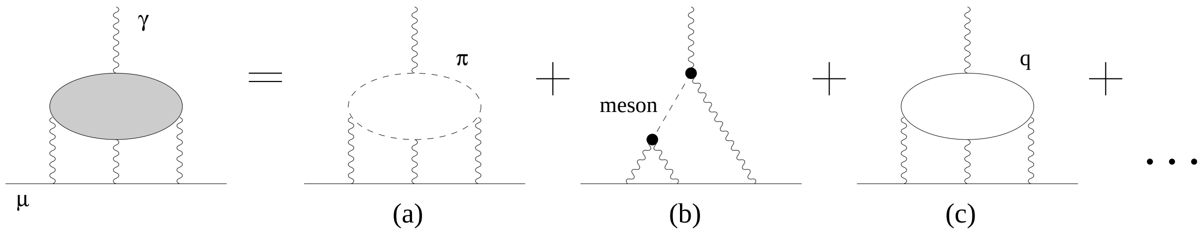


**Figure 2.3**: Hadronic light–by–light contribution to $a_\mu$: (a) – $\pi^\pm$ loop; (b) – pseudo–scalar ($\pi^\circ$, $\eta$, $\eta'$) or axial–vector ($a_1$) pole; (c) – quark loop. Sum over all possible permutations is assumed.

and hence potentially it is a source of a serious problem. At present the hadronic light–by–light contribution was estimated within the framework of chiral perturbation theory and the $1/N_c$ expansion. The leading terms arise from three types of diagrams shown in Figure 2.3: pion loop (a), pseudo–scalar and axial–vector poles (b) and quark loop (c). The result obtained in [5] is:

$$a_\mu(pion\ loop) = -4.5(8.1) \times 10^{-11},$$

$$a_\mu(pseudo-scalar\ pole) = -82.7(6.4) \times 10^{-11},$$

$$a_\mu(axial-vector\ pole) = -1.74 \times 10^{-11},$$

$$a_\mu(quark\ loop) = 9.7(11.1) \times 10^{-11},$$

which add up to

$$a_\mu(hadronic\ light-by-light) = -79(15)\ \times\ 10^{-11}.$$

Note, that recent measurements of the meson–photon transition formfactors of light pseudo–scalar mesons at large momentum transfer at CLEO II [18] put certain restrictions on theoretical model, which substantially reduce error in $a_\mu(pseudo–scalar\ pole)$.

The sum of the leading and next order of vacuum polarization terms and hadronic light–by–light scattering gives the total hadronic contribution:

$$a_\mu(hadronic) = 6771(77) \times 10^{-11}.$$

The error in $a_\mu(hadronic)$ is higher than the anticipated precision of BNL muon (g–2) experiment by a factor of 3.7. Current experiments on $e^+e^- \longrightarrow hadrons$ and $\tau-$lepton physics should significantly lower the uncertainty in $a_\mu(hadronic)$. In section 2.3 we discuss some $e^+ e^-$ experiments.

### 2.1.2 Weak Contribution

The leading one–loop electroweak contribution to the muon (g–2) comes from the Feynman diagrams shown in Figure 2.4. It was calculated in the framework of the Standard Model in [19]:

$$a_\mu(W) = \frac{10}{3}\,\frac{G_F m_\mu^2}{8\sqrt{2}\pi^2} + O\left(\frac{m_\mu^4}{M_W^4}\right),$$

$$a_\mu(Z) = \frac{1}{3}\,\frac{G_F m_\mu^2}{8\sqrt{2}\pi^2}\left[(1-4\,sin^2\,\theta_W)^2 - 5\right] + O\left(\frac{m_\mu^4}{M_W^4}\right),$$

$$a_\mu(H) = 3\,F(R)\,\frac{G_F m_\mu^2}{8\sqrt{2}\pi^2},$$

where $F(R)$ is a function of $R = M_H^2/m_\mu^2$. For $M_H \gg m_\mu$ $F(R) = -\dfrac{2}{3R}\,ln\,R$ and

$$a_\mu(H) = -2\,\frac{m_\mu^2}{M_H^2}\,ln\left(\frac{M_H^2}{m_\mu^2}\right)\frac{G_F m_\mu^2}{8\sqrt{2}\pi^2}.$$

Hence the total one–loop electroweak contribution is

$$a_\mu(weak, one\ loop) = a_\mu(W) + a_\mu(Z) + a_\mu(H) =$$

$$= \frac{G_F m_\mu^2}{8\sqrt{2}\pi^2}\times\left[\frac{10}{3} + \frac{1}{3}\,\left((1-4\,sin^2\,\theta_W)^2 - 5\right) + O\left(\frac{m_\mu^2}{M_W^2}\right) + O\left(\frac{m_\mu^2}{M_H^2}\right)\right] \approx 195 \times 10^{-11}.$$

Here $G_F = \dfrac{\sqrt{2}}{8}\dfrac{g^2}{M_W^2} = 1.166\,39(1)\times 10^{-5}\ \mathrm{GeV}^{-2}$ is a Fermi constant, $g \approx 0.653$ is an an electroweak coupling constant and $\theta_W$ is a Weinberg angle, $sin^2\,\theta_W = 0.224$.

Naively, one might expect higher order (2 loop) electroweak contributions to be of relative order of $\alpha/\pi$ and hence negligible; however, that is not the case. As was found in [20], some two loop corrections can be quite large. They lead to a reduction of $a_\mu(weak)$ by a factor of $1 - 97\alpha/\pi \approx 0.77$ and finally give

$$a_\mu(weak) = 151(4) \times 10^{-11}\ [9].$$

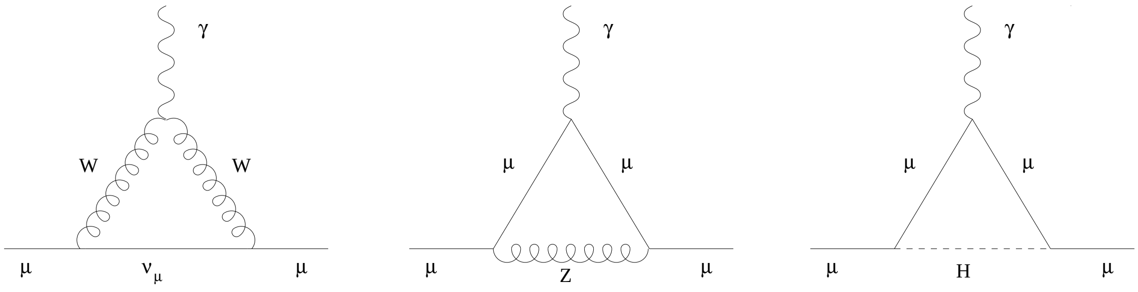


**Figure 2.4**: One loop weak corrections to $a_\mu$.

The assigned error of $\pm 4 \times 10^{-11}$ is due to uncertainties in $M_{Higgs}$, quark 2–loop effects and possible 3–loop (or higher) electroweak contributions. $a_\mu(weak)$ is about 4 times bigger than the anticipated error of the BNL muon (g–2) experiment. That makes the experiment a crucial test of the renormalizability of the Standard Model.

## 2.2 Beyond the Standard Model

The Standard Model of elementary particles is a very successful description of particle physics phenomena extending up to about 200 GeV. It was created in 1960s and got the solid experimental support with $J/\psi$ discovery in 1974 [21]. It predicted the existence and masses of $Z$ and $W$ vector bosons well before they were discovered in 1983 [22]. The most recent triumph of the Standard Model was the discovery of the sixth quark, $t$ [23] in the predicted narrow mass window [24].

Although the Standard Model successfully incorporates all known properties of the strong, weak and electromagnetic forces, it doesn't seem complete: it has too many arbitrary parameters (especially quark masses) and does not incorporate the gravitational force. There should be a more fundamental theory, which reduces to the Standard Model at low energy and describes some new physics at high energy.

There are two types of models of new physics beyond the Standard Model. One type are the models which consist of extending the Standard $SU(3)_C \times SU(2)_L \times U(1)$ gauge model with additional group factors, or of embedding this gauge group into a larger one. We shall call these unification theories. Other models propose compositeness of presently known fundamental particles. We shall call them compositeness theories.

### 2.2.1 Unification Theories

The unification of fundamental interactions seems to be one of the most "natural" and attractive ways to generalize the Standard Model. One of the earliest steps in this direction was done in [25] with grand unification theory (GUT), which proposed unification of electroweak and strong interactions. It suggests that strong, weak and electromagnetic coupling constants merge into one at the GUT scale, $\sim 10^{15}$ GeV.

In the grand unification theory the $SU(3)_C \times SU(2)_L \times U(1)$ symmetry is expanded to a larger gauge group with additional charged and neutral gauge bosons. There are two realistic possibilities: one is a charged $W_R$ boson which couples to right–handed charged currents in left–right symmetric models and another is two extra neutral bosons $Z_\chi$ and $Z_\psi$, which arise in models based on a popular $E_6$ symmetry group.

For the case of a $W_R$ coupled to $\mu_R$ and $\nu_{\mu_R}$ with gauge coupling $g_R$, the contribution to $a_\mu$ will be

$$a_\mu(W_R) = \frac{10}{3}\frac{g_R^2}{64\pi^2}\frac{m_\mu^2}{M_{W_R}^2} = \frac{10}{3}\frac{G_F m_\mu^2}{8\sqrt{2}\pi^2} \times \frac{g_R^2}{g^2}\frac{M_W^2}{M_{W_R}^2} \;[4,\; 26],$$

which resembles equation for $a_\mu(W)$ in section 2.1.2. Assuming the coupling constant $g_R$ to be equal to the $SU(2)_L$ coupling constant $g$, the BNL (g–2) experiment can set the upper limit for the mass of $W_R$ as $M_{W_R} > 250$ GeV.

The contribution from a pair of additional neutral bosons $Z_\chi$ and $Z_\psi$ is completely specified up to a mass mixing angle. The upper limit on the masses of additional bosons can be set on the order of 100 GeV [4].

Enlargement of the Higgs scalar sector of the Standard Model also can have a potentially important effect on $a_\mu$. The muon–Higgs interaction Lagrangian is given by:

$$\mathcal{L}_{int} = \bar{\mu}\left(C_s + C_p\gamma_5\right) F H + h.c.\ ,$$

where H is a Higgs scalar with charge $Q_H$ and F is an arbitrary fermion with mass $m_F$ and charge $-(1+Q_H)$. That gives the following contribution to $a_\mu$:

$$a_\mu(H) = -\frac{Q_H m_\mu^2}{8\pi^2}\int_0^1 dx\, \frac{C_s^2[x^3 - x^2 + \frac{m_F}{m_\mu}(x^2-x)] + C_p^2[x^3 - x^2 - \frac{m_F}{m_\mu}(x^2-x)]}{m_\mu^2(x^2-x) + M_H^2 x + m_F^2(1-x)}$$
$$+\frac{(Q_H+1)m_\mu^2}{8\pi^2}\int_0^1 dx\, \frac{C_s^2[x^2 - x^3 + \frac{m_F}{m_\mu}x^2] + C_p^2[x^2 - x^3 - \frac{m_F}{m_\mu}x^2]}{m_\mu^2(x^2-x) + M_H^2(1-x) + m_F^2 x} \;[26].$$

From this formula it is clear that $a_\mu(H)$ is increased if $m_H$ is relatively light or if $m_F$ and/or $C_s$, $C_p$ are large. None of these possibilities occurs for the Standard Model Higgs, where $m_F = m_\mu$, $C_s = g m_\mu / 2M_W \simeq 10^{-3} g$, $C_p = 0$ and $M_H \geq 25$ GeV. Enlarging the Higgs sector can, however, lead to larger couplings and reopen the possibility of a very light mass. A neutral scalar or pseudo–scalar with mass $M_H < 3m_\mu \simeq 300$ MeV gives a shift in $a_\mu$ of order of 3.5 ppm if $C_s$ and $C_p$ are of order of $10^{-3}g$. Another possibility is that $M_H$ is not so small but $C_s$ or $C_p$ is of order of $g$. In that case the measurement of $a_\mu$ with 3.5 ppm accuracy probes $M_H$ to $\leq 500$ GeV.

A more ambitious theory, Supergravity, makes the next step and combines gravity with other fundamental forces at the energy above the Planck mass $M_P = 1.22 \times 10^{19}$

GeV. Supergravity is based on Supersymmetry [27] (SUSY), which mixes isospin and space–time symmetries in a non–trivial way. Supersymmetry implies the existence of supersymmetric partners for all known fundamental particles.

SUSY superpartners are fascinating targets for forthcoming high energy experiments. But even without high energy colliders we can constrain SUSY models by precision measurements in low energy experiments such as muon (g–2). The superparticles contribute to $a_\mu$ via the loops in Figure 2.5. The expected magnitude of the correction is:

$$\Delta a_\mu \sim O\left(\frac{G_F m_\mu^2}{8\pi^2\sqrt{2}}\frac{M_W^2}{M_{SUSY}^2}\right) \text{ [4].}$$

The BNL (g–2) experiment is capable of probing superparticles up to $M_{SUSY} \leq 130$ GeV. Note, that superparticle loops usually tend to cancel ordinary particle loops and for $M_{SUSY}$ to be of the order of the electroweak scale their loop effects must be comparable to those of $Z$ or $W^\pm$ bosons [28, 29].

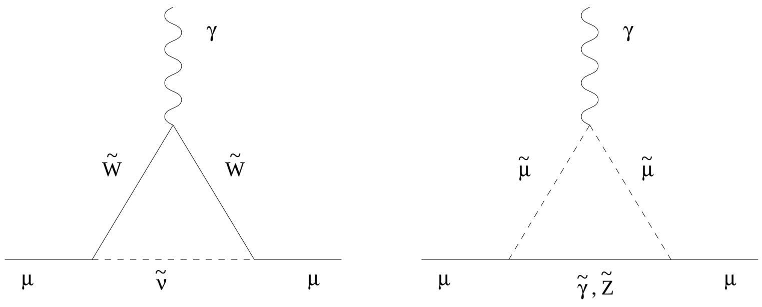


**Figure 2.5**: Supersymmetric loop contribution to $a_\mu$.

It is probably worth considering in more detail the muon (g–2) contribution from leptoquarks. Leptoquarks are hypothetical vector or scalar particles, which decay into quark and lepton. Leptoquarks seem inevitably to arise in any unification scheme at the level of strong and electroweak unification. Recently there has been a lot of interest in leptoquarks theoretically as well as experimentally. There exist already severe constraints on the characteristics of leptoquarks. Flavor–changing neutral currents (FCNC's) force the leptoquarks to be flavor diagonal, i.e. to couple to only a single generation of leptons and quarks [30]. From pseudo–scalar mesons ($\pi$, $K$ and $D$) leptonic decays we also have to conclude that leptoquarks couple only chirally, i.e. they couple either to left–handed or to right–handed quarks, but not to both [31].

The most stringent lower mass bound for the first generation leptoquarks is given by DESY *ep* collider HERA experiments [32] : $m_{\Phi_L} > 145$ GeV, assuming for the leptoquark–electron–up quark coupling $\lambda_{\Phi_L} = e$. For the second generation, the CDF Collaboration at Fermilab presented a lower mass bound of $m_{\Phi_L} > 135$ GeV for a branching ratio into muon and quark of 100% and $m_{\Phi_L} > 95$ GeV for the branching ratio of 50% [33]. The D0 collaboration's numbers are $m_{\Phi_L} > 111$ GeV and $m_{\Phi_L} > 89$ GeV [34] respectively. In [35] the authors obtain, via the leptonic partial width of the $Z$ boson, a lower mass limit of about 680 GeV for a left–type leptoquark and of about 280 GeV for a right–type leptoquark.

The second generation leptoquarks can contribute to the muon (g–2) value through the penguin and self–energy diagrams, see Figure 2.6. $\Delta a_\mu^{\Phi_L}$ was calculated in [36]:

$$\Delta a_\mu^{\Phi_L} = \frac{\lambda_{\Phi_L}^2}{(4\pi)^2}\, g_a^{q2}\, \frac{1}{6}\left(e_{\Phi_L}^q - 2e_q\right)\left(\frac{m_\mu}{m_{\Phi_L}}\right)^2,$$

the sum over polarizations $a = left,\ right$ and second generation quarks $q = s,\ c$ is assumed. Here $\lambda_{\Phi_L}$ is the leptoquark–muon–quark coupling, $g_a^q$ is the chiral coupling: $g_{left}^q = 1, g_{right}^q = 0$ for a left–type leptoquark and $g_{left}^q = 0, g_{right}^q = 1$ for a right–type leptoquark, $e_{\Phi_L}^q = -2/3, -5/3$ for $q = s, c$, respectively. This formula is valid for the mass of the second generation leptoquark $m_{\Phi_L}^2 \gg m_s^2, m_\mu^2$ (first order in the expansion of $1/m_{\Phi_L}^2$). Parameterizing the coupling $\lambda_{\Phi_L}$ with electroweak strength with factor $k = 1 - 10$ [35] one can obtain a lower mass limit of a second generation scalar leptoquark. For the anticipated accuracy of BNL (g–2) experiment and a 4–fold improvement in accuracy of $a_\mu(hadronic)$, this is $m_{\Phi_L} > 156$ GeV for $k = 1$ and $m_{\Phi_L} > 495$ GeV for $k = 10$. These bounds compare well with direct searches at present high energy accelerators such as HERA at DESY and Tevatron at Fermilab.

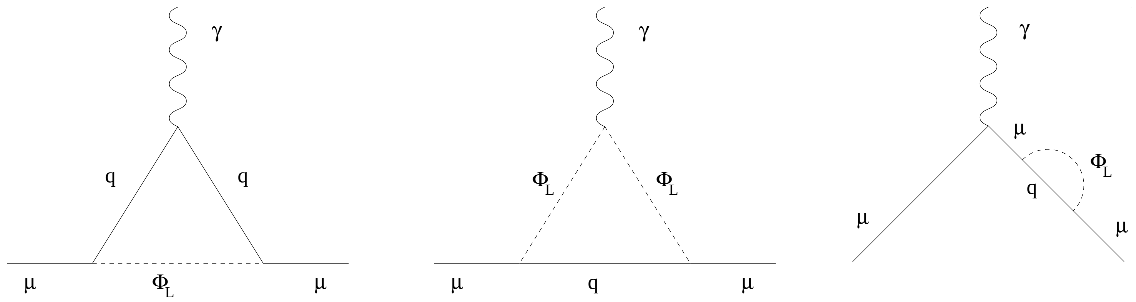


**Figure 2.6**: Second generation scalar leptoquark contribution to $a_\mu$. q denotes a charm or strange quark.

## 2.2.2 Compositeness Model

Theoretical models based on possible substructure of leptons, quarks and/or vector bosons seem very promising. A rich phenomenology of new particles and interactions is often predicted. A detailed investigation of effects on the muon (g–2) arising from a composite (substructure) picture was done in [37]. The underlying substructure can manifest itself as form factor corrections to the vertices, exchange of high mass states (excited leptons, higher vector bosons) or new diagrams involving 4–fermion or 2 fermion – 2 boson contact terms.

The effect of modifying the $\gamma\mu^+\mu^-$, $Z\mu^+\mu^-$ or $W\mu\nu_\mu$ vertex was calculated by introducing a form factor of the type $(1-k^2/\Lambda^2)^{-1}$, where $k$ is the vector boson 4–momentum and $\Lambda$ is the extension scale. For the case of $\Lambda$ equal to the cut–off of loop integrals, the results are:

$$\Delta a_\mu(W\mu\nu_\mu) = \frac{G_F}{2}\,\frac{m_{\mu^2}}{8\pi^2}\,\frac{1}{3}\,\frac{M_W^2}{\Lambda^2}\,\left[14\,ln\,\frac{M_W^2}{\Lambda^2}\ +\ 118\,ln\,2 - \frac{931}{15}\right],$$

$$\Delta a_\mu(Z\mu^+\mu^-) = \frac{G_F}{\sqrt{2}}\,\frac{m_{\mu^2}}{8\pi^2}\,\frac{1}{2}\,\frac{M_Z^2}{\Lambda^2}\,\left[(36\,ln\,2 - 25)\,(1 - 4\,sin^2\theta_W)^2 + \frac{9}{2} - 6\,ln\,2\right],$$

$$\Delta a_\mu(\gamma\mu^+\mu^-) = -\frac{\alpha}{\pi}\,\frac{m_\mu^2}{\Lambda^2}\,(13 - 18\,ln\,2).$$

For the anticipated precision of the BNL muon (g–2) experiment the formula above would set lower limits for $\Lambda$ of 450 GeV, 64 GeV and 184 GeV respectively.

The effect of excited leptons $l^*$ involves more free parameters even for the simplest case of an $SU(2)$ doublet of spin $\frac{1}{2}$ with an excited muon $\mu^*$ and neutrino $\nu^*$. Assuming coupling strengths for various transitions $\mu^*\mu\gamma$, $\mu^*\mu Z$, $\mu^*\nu W$, $\nu^*\mu W$, $\nu^*\nu Z$, $\nu^*\nu\gamma$ are given by $SU(2)\times U(1)$ type relations and have same chiral structure, one finds [37]:

$$\Delta a_\mu = 10\,\frac{\alpha}{\pi}\,f\,\frac{m_\mu^2}{\Lambda^2}$$

and

$$\Delta a_\mu = 5.3\,\frac{\alpha}{\pi}\,f\,\frac{m_\mu^2}{\Lambda^2}$$

for left and right couplings respectively. For a coupling strength $f = 1$, the corresponding bounds on $m_{l^*} = \Lambda$ are 800 GeV and 600 GeV. Calculations for excited bosons lead to the limits $M_{Z^*} > 70 - 140$ GeV, $M_{W^*} > 120$ GeV.

If leptons and quarks are composite objects, subconstituent rearrangements should lead to new types of interactions which at a low energy scale can be represented by a contact 4–fermion term

$$\frac{2\pi}{\Lambda^2}\,\overline{\psi}\,\theta\,(a - b\gamma^5)\,\psi\overline{\psi}\,\theta'\,(c - d\gamma^5)\,\psi,$$

where $\theta\theta'$ means either 1, $\gamma^\mu\gamma_\mu$ or $\sigma^{\mu\nu}\sigma_{\mu\nu}$. Chirality conserving $\gamma^\mu\gamma_\mu$ contact terms do not contribute to the muon (g–2) value. The contribution of a scalar term is

$$\Delta a_\mu = -\,\frac{ac + bd}{4\pi}\,\frac{m_\mu^2}{\Lambda^2}\,ln\frac{m_\mu^2}{\Lambda^2}.$$

The contribution of a tensor term is 12 times bigger than that of a scalar term. With the normalization $|ac + bd| = 1$ one obtains the rather large limits of 6.8 and 25 TeV for $\Lambda$. However, from the chirality violating nature of these terms, one would rather assume that

$$|ac + bd| \approx \frac{m_\mu^2}{\Lambda^2},$$

so that the limits now become 22 and 35 GeV respectively.

There are also 2 fermion – 2 boson type contact terms: $WW\mu\mu$, $\gamma W\mu\nu$ and $\gamma Z\mu\mu$, see Figure 2.7. They contribute

$$\Delta a_\mu(WW\mu\mu) = -\frac{g_c^2}{48\pi^2}\, c\, \frac{m_\mu^2}{\Lambda^2},$$

$$\Delta a_\mu(\gamma W\mu\nu) = -\frac{g_W g_c^2}{32e\pi^2}\,(c+d)\,\frac{m_\mu}{\Lambda},$$

$$\Delta a_\mu(\gamma Z\mu\mu) = -\frac{g_Z g_c^2}{32e\pi^2}\,\frac{m_\mu}{\Lambda}\,[\,(1 - 4\,sin^2\theta_W)\,c + d)\,]\ [37].$$

Here $g_W = -g/2\sqrt{2} = -e/(2\sqrt{2}\,sin\,\theta_W)$, $g_Z = g/(2\,sin\,\theta_W) = e/(4\,sin\,\theta_W\,cos\,\theta_W)$. Coefficients $c$ and $d$ come from $(c - d\gamma^5)$. For coupling $g_c^2 = 4\pi$ and $c = d = 1/\sqrt{2}$ the lower limits for $\Lambda$ are 700 GeV, 1–3 TeV and 1–3 TeV respectively.

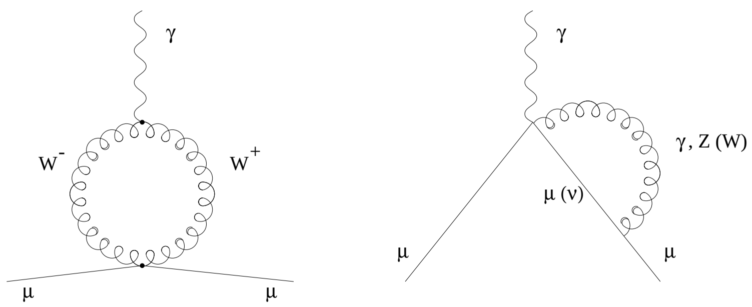


**Figure 2.7**: 2–fermion – 2–boson contribution to $a_\mu$

Finally, the contact term $\gamma\gamma\mu\mu$ gives

$$\Delta a_\mu(\gamma\gamma\mu\mu) = -\frac{g_c^2}{32\pi^2}\, c\, \frac{m_\mu}{\Lambda},$$

which bound $\Lambda > 0.9 - 1.2$ TeV.

An effect of compositeness of $W^\pm$ can reveal itself as an anomalous $WW\gamma$ – coupling, which leads to an anomalous $W$ boson magnetic moment

$$\mu_W = \frac{e}{2M_W}\,(1 + \kappa + \lambda)$$

and electric quadrupole moment

$$Q = -\frac{e}{M_W^2}\,(\kappa - \lambda),$$

where $\kappa = 1$ and $\lambda = 0$ in the Standard Model. The correction to $a_\mu$ is

$$a_\mu(\kappa,\lambda) \simeq \frac{G_F m_\mu^2}{4\sqrt{2}\,\pi^2}\left[(\kappa-1)\,ln\,\frac{\Lambda^2}{M_W^2} - \frac{1}{3}\,\lambda\right]\ [37].$$

For a cut–off $\Lambda$ of order 1 TeV, the anticipated precision of the BNL (g–2) experiment would set bounds on $|\kappa - 1|$ and $\lambda \leq 0.04$ and $\leq 0.6$ respectively.

There are number of other constraints on parameters of compositeness models which would come from the muon (g–2) measurement at BNL, see [37] for details.

## 2.3 Hadronic Contribution and Novosibirsk Experiments

As was mentioned in section 2.1, the hadronic contribution to the muon (g–2) value, in particular $a_\mu(hadronic\ vacuum\ polarization)$, is the source of the largest error for the Standard Model prediction. At the present time, $a_\mu(h.v.p,)$ can not be calculated in the Standard Model due to the strong coupling of QCD in the low energy domain. However, its leading part $a_\mu(h.v.p,\ O(\alpha/\pi)^2)$ can be related to the total cross section for hadron production in electron–positron annihilation by means of dispersion theory and the optical theorem [38]. The result is:

$$a_\mu(h.v.p,\ O(\alpha/\pi)^2) = \frac{1}{4\pi^3}\int_{4m_\pi^2}^{\infty} ds\ \sigma_{e^+e^-\to hadrons}(s)\ K(s),$$

where $s$ is a square of the total center–of–mass energy of $e^+e-$ and

$$K(s) = \frac{1}{2\beta}\left[\frac{(1-\beta)^2}{1+\beta}\left(1 - \frac{2}{1+\beta}\,ln\frac{2}{1-\beta}\right) - \frac{(1+\beta)^2}{1-\beta}\left(1 - \frac{2}{1-\beta}\,ln\frac{2}{1+\beta}\right)\right] - \frac{1}{2},$$

$$\text{with}\ \ \beta = \sqrt{1 - 4m_\pi^2/s}.$$

The plot of K(s) as a function of the total $e^+e^-$ energy is shown in Figure 2.8. At high energy K(s) is decreasing as $\sim 1/s = 1/E_{total}^2$. This makes the contribution from $e^+e^- \to hadrons$ at high energy ($E_{total} > \sim 1$ GeV) in general smaller than that at low energy.

By now the energy interval from $\sqrt{s} = 360$ MeV to 1.4 GeV was covered mostly by different experiments at the VEPP–2M $e^+e^-$ collider in Budker Institute of Nuclear Physics, Novosibirsk, Russia. We discuss here the CMD experiment which measured

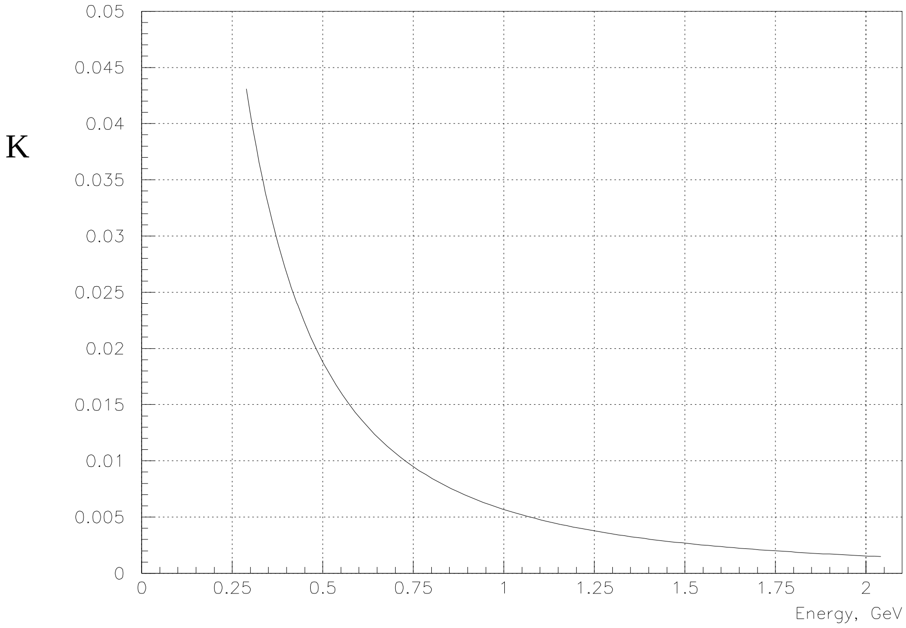


**Figure 2.8**: K as a function of $e^+e^-$ total energy.

the cross sections for $e^+e^- \to \pi^+\pi^-$ [39], $\pi^+\pi^-\pi^\circ$ [40, 41], $K^+K^-$ and $K_LK_S$ [42], $2\pi^+2\pi^-$, $2\pi^+2\pi^-\pi^\circ$, $3\pi^+3\pi^-$ and $2\pi^+2\pi^-2\pi^\circ$ [43] reactions.

The Cryogenic Magnetic Detector (CMD, [44]) is shown in Figure 2.9. The cylindrical optical spark chamber with six gaps was mounted inside a superconducting solenoid. It operated in the track mode. Photographs of events in the spark chamber were taken by the camera located at the focus of the spherical glass lens. The spark coordinates along the chamber were measured using a set of prisms located between the chamber and the lens, so that part of the spark light (about 1/3 of the spark length) reached the camera after passing through the prism. On the film this part is shifted with respect to the rest of the spark by an amount, proportional to the distance between the spark and the prism.

With a gas mixture of $Ne$+8% $Ar$+2.5% $CO_2$ at low temperature 170–180 K and at a pressure of about 2 atm, a spatial resolution of $\sim 50\,\mu$m was obtained. With a magnetic field of 32 kG in the main solenoid a momentum resolution for the charged particles of $\sigma_p/p \cong 0.05\,p\,$(GeV/c) was obtained. The detector was triggered by two cylindrical proportional wire chambers. Only charged particles were detected. Parameters of one neutral particle (if any) in the final state of the reaction can be reconstructed by the momentum–energy balance.

The detector was in operation from 1979 to 1984. Some results of measurements of different cross sections by the CMD detector are shown in Figures 2.10 – 2.18 together with results from other groups (error bars for the most of groups indicate statistical

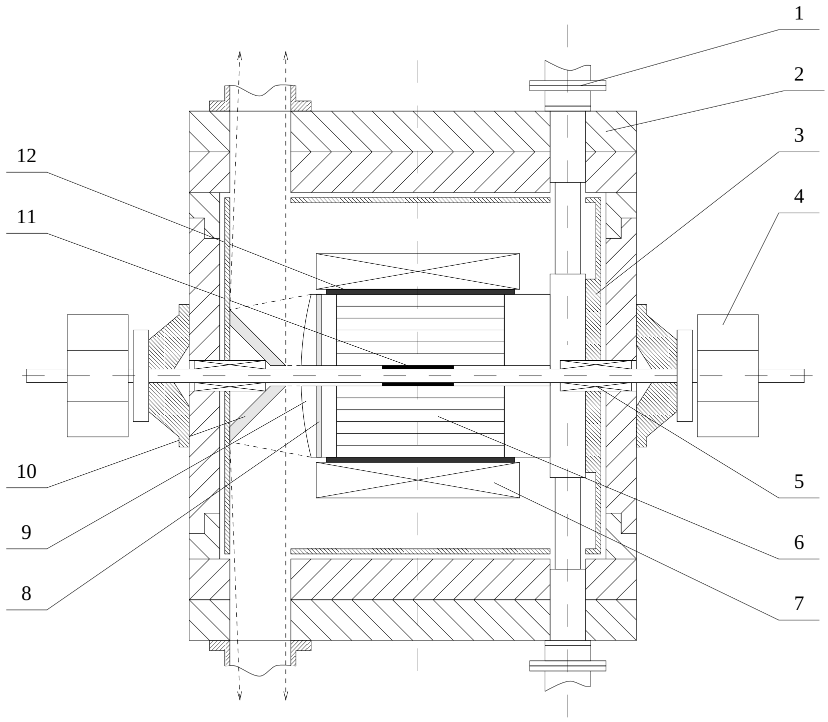


**Figure 2.9**: Detector CMD. 1 – high voltage feeding, 2 – yoke, 3 – nitrogen screen, 4 – magnetic lens of the storage ring, 5 – compensating solenoid, 6 – spark chamber, 7 – main solenoid, 8 – system of optical prisms, 9 – optic lens, 10 – mirror, 11 – inner proportional wire chamber, 12 – outer proportional wire chamber.

errors only). The detailed analysis of the contribution of different reaction channels $e^+e^- \to hadrons$ to the $a_\mu(h.v.p)$ is given in reference [45]. Some results of this analysis are shown in Table 2.1. One can see that the main contribution to the $a_\mu(h.v.p)$ and its uncertainty arises from the channel $e^+e^- \to \pi^+\pi^-$ for $\sqrt{s} < 1.4$ GeV, i.e. in the energy region of the VEPP-2M Collider.

Soon after the completion of the CMD program, the CMD group started to build a new detector called CMD–2. The CMD–2 detector was designed to improve the precision of measurements of $a_\mu(hadronic)$, particularly by reducing the systematic error. The CMD–2 program also includes a detailed study of the $\phi(1020)$ meson region as a first step toward a future $\phi-$factory program.

The scheme of detector CMD–2 is shown in Figure 2.19. The tracking system of the detector consists of a cylindrical drift chamber with 80 jet–type cells and a double layer multiwire proportional chamber called the Z–chamber. They are mounted inside a thin (0.4 radiation length) superconducting solenoid with a magnetic field of 1.0 T. The spatial resolution of the drift chamber is about 250 $\mu$m in the plane transverse to the beam and 0.4–0.5 mm in the longitudinal direction (Z–coordinate). The latter is measured by a charge division method. The momentum resolution is 3–4%

**Table 2.1**: Hadronic contribution to $a_\mu$

| Mode | Energy Region, GeV | $10^{11} \times a_\mu^{mode}(\sigma_{stat})(\sigma_{syst})$ |
|---|---|---|
| $\pi^+\pi^-$ | $< 1.4$ | 5022 (70) (88) |
| $\pi^+\pi^-\pi^\circ$ | $< 1.4$ | 509 (15) (13) |
| $K^+K^-$ | $< 1.4$ | 251 (10) (19) |
| $K_LK_S$ | $< 1.4$ | 148 (2) (6) |
| $\omega\pi^\circ$ | $< 1.4$ | 62 (3) (4) |
| $\pi^+\pi^-2\pi^\circ$ | $< 1.4$ | 105 (4) (19) |
| $2\pi^+2\pi^-$ | $< 1.4$ | 52 (1) (3) |
| $2\pi^+2\pi^-\pi^\circ$ | $< 1.4$ | 2 (1) (0.4) |
| *hadrons* | $> 1.4$ | 905 (24) (46) |

for 200 MeV/c pions from neutral kaon decays and about 6% for 500 MeV electrons from $e^+e^-$ elastic scattering (Bhabha) events. The Z–chamber is used for the fast trigger (signals from anode wires) and for measurement of the longitudinal coordinate of charged tracks (signals from anode strips) with $\sim$ 0.5 mm resolution.

The CsI barrel calorimeter consists of 8 octants, each with 112 CsI crystals. The calorimeter is 8.1 radiation length deep and has an energy resolution of 8–10% and an angular resolution of 0.02–0.03 radians in the energy range 100–500 MeV. Two BGO endcap calorimeters each contain 340 $2.5 \times 2.5 \times 11$ cm$^3$ BGO crystals. The BGO calorimeter has an energy resolution of 5–8% and an angular resolution of 0.01–0.02 radians.

The muon range system of the CMD–2 detector consists of two double layers of streamer tubes operating in a self–quenching streamer mode. The inner part of the system contains 8 modules with 48 tubes each. The outer one contains 5 upper modules with 32 tubes each and 3 lower modules with 24 tubes each. The spatial resolution along a tube was measured to be 5–7 cm and the detection efficiency of the double layer is better than 99%. The probability for a pion to hit the inner part of the muon range system and imitate a muon is 35% and that for both the inner and outer parts is 10%.

More details about the CMD–2 detector can be found in reference [46].

The CMD–2 experiment has been running since 1992. The CMD–2 group measured parameters of the $\phi(1020)$ meson, in particular all four major decay mode were measured in a single $e^+e^-$ experiment [47], studied $K_LK_S$ coupled decays and $K_L - Be$ interaction [48], discovered the $\phi \to \eta'\gamma$ decay mode, etc. Preliminary results on $e^+e^- \to \pi^+\pi^-$ are shown in Figure 2.20. Work is in progress to understand better the systematic uncertainties which are currently estimated at 1.5%.

The author took part in the CMD experiment since 1980 first as a student in Novosibirsk State University and then as a junior staff scientist. His major responsibility was offline analysis of multipion $e^+e^-$ annihilation, i.e. reactions $e^+e^- \rightarrow 2\pi^+2\pi^-$, $2\pi^+2\pi^-\pi^\circ$, $3\pi^+3\pi^-$ and $2\pi^+2\pi^-2\pi^\circ$. After completion of this work and publishing results in [43] (see Appendix II) in 1988, the author worked for preparation and first data taking for the CMD–2 experiment until 1993 when he joined the BNL muon (g–2) collaboration.

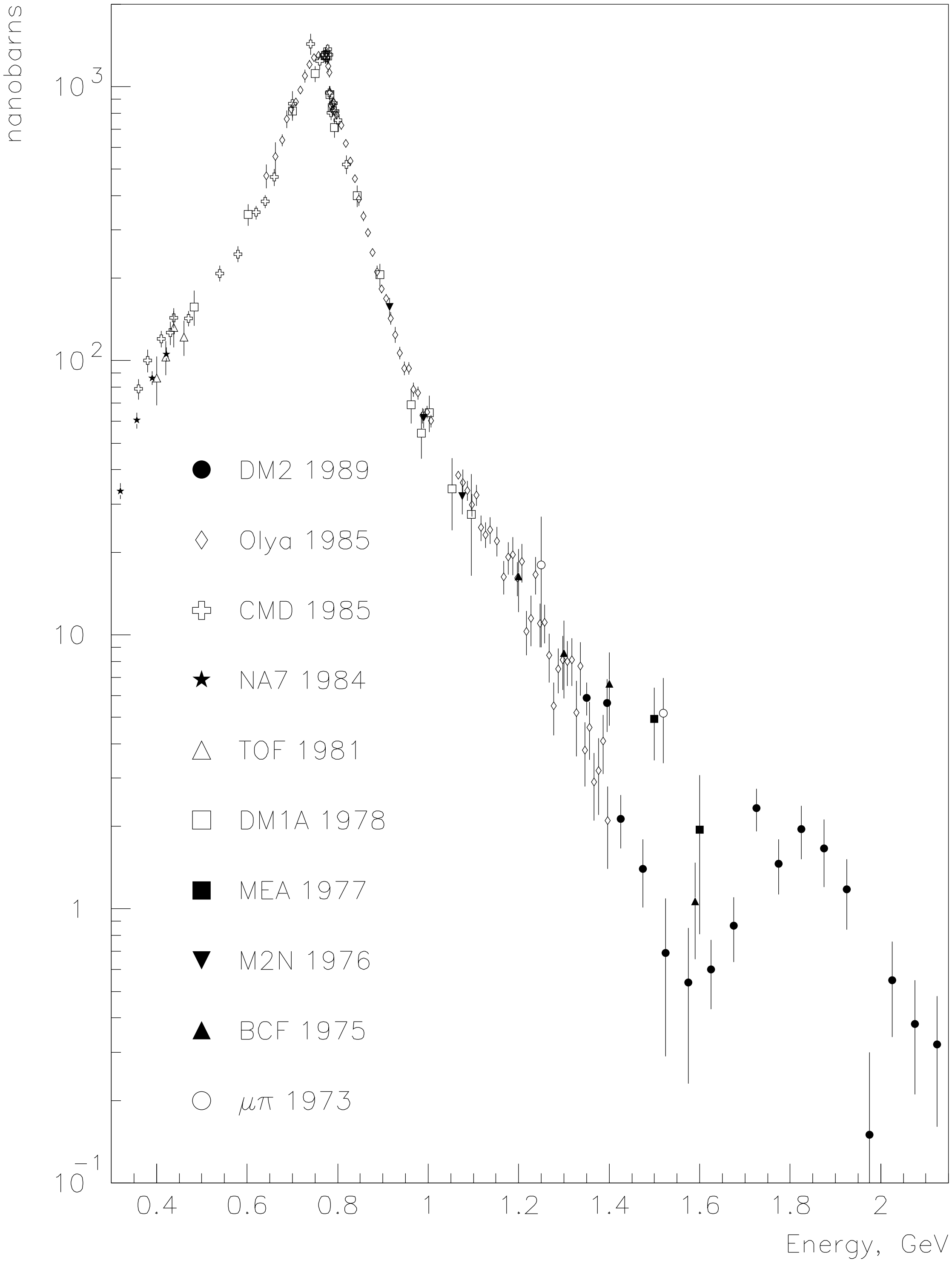


**Figure 2.10**: $e^+e^- \to \pi^+\pi^-$ cross section. Results from DM2 [49], Olya [39, 50], CMD [39], NA7 [51], TOF [52], DM1 [53], MEA [54], M2N [55], BCF [56] and $\mu\pi$ [57] experiments.

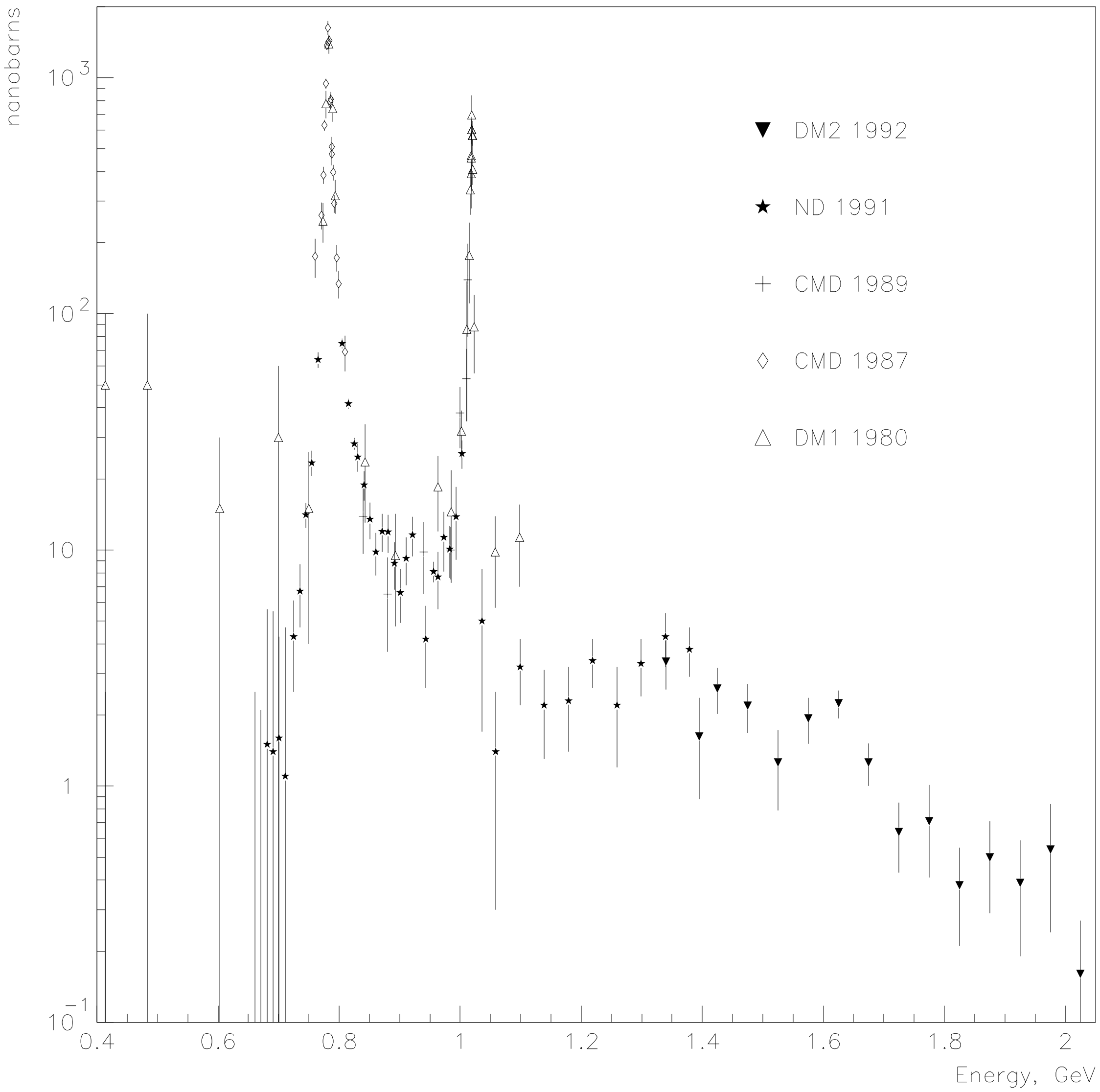


**Figure 2.11**: $e^+e^- \to \pi^+\pi^-\pi^\circ$ cross section. Results from DM2 [58], ND [59], CMD [40, 41] and DM1 [60] experiments.

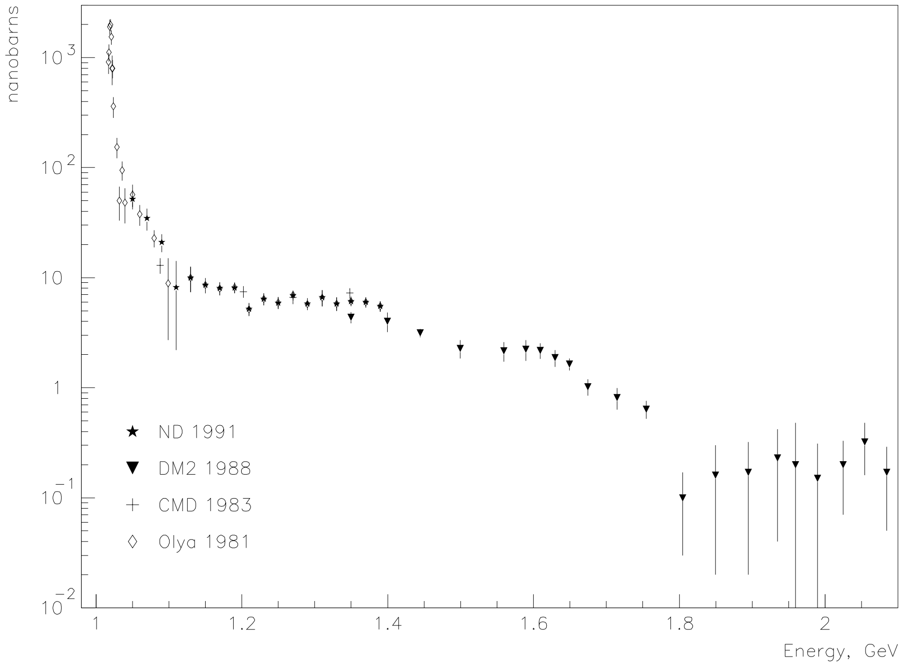


**Figure 2.12**: $e^+e^- \to K^+K^-$ cross section. Results from ND [59], DM2 [61], CMD [42] and Olya [62] experiments

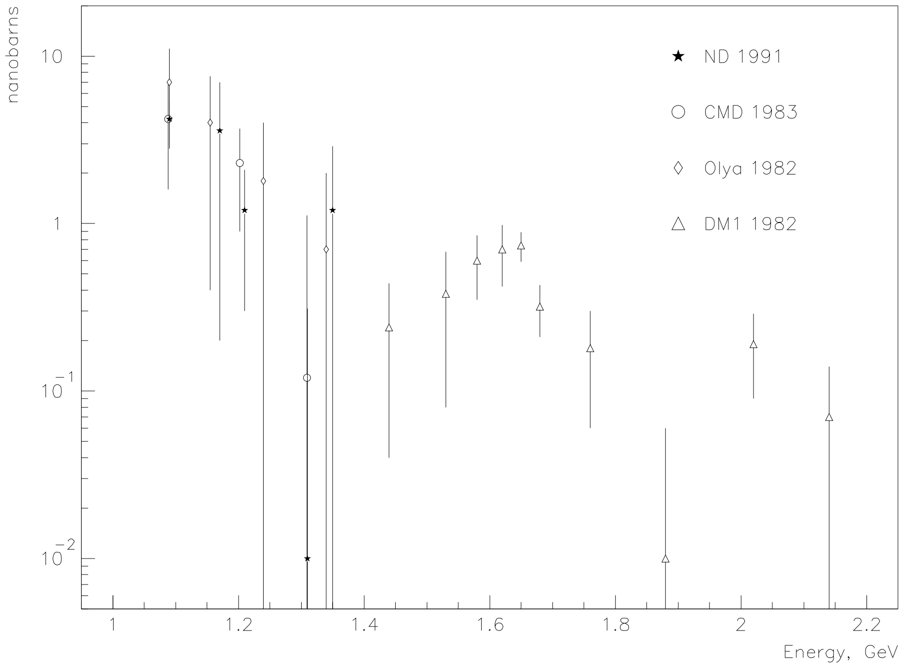


**Figure 2.13**: $e^+e^- \to K_LK_S$ cross section. Results from ND [59], CMD [42], Olya [62] and DM1 [63] experiments

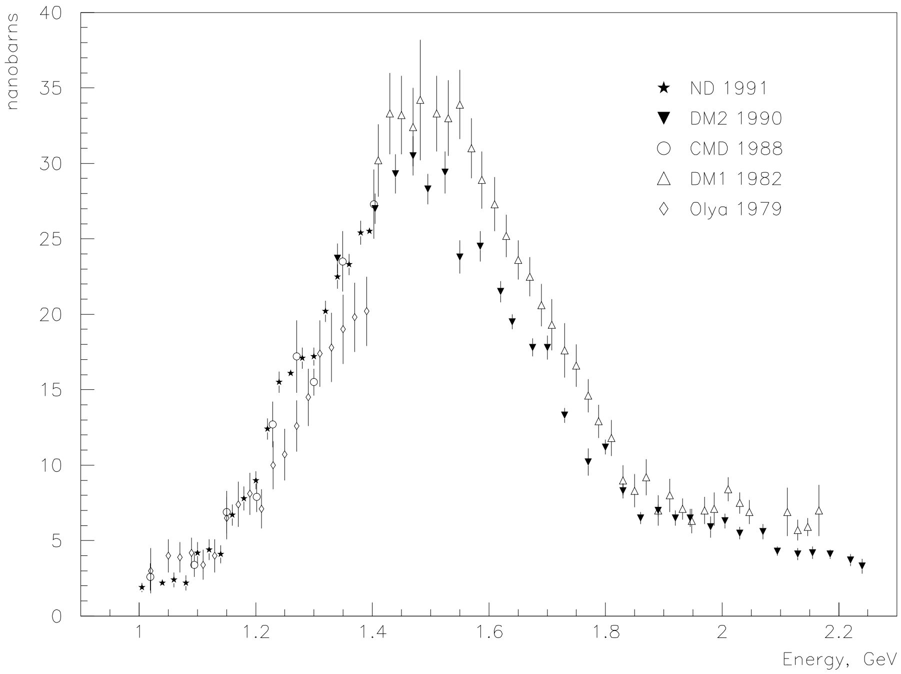


**Figure 2.14**: $e^+e^- \to 2\pi^+2\pi^-$ cross section. Results from ND [59], DM2 [64], CMD [43], DM1 [65] and Olya [66] experiments

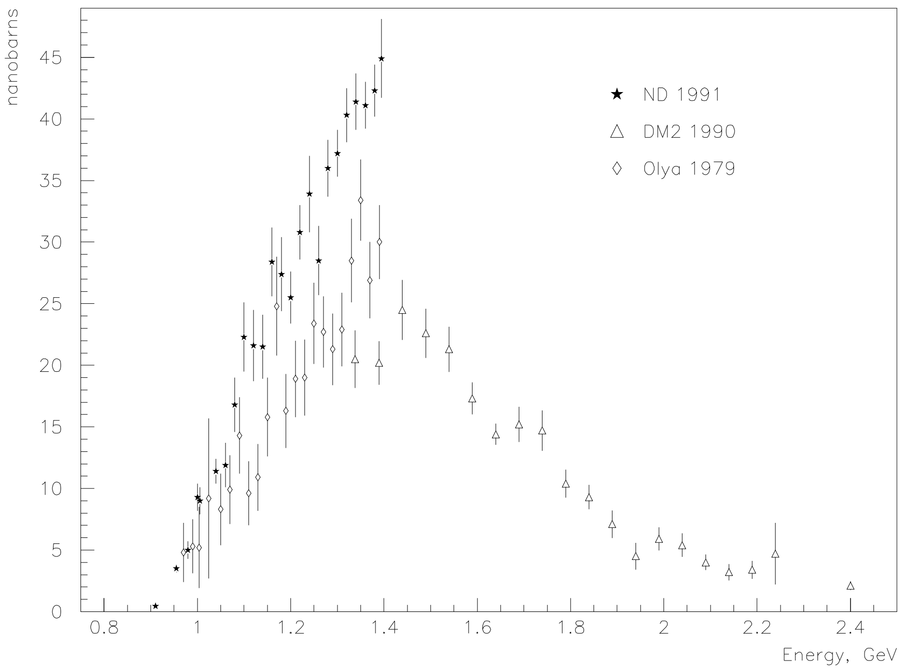


**Figure 2.15**: $e^+e^- \to \pi^+\pi^-2\pi^\circ$ cross section. Results are from ND [59], DM2 [64] and Olya [67] experiments.

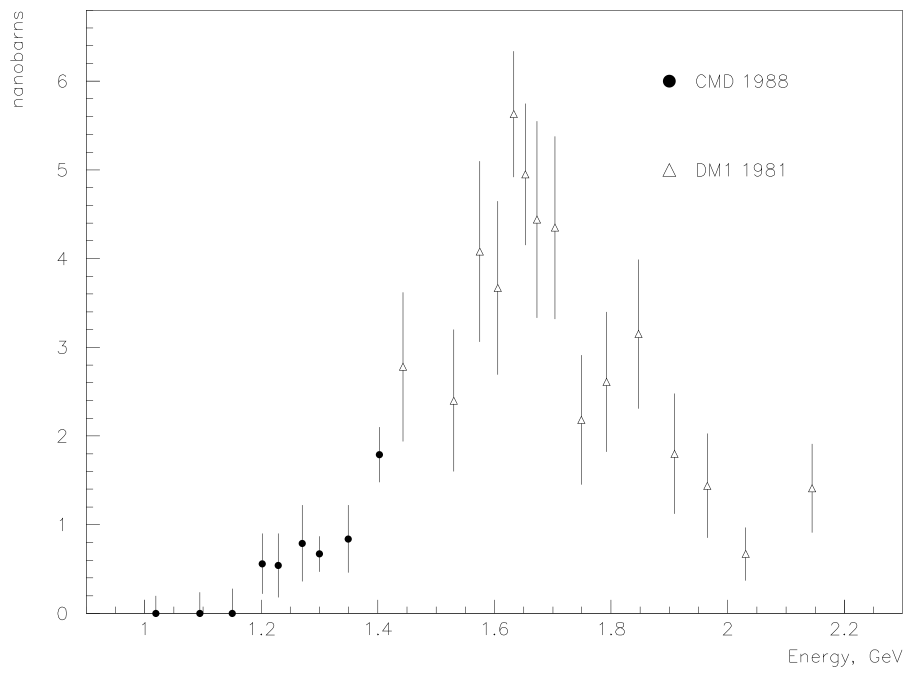


**Figure 2.16**: $e^+e^- \to 2\pi^+2\pi^-\pi^\circ$ cross section. Results are from CMD [43] and DM1 [68] experiments.

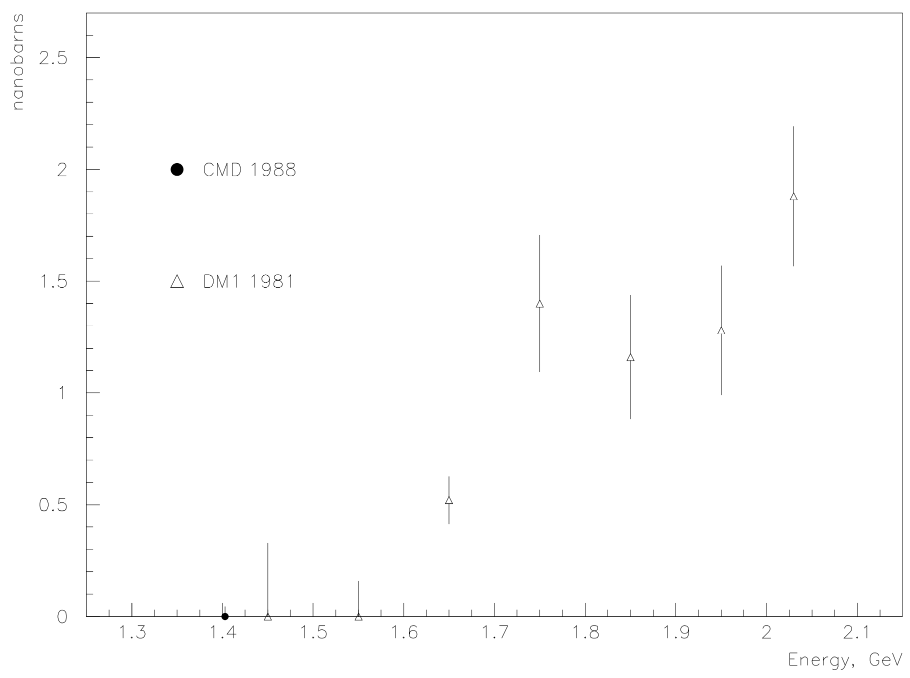


**Figure 2.17**: $e^+e^- \to 3\pi^+3\pi^-$ cross section. Results are from CMD [43] and DM1 [69] experiments

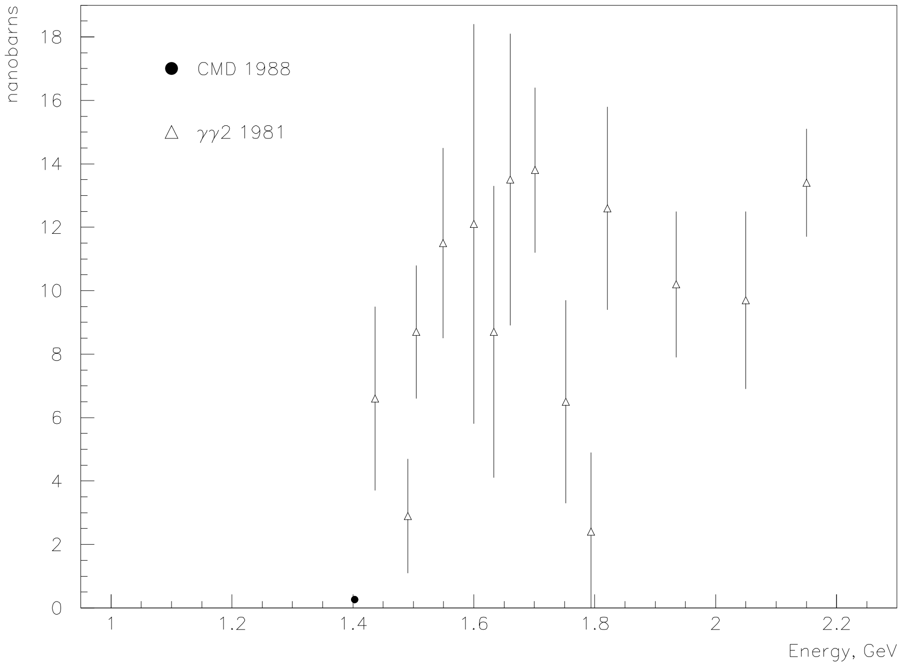


**Figure 2.18**: $e^+e^- \to 2\pi^+2\pi^-2\pi^\circ$ cross section. Results are from CMD [43] and $\gamma\gamma 2$ [70] experiments.

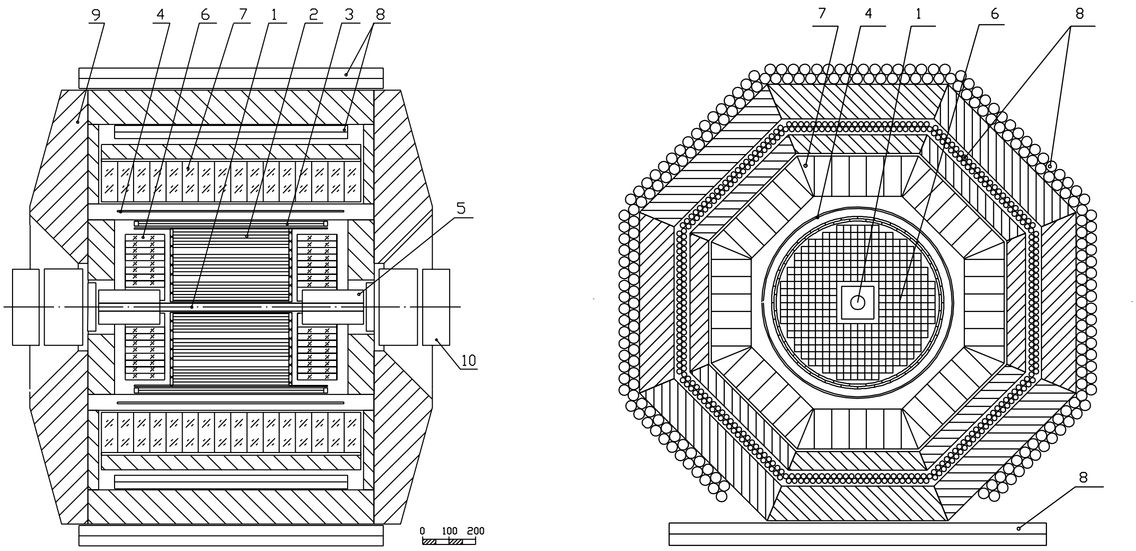

**Figure 2.19**: Horizontal and vertical cross sections of the CMD–2 detector. 1 – vacuum chamber; 2 – drift chamber; 3 – Z–chamber; 4 – main solenoid; 5 – compensating solenoid; 6 – BGO calorimeter; 7 – CsI calorimeter; 8 – muon range system; 9 – magnet yoke, 10 – storage ring lenses.

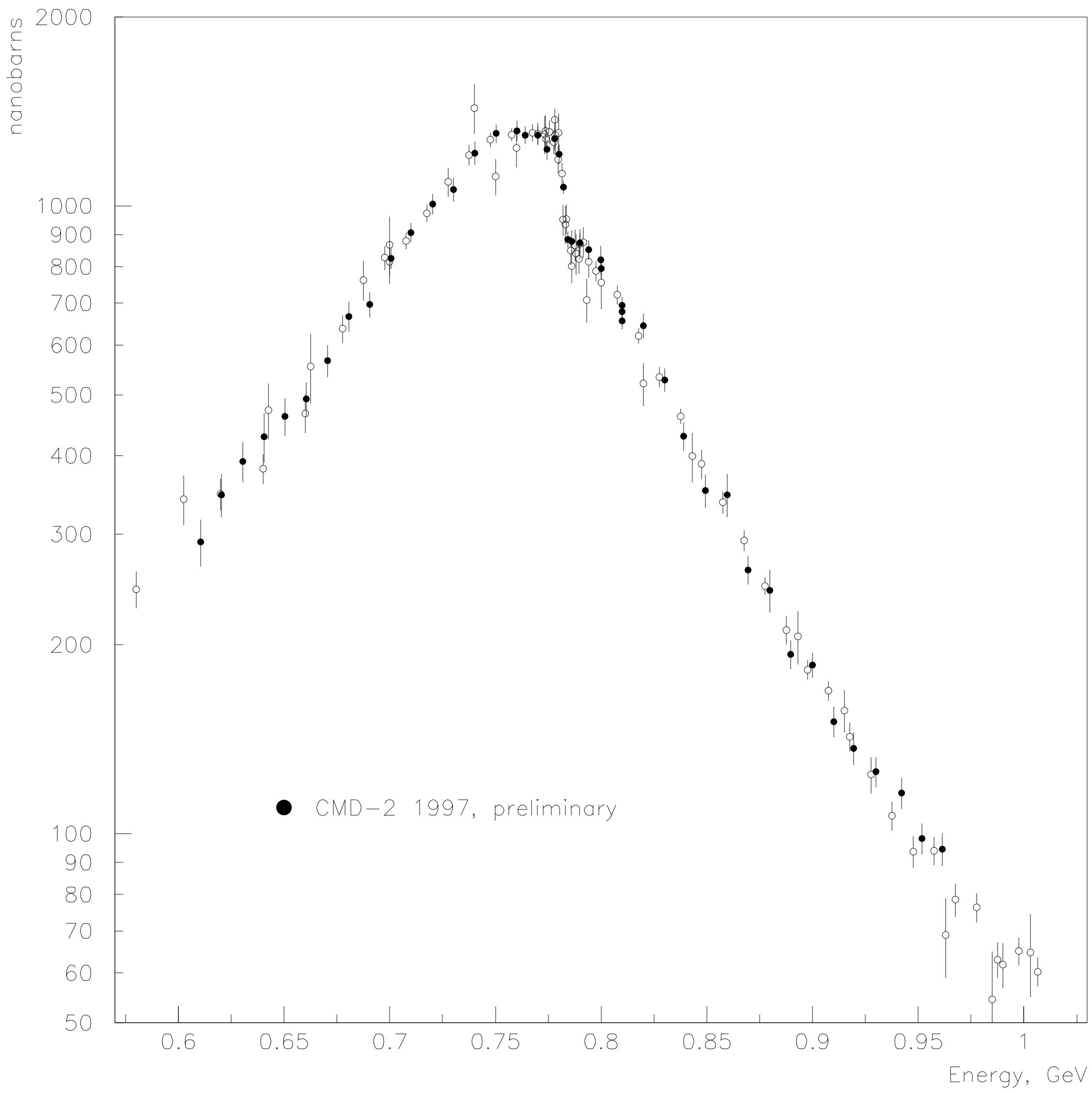


**Figure 2.20**: $e^+e^- \to \pi^+\pi^-$ cross section. Preliminary results from the CMD–2 experiment [71] are shown together with previous results, see Figure 2.10

# Chapter 3

# Muon (g–2) Experiments at CERN

## 3.1 CERN I Experiment, 1958–1962

The muon was discovered in 1947 in cosmic rays [72]. By 1958 evidence was accumulating that the muon behaves as a heavy electron of spin 1/2. QED theory then predicted that the anomalous gyromagnetic ratio of the muon $a_\mu$ should be of the same order as that of the electron, but due to higher momentum transfer $q^2 \approx m^2$, an experiment on the muon would test the theory at much shorter distances. An energy-momentum cut–off $\Lambda$ of order 1 GeV, discussed at that time, would have a 0.5% effect on $a_\mu$. On the other hand, it was believed that the muon should have an extra interaction that gives it its higher mass. The corresponding field should have its own quantum fluctuations and give an extra contribution to the $a_\mu$. The muon (g–2) experiment was recognized as a very sensitive test of the existence of such fields.

The layout of the first muon (g–2) experiment [73] is shown in Figure 3.1. The polarized muon beam from the CERN Synchro–cyclotron was injected into a 6 m long magnet. Muons hit a beryllium absorber, lost energy and therefore trapped inside the magnet. The longitudinal gradient of the magnetic field produces a muon drift of about 0.4 cm/turn along the magnet from the injection to the ejection region. The drift was 2 cm/turn at the injection region to prevent muons from reentering the absorber and 11 cm/turn at the ejection region to provide ejection from the magnet. After ejection muons fell onto the polarization analyzer, where they stopped and decayed to $e^+$. Using flip coils one can rotate the muon spin direction after it has stopped to allow use of a single counter setup to measure the polarization. The electron counts $c_+$ and $c_-$ in forward counters $7{\cdot}\overline{7}'$ were recorded in separate runs with the spin flipped through $+90°$ and $-90°$, respectively.

The asymmetry

$$A \equiv \frac{c_+ - c_-}{c_+ + c_-} = A_\circ \sin\theta_s,$$

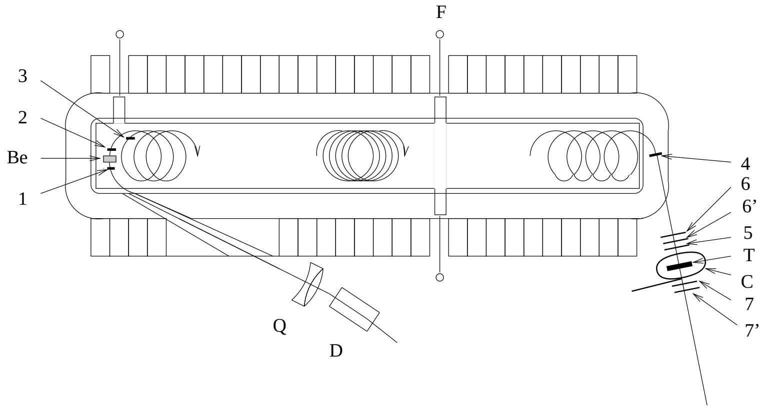


**Figure 3.1**: Scheme of the CERN I experiment: 1, 2, 3, 4, 5, 6, 6′, 7, 7′ – counters; Be – beryllium absorber; C – coil; T – target; D, Q – dipole and quadrupole magnets of the muon beam line.

where $\theta_s$ is the direction of the muon spin before flipping with respect to the muon beam. $\theta_s$ depends on the time t spent by muon in the magnetic field:

$$\theta_s = a_\mu \frac{e}{mc} Bt + const.$$

The time t was measured by counters 1·2·3 at the input and counters $4{\cdot}5{\cdot}6{\cdot}6'{\cdot}\overline{7}$ at the output of the magnet. The decay electron counting rate was about 0.25 per second.

The asymmetry A of decay electron counts as a function of the storage time t is shown in Figure 3.2 together with the fitting function $A_\circ \sin(a_\mu \frac{e}{mc} Bt + \phi_\circ)$.

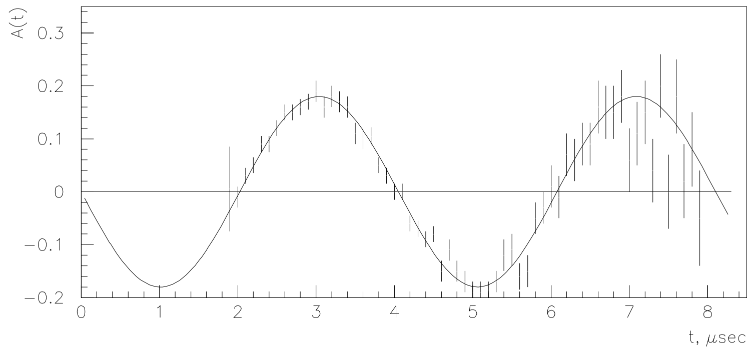


**Figure 3.2**:

The first CERN (g–2) experiment gave $\pm\, 0.4\%$ accuracy in $a_\mu$:

$$a_\mu = (1162 \pm 5) \times 10^{-6}.$$

Within experimental errors it agreed with the QED prediction at that time

$$a_\mu(QED) = \frac{\alpha}{2\pi} + 0.76\frac{\alpha^2}{\pi^2} = 1165 \times 10^{-6} \text{ [74]}.$$

For comparison we list experimental and theoretical values of the anomalous gyromagnetic ratio of electron at that time:

$$a_e(exp) = (1159.622 \pm 0.027) \times 10^{-6} \text{ [75]},$$

$$a_e(QED) = \frac{\alpha}{2\pi} - 0.328\frac{\alpha^2}{\pi^2} = 1159.615 \times 10^{-6} \text{ [76]}.$$

As a result of the experiment, the muon became commonly accepted as a structureless point–like QED particle.

## 3.2 CERN II Experiment, 1962–1968

After the first CERN experiment the muon (g–2) measurement became the best test of QED at short distances. For this reason and to search again for a new interaction, it was desirable to increase the accuracy of the experiment. Hence it was necessary to increase the number of (g–2) cycles observed, either by increasing magnetic field or by lengthening the storage time. The second CERN (g–2) experiment [77] used high-energy muons with relativistically dilated lifetimes, accumulated in a muon storage ring.

The muon storage ring in this experiment was a weak-focusing ring with orbit diameter 5 m, a useful aperture of 4 cm $\times$ 8 cm (height $\times$ width), a beam momentum 1.28 GeV/c corresponding to $\gamma = 12$ and a laboratory muon lifetime of 27 $\mu$sec. The mean field at the central orbit was 1.71 Tesla.

The layout of the experiment is shown in Figure 3.3. A bunch of 10.5 GeV/c protons from the CERN PS was brought onto a target located inside the ring. About 70% of the protons interact, producing, among other things, pions of 1.3 GeV/c that orbit around the ring. About 20% of the pions decay in one turn. The decay of pions at small forward angles give rise to muons of slightly lower momentum, and some of these fall into orbits that miss the target and remain permanently stored in the ring. These muons are longitudinally polarized. About 200 muons were stored per cycle of the proton synchrotron.

To determine the muon spin direction, decay electrons were counted on the inside the ring. The detectors were adjusted to respond only to the high-energy electrons emitted in forward direction in the muon rest frame. Thus as the muon spin rotates, the electron counting rate would be modulated at the (g–2) frequency:

$$N(t) = N_\circ\, e^{-t/\tau}\,[1 + A\,\cos(a_\mu \frac{e}{mc} Bt + \phi)\,]$$

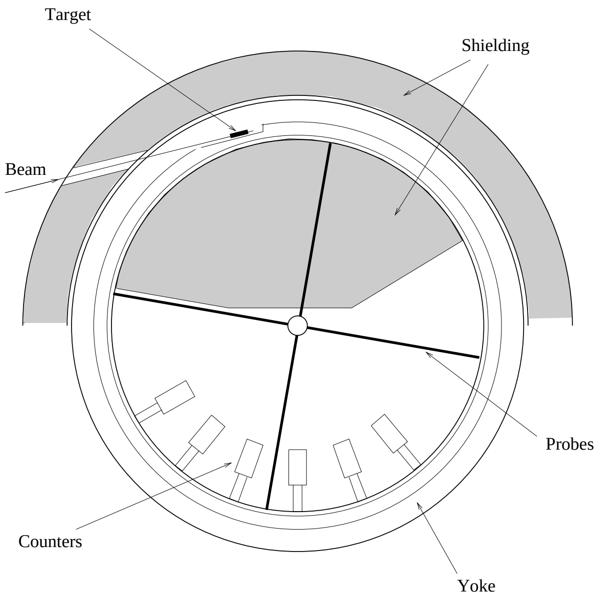


**Figure 3.3**: Scheme of the CERN II experiment

Due to the presence of a constant background and to muon losses at early times, the fitting function was:

$$N(t) = N_\circ \, e^{-t/\tau} \, [1 + A \, \cos(a_\mu \frac{e}{mc} Bt + \phi) \,] \, (1 + A_L \, e^{-t/\tau_L}) + W$$

Decay electron counts as a function of time after injection are shown in Figure 3.4 together with the fitting function. The frequency of (g–2) oscillations was determined to 215 ppm (statistical error). Another principal limitation of accuracy comes from uncertainty in the magnetic field. To provide vertical focusing of the muon beam the magnetic field had a radial gradient

$$\frac{\Delta B}{B} = n \frac{\Delta r}{r} = 0.13 \frac{\Delta r}{r}.$$

Hence one needs to know the radial distribution of the stored muons as well as magnetic field distribution. The radial distribution was determined from the muons debunching between 1.8 and 5.5 $\mu$sec after injection (Figure 3.4, lower histogram) and is shown in Figure 3.5. NMR probes were used for the magnetic field measurements. The averaging magnetic field over the muon distribution was determined to a precision of 160 ppm, leading to the overall accuracy of 270 ppm in $a_\mu$ :

$$a_\mu = (116616 \pm 31) \times 10^{-8} \, (270 \, ppm).$$

The experiment agreed with theory within experimental error:

$$a_\mu^{exp} - a_\mu^{th} = 240 \, \pm \, 270 \, ppm.$$

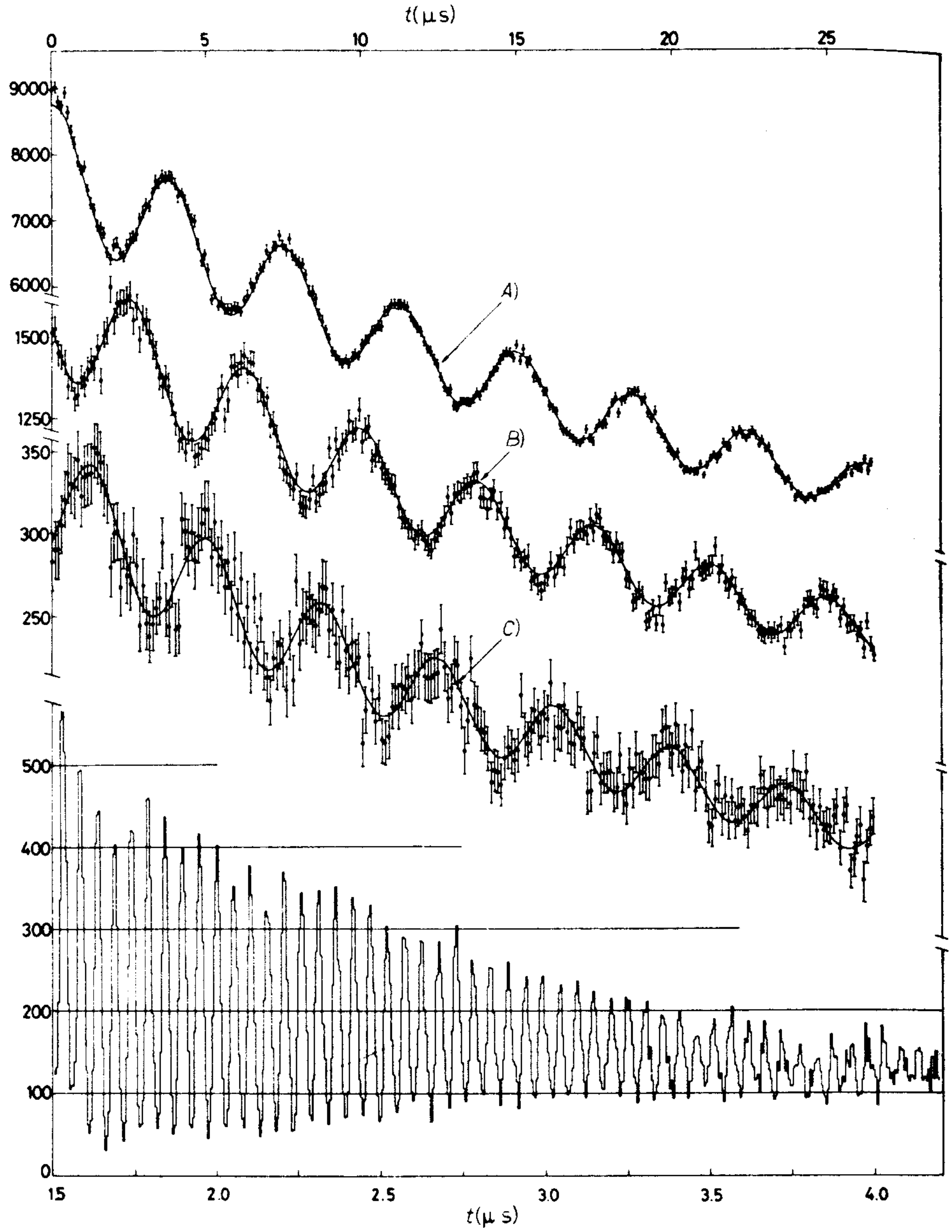


**Figure 3.4**: CERN II experiment. Distribution of decay electrons as a function of time. A) from 20 to 45 $\mu$sec, B) from 65 to 90 $\mu$sec, C) from 105 to 130 $\mu$sec (upper scale of time). The lower histogram shows the rotation frequency of the muon as seen at the earlier times (lower scale of time).

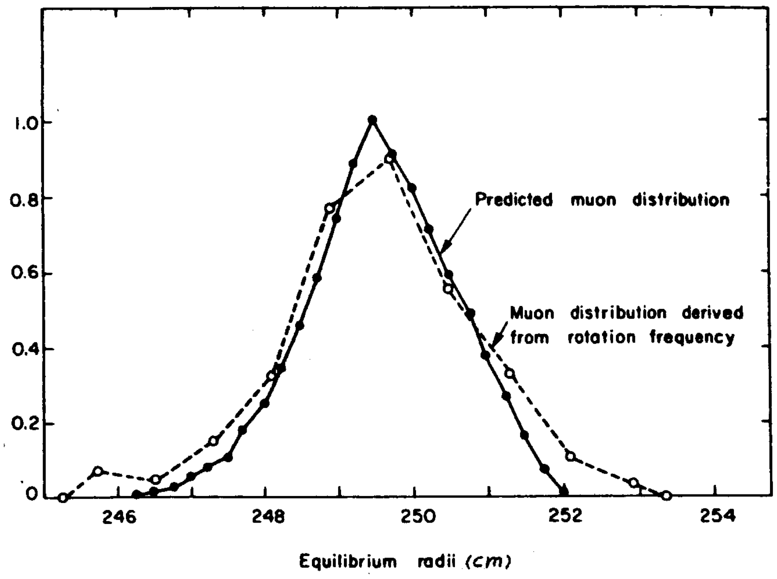


**Figure 3.5**: CERN II experiment. Distribution of equilibrium radii of stored muons.

## 3.3 CERN III Experiment, 1969–1976

The third CERN (g–2) experiment [1] had its origins in the previous one. Its design was an attempt to overcome the major sources of uncertainty arising in that experiment:
— Use a ring magnet with a uniform magnetic field and focusing vertically with an electric quadrupole field in order to eliminate the radial dependence of the frequency of (g–2) oscillations.
— Inject a momentum–selected beam of pions, instead of protons, into the ring in order to reduce the background and use more space inside the ring for detectors. This would increase statistics of the experiment.
— Increase the product $\gamma \cdot B$, and thus increase the number of (g–2) cycles per muon lifetime.

In the presence of a transverse electric field the precession of the spin relative to the velocity is given by:

$$\vec{\omega_a} = \frac{e}{mc}\,[a_\mu \vec{B} + (\frac{1}{\gamma^2 - 1} - a_\mu)\,\vec{\beta} \times \vec{E}]$$

Choosing $\gamma = \sqrt{1 + 1/a_\mu} = 29.304$ ("magic gamma") eliminates the dependence of $\omega_a$ on the electric field. This "magic gamma" corresponds to a muon energy E = 3.096 GeV/$c^2$ and momentum P = 3.094 GeV/c. Hence the "magic gamma" muons are stored in a uniform magnetic field which determines the spin motion, while focusing is provided by an electric field which has no influence on $\omega_a$. In practice, muons are uniformly distributed over available phase space of the storage ring and some of them can be off the "magic momentum" by about $\pm 0.5\%$. In the quadrupole electric field, this leads to correction of $\sim 1$ ppm in $\omega_a$. The "magic gamma" principle is the essential basis of both the CERN III and new BNL (g–2) experiments.

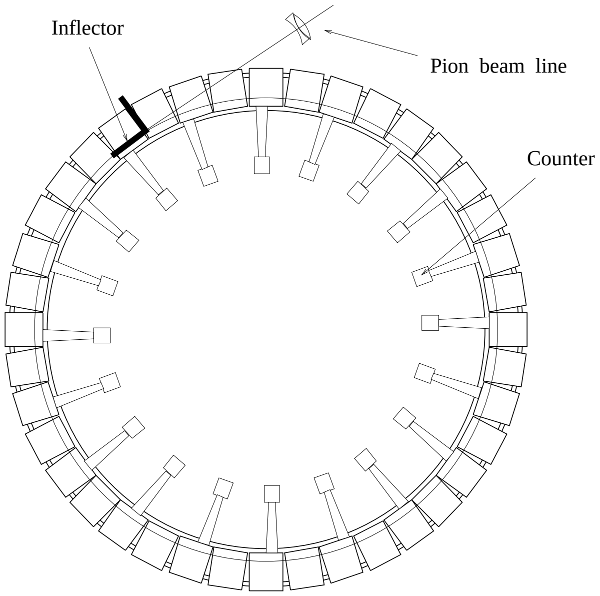


**Figure 3.6**: Scheme of the CERN III experiment

The top view and cross-section of the muon storage ring are shown in Figures 3.6 and 3.7 respectively. The storage ring consists of 40 C–shaped bending magnets, each about 1 m long, fit together to form a polygon with open sides facing the center of the ring. The pole gap is 14 cm high and 38 cm wide. The magnets were energized in series by four large circular coils. Each coil was divided into five sectors for cooling purposes. The field in every sector was stabilized at 1.472 T with 40 NMR probes located just outside the muon storage region. The signal from these probes was used to control the current through 40 compensating coils wound around the yoke close to each pole. During data-taking the magnetic fields were monitored in 37 magnets with small NMR probes which could be inserted into the muon storage ring along a radial line in the median plane without destroying the vacuum. The procedure was controlled by a computer program and took only 10 minutes. This provided monitoring the field during the period between full–scale field maps.

A momentum-selected pion beam was injected into the ring by a pulsed inflector. The inflector was a coaxial line in which a 10 $\mu$sec current pulse of peak value 300 kA produced the required field of about of 1.5 T.

The electrostatic quadrupole electrodes covered about 80% of the circumference of

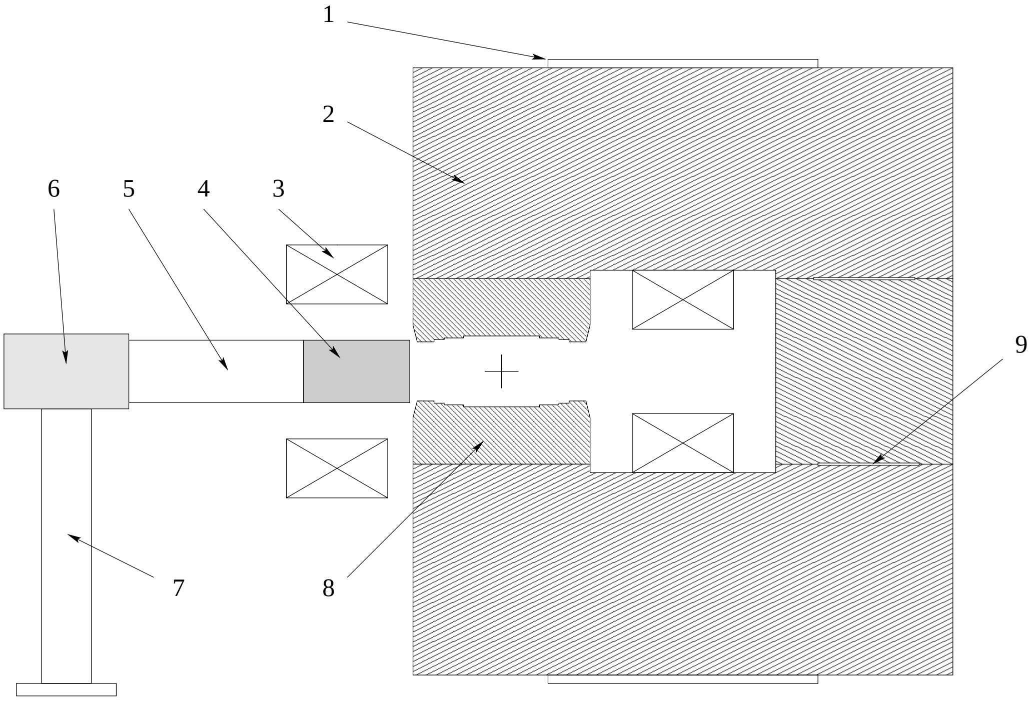


**Figure 3.7**: Cross section of the CERN III magnet and detector station: 1 – iron plate of variable size; 2 – yoke; 3 – copper coil; 4 – lead/scintillator sandwich; 5 – air light guide; 6 – PMT; 7 – support; 8 – pole; 9 – air gap

the ring. The shape of the electrodes approximated a pair of hyperbolae which would give a perfect quadrupole field. The applied voltages were flat-topped pulses about 1 msec long and of magnitude 24 kV for the side electrodes and –3.7 kV for the top and bottom electrodes. The pulses were switched on about 6 $\mu$sec before the arrival of the pion bunch. The electrodes were switched asymmetrically, with 1 and 10 $\mu$sec rise times, so that the muon orbits were moved radially outward on one side of the ring and radially inwards on the other and vertically downward. This shift of the orbits at early times was done in order to diminish or "scrape" those muons most likely to be lost, thus reducing muon losses at later time.

The decay electrons were detected by a system of 20 shower counters spaced uniformly around the inside of the ring. Each counter was made up of 13 sheets of plastic scintillator of 1 cm thick, interspersed with 0.5 cm thick sheets of lead. The light was transmitted through an air light guide onto 5-inch photomultiplier (PMT). To reduce effect of the large initial flash of light when the beam was injected into the storage ring, the PMTs were blanked off during this period.

Information on the radial distribution of the stored muons was obtained as before by analysis of the bunch structure of the muons in the ring at early times, see Figure 3.8. The reconstructed radial distribution of muons is shown in Figure 3.9.

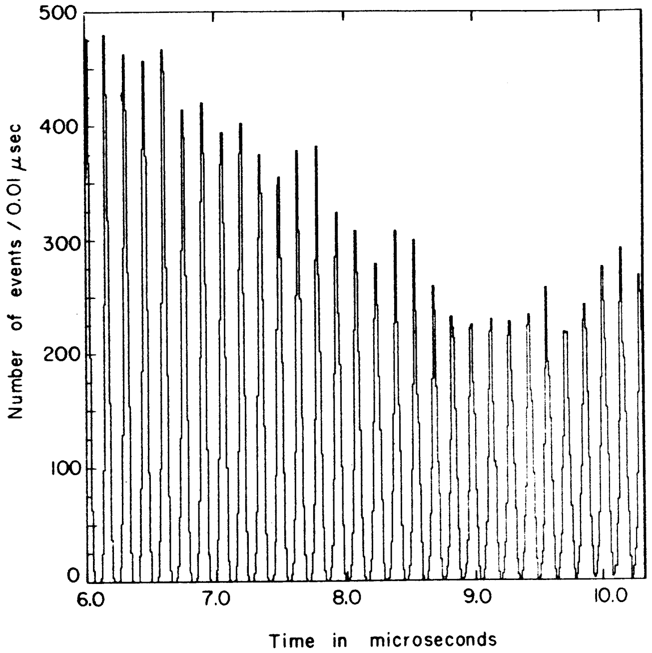


**Figure 3.8**: CERN III experiment. Count rate of decay electrons at early time.

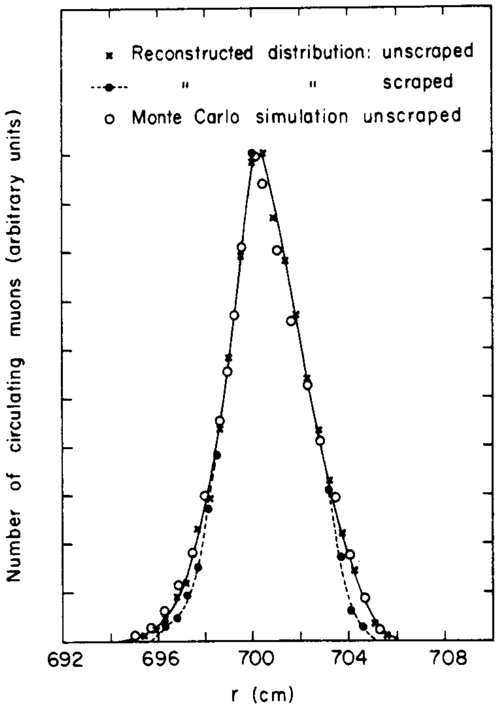


**Figure 3.9**: CERN III experiment. Distribution of equilibrium radii of stored muons.

Figure 3.10 shows the total decay electron counts versus storage time. As in the second CERN (g–2) experiment the eight-parameter function

$$N(t) = N_\circ\, e^{-t/\tau}\, [1 + A\, \cos(a_\mu \frac{e}{mc} B t + \phi)\,]\, (1 + A_L\, e^{-t/\tau_L}) + W$$

was used to fit the data. The results of the CERN III experiment are:

$$a_{\mu^+} = 1\,165\,910\,(11) \times 10^{-9}\ (9.4\, ppm)$$

$$a_{\mu^-} = 1\,165\,937\,(12) \times 10^{-9}\ (10.3\, ppm)$$

and for $\mu^+$ and $\mu^-$ combined

$$a_\mu = 1\,165\,923\,(8.4) \times 10^{-9}\ (7.2\, ppm).$$

The current theoretical value

$$a_\mu(theory) = 1\,165\,916.3\,(0.8) \times 10^{-9}$$

is in good agreement with the experimental value:

$$a_\mu(exp) - a_\mu(theory) = (6.7 \pm 8.4) \times 10^{-9}.$$

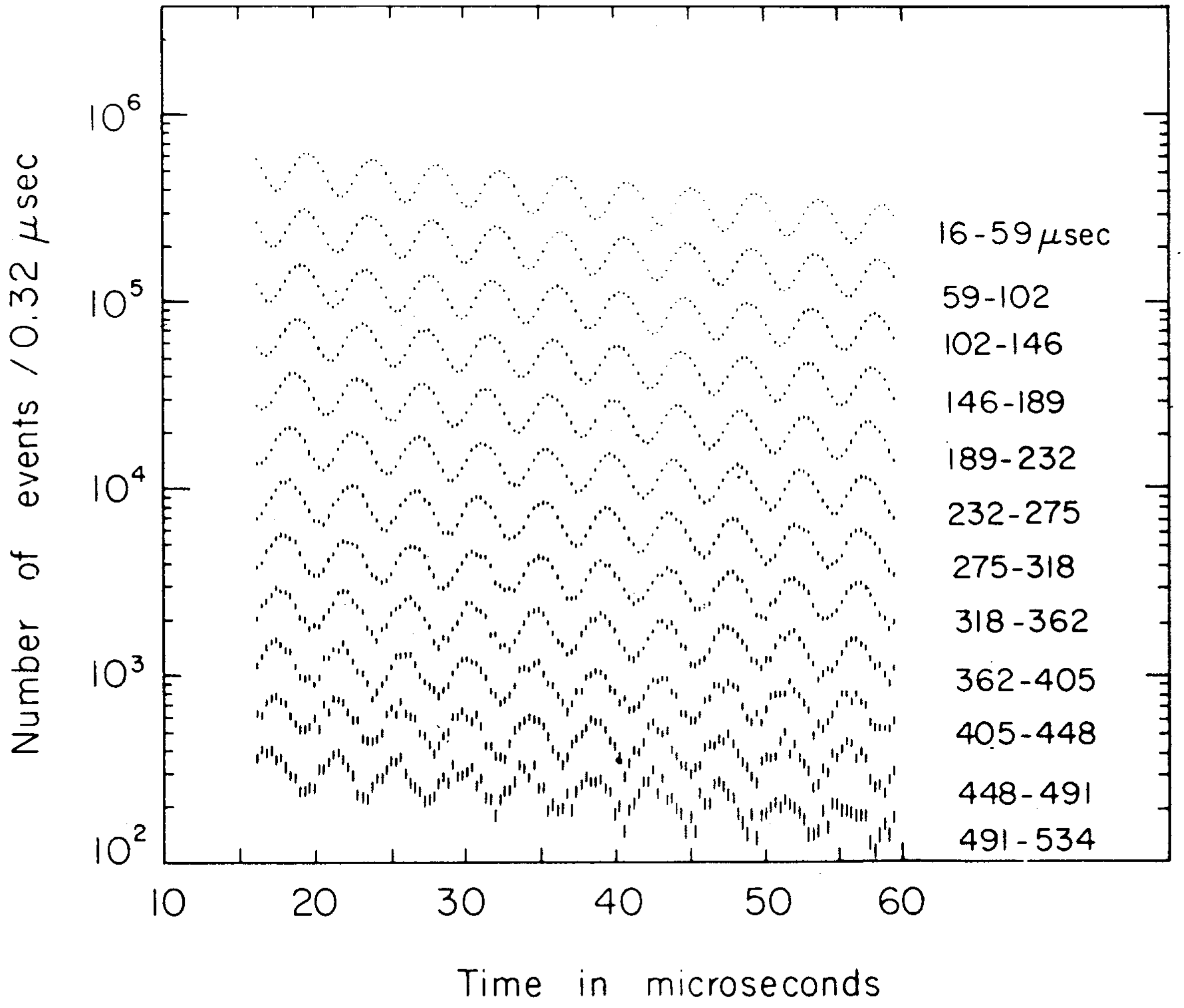


**Figure 3.10**: CERN III experiment. Distribution of decay electrons as a function of time

# Chapter 4

# BNL E821 Experiment

## 4.1 Introduction

The goal of the new BNL (g–2) experiment is a measurement of $a_\mu$ to 0.35 ppm, a factor of 20 improvement over that of the CERN III experiment. Starting in 1983 several possible schemes for a new (g–2) experiment, including use of superconducting storage ring at 5T [78], were discussed. Finally a method similar to that used at CERN was chosen and a formal proposal was submitted in 1985 [11]. As for CERN III we use a beam of polarized muons with a momentum P = 3.094 GeV/c ("magic gamma") captured in a superferric muon storage ring with a diameter for the central orbit of 14.224 m and a magnetic field of 1.45 T. Twenty four detector stations detect decay electrons inside of the ring. The new experiment, however, incorporates several major new features and advances which should allow us to achieve the desired accuracy.

The main contribution to the final experimental error of the CERN III experiment was the statistical error of 7 ppm. The BNL AGS with its booster provides a primary proton beam intensity some 200 times greater than the CERN PS at the time of the CERN III experiment. Also the BNL experiment will use direct muon injection into the ring, instead of proton injection in CERN II experiment and pion injection in CERN III experiment and this should provide a major increase in the number of stored mouns and also a large reduction in background, especially at early times. A fast muon kicker is required for muon injection. The pion injection option was used for our initial run and has provided the result for the present thesis.

The major systematic error in the CERN III experiment was a 1.5 ppm error in knowledge of the magnetic field averaging over space, time and muon distribution as well as its absolute value, i.e. calibration of the NMR probes with respect to a standard probe. An improvement by about a factor of 10 is expected for our experiment due to:
— better uniformity and stability of magnetic field;

— control and more frequent measurements of the field, including NMR beam tube trolley measurements during the runs;
— improved absolute calibration of the NMR probes;
— several methods to measure muon distribution over the beam aperture at wide time interval are being implemented.

## 4.2 Alternating Gradient Synchrotron

In July 1960, the Alternating Gradient Synchrotron (AGS) at the Brookhaven National Laboratory (BNL) first accelerated protons to about 30 GeV and had an intensity $\sim 10^{10}$ protons per pulse. Since then, the AGS has been periodically upgraded, improved and modified: the initial 50 MeV LINAC injector was replaced by the 200 MeV LINAC in 1970, the AGS was connected to the existing Tandem Van de Graaff accelerator in 1983 for acceleration of heavy ions, the 1.6 GeV Booster was added in 1991, the transfer U and V lines from the AGS to the Relativistic Heavy Ions Collider (RHIC) and the muon (g–2) storage ring were commissioned in 1995 and 1996 respectively. A schematic diagram of the AGS complex is shown in Figure 4.1.

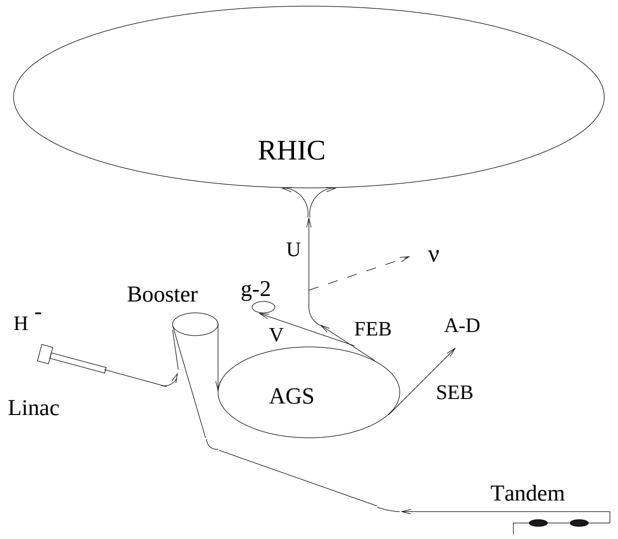


**Figure 4.1**: AGS – RHIC complex

Today the AGS accelerator complex can
— accelerate heavy ions up to gold ($Au^{77+}$) at various energies for the heavy ion physics program;
— produce a slow–extracted proton beam (SEB) of about $60 \cdot 10^{12}$ protons per pulse

at 25 GeV/c with a 1.6 sec uniform spill time for various particle physics experiments such as rare K–decay studies;
— operate in a fast–extracted beam (FEB) mode, i.e. produce bunched beams of $\sim 5 \cdot 10^{12}$ protons 8 times per AGS cycle for the muon (g–2) experiment and for RHIC.

The 200 MeV LINAC produces an average $H^-$ current of 20 mA which is injected through charge exchange into the AGS Booster. The Booster accelerates the protons to a kinetic energy of 1.6 GeV and then the protons are injected into the AGS. This process is repeated four times, filling the AGS ring in about one half second. The AGS accelerates the protons to 22–25 GeV/c and they are extracted in 8 bunches with a 33 msec time intervals between. The total AGS cycle is about 2.6 second.

After 1999 the AGS will become an injector for RHIC to fill its two rings with heavy ions such as gold or with polarized protons with a filling time of a few minutes every 8–10 hours. The AGS could be available between RHIC fills for particle and nuclear physics experiments including our muon (g–2) experiment.

More information about the AGS complex can be found in [79].

## 4.3 Beam Line

In the fast–extracted beam mode the AGS provides one bunch of protons at a time and sends it into the U/V channel to supply RHIC by the U line or the (g–2) muon storage ring by the V line. The scheme of the (g–2) beam line is shown in Figure 4.2. After exiting from the AGS the primary proton beam is carried in the U/V line to the dipole magnets VD3, VD4 where it is deflected about 3.0 degrees to the V targeting area. The beam is focused on the V target by quadrupole magnets VQ9 – VQ12 (not shown in Figure 4.2). The target is designed to withstand high beam heating for intensities up to $60 \cdot 10^{12}$ protons per AGS cycle. Beyond the target the residual proton beam bends only 2.1 degrees in D1, misses D2 and is absorbed in the beam stop.

Secondary pions are collected by quadrupoles Q1 and Q2 and focused onto the collimator K1–K2, which selects the required momentum bite of pions. Dipole magnets D1 – D4 bend the pion beam into a 72 m straight $\pi/\mu$ transport channel with quadrupole magnets Q7 through Q20. Dipoles D5 and D6 and the quadrupoles Q21 – Q25 provide the final momentum selection and direct the beam into the ring through the inflector. The plane of the muon ring is about 2.1 meters below the AGS plane. The necessary drop is accomplished by bending the beam 2.41 degrees downward by the pitching magnet P1 and restoring to a horizontal by the pitching magnet P2. Ion chambers IC1 – IC8 are used for beam profile and intensity measurements.

The long transport channel allows use of both pion and muon injection into the ring. For pions the injection momentum is 3.1 GeV/c and the associated decay length is 174 m, so that 50% of the pions decay along the transport channel. For muons the

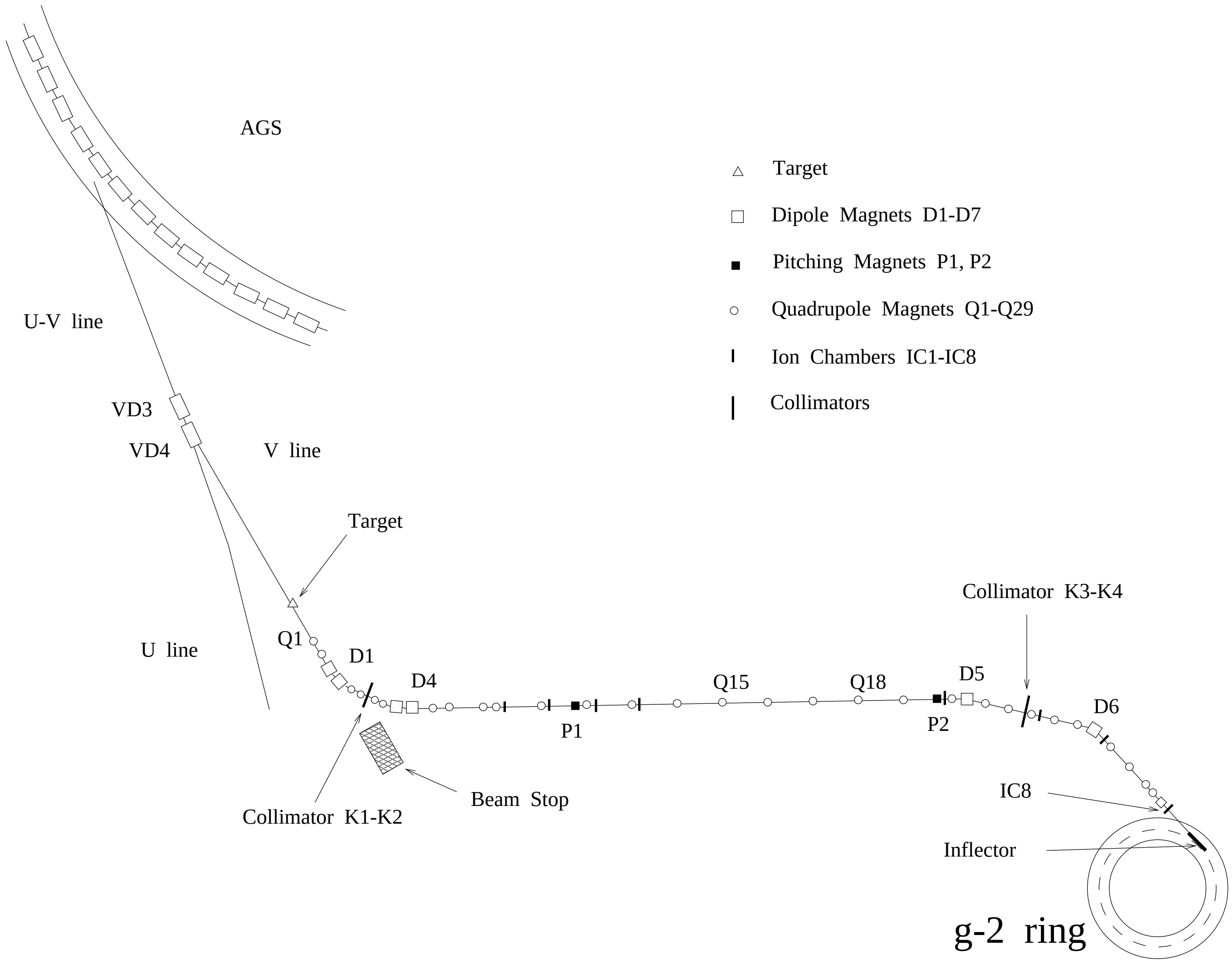


**Figure 4.2:** g−2 beam line

distance is from the pion selecting slit K1–K2 at 8.7 m downstream of the target to the pion rejection slit K3–K4 at 97.5 m. Thus, the fraction of the original pions at the target, which decay within this region, is $(e^{-8.7/174} - e^{-97.5/174}) = 38.0\%$. For pion injection the pion flux at the inflector entrance is calculated to be $N_\pi = 2.6 \cdot 10^7$ pions per $10^{12}$ protons at the target [10, 80]. For muon injection the expected muon flux at the inflector entrance is $N_\mu = 10^5$ muons per $10^{12}$ protons at the target.

(g–2) beam $\pi/\mu$ line was constructed in 1991–1995 and commissioned with the beam in May–June 1996.

## 4.4 Muon Storage Ring

The muon storage ring provides a magnetic field of about 1.45 Tesla over the muon storage region, which is of toroidal shape with the radius of the central orbit being 711.2 cm (280 inches) and cross sectional diameter being 9 cm. The requirements on the magnetic field are very stringent: the field must be homogeneous to 1 ppm over the storage region (after averaging over azimuth) and must be known and stable to 0.1 ppm.

The cross section of the muon storage ring is shown in Figure 4.3. The magnet has a C-shape to allow decay electrons to be observed inside the ring. The yoke consists of twelve 30° sections, bolted together to form a circle. The yoke pieces are made of conventional quality steel 1006 (0.06% carbon content). Better quality steel 10003 (0.003% carbon) with greatly minimized inclusions of ferric material, air bubbles, etc. was used to produce the pole pieces. Thirty six top and bottom pole pieces, each about 124 cm (10°) long form two circles. The field in the storage region is determined dominantly by the iron, i.e. its geometry, construction tolerances, temperature control, etc. The air gap between the pole pieces and the yoke serves to decouple the magnetic field in the storage region from that in the yoke. This gap is believed to be a very important feature of our magnet design.

Part of the gap between the pole pieces and the yoke is occupied by iron wedges. They can compensate for the larger reluctance due to greater iron path length farthest from the return. The wedges are about 10 cm in the azimuthal direction and can be individually moved in the radial direction. They can be used for fine adjustment of the magnetic field, see Chapter 5.

The magnet is excited by four ring-shaped superconducting coils. The use of superconducting coils has advantages over copper coils. They provide thermal stability, low power consumption, low resistance R and hence use of a low voltage well regulated (to 0.3%) power supply, high L/R and hence low ripple currents; thermal independence of the coils and the iron.

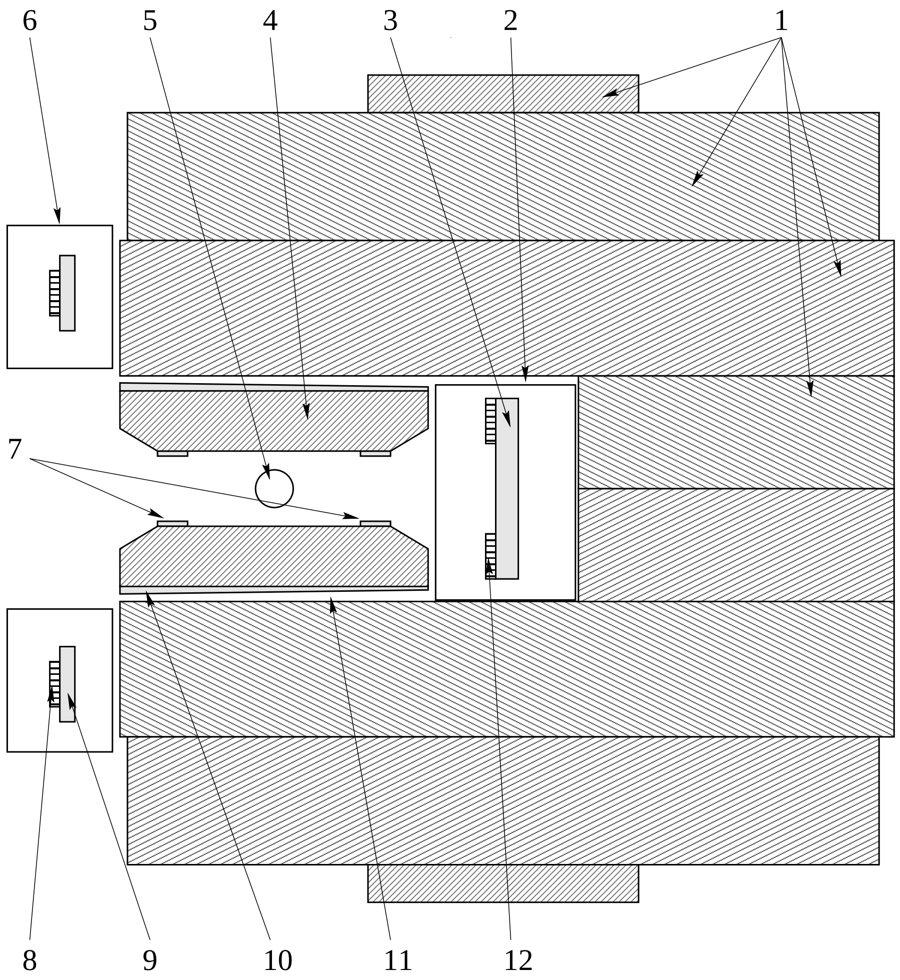


**Figure 4.3**: Muon storage ring. 1 – yoke plates, 2 – outer cryostat, 3 – outer mandrel, 4 – pole, 5 – muon storage region, 6 – inner upper cryostat, 7 – Rose shims, 8 – inner lower coil, 9 – inner lower mandrel, 10 – wedge, 11 – air gap, 12 – outer lower coil.

## 4.5 Magnetic Field Measurement and Control

To measure and control the magnetic field with 0.1 ppm relative accuracy, a pulsed NMR system has been developed. The high resolution of an NMR device arises from the sharp resonance lines observed in many liquid or gaseous samples containing nuclei with nonzero spin. In an external magnetic field $B_\circ$ a nucleus with spin $\frac{1}{2}$ has two eigenstates separated in energy by

$$\Delta E = \hbar\omega_L, \ \ \omega_L = \gamma_I B_\circ,$$

where $\omega_L$ is the Larmor frequency and $\gamma_I$ is the gyromagnetic ratio of the nucleus. For a free proton $\gamma_p = 2\pi \times 42.577\ 469(13)$ MHz/T [81]. In thermal equilibrium the magnetic moments of nuclei in a sample give rise to a static macroscopic magnetic moment $\vec{M}$, which is parallel and proportional to the applied field $\vec{B}_\circ$. If we now apply an additional rf-pulsed field $\vec{B}_1$, orthogonal to the field $\vec{B}_\circ$ and circularly polarized with angular frequency $\omega_L$, the magnetization $\vec{M}$ will precess around $\vec{B}_\circ$ with angular frequency $\omega_L$. For a pulse duration of $t = (\pi/2)/\gamma_I B_1$, the magnetization will tilted by 90°. For complete description of the time evolution of $\vec{M}$ relaxation effects which drive the magnetization back to its thermal equilibrium value must be considered. The behavior of $\vec{M}$ is described by the Bloch equations [82] :

$$\frac{dM_z}{dt} = \frac{M_\circ - M_z}{T_1},$$

$$\frac{dM_{x,y}}{dt} = \gamma_I \, (\vec{M} \times \vec{B}_\circ)_{x,y} - \frac{M_{x,y}}{T_2},$$

where $T_1$ and $T_2$ are time constants for the decay of parallel and orthogonal components of $\vec{M}$ with respect to $\vec{B}_\circ$. For the proton magnetization in pure water at room temperature $T_1 = T_2 \approx 3$ second, corresponding to a linewidth $\Delta\omega$ of $2\pi \times 0.1$ Hz. In a field of 1.45 T, $\omega_L = 2\pi \times 61.7$ MHz and hence the high resolution of order of $\Delta\omega/\omega_L = 1.6 \times 10^{-9}$ can be achieved.

The proton frequency in our experiment is measured by a pulsed NMR magnetometer described in [83, 84] and shown in Figure 4.4. A VME computer triggers a pulse amplifier to deliver an rf–pulse of about 4 $\mu$s duration derived from a synthesizer which is stabilized by the LORAN–C frequency standard. The frequency of the synthesizer output, $\nu_{ref}$, is chosen to be close to the NMR frequency, $\nu_p$. The rf–pulse produces a linearly polarized rf–field $\vec{H}_1$ in a coil $L_S$. One of the circularly polarized components of $\vec{H}_1$ tilts the magnetization by 90°. The precessing component of the proton magnetization induces a voltage of frequency $\nu_p$ in the coil $L_S$. This NMR signal is transmitted by a duplexer to the input of a low noise preamplifier. The amplified NMR signal is mixed with the synthesizer output and the frequency difference $\nu_{FID} = \nu_p - \nu_{ref}$ is selected by a low pass filter and further amplified. The frequency $\nu_{FID}$ ( FID is an abbreviation for free induction decay) is in the kHz range and is measured with a frequency counter. A multiplexer allows use of up to 20 NMR probes with a single magnetometer.

The majority of NMR probes in the BNL muon (g–2) experiment are the 366 fixed probes embedded in the upper and lower plates of the muon vacuum chamber. The design of these probes is shown in Figure 4.5. A dilute aqueous solution of $CuSO_4$ is used to reduce the relaxation time to $\approx$ 30 msec in order to increase the repetition rate of the field measurements. Twenty five NMR probes were mounted on a movable platform (shimming trolley) and used for the magnet shimming in 1996, see section 5.5. Seventeen NMR probes were mounted on a beam tube trolley and used for the mapping the magnetic field during the first run in 1997, see section 6.4.

The absolute calibration of 25 NMR probes mounted on the shimming trolley and 17 probes on the beam tube trolley was done with a calibration probe, shown in Figure 4.6. The calibration probe in turn was calibrated with a standard NMR probe

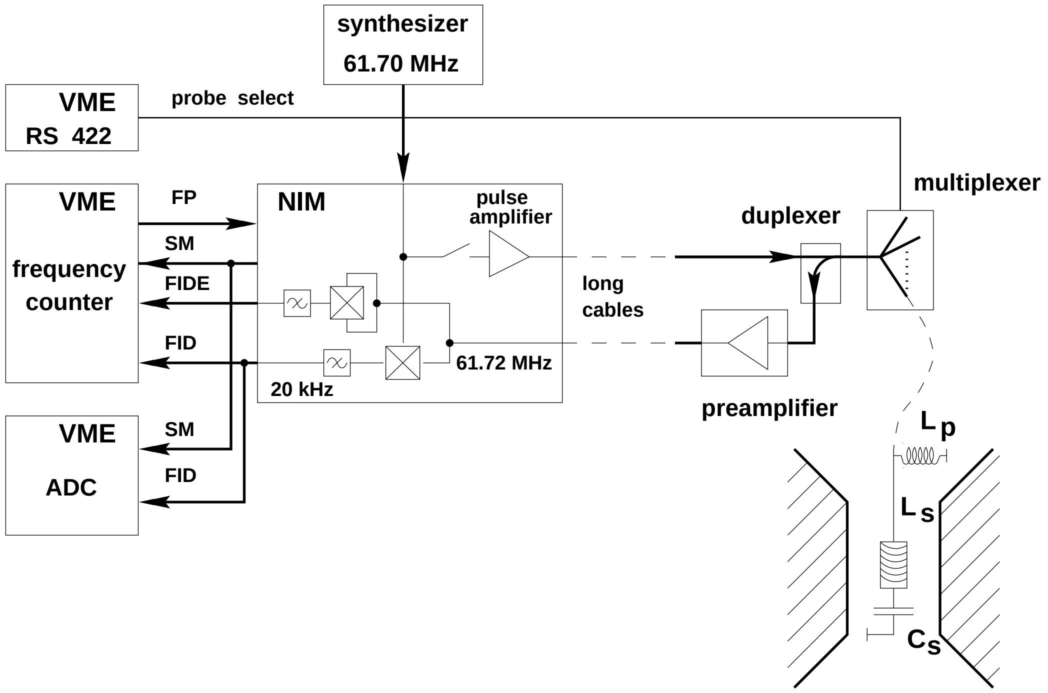


**Figure 4.4**: NMR magnetometer

(see Figure 4.7), which was constructed to measure the NMR frequency of protons in a spherical sample of pure water with a systematic uncertainty of 0.034 ppm [85]. The ratio of the proton magnetic moment in a spherical water sample to the magnetic moment of the free proton $g_p(H_2O)/g_p = 658.216\,009\,1(69)$ [86], measured at 34.7°C, and its temperature dependence $-10.36(30) \times 10^{-9}$ /°C [87] were used to find the absolute field value in terms of the free proton resonance frequency $\omega_p = 2\pi \times \nu_p$.

## 4.6 Superconducting Inflector

In a usual accelerator application the inflection of a particle beam into a storage ring is done with a pulsed electromagnetic inflector, which locally cancels the field of the main magnet, so that the beam enters the storage region close and almost tangent to the equilibrium orbit in the ring. We use a DC, non–ferrous superconducting inflector which avoids the noise and the time varying fringe magnetic field associated with a pulse inflector. Our inflector design minimized the fringe field, which indeed was reduced further by shimming also be measured.

The cross section of the inflector, vacuum chamber, outer cryostat, and magnet poles at the injection point is shown in Figure 4.8. The current distribution in the inflector coils, described in [88], produces a homogeneous dipole magnetic field of 1.5 T over a

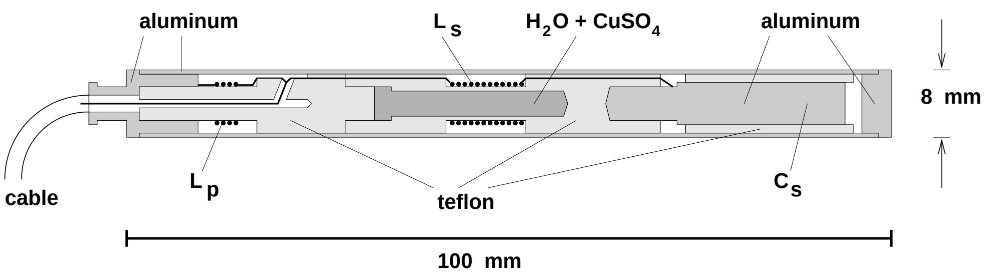


**Figure 4.5**: Fixed NMR probe

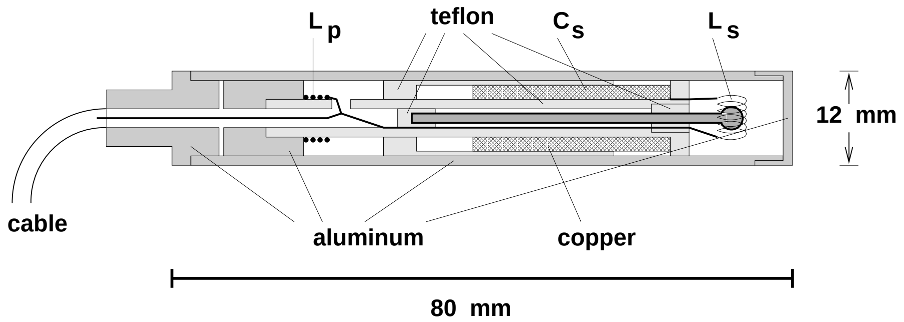


**Figure 4.6**: Calibration NMR probe

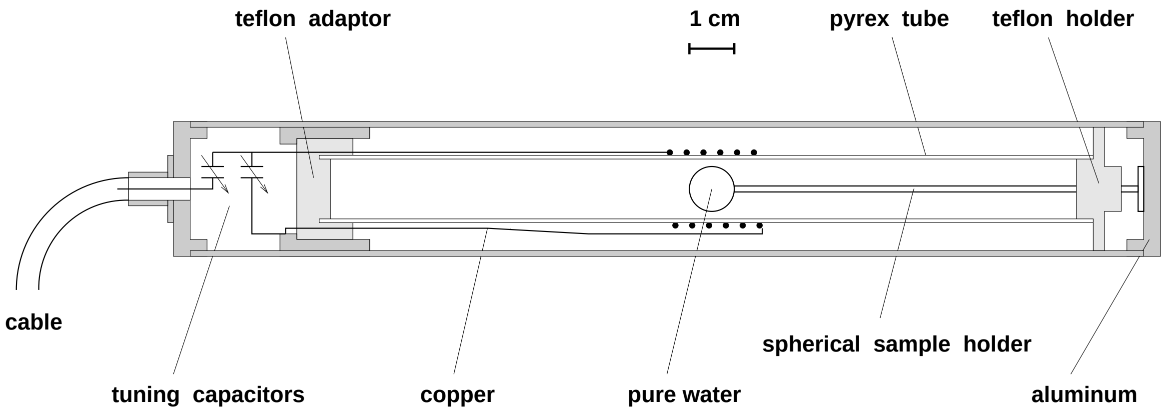


**Figure 4.7**: Standard NMR probe

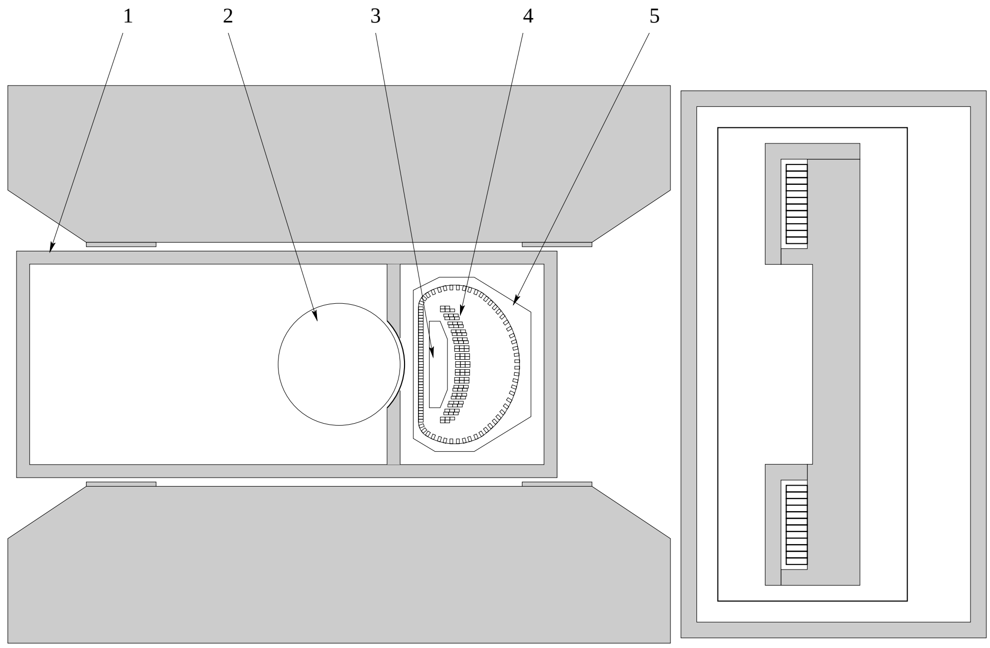


**Figure 4.8**: Superconducting inflector: 1 – inflector vacuum chamber, 2 – muon storage region, 3 – beam channel, 4 – electrical currents, 5 – inflector body.

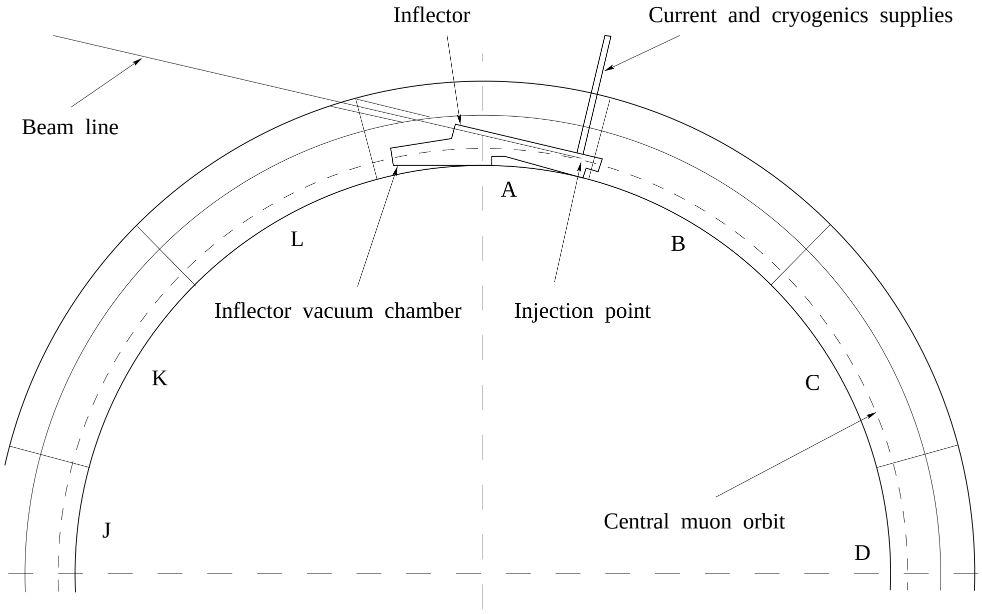


**Figure 4.9**: Inflector installed on the ring.

length of 1.7 m which cancels the magnetic field in the injection channel.

The top view of the inflector installed in the ring is shown in Figure 4.9. Beam enters the inflector through a hole in a yoke backleg in section A. The beam is injected tangential to and 77 mm outside the muon central orbit. The transmission efficiency of the inflector was calculated to be 70% [10, 80].

## 4.7 Pion or Muon Injection

The (g–2) beam line allows either pion beam or a beam of muons from pion decays in the transport channel to be brought to the inflector entrance. One can select pions or muons with the momentum slit K3–K4 near the end of the beam line: the slit should be tuned to the beam line momentum for the pion selection and 1–2% lower for the muon selection.

With the pion injection 3.15 GeV/c pions are brought to the ring. As the pions move along the ring, some of them decay, and some of the decay muons have a momentum compatible with the acceptance of the storage ring. The muon capture efficiency was calculated to be $2.6 \times 10^{-5}$ for the pion injection [10, 80], which gives $2.6 \cdot 10^{7} \times 0.7 \times 26 \cdot 10^{-6} \approx 470$ muons per $10^{12}$ protons at the target.

In the direct muon injection since muons exit the inflector at a radial point which lies outside of the storage volume, a kick is needed to store muons onto a stable orbit in the storage ring. The muon injection is provided by giving the muon beam a kick of $\sim 0.1$ Tesla–meter at $90^\circ$ downstream of inflector exit. The kick can be accomplished either by electric, magnetic or a combination of these two fields. Magnetic kicker was chosen on a base of minimal residual magnetic field, reliability and cost. The muon capture efficiency was calculated to be 7% for the muon injection [10, 80], which gives $10^{5} \times 0.7 \times 0.07 = 4900$ muons per $10^{12}$ protons at the target.

## 4.8 Muon Kicker

The basic design of the magnetic kicker is two parallel current sheets connected so that the current goes in opposite directions in the two plates, see Figure 4.10. The kicker is divided into three 1.7 m sections as shown in Figure 4.11. Each section is driven by a separate modulator, which delivers a current pulse of 4500 Amp with a voltage 95 kV. Figure 4.12 shows the current waveform obtained with the thyratron tube CX1699 used as a high voltage switch.

The magnetic field created by this current pulse and measured from the Faraday effect [89] is shown in Figure 4.13. The cyclotron period of the beam is 149 nsec, so the beam is kicked in the desired direction 2 to 3 times before it is kicked in the opposite

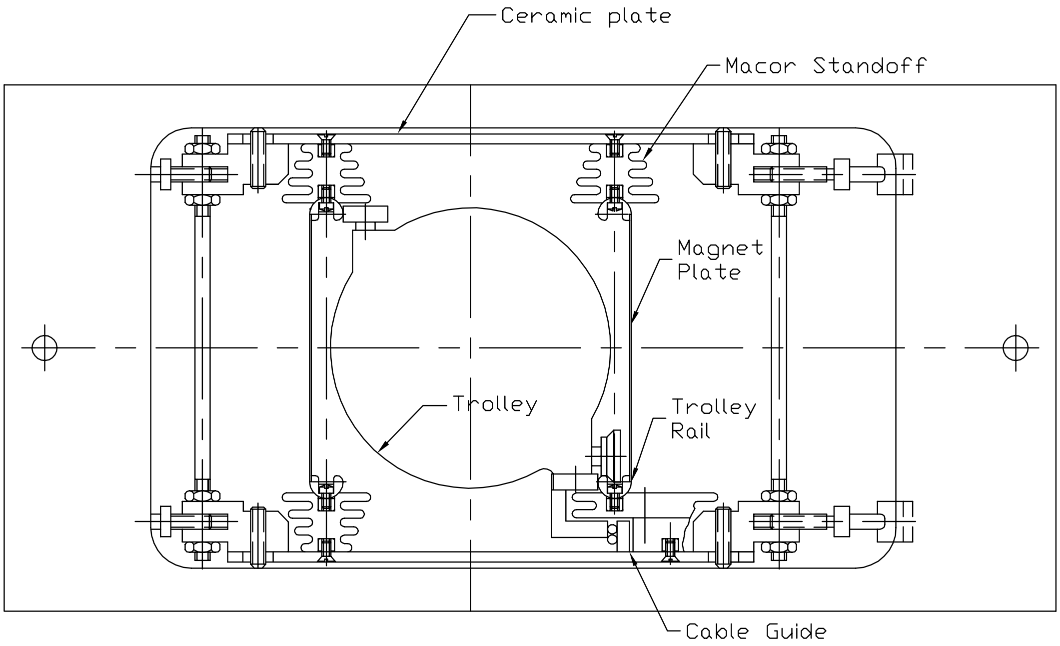


**Figure 4.10**: A cross section view of the kicker electrode assembly inside the vacuum chamber

direction by the pulse overshoot. For the magnetic pulse shown in Figure 4.13, the muon injection efficiency was calculated to be 7%. This is close to the efficiency for an "ideal" step function kick, which was calculated to be 7.5%. The residual magnetic field at later times, which is produced mainly by the eddy currents on the kicker plates, was measured to be less than 20 mG 20 $\mu$sec after the current pulse. This is in good agreement with OPERA simulation [90]. The expected error in the (g–2) value from this residual magnetic field, if not measured and accounted for, is less than 0.02 ppm and hence is negligible.

## 4.9 Electrostatic Quadrupoles

As in the CERN III experiment the use of a muon beam at the "magic gamma" ($P_\mu$ = 3.094 GeV/c) allows us to use electrostatic quadrupoles for vertical focusing of the stored muons. For stored muon beam the (g–2) muon storage ring is a weak focusing machine with an average field index

$$n = -\frac{\rho}{\beta B}\frac{\partial E_r}{\partial r}.$$

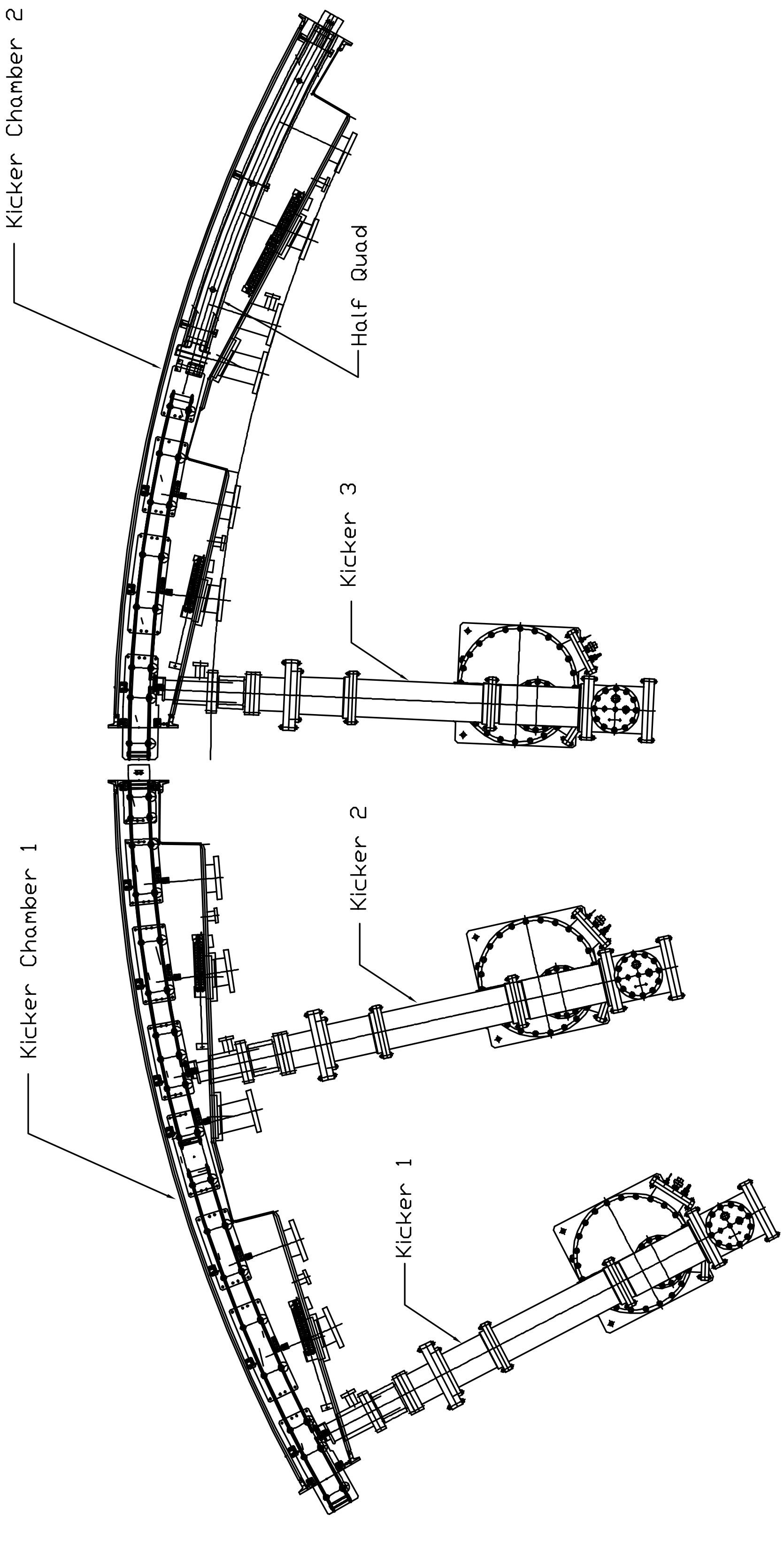


**Figure 4.11**: g–2 kicker layout

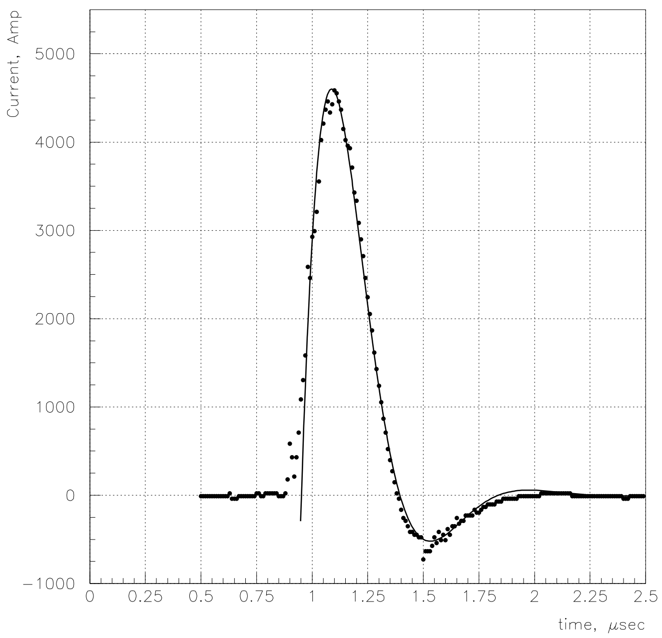


**Figure 4.12**: The measured kicker waveform at 95 kV with the thyratron switch. The solid line is the waveform for an LCR circuit that matches the measurement.

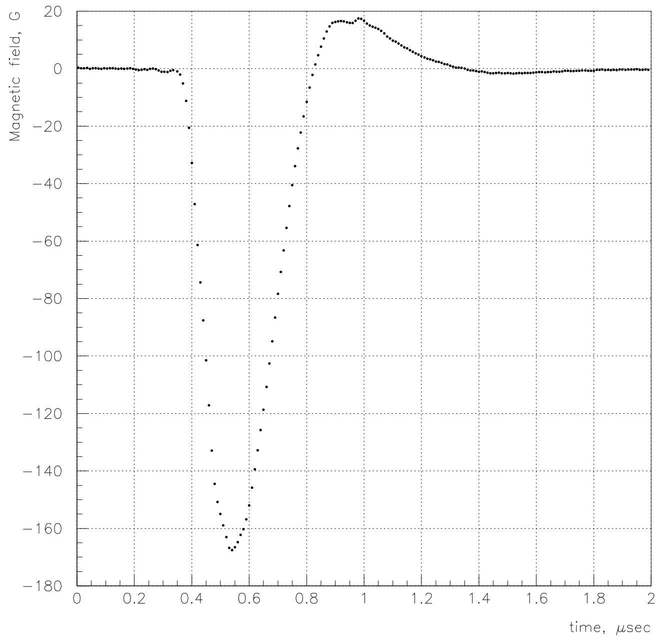


**Figure 4.13**: Magnetic field measured from the Faraday effect.

Here $\rho$ = 711.2 cm is the radius of the central orbit, $\beta = v_\mu/c \approx 1$, B = 1.45 T is the magnetic field at the central orbit [91]. Muon losses due to betatron resonances are small for n = 0.135. For this n value, the wavelength of the betatron oscillation is $1/\sqrt{1-n} = 1.08$ turns (orbit circumference) for the horizontal motion and $1/\sqrt{n} = 2.72$ turns for vertical motion.

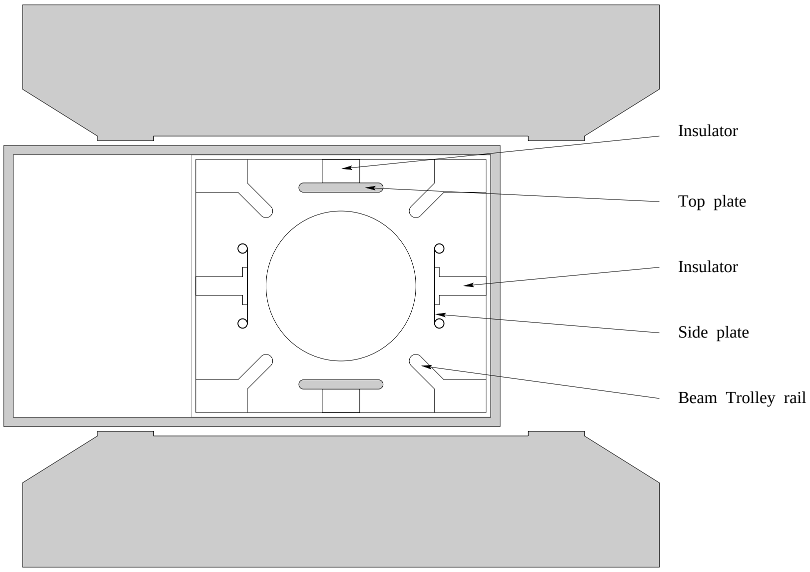


**Figure 4.14**: Electrostatic quadrupoles

The cross section of the vacuum chamber with the installed electrostatic quadrupoles is shown in Figure 4.14. The aluminum electrode plates are 4.7 cm wide, and spacing between them is 10 cm. The aluminum beam tube trolley rails are at ground potential. Calculations show that this configuration forms almost perfect quadrupole electrical field. The positioning of a chamber relative to the poles is accurate to about 1 mm and hence the overall positioning of electrostatic quadrupoles with respect to the muon storage region is also accurate to 1 mm.

To provide the field index value n = 0.135 with the electrostatic quadrupoles configuration shown in Figure 4.14, we required the voltage $V = 10.6\, kV/f$, where $f = 43\%$ is the fraction of the ring occupied by the quadrupoles, and hence $V = 24.5\, kV$. Each quadrupole segment is powered from feedthroughs upstream in the vacuum chamber.

To minimize the effect of electron trapping and to avoid electrical breakdown, the high voltage is pulsed on only for 800 $\mu$sec for each beam injection. On some electrodes the high voltage reaches full value only some time after the beam is stored in order to displace the muon beam. This results in the loss of muons at the edges of the distribution, which are most likely to be lost uncontrollably at later times.

Special care was taken to ensure that no impurities with high magnetic susceptibility are in the insulators and no sharp metal points are in a high electric field region.

## 4.10 Detectors

The detector system [92] for the (g–2) experiment consists of 24 stations positioned at 15 degree intervals around the inside of the storage ring, as shown in Figure 4.15. Each station must determine the time of arrival and energy of each detected decay electron. Each detector station consists of an electromagnetic calorimeter and a horizontal array of five scintillator paddles on the front face of the calorimeter (front scintillator detector, FSD), see Figures 4.16, 4.17. The calorimeters are made of 1 mm scintillator fibers embedded in lead. Stretched "nets" of evenly spaced fibers are placed on top of grooved lead/antimony (6%) plates and are held in the grooves by an optical epoxy. The fibers occupy 35% of the calorimeter's volume. The radiation length of this composition is about 1 cm. Each calorimeter is 22.5 cm wide, 14 cm high and 15 cm deep and consists of four separate modules glued together to form the complete block. The energy resolution of the calorimeter is $\sigma = 10 - 13\%/\sqrt{E(\mathrm{GeV})}$.

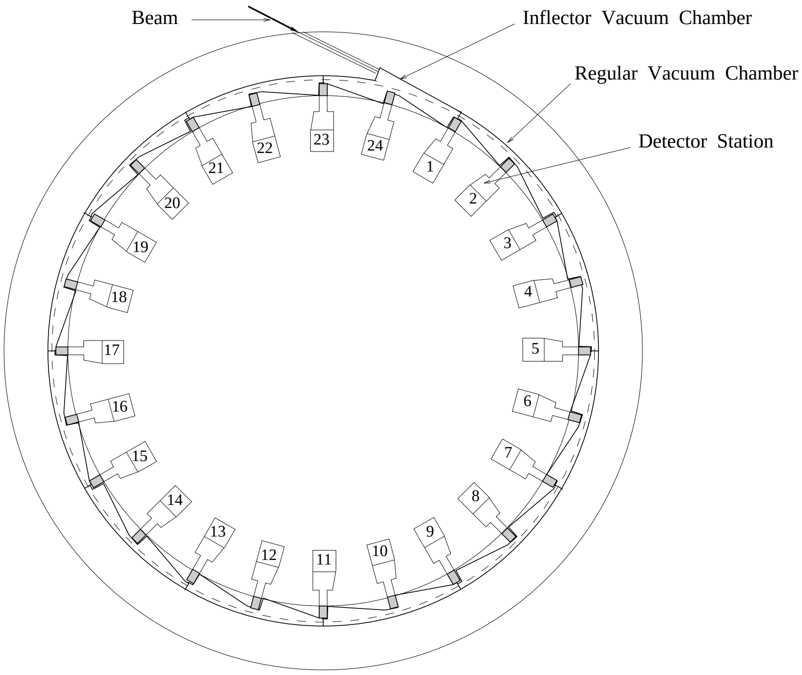


**Figure 4.15**: Detector stations on the ring

The front scintillation detector consists of five 2.8 cm × 23 cm radially oriented scintillator fingers 3/8 inch (9.5 mm) thick. Together, the five fingers cover the entire front face of the calorimeter. They provide rough information about the vertical coordinate of the entrance point of the electron into the calorimeter and can be used to veto multi–electron events (pileup rejection). For timing purposes, the FSD signal has the advantage that the pulse height is independent of the electron energy. Pulse height and an additional time measurement for a given event come from the calorimeter.

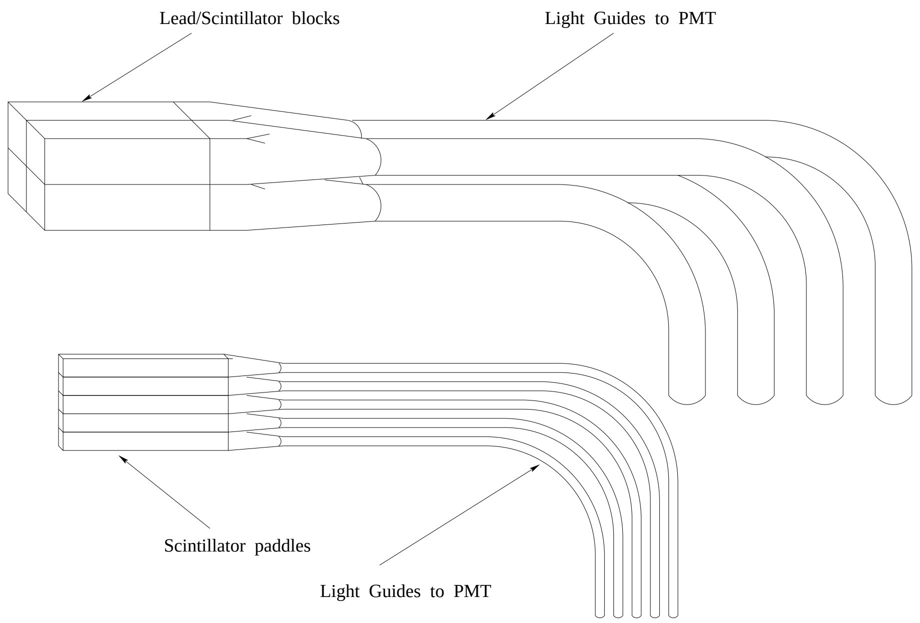


**Figure 4.16**: Calorimeter (top) and front scintillation detector (bottom)

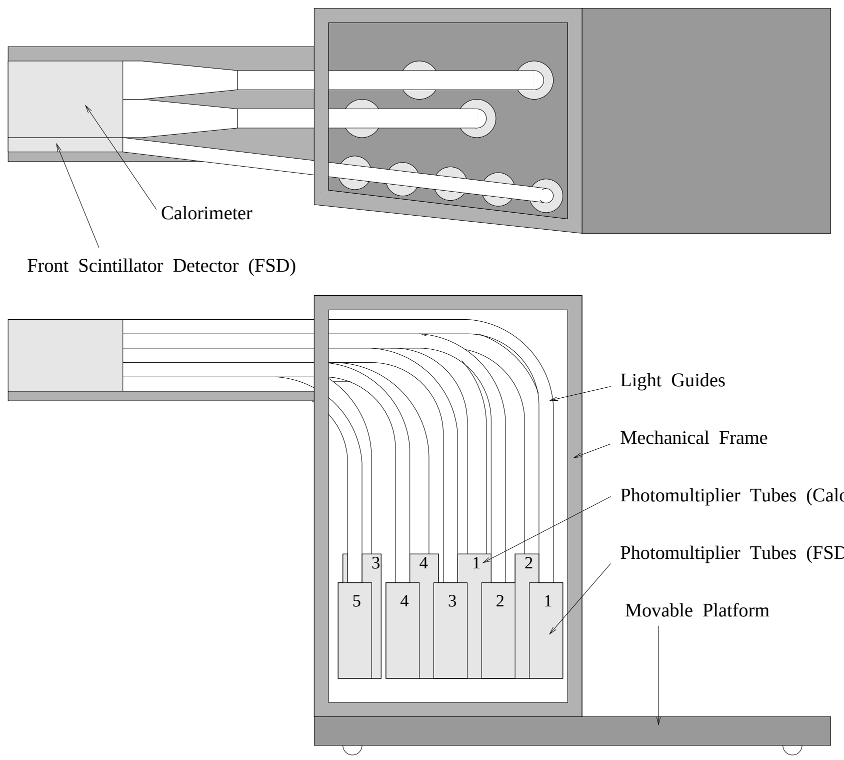


**Figure 4.17**: Detector station, top and side views

Some detector stations have a position sensitive detector (PSD) on the front of the calorimeter. The PSD is a scintillating fiber hodoscope with 0.7 cm segmentation in both radial and vertical directions. The PSD gives the coordinates of the entrance point of the electron into the calorimeter and can be used for additional pileup suppression. The vertical position information from the PSD provides data which will prove useful for our measurement of the muon electric dipole moment [93].

For pion injection about $10^8$ pions are injected into the ring. Most of them collide with the vacuum chamber, electrostatic quadrupoles, inflector, etc., which produces an intense flash in the detectors. Special PMT base was designed to turn off the PMT during the flash and then turn it on. The PMT gain recovered to 90% pulse height in $\leq 400$ nsec and reached full operational value in several $\mu$sec. In a number of test beam studies we have observed a long tail ($\sim 100$ $\mu$sec) of activity following the prompt flash when the PMT was directly in the pion beam. The tail was gone when the PMT was pulled out of beam, whether the scintillators or light guides were directly in the beam or not. Since PMTs are quite sensitive to passing particles, we decided to move them off the midplain of the storage ring, as seen in Figure 4.17.

In order to reach our goal of a 0.35 ppm measurement, systematic errors in the average detection time of the electrons must be less than 0.1 ppm. The clock which gives the time standard for the electronics is a highly stable 200 MHz oscillator clock, phase–locked to the LORAN–C frequency signal. The LORAN–C frequency standard provides accuracy much better than required for this experiment. The same frequency standard is used for the NMR system.

Data are collected for a time interval of about 600 $\mu$sec after injection. The event rate at any detector station decreases by a factor of about $10^4$ by the end of the 600 $\mu$sec interval. Since a systematic timing shift from early to late times would lead directly to an error in the (g–2) frequency, reliable control over any possible rate dependent time shift such as PMT transit time, discriminator response, etc. is needed. A $N_2$ laser–based calibration system was implemented for this control. It illuminates all detectors with a pulse of UV light from a common source. The laser pulse is delivered to each of the calorimeter segments through quartz fibers. The laser calibration provides a good timing standard and also tests complete system integration and relative gain stability. During the 1997 run the PMT gain shifts, as measured by the laser calibration system, were less than 1% and the early–to–late timing shifts over the first 200 $\mu$sec were less than 20 ps.

## 4.11 Detector Electronics and Data Acquisition System

The detector electronics system is built around a few modular components: multi–hit time to digital converter (MTDC), a so called “derandomizer”, and a wave form digitizer (WFD). The readout electronics for the calorimeter and FSD systems are illustrated schematically in Figures 4.18, 4.19.

The MTDC records the time of the leading and trailing edges of the logic pulses. The width of the pulse can be used for pileup suppression. Data from the FSD and calorimeter are read out by separate channels of the MTDC so that correlation of data from each of these devices may be easily achieved. The MTDC is read out into a local 512 kilobyte memory.

A second component of detector electronics is a “derandomizer”. It unambiguously associates asynchronous logic pulse from a discriminated FSD (or calorimeter) with synchronous clock cycles by shifting its leading edge to the center of the proper clock pulse. Since a single 200 MHz clock is used for the derandomizer, MTDC and WFD, they are all in phase. The time boundaries of each 5 nsec bin must be stable to 20 psec over 200 $\mu$sec, which is 0.1 ppm. The MTDC board has a double frequency multiplier to provide the necessary 400 MHz.

For the calorimeter energy measurement we use a two phase waveform digitizer (WFD) system. The WFD is a VME bus slave module designed to digitize and store analog input data at a rate up to 200 MHz. With a pair of channels operating 180 degrees out of phase on the same analog pulse, we can effectively sample at 400 MHz. Each WFD channel has four analog inputs, corresponding to the four PMTs on each calorimeter. Each of the four inputs is separately discriminated and sum of the four is digitized by a 300 MHz, 8 bit (1 byte) Flash ADC. After every four conversions the digitized data are stored as a parallel group of four bytes. In zero–suppression mode, the data are transferred to the on–board memory only if the summed analog signal exceeds a programmed threshold. Same time 16 bit (2 byte) time word (incremented every 5 nsec) plus 2 bytes of discriminator information are also stored. In total, eight bytes of information is stored at a rate up to 50 MHz. Each channel WFD has 64 K (kilobytes) of storage: 32 K for pulse samples and 32 K for time and discriminator data.

The data acquisition system for BNL (g–2) experiment consists of six front–end VME crates, containing the detector readout electronics and one central, or event builder, VME crate, see Figure 4.19. The six front end VME crates are linked to a central VME crate in a star formation by a fast VME interconnect MXI–bus. The central crate CPU pulls the data from front–end crates through the MXI between AGS cycles and controls all crate functions. For the muon injection runs the CPUs will be added to the front–end crates to read out and store data between each fill of the storage ring.

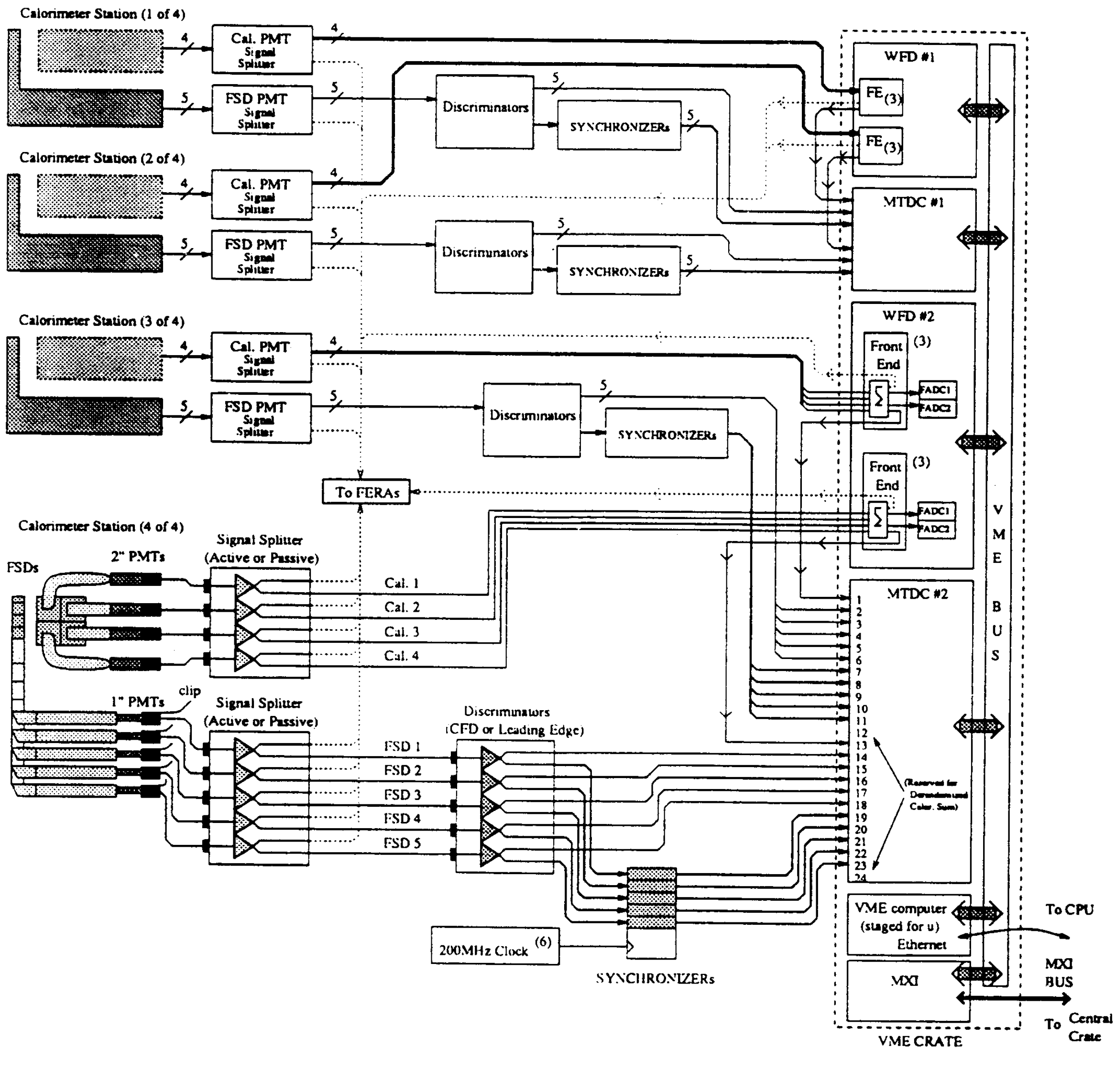


**Figure 4.18**: Front–end electronics station (1 of 6).

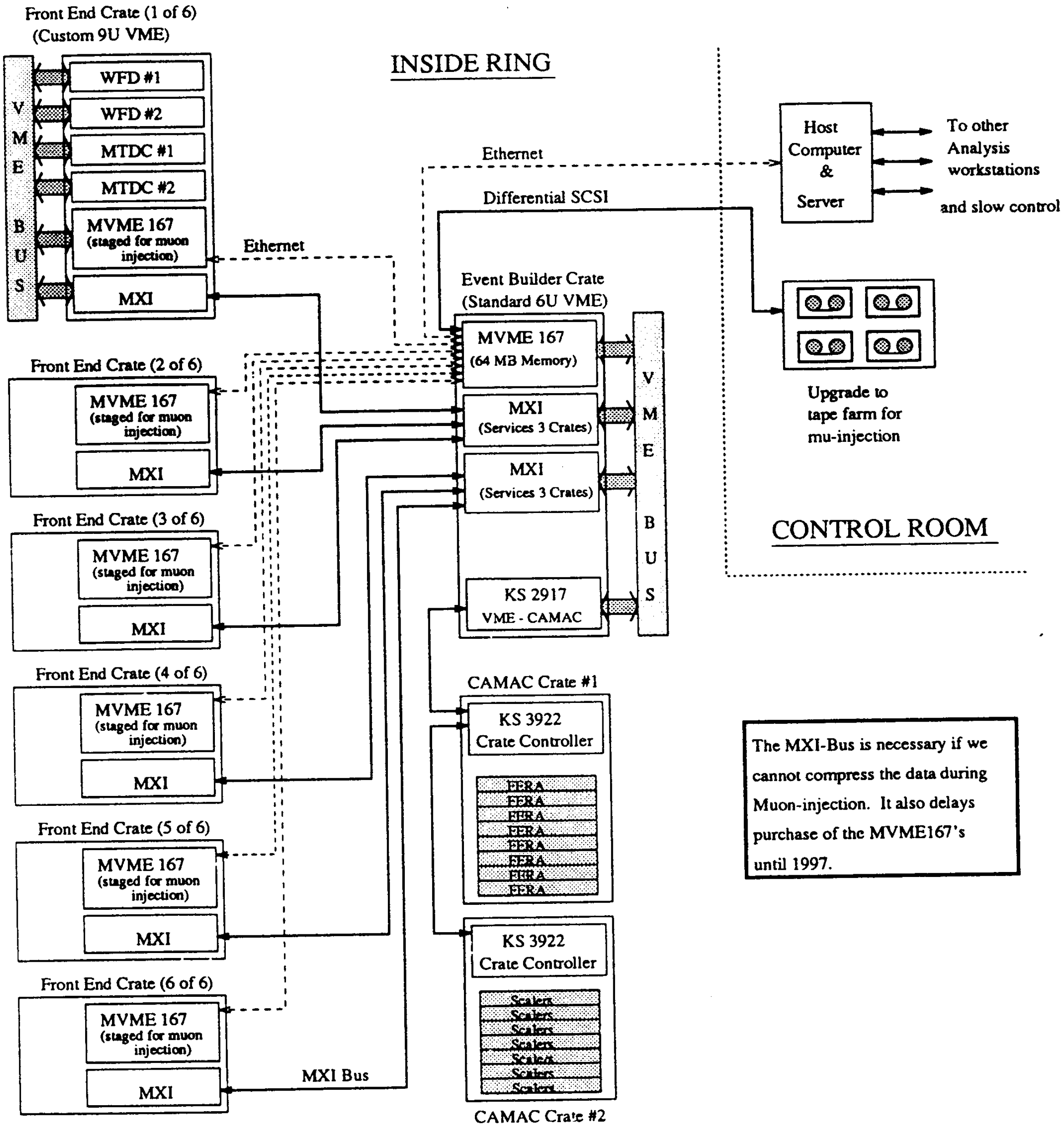


**Figure 4.19**: Baseline of DAQ architecture

## 4.12 Monitoring and Control of the Beam in the Storage Ring

The muon decay electron detectors provide substantial information on the beam inside the storage ring. The muon beam has a mean orbital period of 149 nsec and at early times after injection is bunched within a time interval of $\sim$ 30 nsec. Eventually the bunch spreads out: particles of lower momentum on orbits with smaller radii advance ahead of those of higher momentum. Thus the beam debunches and fills the ring uniformly in the azimuthal direction. From accurate measurements of the decay electron arrival times, the electron detectors provide information on the rotation frequency spectrum and hence information on the radial and momentum distribution of the muons, particularly for early times after injection.

In addition to the electron detectors, there are several other devices to monitor the beam in the storage ring. Scintillating fiber monitors measure the beam profile immediately after injection and provide crucial information on muon distribution after injection. A system of wire chambers has been built to trace decay electron trajectories back to their decay point, and thus determine the muon distribution in the ring.

Two scintillating fiber monitor units each consisting of an $x$ and $y$ plane, are located at 180° and 270° downstream of the inflector exit. The 0.5 mm diameter fibers are spaced by 10 mm in a "harp" configuration as shown in Figure 4.20. Each fiber is read out by a separate photomultiplier tube. For calibration of the fiber/PMT channels the fibers harp can be rotated by 90° to place all fibers just downstream of the next, thus presenting the same portion of the beam to all fibers, see Figure 4.20. The fiber monitors are retractable and can be removed from the storage region during data taking.

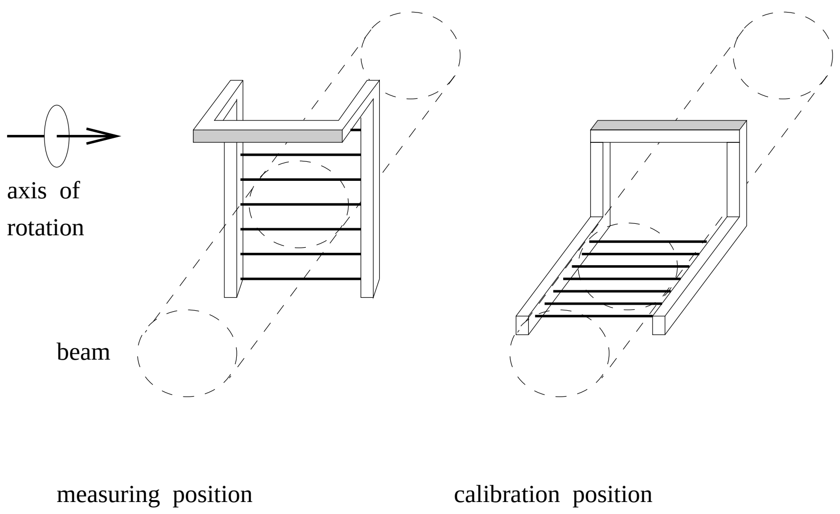


**Figure 4.20**: Scintillating fibers monitor

The electron traceback system consists of a set of wire chambers which measure the trajectory and momentum of decay electrons in one section of the storage ring. The goal is to propagate the electron back along its trajectory up to the point where its radial component of motion is zero. This point is typically within 1 mm in radial and vertical directions from the actual site of the muon decay.

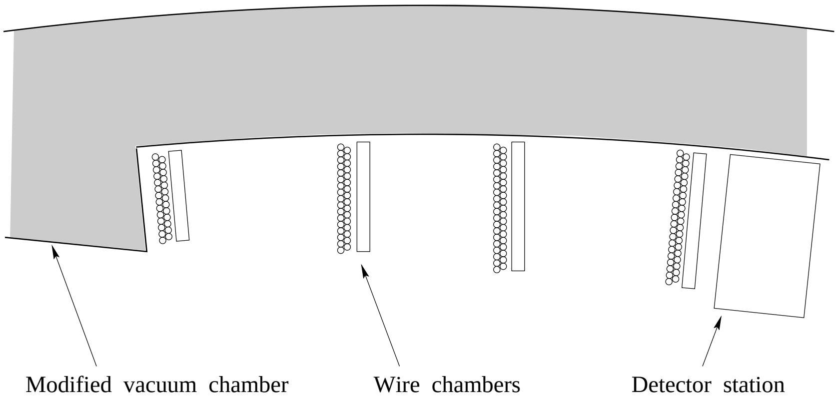


**Figure 4.21**: Electron traceback system

The traceback system layout is shown in Figure 4.21. It contains four chambers separated by about 25 cm each. Each chamber consists of two layers of vertical and horizontal (radial) drift tubes. Each tube has a diameter of 10 mm and made of 25 $\mu$m thick aluminized mylar and filled with $CO_2$ – iso $C_4H_{10}$ gas. Such a drift tube has a small Lorenz angle, i.e. the angle between the velocity vector $\vec{v}$ of the drifting electrons and the electric field which arises from the Lorentz force $e\,[\vec{v} \times \vec{B}]$. The highly nonuniform magnetic field over the trajectory affects the drift time and limits the position resolution of the drift chamber to $\sim 100$ $\mu$m. With this position resolution and a magnetic field measured with relative precision of order of $10^{-3}$, the reconstruction of vertical and radial coordinates of the point of muon decay should be good to about 3 mm.

Both scintillating fiber monitors and electron traceback system were commissioned during the 1997 run, but did not provide useful information: several fiber/PMT channels were broken or disintegrated during installation of the former, challenging electron tracking algorithm for the latter was not ready in time. Both systems were fixed and improved for the next run. For the 1997 run we used simple aluminum foils activation and photodiode/scintillator techniques to measure profile and intensity of the pion beam in the (g–2) ring, see section 6.5.

# Chapter 5

# Magnet Commissioning and Shimming

## 5.1 Magnet Assembling

Construction of the BNL (g–2) magnet began in 1989 with the winding of the superconducting coils. The coils were made of an aluminum stabilized Niobium–Titanium superconducting cable provided by KEK laboratory, Japan. The coils were wound on ring–shaped aluminum mandrels, two outer coils on the same mandrel and two inner coils separately, see Figure 4.3. Three cryostats were fabricated and the coil–mandrel assemblies were installed in the cryostats. Upon completion, the cryostats were removed from the (g–2) building to make room for assembling of the yoke.

The order for steel for the yoke was placed in July 1989 to Lukens Steel Co., Coatesville, Pa. The yoke was fabricated in $30^\circ$ sectors with each sector having two upper, two lower and two spacer plates, see Figure 5.1. The total weight of the yoke steel as supplied in plates was $9.19 \cdot 10^5$ kg. The order for steel machining was placed in September 1991 to Ranor Co., Westminster, Mass. All surfaces of each plate were machined to the design values. The final machining operations were to machine the horizontal surfaces flat to 0.1 mm and to machine the ends of each sector to an exact $30^\circ$. The finished weight of the yoke was $6.76 \cdot 10^5$ kg.

Pole pieces were supplied by Nippon Steel by KEK, Japan, and were of ultra low carbon steel with less than 0.01% of carbon. All surfaces of each pole piece were machined to a flatness of 0.02 mm and each was annealed before final machining. These were also machined by the Ranor Co.

The magnet assembly was started in October 1993 when all of the parts were recieved. Figure 5.1 illustrates the assembling procedure. The base plates were installed first at the proper radius and bolted to the floor of the building at a uniform height.

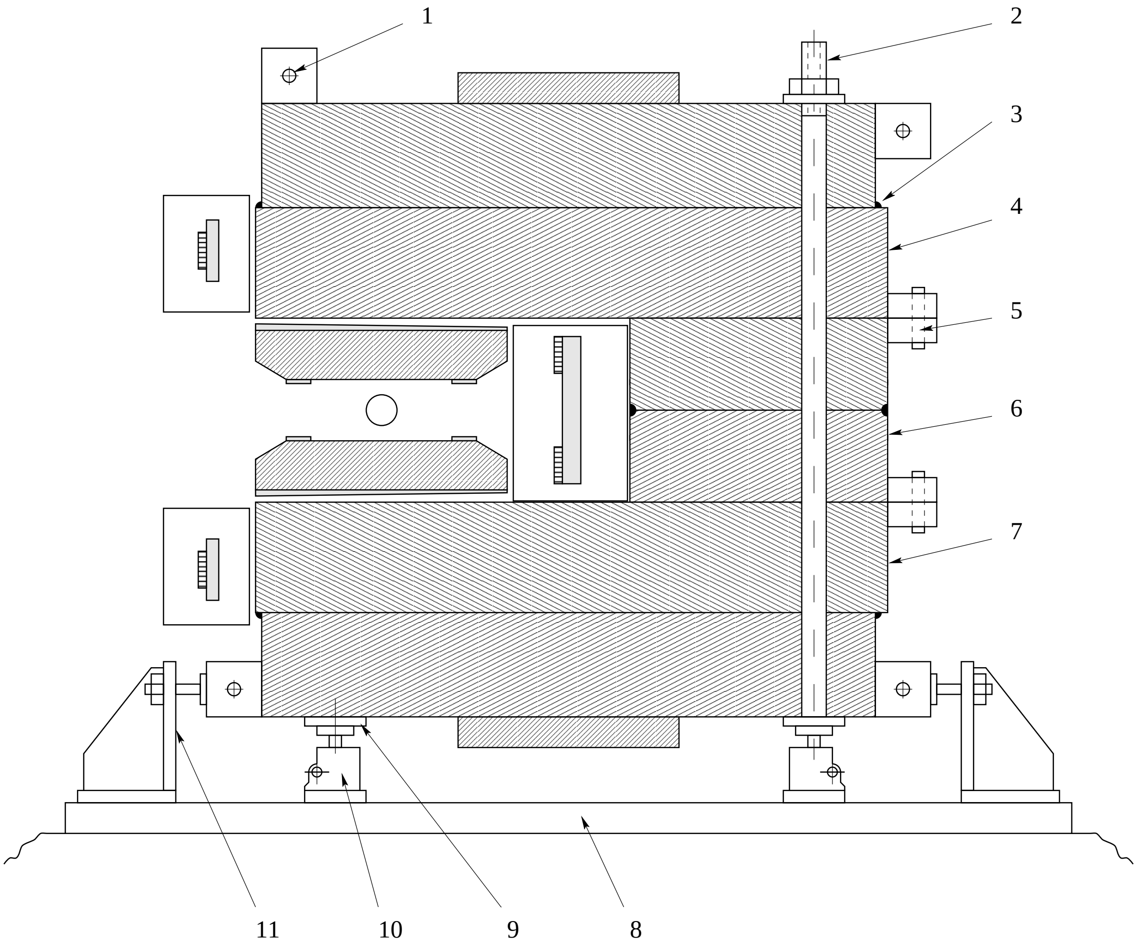


**Figure 5.1**: Magnet assembling scheme. 1 – sector bolt, 2 – tension bolt, 3 – weld, 4 – upper yoke, 5 – taper pin, 6 – spacer, 7 – lower yoke, 8 – base plate, 9 – sliding pad, 10 – vertical jack, 11 – horizontal jack.

Mechanical screw jacks were installed on the base plates to adjust the vertical position of the magnet. The lower yoke plates were put in place and adjusted to the proper radius using horizontal jacks and to the right height. The spacer plates were installed on the top of the lower yoke and adjusted to the right radius. Then the upper yoke plates were installed using jacks in the gap to support the upper yoke at smaller radius. In all the steps listed above, the ends of each sector were adjusted to be in a true plane.

When the yoke was assembled, eight tension bolts of 50 mm diameter were installed on each 30° sector and pretensioned to $4.55 \cdot 10^4$ kg each. Then holes for taper pins were machined to maintain magnet alignment when disassembling parts of the magnet yoke. Finally at each sector end, 4 sector bolts of 50 mm diameter were installed and tightened to make the magnet a complete unit ring.

The superconductive coils were installed by disassembling the upper yoke of the magnet. On December 20, 1994 two outer coils were tested in the ring using partially installed cryogenic system. The coils were cooled by liquid helium to 9.6 K and went supercondactive at the first attempt. Then the pole pieces were installed in the gap and adjusted, the upper yoke was reassembled and the upper inner coil was installed. The next step was connecting of the three coils, assembling and test of the cryogenic system. By the end of 1995 construction of the magnet was completed and cryogenic system get ready for the first powering of the magnet.

## 5.2 Commissioning of the Superconducting Coils up to Half Current

The (g–2) magnet is energized by a 6000 Amp – 6 V power supply from the Bruker Co. Both energizing and de–energizing of the coils are usually computer controlled with typical constant ramping rates of 2 to 5 Amp/sec. In an emergency the energy can be extracted by discharging through an 8 $m\Omega$ dump resistor. This energy extraction can be triggered by the quench protection system or manually. The quench protection system generates a trigger if some portion of the coil goes normal and hence the vortage across the coil drops. The quench recording system continually records the voltages across coils, mandrel temperatures and some other parameters into a cycling buffer.

For normal operation with a magnetic field of 1.45 T the superconducting coils have a current of about 5200 Amp. We decided to commission the coils to full current in several steps:
(1) power the coils with a current of 100 Amp, and then extract the energy to check the quench recording system;
(2) power the coils with a current of 1000 Amp, and then extract energy;
(3) power the coils with a current of 2450 Amp ("half" current), make intensive NMR field measurements and extract the energy;
(4) power the coils with a current of 5200 Amp ("full" current), extract the energy, make intensive NMR field measurements and start magnet shimming.
In practice, we also powered to currents of 1500 Amp and 3500 – 3700 Amp.

Commissioning of the coils with a current of 100 Amp started in late October 1995. The data from the quench recording system were recorded using a four channel digital scope The magnet current $I$ and the voltages across the outer upper and lower coils $V_{ou}, V_{ol}$ and the inner upper coil $V_{iu}$ were recorded. For analysis of the data it was assumed that $V_{il} = V_{iu}$, where $V_{il}$ is the voltage across the inner lower coil. Several data sets were taken with constant ramping rates from $\pm$ 0.5 Amp/sec to $\pm$ 6.2 Amp/sec and one set with energy extraction. From the data in which the current was ramped down at – 0.5 Amp/sec we found inductance of the two outer coils to be $L_{outer} = 0.46$ H and the total inductance of the four coils to be $L = 0.49$ H, comparable with the calculated value $L = 0.39$ H [94]. The time constant of the outer mandrel/cryostat system $\tau' = L'/R' = 14.9$ sec. Assuming that $L'$ differs from $L$ by number of turns only, we can calculate

$$R' = \frac{L/48^2}{\tau'} = 11.6\,\mu\Omega.$$

Several parameters of the system were obtained from the energy extraction data. The most important is the energy deposition in different elements of the system, i.e. outer mandrel/cryostat (48.1%), two inner mandrel/cryostats (1.1%), leads (1.9%), dump resistor (16.7%) and a Westcode diode in the dump resistor circuit (32.2%). The total energy deposition was found to be 2690 J, compared to $\frac{1}{2}LI^2 = 2450$ J.

Energy deposition in a mandrel leads to warming and evaporation of liquid Helium in the cooling lines and to warming of the superconducting coils. For large enough energy deposition, a coil can go to the normal (non–superconducting) state, i.e. quench. The amount of energy deposition which leads to the quenching can be estimated roughly as the energy required to evaporate all the Helium in the cooling lines, which is about 70 kJ. Extrapolating this data for energy extraction for magnet current 100 Amp leads to the prediction that energy extraction will cause a quench to currents $> 650$ Amp.

In late December 1995 we successfully ramped up the current to 1000 Amp and then ramped down at the rate 1.5 Amp/sec. We then varied the ramp rate from 3 to 6 Amp/sec to look for mandrel eddy current heating. No temperature changes were found. We extracted energy at 1000 Amp and the average temperature of the outer mandrel increased from 5 to 5.5 K and of the lead/interconnect region from 7.7 to 8.5 K. The system returned to its previous temperatures in three minutes. Analysis of the coil voltages recorded by the quench recording system indicated that the magnet did not go normal.

After the 1000 Amp test we had decided to modify the magnet commissioning plan and extract energy at 1500 Amp before we would go to half current (2450 Amp). We ramped up to 1000 Amp at 3 Amp/sec and then to 1500 Amp at 2 Amp/sec and extracted energy. From the recorded data we saw a difference in the outer upper and lower coil voltages from about 20 seconds after the start of extraction, probably due to a quench. Later analysis of measurements of temperatures and pressures around the ring recorded by the cryogenic control system confirmed that a quench had occured. We then ramped again to 1500 Amp at 3 Amp/sec with no cryogenic problems and continued to 2450 Amp at 2 Amp/sec. The magnetic field in the ring was measured with NMR probes. Then we ramped down to 0 Amp at 2 Amp/sec without any problem.

Subsequently additional field measurements were made at 2450 Amp. On January 16 night the energy was extracted at the current of 2450 Amp and a quench occured 7 seconds later. The current was ramped up again to 2450 Amp and NMR field measurements were taken. We shall discuss the results of the NMR field measurements at half current in section 5.4.

## 5.3 Commissioning of the Superconducting Coils with Full Current

On January 27, 1996 we made the first attempt to power the magnet to the full current of 5200 Amp and thus abtain the desired magnetic field of 1.45 T. We ramped up to 2500 Amp and then continued in 200 Amp steps at a rate of 2.5 Amp/sec. On the ramp from 3500 to 3700 Amp, we heard deep resonant noises. After about 20 seconds at 3700 Amp, energy extraction was started by the quench protection system. From the recorded data we concluded that the energy extraction was triggered by a 60 mV voltage difference between the upper and lower outer coils. Prior to the energy extraction on the voltage difference had several spikes below 50 mV over about a 16 seconds period. Until the energy extraction started the coil temperatures did not change, so we believe that the coils did not go normal and that the voltage difference was induced by movement of the outer mandrel/coils assembly.

Figure 5.2 shows the mandrel/coils assembly mounted in the cryostat box. The mandrel assembly hangs on 16 G10 straps which swing radially up and to an angle of about 9° as the mandrel is cooled. When the coils and mandrel are cooled they shrink ~3 cm in radius. Four radial stops position the mandrel when it cold with respect to the cryostat box. Then when the magnet is powered, the coils expand due to the magnetic force. The radial stops are designed to be just engaged when the coils are cold and powered by full current. When the coils are cold and unpowered the mandrel is deformed into a scallopped shape such that at half–way between the stops the mandrel radius will be 4 mm less than at the stops.

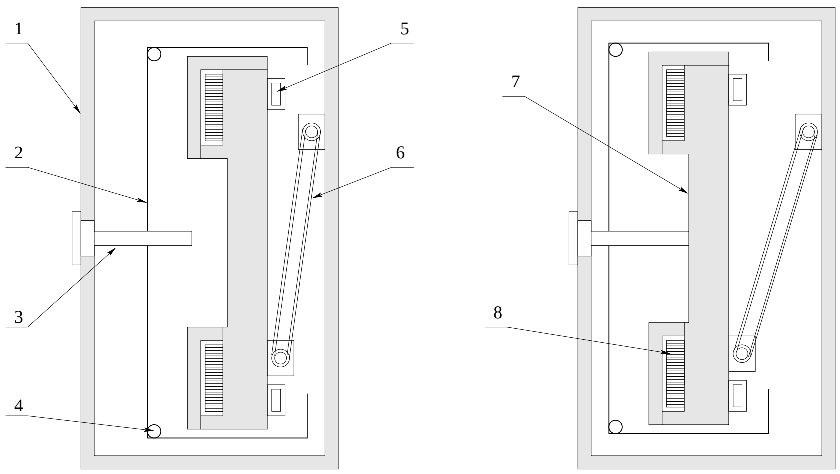


**Figure 5.2**: Cross section of the outer cryostat in warm (left) and cold (right) states. 1 – cryostat wall, 2 – nitrogen screen, 3 – radial stop, 4 – liquid nitrogen supply pipe, 5 – liquid helium supply pipe, 6 – G10 strap, 7 – mandrel, 8 – superconducting coil.

We believed that the noises arose from scraping of the outer mandrel/coils assembly on the radial stops. As the magnet is powered, the load on the radial stops decreased. An unbalanced magnetic force (if any) on the coils can release the mandrel and move it into some more stable position and/or shape. This sudden movement induces a voltage in the two outer coils, positive on one coil and negative on another. This voltage difference may exceed the trigger level which causes energy extraction.

For the next test on January 31 we could monitor online several coil voltage differences by the digital scope and also had readouts from strain gauges on the 4 radial stops. We raised the threshold for energy extraction trigger to 100 mV and slowly ramped up the current. At 3600 Amp significant positive coil voltage difference appeared. We stopped ramping the magnet and lowered the current. In about 10 seconds the coil voltage difference rose to 60 mV and then dropped to zero. We went up again and at 3757 Amp saw another voltage difference pulse ~30 mV and then almost immediately another at ~40 mV. Finally, the voltage difference exceeded 100 mV and triggered energy extraction. The most probable explanation of what we saw was a vertical motion of the mandrel/coils with respect to the radial stops.

On February 1 we set the energy extraction trigger to 200 mV. While ramping up, we saw an large positive voltage difference pulse (about 80 mV) and about 10 other smaller ones and usually at the same we heard noise pulses from the cryostat. We then ramped down and saw several negative pulses, most accompanied with a noise pulse. We concluded that the mandrel/coils moved up as we ramped up and dropped down as we ramped down.

The most likely explanation of these effects is that the center plane of outer mandrel/coils is higher than the magnet midplane. In this case the magnetic force on the mandrel/coils assembly is directed upward. If the midplane of the two coils is below the magnet midplane, the force is directed downward. In both cases the force is proportional to the distance between the two midplanes. Note that the coil midplane was designed to be 0.5 – 1 mm below the magnet midplane for the case of cold and powered magnet.

We wished to measure the shift of the coil midplane with respect to the magnet midplane. R. Prigl suggested measuring the radial component of magnetic field at the cryostat to evaluate this shift. The apparatus for these measurements was developed by N. Ryskulov from Novosibirsk, Russia and the author. The measurement scheme is shown in Figure 5.3. A Hall probe was mounted on the center of a rectangular aluminum bar. The probe is in the $Z-\phi$ plane as shown in Figure 5.3, where it is sensitive only to the radial component of the field. The bar is lying on the set of aluminum shims and two aluminum cubes, resting on the bottom pole of the magnet. The bar can move on these shims along the radial direction. The vertical position of the bar and hence the Hall probe can be varied by changing the number of shims. To avoid systematic errors due to misalignment, we make two measurements in each position, the second one after rotating the bar by 180° around the radial axis, and take the average.

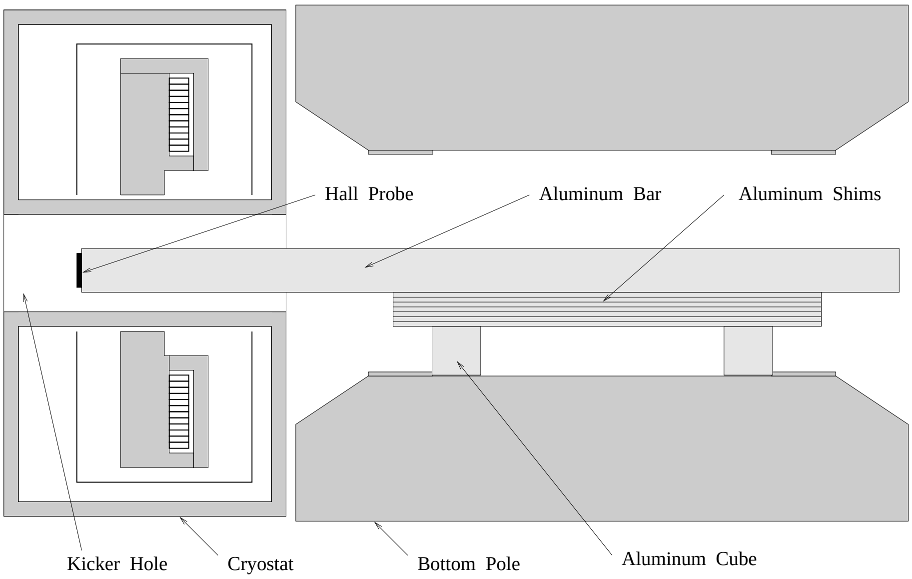


**Figure 5.3**: Scheme of measurements in the kicker hole

Figure 5.3 shows the apparatus installed at some special location where the outer cryostat has a hole for the kicker installation. Of course, at this location the outer mandrel, nitrogen screen and superinsulation inside the cryostat also have a hole. Using this hole we can make measurements in the region close to the coils.

The idea of the measurements is the following. If midplane of the coils coincides with the magnet midplane, the radial component of the field everywhere on the midplane is zero due to symmetry. If the coils' midplane is shifted with respect to the magnet midplane, the symmetry is broken and the radial component of the field in general is not zero on the magnet midplane. Generally, the shape of the magnetic field is determined mostly by the configuration of iron, i.e. yoke and poles. However, in the kicker hole the influence of the coils is relatively large. In particular, at the radial position of the coils the point $B_r = 0$ will be move towards the center of the coils so that if the center of the coils is above the magnet midplane, the point $B_r = 0$ will be also above and vice versa.

For direct comparison between measurements and calculations, we find for a given radial coordinate $R$ the vertical coordinate $Z$ where $B_r = 0$ and plot this point on the $R - Z$ graph. Figure 5.4 shows the results of measurements of the radial magnetic field in the kicker hole. These measurements were taken on February 5 for a current of 1000 Amp. The calculations made by W. Meng for the $B_r = 0$ curve when the position of the center of the coils is 2 mm above the magnet midplane and for the current of 1000 Amp are shown by dashed line in Figure 5.4. The calculations and the measurements agree quite well and we conclude that the midplane of the coils is about 2 mm higher than the magnet midplane.

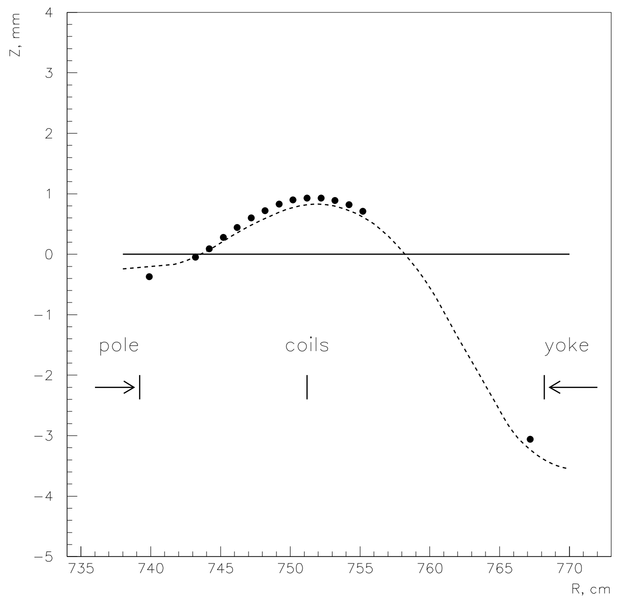


**Figure 5.4**: Radial magnetic field measurements in the kicker hole at 1000 Amp. Dashed and solid lines are calculations for position of the center of coils below the magnet midplane by 2 and 0 mm respectively.

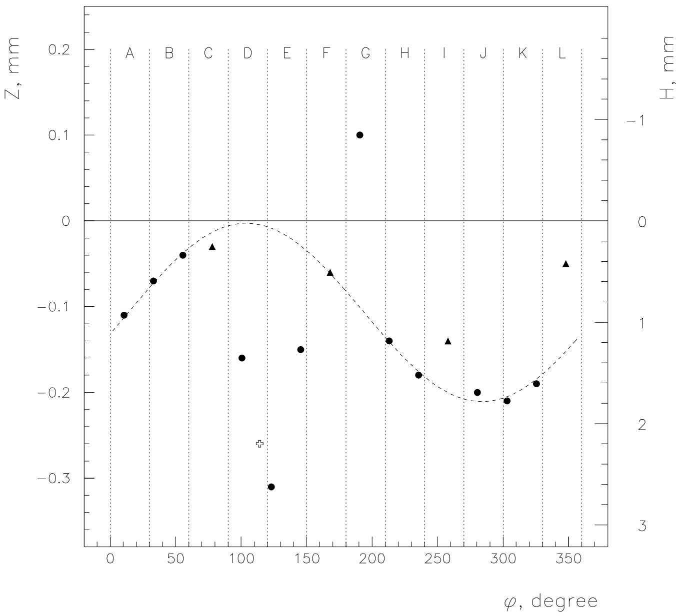


**Figure 5.5**: Radial magnetic field measurements around the ring at 1000 Amp. Dashed line is a sine wave.

On February 5 we also made measurements for a current of 1000 Amp at a number of other locations around the ring close to the cryostat wall, $R \approx 740\,cm$. The results are shown in Figure 5.5. The left scale is the vertical position $Z$ of the point $B_r = 0$, the right scale is the vertical displacement $H$ of the center of the coils with respect to the magnet midplane. The coefficient relating $Z$ and $H$ was obtained from the kicker hole data with the assumption that $H$ is proportional to $Z$. All points except one have positive $H$, i.e. the center of the coils is higher than the magnet midplane. The precision of these measurements is much poorer than those in the kicker hole. Nevertheless, many of points in Figure 5.5 lie on the sine wave (dashed line), which is expected if the coils are slightly tilted with respect to the magnet midplane. Measurements in sectors C, F, I and L were made close to the radial stops, which might locally deform the mandrel. That could explain deviations of the two points in sectors I and L from the sine wave. Major deviations from the sine curve are shown by points in sectors D, E, and G (the one of them in D shown by a cross comes from the kicker hole measurements and hence is much more precise). These points, however, may lie on a different smooth curve and thus indicate some deformation of the coils and not be due to a poor precision of measurement.

Our conclusion was that at a low current (1000 Amp) and most likely in the unpowered state, the center of the coils is on average about 1 mm higher than the magnet midplane and hence the magnetic force on the coils is upward. The magnetic force increases quadratically with current and at some current will exceed the mandrel/coils weight, creating the net upward force. The present design of the mandrel support does not adequately prevent the mandrel from upward motion. To avoid this instability the mandrel/coils assembly must be lowered with respect to the cryostat and hence to the magnet midplane.

For the next test on February 8 a strain gauge was installed under the cryostat near the kicker hole to measure the effective weight of the cryostat and hence the magnetic force on the coil. Figure 5.6 shows the strain gauge readings taken on February 8. For currents up to 2700 Amp essentially no change in the strain gauge reading was observed, but above 2700 Amp the reading decreased indicating an upward magnetic force on the coil. On ramping from $I = 2700$ to 3471 Amp the strain gauge reading decreased with current continuously and faster than $I^2$ (dotted lines on Figure 5.6), which is expected for a stable coil. At 3471 Amp we observed an 80 mV coil voltage difference and stopped ramping up the current. As seen in Figure 5.6, in that point the strain gauge reading dropped suddenly below the unloaded value, indicated in Figure 5.6 by solid line. So, the coil moved (at least locally near the kicker hole location) as we ramped up above 2700 Amp and then jumped up at 3471 Amp. During the current ramp down from 3471 to 3088 Amp (and probably in some current intervals below 3088 Amp), the reading of the strain gauge follows a quadratic curve (see Figure 5.5), suggesting the mandrel is held fixed, presumably by friction on the radial stops. At I = 3088 Amp there is a discontinuous drop. Apparently friction is important during ramp down but not during ramp up.

Figure 5.7 shows measurements of the radial magnetic field in the kicker hole taken on February 8 at the current 3471 Amp along with calculation for the same current and with the center of the coils above the magnet midplane by 7 mm. The calculation curve is in excellent agreement with the measurements when it is shifted 2 cm to the left. The conclusion follows that the mandrel/coils assembly moved up from its initial position of 2 mm to final 7 mm above the magnet midplane and also moved radially inward by 2 cm. With four radial stops this can only be explained if the mandrel changes in shape from a circle to an oval shape. Indeed estimation showed that at a current $\geq 2700$ Amp the magnetic force will exceed the elastic restoring force of the mandrel and deformation of the coil into an oval shape should occur.

So, we believe that at 3471 Amp the mandrel took an oval shape with smaller radius at the kicker location, which is between two radial stops, and at the opposite side of the ring. At these two points the supporting straps raised the mandrel by several mm. At the larger radii the straps pushed the mandrel downward. The net effect was to raise the average coil position up by 0.1 mm, which agrees with the observed coil voltage difference. This model was confirmed later by the observation of scratches of length 1 to 2 cm on the mandrel made by the radial stops.

To prevent the mandrel from buckling to an oval shape, the number of radial stops was doubled to 8 and their design was modified. The new stops have a spring system which provides a fixed mandrel position. The mandrel was lowered by 2 mm to put the center of the coils below the magnet midplane. Seven windows were installed on the cryostat for direct optical monitoring of the mandrel position.

On June 27, we ramped the current up to 2450 Amp. The optical measurements indicated no motion of the mandrel. We measured the radial field in the kicker hole and found that the center of the coils was now 2 mm below the midplane. In this position the coils should be stable with respect to vertical motion. We ramped higher, passed the previously troublesome region of 3500 – 3700 Amp with no motion observed by the optical monitoring of the mandrel, and finally got to the full current 5200 Amp. We measured radial field, and the center of the coils was 3 mm below the midplane, see Figure 5.8. The world's largest diameter superconducting magnet was finally commissioned with the full current of 5200 Amp.

## 5.4 Measurements of the Magnetic Field with NMR Probes at Half Field

As was mentioned above, a series of magnetic field measurements with NMR probes were done in January 1996 at half field. Six fixed probes were attached firmly to the surface of the upper poles equally spaced around the ring. Nine probes were mounted

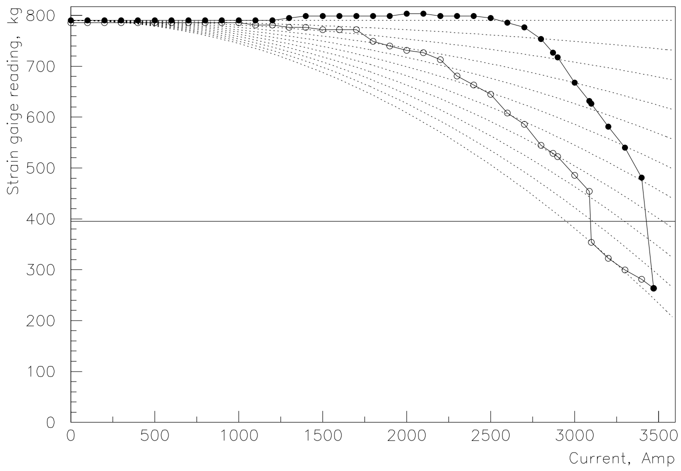


**Figure 5.6**: Strain gauge reading during ramp up (black circles) to 3471 Amp and ramp down (open circles). Dotted lines are set of parabolae $k \cdot I^2$, solid line indicates the strain gauge reading value for unloaded state.

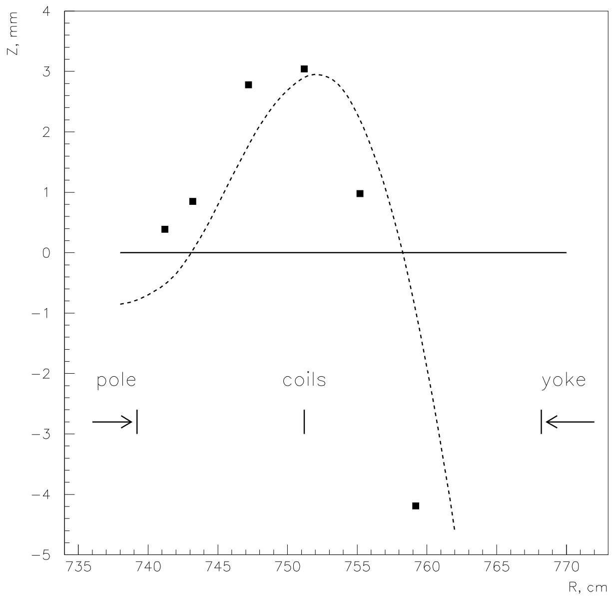


**Figure 5.7**: Radial magnetic field measurements in the kicker hole at 3471 Amp. Dashed and solid lines are calculations for position of the center of coils below the magnet midplane by 7 and 0 mm respectively.

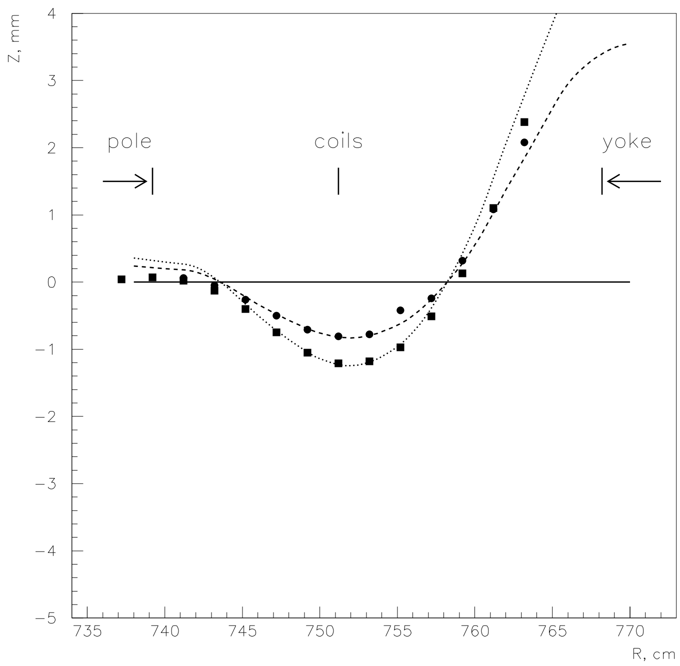


**Figure 5.8**: Radial magnetic field measurements in the kicker hole at 2450 Amp (circles) and 5200 Amp (squares). Dashed, dotted and solid lines are calculations for position of the center of coils below the magnet midplane by 2, 3 and 0 mm respectively.

on a shimming trolley which can be moved around the ring. One probe was mounted on the muon central orbit, four probes 2 and 4 cm vertically above and below the central probe and four 2 and 4 cm radially inward and outward from the central probe.

The field measured by the central probe on the trolley is shown in Figure 5.9 as a fractional deviation from 0.7 T. The field variations in azimuth were up to 1400 ppm with rapid changes across the boundary between two adjacent pole pieces. These field jumps can be explained by variations in the air gap between upper and lower poles at the crossover points as was established by mechanical measurements of the air gap.

During the energy extraction the strong eddy currents in the iron poles and yokes create additional magnetic fields. These fields are very strong at the edges of individual poles and yoke sections and cause strong local magnetization of the iron. This is called the Umbrella effect [95]. Figure 5.10 shows the difference between two field maps before and after energy extraction at half field. The current in the (g–2) magnet decayed during energy extraction with a time constant of $\sim$ 70 seconds. The associated Umbrella effect is about 20 ppm. The Umbrella effect disappears after a few ramp up – ramp down cycles.

The field drift was at the level of 3 ppm/hour. In one of the fixed probes we saw

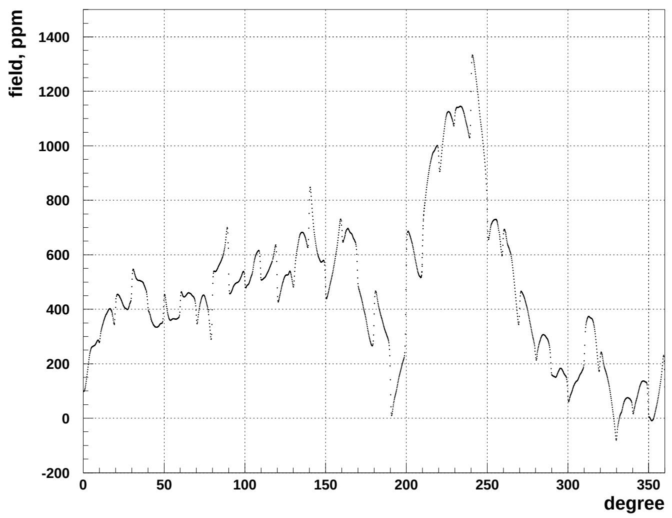


**Figure 5.9**: Magnetic field at half current

field variations of the order 1 ppm due to an electrical heater which periodically blew hot air toward this particular sector of the ring. This demonstrates the high sensitivity of the magnet to temperature changes on a relatively short time scale. The fixed NMR probes showed about a 20 ppm increase in the field when the shimming trolley passed by. This was caused by commercial cable connectors at the end of probes.

Multipole analysis is used to study the field distribution in the cross section of the muon storage region. The toroidal muon storage region with small cross sectional dimensions of $\sim 9$ cm compared to the longitudinal circumference of 44.7 m can be treated approximately as a straight region. Let us denote the vertical axis as Y, the horizontal as X and the azimuthal as Z. If the geometry of the problem is 2 – dimensional, i.e. does not depend on Z, then the magnetic field can be decomposed into a series of multipoles:

$$B_Y = \sum_{n=0}^{\infty} C_n r^n \cos(n\phi) - \sum_{n=0}^{\infty} D_n r^n \sin(n\phi)$$

$$B_X = \sum_{n=0}^{\infty} C_n r^n \sin(n\phi) + \sum_{n=0}^{\infty} D_n r^n \cos(n\phi),$$

where $r$ and $\phi$ are polar coordinates: X $= r \cdot cos\,\phi$, Y $= r \cdot sin\,\phi$. The coefficients $C_n$ and $D_n$ are normal and skew multipoles respectively. They are called dipole ($C_\circ$ and $D_\circ$), quadrupole ($C_1$, $D_1$), sextupole ($C_2$, $D_2$), octupole ($C_3$, $D_3$), decapole ($C_4$, $D_4$), 12-pole ($C_5$, $D_5$), 14-pole ($C_6$, $D_6$) and so on.

For the (g–2) experiment with the dominantly vertical magnetic field we call the normal dipole term $C_\circ$ the dipole field and the skew dipole term $D_\circ$ the radial field. We normalize the multipoles at the edge of the muon storage region, r = 4.5 cm:

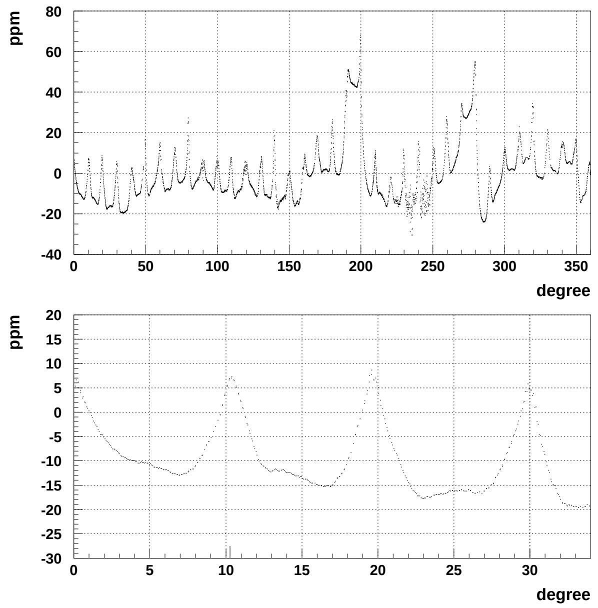


**Figure 5.10**: Umbrella effect for the entire ring (top) and for one yoke section (bottom)

$$B_Y = B_{dipole} +$$

$$B_{quad}^{norm}\left(\frac{r}{4.5}\right)\cos\phi + B_{sext}^{norm}\left(\frac{r}{4.5}\right)^2\cos 2\phi + B_{octu}^{norm}\left(\frac{r}{4.5}\right)^3\cos 3\phi + B_{deca}^{norm}\left(\frac{r}{4.5}\right)^4\cos 4\phi + ... \tag{5.1}$$

$$-B_{quad}^{skew}\left(\frac{r}{4.5}\right)\sin\phi - B_{sext}^{skew}\left(\frac{r}{4.5}\right)^2\sin 2\phi - B_{octu}^{skew}\left(\frac{r}{4.5}\right)^3\sin 3\phi - B_{deca}^{skew}\left(\frac{r}{4.5}\right)^4\sin 4\phi - ...$$

$$B_X = B_{radial} +$$

$$B_{quad}^{norm}\left(\frac{r}{4.5}\right)\sin\phi + B_{sext}^{norm}\left(\frac{r}{4.5}\right)^2\sin 2\phi + B_{octu}^{norm}\left(\frac{r}{4.5}\right)^3\sin 3\phi + B_{deca}^{norm}\left(\frac{r}{4.5}\right)^4\sin 4\phi + ... \tag{5.2}$$

$$B_{quad}^{skew}\left(\frac{r}{4.5}\right)\cos\phi + B_{sext}^{skew}\left(\frac{r}{4.5}\right)^2\cos 2\phi + B_{octu}^{skew}\left(\frac{r}{4.5}\right)^3\cos 3\phi + B_{deca}^{skew}\left(\frac{r}{4.5}\right)^4\cos 4\phi + ...$$

For the (g–2) magnet with its very homogeneous field all multipoles but $B_{dipole}$ are relatively small. We normalize all multipoles except $B_{dipole}$ on 1.45 T and use ppm units rather than Tesla. The center of the muon storage volume is relatively far from the iron and even much farther from the coils. Since there are only smooth variations of the magnetic field in the storage volume, higher multipoles in formulae 5.1, 5.2 are expected to be significantly smaller than lower ones.

For the (g–2) magnet the radial field in the muon storage volume is of order of 100 ppm or less, hence

$$|\vec{B}| = \sqrt{B_Y^2 + B_X^2} \approx |B_Y| + \frac{B_X^2}{2|B_Y|} = |B_Y| \times (1 + O(0.01\,ppm)).$$

The NMR probes measure only the absolute value of magnetic field and hence essentially measure the vertical component $B_Y$. With several probes in the X–Y plane we can determine several low order normal and skew multipoles using formulae 5.1, 5.2. However, the radial field can not be found from NMR measurements. A special Hall probe device designed by N. Ryskulov and the author was used to measure the radial component of the field, see section 5.6.

For the half field measurements with nine NMR probes we used dipole, normal quadrupole, sextupole, octupole and decapole and skew quadrupole terms in equations 5.1, 5.2 to fit the data. The normal quadrupole varied between 110 and 180 ppm in azimuth, skew quadrupole varied between – 30 and 50 ppm, other multipole were more uniform in azimuth: the sextupole was about 190 ppm all over the ring, the octupole $\sim$ – 45 ppm and the decapole $\sim$ 40 ppm. This result agrees with our expectations based on the mechanical tolerances for the magnet construction.

## 5.5 Shimming of the Magnet

To measure the magnetic field at full current the system of 25 NMR probe was mounted on the shimming trolley. The disposition of the probes in X–Y plane is shown in Figure 5.11. With our large number of probes we use nine multipoles (dipole, four normal and four skew lowest multipoles) to fit the data. Capacitec position sensors were used to measure the spacing between top and bottom poles along the ring in two radial positions, see Figure 5.11.

Figure 5.12 indicates the many techniques used to shim the magnet. We started shimming by leveling the pole pieces to eliminate steps between adjacent poles to 0.0005 inch or less. Also we adjusted the poles at certain small angle to the horizontal plane such that both top and bottom poles would be horizontal in the full powered state. Figure 5.13 shows the tilt of the bottom pole as a function of the magnet current. The tilt was measured by Electrolytic Tilt Sensor device, see section 5.6. For the full current of 5200 Amp the bottom pole tilts by $\sim$ 100 $\mu$rad. The relative tilt of the top pole with respect to the bottom one is shown in Figure 5.14 as a function of the magnet current as measured with the Capacitec device. At a current of 5200 Amp the relative tilt was $\sim$ 300 $\mu$rad. Hence, to achieve horizontal plane at 5200 Amp, the bottom poles should be “pretilted” to 100 $\mu$rad and the top poles to 200 $\mu$rad at zero current, see Figure 5.15.

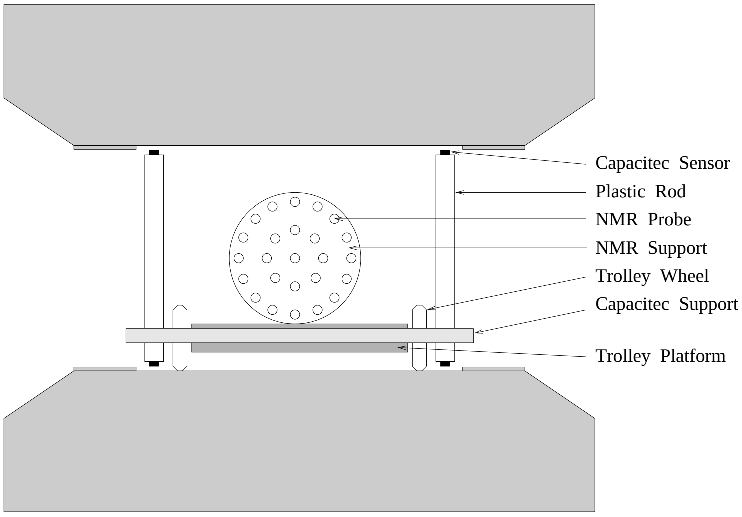


**Figure 5.11**: Shimming trolley

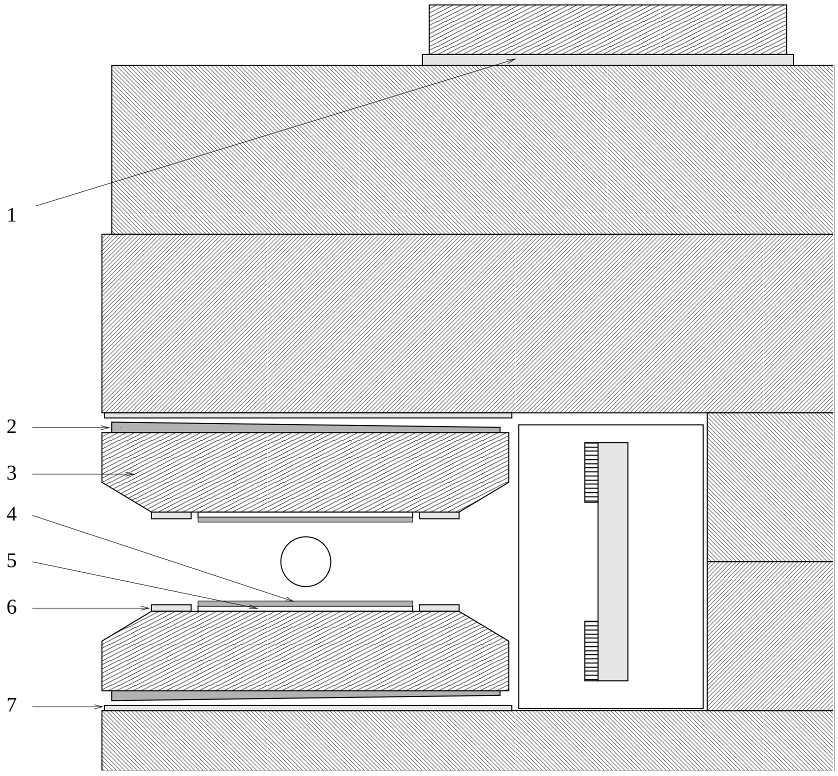


**Figure 5.12**: Shimming techniques: 1 – aluminum or iron shims between top and/or bottom iron plate and the rest of the yoke; 2 – wedges; 3 – tilting of poles; 4 – aluminum/iron sandwiches; 5 – surface correction coils; 6 – Rose shims; 7 – dipole correction coils

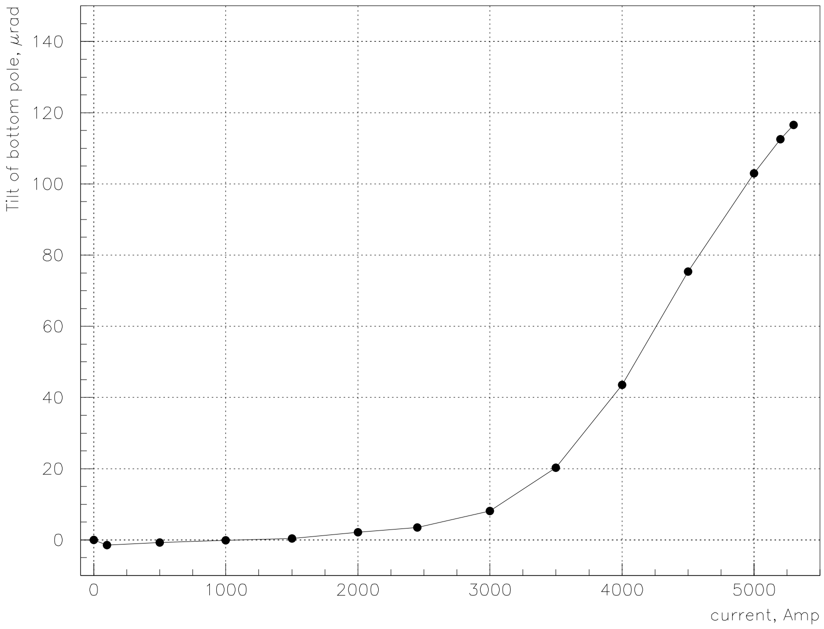


**Figure 5.13**: Tilting of a bottom pole in magnetic field

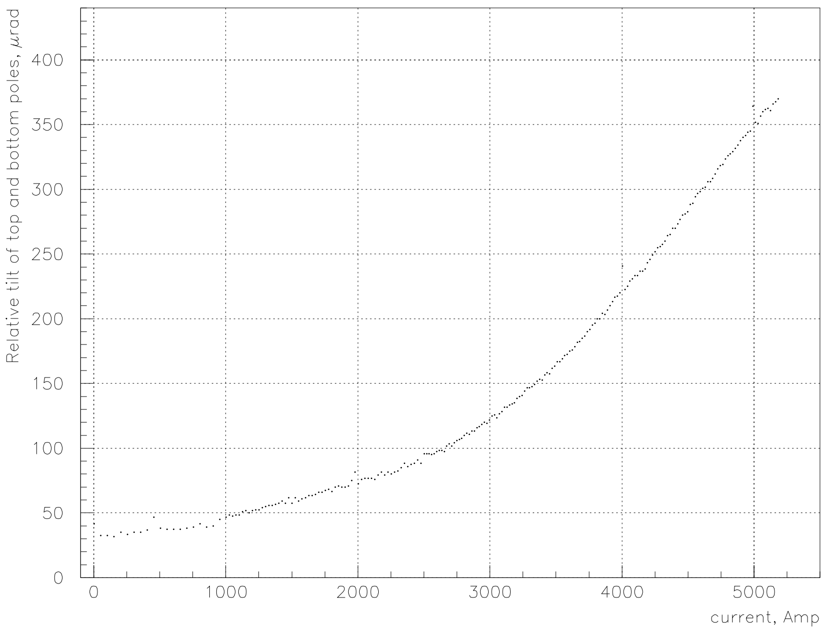


**Figure 5.14**: Relative tilt of top and bottom poles

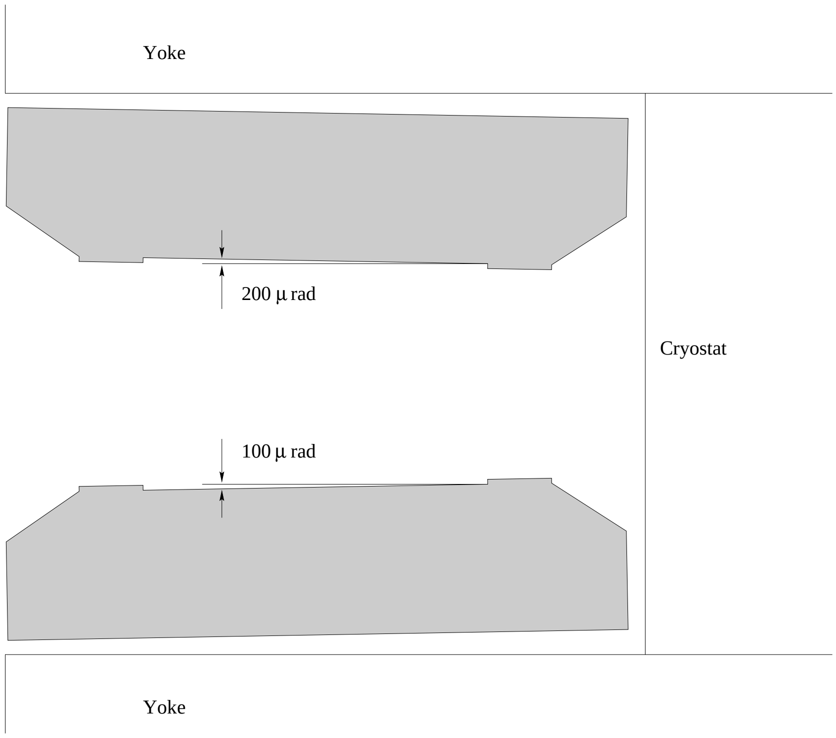


**Figure 5.15**: Pretilting of top and bottom poles at 0 Amp

The leveling of the poles was done by (g–2) technician D. Von Lintig and took about four months of hard and accurate work. Meanwhile, several field maps were taken by the NMR probes in order to test and apply other shimming techniques. Figure 5.16 shows the effect of the gap of 3 mm created by aluminum shims between the main body of the yoke and the top yoke plate (shimming technique shown in Figure 5.12, 1). Because of long azimuthal size of the plates (15°) and rather large distance from the muon storage volume, its shimming effect is very wide in azimuth: the full width at the half maximum is about 30°. This shimming creates only a dipole correction and was used to reduce the wide azimuthal variations of $\sim$ 1400 ppm, seen in Figure 5.9, to 300 ppm level.

Shimming studies were done with iron wedges installed in the gaps between poles and yoke, see Figure 5.12. Each pole region (10°) contains 12 wedges, each of 4 inch width in azimuth. Figure 5.17 shows effect of moving wedges in one pole region by 9 mm radially inward. The dipole field changed by –18 ppm/mm, the normal quadrupole by –0.43 ppm/mm, the skew quadrupole by –0.42 ppm/mm, and the higher multipoles did not change. With the Hall probe device (to be discussed in the next section) the radial field (skew dipole) was found to change by –1.44 ppm/mm. To study the effect of wedge thickness, 0.015 inch iron strips were attached to the wedges. The effect was –825 ppm/mm for dipole, –13 ppm/mm for skew quadrupole and no change in other

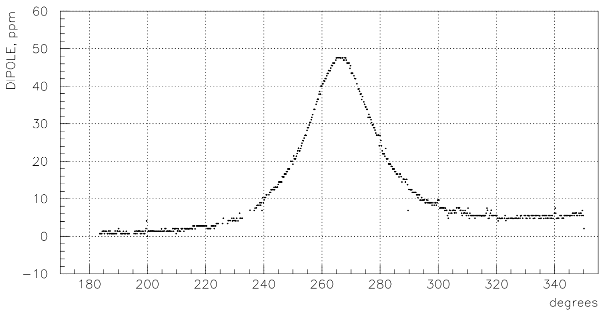


**Figure 5.16**: Effect of iron shim between top plate and the rest of the yoke

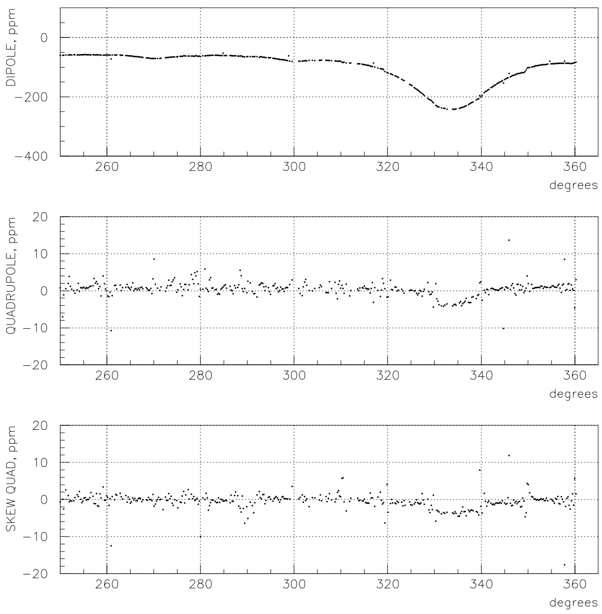


**Figure 5.17**: Effect of moving wedges

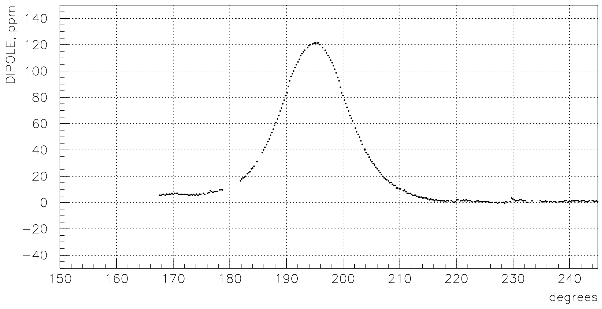


**Figure 5.18**: Effect of dipole correction coil

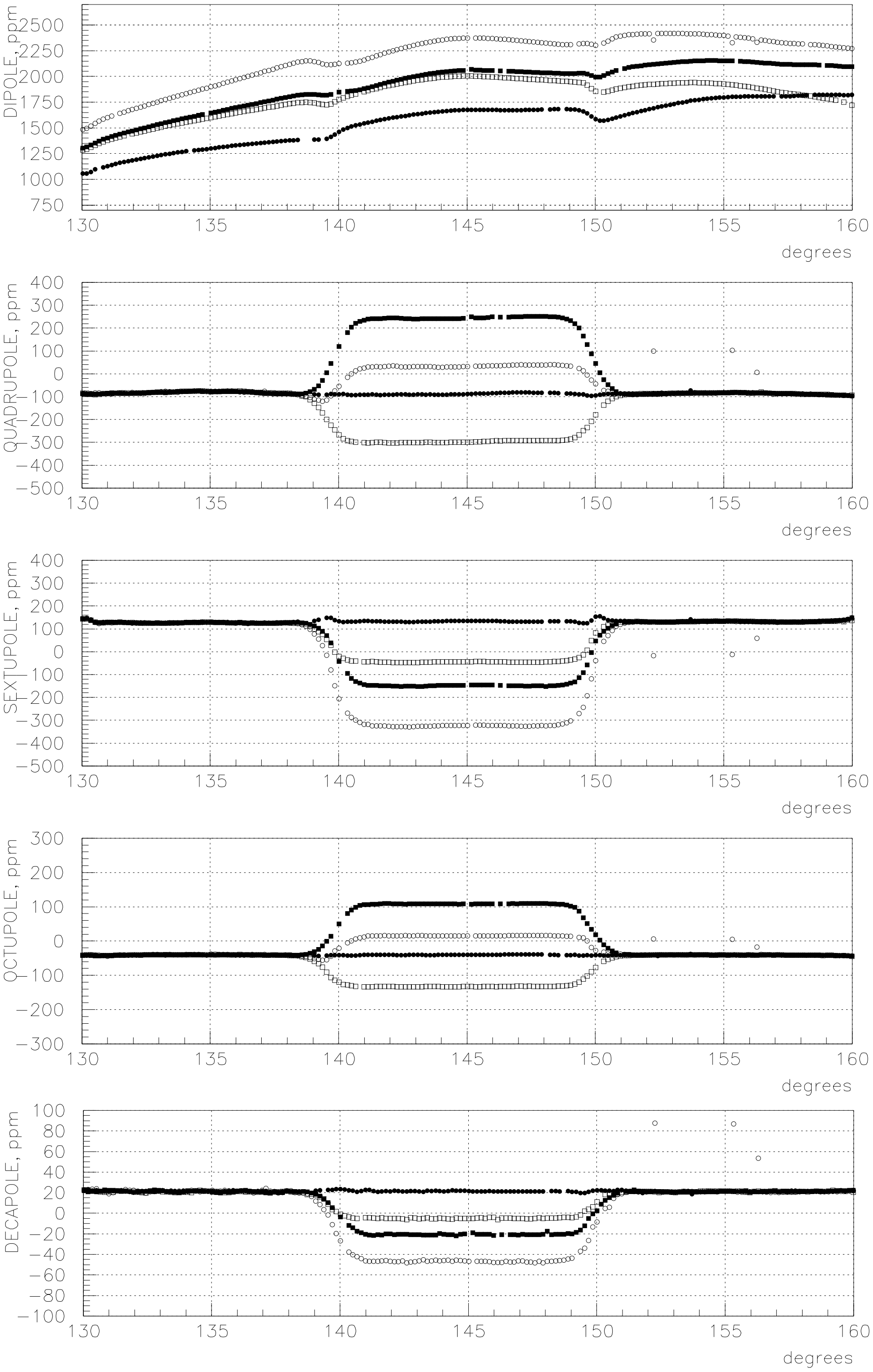


**Figure 5.19**: Rose shims study, normal multipoles

multipoles. Both effects are relatively wide in azimuthal direction and can not be used for local (say 20 cm in azimuth) field correction, as it was intended.

The dipole correction coils are also located in the air gaps between the poles and the yoke, see Figure 5.12. They are 10° wide in azimuth and designed to correct dipole field variations over $10° - 20°$ online using feedback from the fixed NMR probes mounted on the vacuum chamber. These coils are powered by 36 independent power supply units, the top and bottoms coils of the same section are connected in series to a single power supply. Figure 5.18 shows the effect of a pair of the dipole correction coils (top and bottom) in section G2, operating at 0.8 Amp.

For correction of higher multipoles it was extremely fruitful to use so called Rose or edge shims. These are iron strips 5 cm wide on the edges of the poles surfaces as shown in Figure 5.12. They are 10° long in azimuth, their thickness can be machined to correct higher multipoles. Because the Rose shims are close to the muon storage region, they are a very powerful tool for both wide and local corrections. There are four Rose shims in any pole section: inner upper (IU), inner lower (IL), outer upper (OU) and outer lower (OL). To measure the "shimming ability" of each of them or some combinations, they were taken out of magnet between two field measurements. As an example, Figure 5.19 shows the effect of removing the IU + IL pair (black squares), the OU + OL pair (white squares) and all four shims (white circles) from pole section E3. Multipoles with all shims installed are shown by black circles. These combinations correct normal multipoles and leave the skew ones unchanged. Figure 5.20 shows the effect of removing shims IU from pole section H2 ($\Theta = 220° \div 230°$) and IL from L1 ($\Theta = 330° \div 340°$), black circles, and removing OU from H2 and OL from L1, white circles, on the skew multipoles. The total list of shimming effects of individual Rose shims is shown in Table 5.1. The data for radial magnetic field were obtained using the Hall probe device. Using Table 5.1, we can calculate the optimal thickness of Rose shims to correct the field distribution in the muon storage region.

**Table 5.1**: Shimming ability of Rose shims, ppm per 0.001 inch of machining out

| Shim | Normal | | | | Skew | | | | Radial |
|---|---|---|---|---|---|---|---|---|---|
| | quad | sext | octu | deca | quad | sext | octu | deca | field |
| Inner Upper | 0.95 | -0.78 | 0.40 | -0.15 | -5.40 | 2.03 | -0.49 | 0.07 | 7.44 |
| Outer Upper | -0.83 | -0.66 | -0.33 | -0.12 | -4.88 | -1.85 | -0.43 | -0.07 | -6.51 |
| Inner Lower | 0.95 | -0.78 | 0.40 | -0.15 | 5.40 | -2.03 | 0.49 | -0.07 | -7.44 |
| Outer Lower | -0.83 | -0.66 | -0.33 | -0.12 | 4.88 | 1.85 | 0.43 | 0.07 | 6.51 |

Shimming with the Rose shims was done in several steps. First, we machined 0.6 mm, 1.1 mm, and 0.85 mm off the IU + IL shim pairs in poles K1, K2, and K3, respectively and verified the values given in Table 5.1. Then we calculated thicknesses

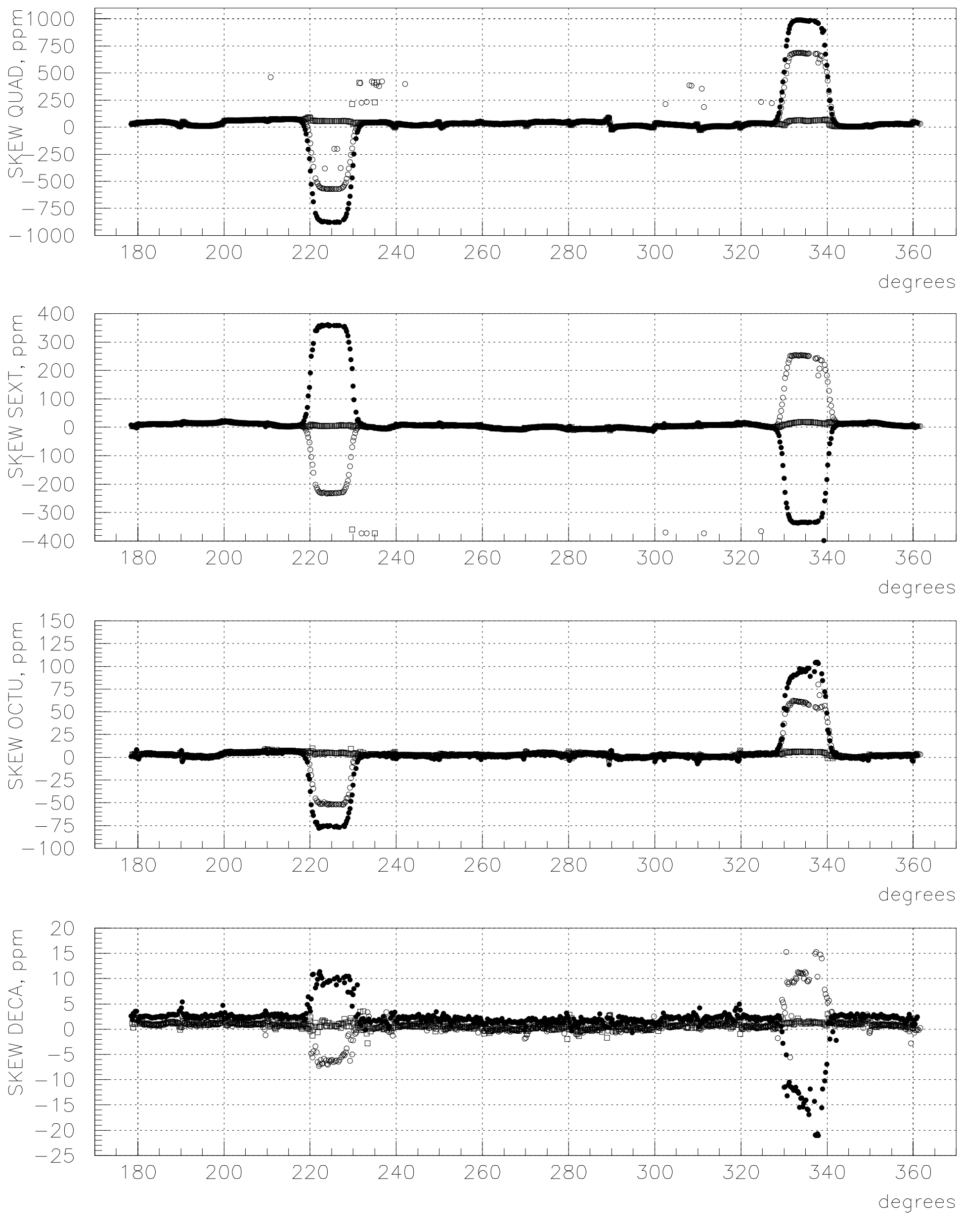


**Figure 5.20**: Rose shims study, skew multipoles

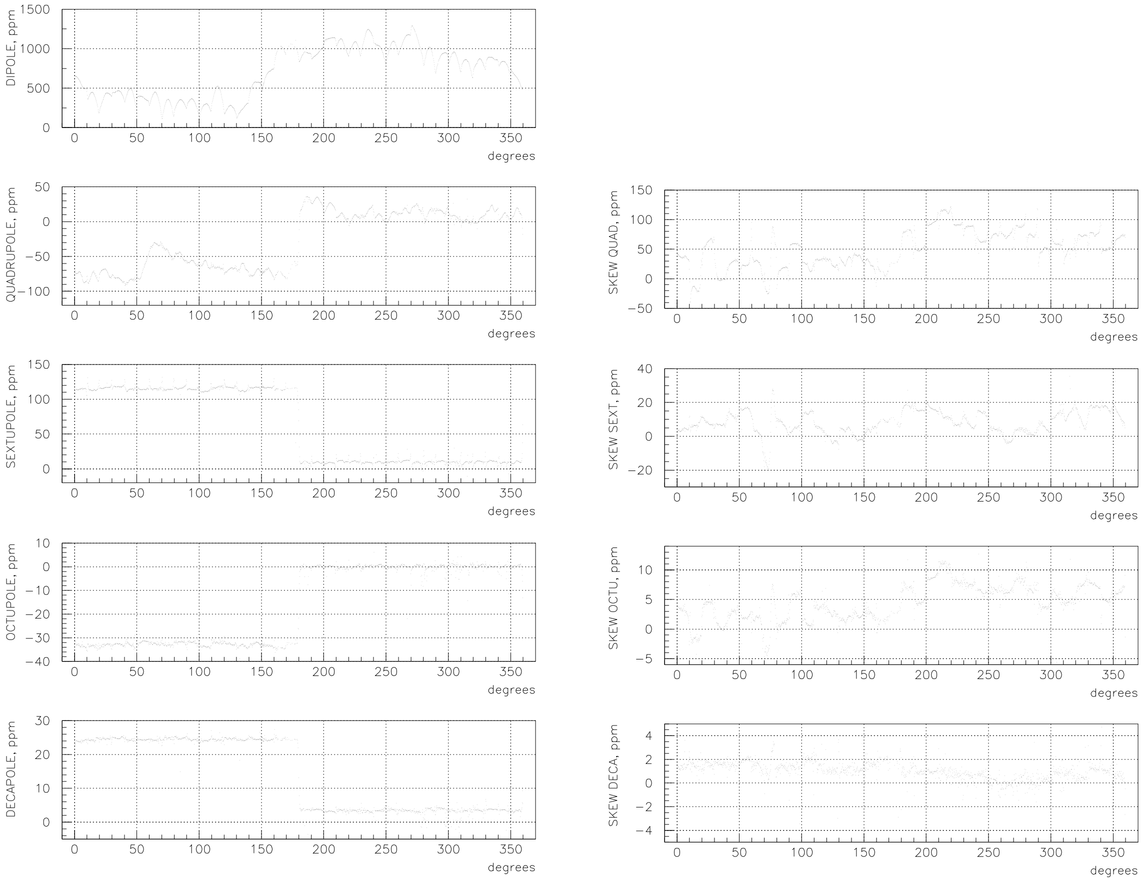


**Figure 5.21**: October 3, 1996 field map

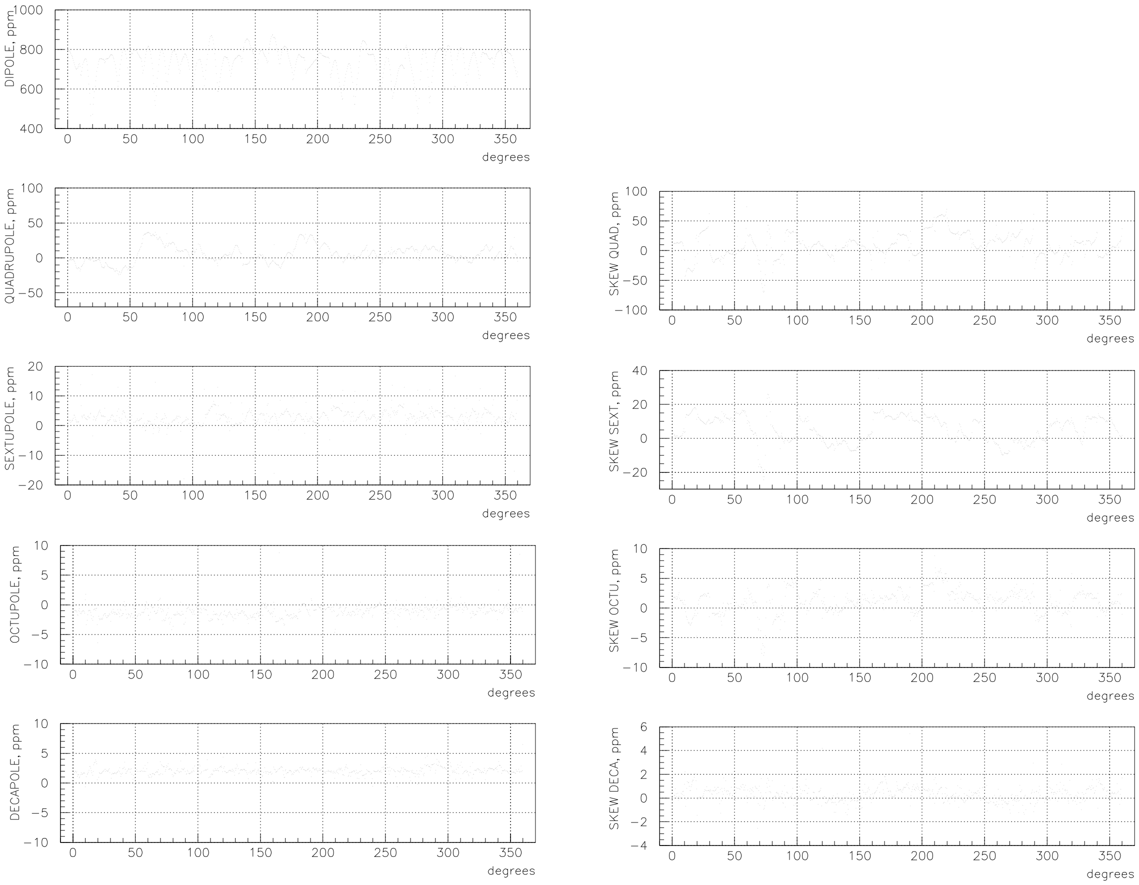


**Figure 5.22**: November 10, 1996 field map

of Rose shims to bring the normal and skew multipoles from quadrupole to decapole to the 10 ppm level. The shims for the half of the ring from 180° to 360° were then machined and installed in the ring. The field map taken after the installation is shown in Figure 5.21. Unfortunately, on the written order for machining we had interchanged the numbers for upper and lower shims and hence the skew multipoles were in average not a zero as desired but twice their original value. This mistake was corrected later when we machined Rose shims for the entire ring.

The final field configuration is shown in Figure 5.22. Averaged over the ring, all multipoles but the dipole are less than 10 ppm. However, some of them have significant variations in azimuth. The normal quadrupole changes from – 20 to 40 ppm for $\Theta$ from 40° to 80° and increases rapidly to 35 ppm at $\Theta = 190°$. This structure was proved to be due to azimuthal variations of the tilt of the top poles with respect to the bottom poles, see section 5.6. Even more azimuthal variations are shown by the skew quadrupole (from – 60 to 60 ppm) and the skew sextupole (from – 20 to 20 ppm). The origin of these variations of the skew multipoles is not well understood. However they are reproducible and can be corrected.

It is also useful to know the lowest azimuthal Fourier harmonics for each multipole. The multipoles in Figure 5.22 were fit by the function

$$F(\Theta) = \sum_{k=0}^{7} A_k \cos(k\Theta + \phi_k),$$

where $A_k$ and $\phi_k$ are the amplitude and the phase of the $k^{th}$ harmonic. The results of the fit are shown in Table 5.2. For completeness, the Fourier harmonics of the radial field (skew dipole) were added in Table 5.2. The radial field measurements will be discussed in the next section.

There are several requirements associated with muon beam dynamics and precision of the average magnetic field $B_{aver}$ on the amplitudes of these azimuthal harmonics:

— The azimuthal harmonics of the dipole field can cause a muon orbit distortion in the horizontal plane, hence muon losses. For this distortion to be within $\pm$ 1 mm, the first harmonic of the dipole field should be less than 20 ppm, the second harmonic less than 400 ppm, etc.

— The radial magnetic field causes a vertical shift of the muon orbit. To keep the shift within $\pm$ 1 mm, the average radial magnetic field in the ring should be less then 20 ppm, the first harmonic of the radial field less than 120 ppm, etc.

— According to equations 5.1 and 5.2 the magnetic field averaged around the ring varies with the average radius if any of the normal multipoles except the dipole is not zero. In such a case muons with a larger radius and larger momentum will see in general different average magnetic field than muons with smaller radius. To determine $a_\mu$ from equation 1.1, magnetic field $B_{aver}$ (averaged over the ring) must be weighted by the muon distribution. To know $B_{aver}$ to 0.1 ppm with a 10% precision of the muon radial distribution, it is necessary to maintain the average of the normal quadrupole less than

**Table 5.2**: Azimuthal harmonics of multipoles

| | 1 | $\cos\theta$ | $\cos 2\theta$ | $\cos 3\theta$ | $\cos 4\theta$ | $\cos 5\theta$ | $\cos 6\theta$ | $\cos 7\theta$ |
|---|---|---|---|---|---|---|---|---|
| NORMAL | | | | | | | | |
| dipole | | 16.5 | 26.0 | 11.3 | 20.9 | 3.3 | 13.3 | 19.9 |
| quadrupole | 5.5 | 3.5 | 4.4 | 8.0 | 5.5 | 6.2 | 5.1 | 3.4 |
| sextupole | 3.3 | 0.2 | 0.1 | 0.2 | 0.4 | 0.3 | 0.1 | 0.1 |
| octupole | –1.2 | 0.2 | 0.0 | 0.1 | 0.0 | 0.0 | 0.2 | 0.3 |
| decapole | 2.0 | 0.0 | 0.2 | 0.1 | 0.1 | 0.0 | 0.0 | 0.2 |
| 12–pole | –0.1 | 0.1 | 0.1 | 0.1 | 0.0 | 0.0 | 0.0 | 0.0 |
| 14–pole | –0.7 | 0.0 | 0.0 | 0.2 | 0.2 | 0.1 | 0.1 | 0.3 |
| SKEW | | | | | | | | |
| dipole | 18.8 | 21.1 | 35.8 | 41.4 | 5.8 | 10.1 | 2.8 | 16.7 |
| quadrupole | 9.0 | 8.5 | 0.2 | 4.3 | 1.3 | 1.9 | 5.3 | 1.7 |
| sextupole | 5.3 | 1.2 | 5.5 | 2.1 | 0.1 | 3.6 | 1.0 | 0.7 |
| octupole | 0.8 | 0.7 | 0.1 | 0.6 | 0.3 | 0.1 | 0.6 | 0.1 |
| decapole | 0.4 | 0.1 | 0.4 | 0.2 | 0.1 | 0.1 | 0.2 | 0.1 |
| 12–pole | –0.1 | 0.0 | 0.1 | 0.2 | 0.2 | 0.1 | 0.1 | 0.1 |
| 14–pole | 0.2 | 0.0 | 0.1 | 0.0 | 0.0 | 0.1 | 0.1 | 0.0 |

10 ppm, of the normal sextupole $<$ 30 ppm, of the normal octupole $<$ 100 ppm and of the decapole $<$ 250 ppm. Without any knowledge of the muon radial distribution $B_{aver}$ is known to 0.1 ppm if the multipoles are maintained a factor of 10 less than listed above.

— A nonuniform magnetic field gives rise to a periodic force which disturbs the muon orbits. If the periodicity of the force is in resonance with betatron oscillations, the amplitude of the horizontal or vertical oscillations of the muon may increase, leading to a loss of particles from the storage region. Although the field index n = 0.135 was chosen so that betatron oscillations frequencies are far from strong resonances, they can, nevertheless, cause amplitude modulation of the betatron oscillations. Table 5.3 lists azimuthal harmonics of lowest multipoles, which can create driving forces capable of causing $\pm$ 1% beating. For completeness, the other requirements discussed above are also included in Table 5.3.

Comparison of the measured magnetic field harmonics of Table 5.2 with the requirements of Table 5.3 indicates that by the end of 1996 the (g–2) magnet was ready for the first run of (g–2) experiment.

There are two more shimming techniques shown in Figure 5.12, namely surface correction coils and aluminum/iron sandwiches. These were tested before and during the 1997 run, but were not used for shimming the field. Surface correction coils are

**Table 5.3**: Limits on the azimuthal harmonics of multipoles

| Harmonics | | Limit, ppm | Reason |
|---|---|---|---|
| NORMAL | | | |
| Dipole | $\cos\theta$ | 20 | orbit distortion within $\pm 1$ mm |
| | $\cos 2\theta$ | 400 | orbit distortion within $\pm 1$ mm |
| Quadrupole | 1 | 10 | $B_{aver}$ correct to 0.1 ppm with 10% precision of muon radial distribution |
| | $\cos\theta$ | 32 | n = 0.25 resonance, 1% amplitude modulation |
| Sextupole | 1 | 30 | $B_{aver}$ correct to 0.1 ppm with 10% precision of muon radial distribution |
| | 1 | 21 | n = 0.2 resonance, 1% amplitude modulation |
| | $\cos\theta$ | 6 | n = 0.0 resonance, 1% amplitude modulation |
| | $\cos 2\theta$ | 22 | n = 0.36 resonance, 1% amplitude modulation |
| Octupole | 1 | 100 | $B_{aver}$ correct to 0.1 ppm with 10% precision of muon radial distribution |
| | $\cos\theta$ | 16 | n = 0.169 resonance, 1% amplitude modulation |
| | $\cos 2\theta$ | 22 | n = 0.0 resonance, 1% amplitude modulation |
| Decapole | 1 | 500 | $B_{aver}$ correct to 0.1 ppm with 10% precision of muon radial distribution |
| | 1 | 67 | n = 0.06 resonance, 1% amplitude modulation |
| | $\cos 2\theta$ | 3 | n = 0.148 resonance, 1% amplitude modulation |
| 12–pole | $\cos 3\theta$ | 2 | n = 0.132 resonance, 1% amplitude modulation |
| SKEW | | | |
| Dipole | 1 | 20 | orbit vertical shift within $\pm 1$ mm |
| | $\cos\theta$ | 120 | orbit vertical oscillations within $\pm 1$ mm |
| | $\cos 2\theta$ | 540 | orbit vertical oscillations within $\pm 1$ mm |
| Quadrupole | $\cos\theta$ | 17 | n = 0.0 resonance, 1% amplitude modulation |
| Sextupole | $\cos\theta$ | 19 | n = 0.111 resonance, 1% amplitude modulation |
| Octupole | 1 | 36 | n = 0.1 resonance, 1% amplitude modulation |
| | $\cos 2\theta$ | 11 | n = 0.126 resonance, 1% amplitude modulation |
| Decapole | $\cos 3\theta$ | 9 | n = 0.148 resonance, 1% amplitude modulation |
| 14–pole | 1 | 9 | n = 0.138 resonance, 1% amplitude modulation |

printed circuit (PC) boards glued to the surfaces of the poles. Each PC board has 120 etched azimuthal strips, equally spaced and occupy altogether 12 inch in radial direction and cover surface of one pole. Strips from adjacent PC boards are electrically connected by pin connectors, forming 120 conductive rings on the top and bottom poles. We used 60 stabilized power supply units to energize the surface correction coils combining 4 rings in series. The field effect of each group was measured individually. An algorithm was developed by the author to calculate the optimal current distribution to correct given set of multipoles.

The aluminum/iron sandwich is a set of strips made of thin iron foil and glued between two aluminum sheets for mechanical stability. This technique can correct local field inhomogeneities. There are two major applications for this technique. One is to correct azimuthal variations of the field, particularly at boundaries between adjacent poles. In this case iron strips should be installed along the radial direction and extend from the inner to outer Rose shims. The second application is to correct locally a set of multipoles. In this case iron strips should be installed along azimuthal direction. Both these applications were tested prior to the 1997 run.

## 5.6 Measurements of the Magnetic Field with Hall Probes

A number of measurements of the magnetic field with Hall probes were made by the author alone or in collaboration with N. Ryskulov and G. Fedotovich from Novosibirsk, Russia. Measurement of the radial field in the kicker hole during the magnet commissioning was already discussed in section 5.3. Hall probes have less accuracy in magnetic field measurements than NMR probes. However for measurement of an inhomogeneous magnetic field or for determination of the direction of the field NMR can not be used and Hall probes are useful.

One of the most important applications of Hall probes was measuring the radial component of magnetic field in the muon storage ring. In order to limit the vertical shift of the muon orbit, the radial component should be less than 50 ppm. Our measurement used Hall probes and achieved an accuracy of 10 ppm. This provides adequate accuracy for shimming and control of the radial field.

The Hall probes device contains two Hall probes BH–206 from F.W. Bell company and the electrolytic tilt sensor RG33A from Spectron Systems Technology Inc. The probes are thin 1 mm $\times$ 3 mm rectangular plates with current electrodes along the short sides and voltage outputs from the centers of the long sides of the plate. The Hall probes are installed on the $Z - \Theta$ plane and the electrolytic tilt sensor along the $R$ axis on aluminum support as shown in Figure 5.23. The support itself is mounted on the system of platforms in such a way, that can be tilted (adjusted) within $\pm 0.5°$ from horizontal in $Z-R$ plane and rotated around the vertical $Z$ axis by 180°.

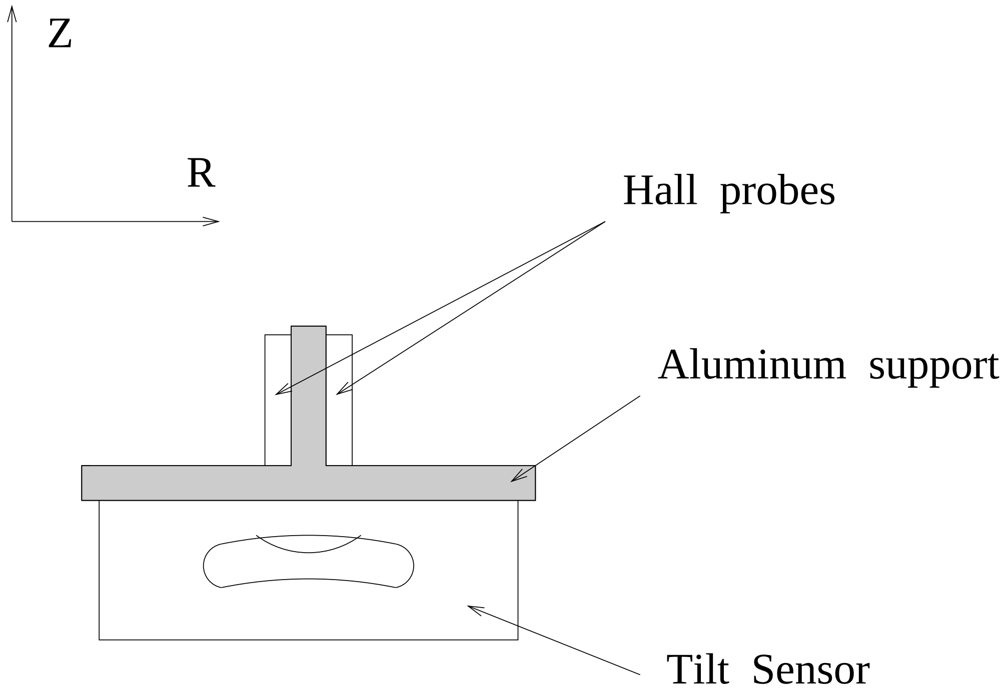


**Figure 5.23**: Hall probe device for the radial magnetic field measurements

The principle of operation of this device is following. First we set the tilt of the aluminum support at some arbitrary angle $\delta$ (readout of the tilt sensor), usually close to zero, and record the output voltage from the Hall probe $V$. Then we make 180° rotation, adjust the angle of the support to the same angle $\delta$ and take another Hall probe voltage, $V'$. The angle $\alpha$ between the magnetic field and the vertical axis is given by

$$\alpha = \frac{1}{2}\frac{(V-V')}{V(1.45\,T)}\,, \tag{5.3}$$

where $V(1.45\,T)$ is a Hall probes output for magnetic field of 1.45 T.

The formula above is insensitive to the following sources of systematic errors:
– the axis of the 180° rotation is not exactly vertical in $Z-R$ plane,
– the Hall probes output has offset,
– the electrolytic tilt sensor output has offset,
– the axis of the electrolytic tilt sensor is not exactly orthogonal to the plane of the Hall probes,
– temperature change over time larger than one measurement cycle (before and after flip), which is about 5 minutes.
Also note that the systematic error due to not exactly 180° rotation is of second order.

A potentially important systematic error is the planar Hall effect. The electric field $\vec{E}$ inside a semiconductive probe in a magnetic field $\vec{B}$ can be written

$$\vec{E} = \rho\,\vec{J} + R_h\,\vec{B}\times\vec{J} - M\,\rho\,\vec{B}\times[\vec{B}\times\vec{J}]\;\;[96],$$

where $\rho$ is resistivity, $\vec{J}$ is current density, $R_h$ is the Hall magnetoresistivity and $M$ is the transverse magnetoresistivity. Hence, the voltage across the probe can be written as

$$V = k_1 B_\perp I + k_2 \vec{B}_{||}^2\, I\;\sin\,2\psi, \tag{5.4}$$

where $B_\perp$ is the component of the magnetic field perpendicular to the plane of the Hall probe, $\vec{B}_{||}$ is the magnetic field in the plane of the Hall probe and $\psi$ is the angle between $\vec{B}_{||}$ and $\vec{I}$. The quantities $k_1$ and $k_2$ are the Hall coefficient and the planar Hall coefficient, respectively. In our case, when $|\vec{B}_{||}| = 1.45$ T and $B_\perp \ll |\vec{B}_{||}|$, the second term in equation 5.4, which is the planar Hall effect, typically is much larger than the direct Hall effect.

For the case of ideal mechanical alignment the planar Hall effect acts as an additional zero offset and hence is irrelevant. However, if the axis of the 180° rotation is not exactly vertical and has a small component $\epsilon$ in the azimuthal direction, equation 5.3 will give an incorrect value for $\alpha$ by

$$\Delta\alpha = \frac{1}{2}\,\frac{k_2\,\vec{B}_{||}^2\,I}{V(1.45\;T)}\;\sin\,2\epsilon.$$

To avoid this systematic error, we use two Hall probes with parallel planes, but with orthogonal directions of the Hall currents, in the vertical and horizontal (azimuthal) direction, respectively. If we apply equation separately to both Hall probes, which are chosen to have the same planar Hall coefficient $k_2$, and then take an average, the net result will not be affected by this source of systematic errors:

$$\Delta\alpha = \frac{1}{2}\,(\Delta\alpha_1 + \Delta\alpha_2) = \frac{1}{4}\,\frac{k_2\,\vec{B}_{||}^2\,I}{V(1.45\;T)}\;[\,\sin\,2\epsilon + \sin\,2(90^\circ + \epsilon)\,] = 0$$

So, the formulae to be used are:

$$\alpha = \frac{1}{2}(\alpha_1 + \alpha_2), \quad \alpha_i = \frac{1}{2}\,\frac{(V_i - V_i')}{V(1.45\;T)}, \tag{5.5}$$

where i = 1,2 − number of Hall probe.

The Hall probe device, described above, was built and tested in the test magnet with a magnetic field of 1.45 T. We measured the angle $\alpha$ between the magnetic field and the vertical axis for 11 different tilts $\delta$ over the whole range of the tilt sensor, which is about ±15 arc minutes. No dependence of $\alpha$ on $\delta$ was observed. Averaging all the results gave:

$\alpha_1 = 1894.7 \pm 4.6\;\mu$rad

$\alpha_2 = 1918.3 \pm 4.4\ \mu$rad
$\alpha = 1906.5 \pm 3.7\ \mu$rad,
where the r.m.s. values $\pm 4.6\ \mu$rad and $\pm 4.4\ \mu$rad are a measure of the precision of the device. Note that the planar effect is $\alpha_1 - \alpha_2 = -23.6\ \mu$rad in this case. This test showed that this Hall probe device can provide an accuracy of better than 10 ppm in the measurement of the radial magnetic field.

Two electrolytic tilt sensors of the same type as in the Hall probe device were used to make two very sensitive levels to measure the tilts of top and bottom poles. Figure 5.24 shows these levels and the scheme of measurements. The angle of tilt of poles in the radial direction is given by the average of two measurements, one before and one after the 180° rotation. Voltage versus angle characteristics of tilt sensors were measured on a test stand. They have a good angular resolution $\sim 1\ \mu$rad, but rather poor linearity over the whole range $\pm 15$ arc minutes ($\pm 4500\,\mu$rad) from the horizontal plane. However, over the range of pole tilts of $\pm 150\,\mu$rad the nonlinearity is small. The overall precision of the measurements of the tilts is of the order of 5 $\mu$rad.

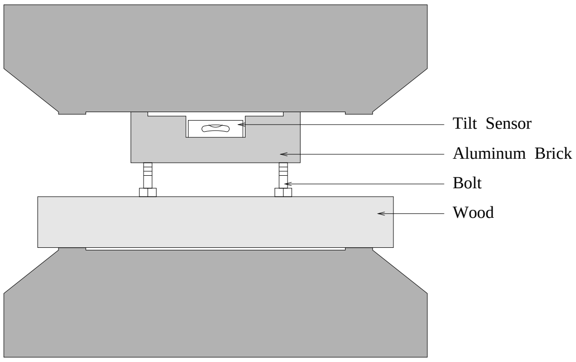


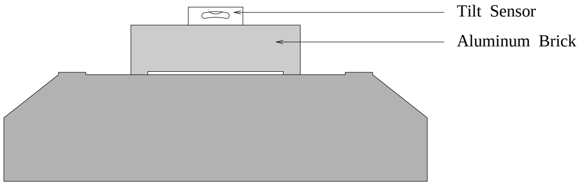


**Figure 5.24**: Scheme of measurements of tilts of top pole (top) and bottom pole (bottom)

The apparatuses for radial magnetic field measurements and for measurements of pole tilts were combined in the single movable station as shown in Figure 5.25. The Hall probe device was installed in the center of some pole section to measure the radial magnetic field and two levels were installed in two adjacent sections to measure the tilts of top and bottom poles. It took about 10 minutes to complete measurements in one location. Then the apparatus was moved to measure the next pole section. Measurements were made over the entire ring.

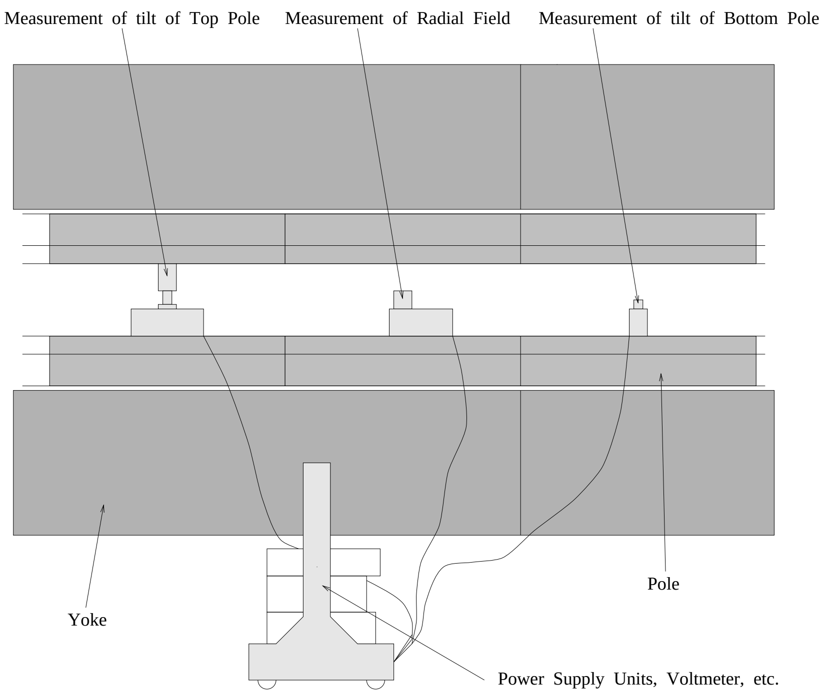


**Figure 5.25**: Scheme of measurements on the floor

The measurements of the radial magnetic field in the (g–2) ring and the tilts of the poles were started shortly after successful commissioning of the magnet with the full field of 1.45 T in late June 1996. We made several sets of measurements during the shimming and a final one on November 8. Results of the last measurements are shown in Figures 5.26 and 5.27 with the convention for positive angles and radial field shown in Figure 5.28. The radial magnetic field averaged over the ring was about 20 ppm. Several low azimuthal Fourier harmonics of the radial field (skew dipole) are listed in Table 5.2.

There is a strong correlation between the tilts of the poles and the magnetic field in the muon storage volume. If top and bottom poles are parallel to each other and both are tilted in the radial direction by some angle with respect to the horizonal, the magnetic field should be tilted from the vertical by this same angle, and hence have a radial component. Indeed Figure 5.29 clearly shows the correlation between the radial field (points) and the average tilt of top and bottom poles (histogram).

If top and bottom poles are not parallel, the magnetic field is stronger where the gap between top and bottom poles is smaller. This results in a linear dependence

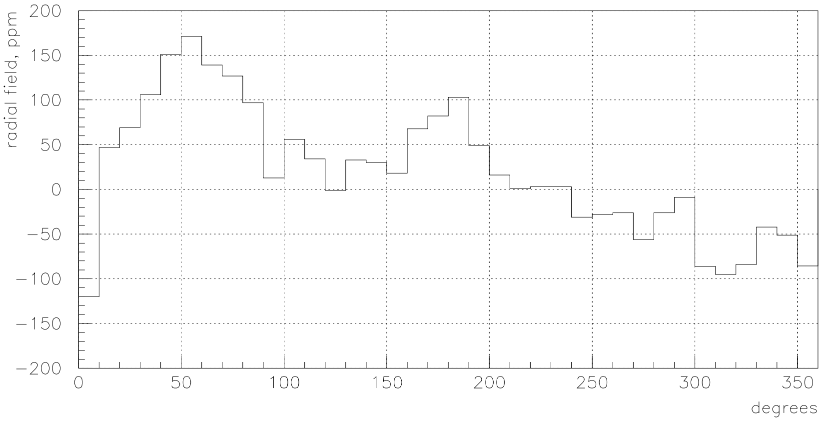


**Figure 5.26**: Radial magnetic field map

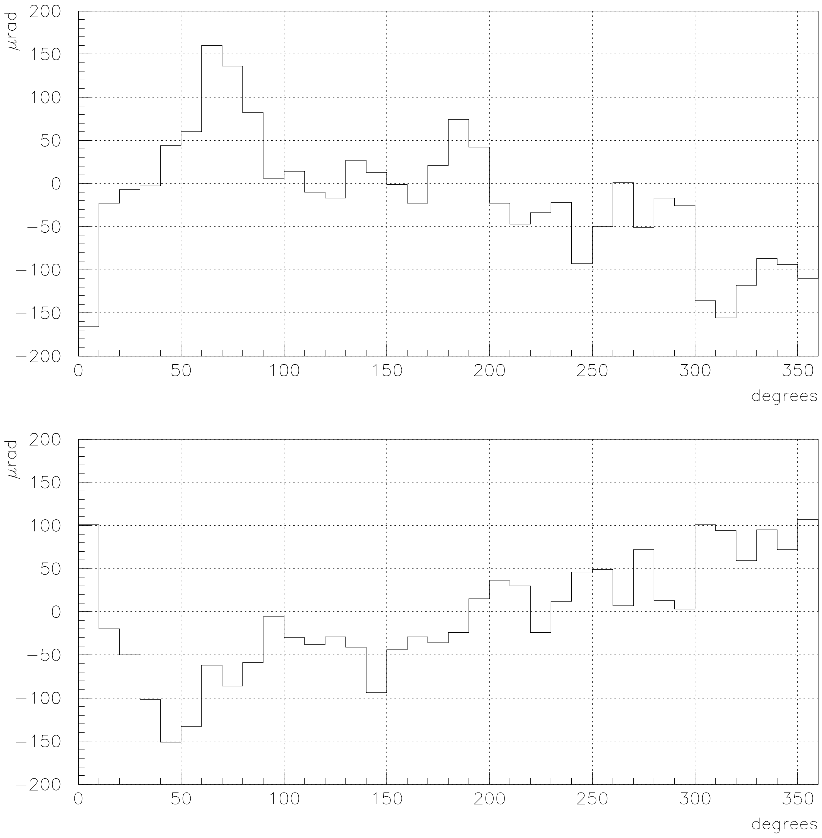


**Figure 5.27**: Tilts of top poles (top) and bottom poles (bottom)

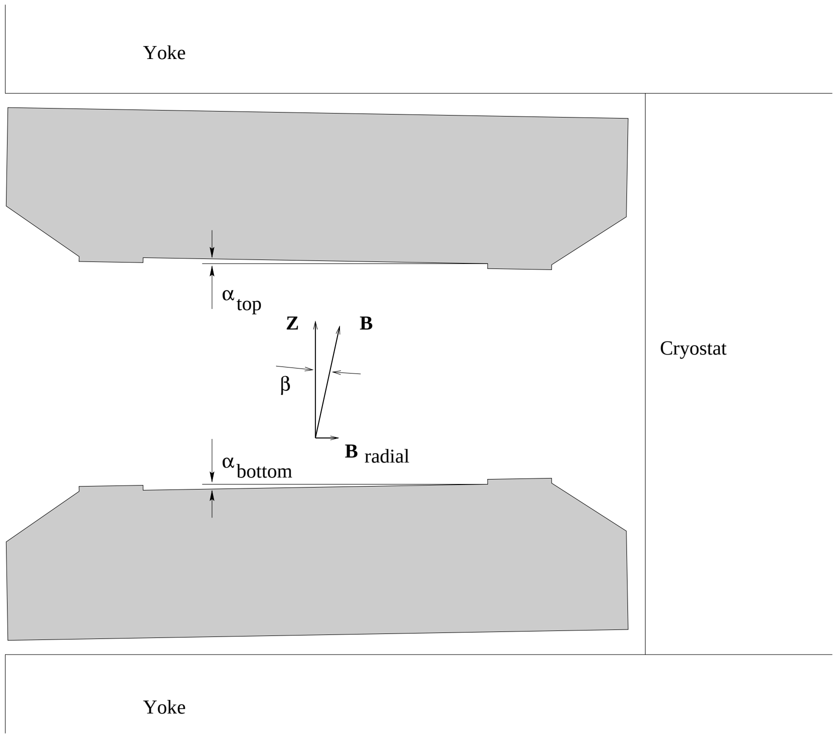


**Figure 5.28**: Positive angles and radial field convention

of the magnetic field on the radius, i.e. creates the normal quadrupole $B_{quad}^{norm}$, see equations 5.1, 5.2. For a relative tilt $\alpha$ of the top and bottom poles

$$B(x) = B_\circ + \frac{h(0) - h(x)}{h(0)}\, B_\circ = B_\circ + \frac{-x\, tan(\alpha)}{18\, cm}\, B_\circ = B_\circ - B_\circ\, \frac{x}{4.5\, cm}\, \frac{4.5\, cm}{18\, cm}\, tan(\alpha) =$$
$$= B_\circ - \frac{1}{4}\, tan(\alpha)\, B_\circ\, \frac{x}{4.5\, cm} \approx B_\circ - \frac{1}{4}\, \alpha\, B_\circ\, \frac{x}{4.5\, cm},$$

and hence

$$B_{quad}^{norm}\ [ppm] = -\frac{1}{4}\, \alpha\ [\mu rad].$$

Here $h(0) = 18$ cm is the nominal gap between top and bottom poles. Rose shims also contribute to the normal quadrupole uniformly around the ring. Figure 5.30 (bottom) shows the relative tilt of top and bottom poles (histogram) and the normal quadrupole component of the magnetic field (points) around the ring. The normal quadrupole data in Figure 5.30 were taken from Figure 5.22, multiplied by –4 and uniformly shifted by 50 $\mu$rad. The correlation in Figure 5.30 (bottom) is excellent providing that the large azimuthal variations of the normal quadrupole in Figure 5.22 are caused by the relative tilts of top and bottom poles.

For completeness, Figure 5.30 (top) shows relative tilts of top and bottom poles measured with tilt sensor levels (histogram) and with the Capacitec device. The agreement between these two is also good.

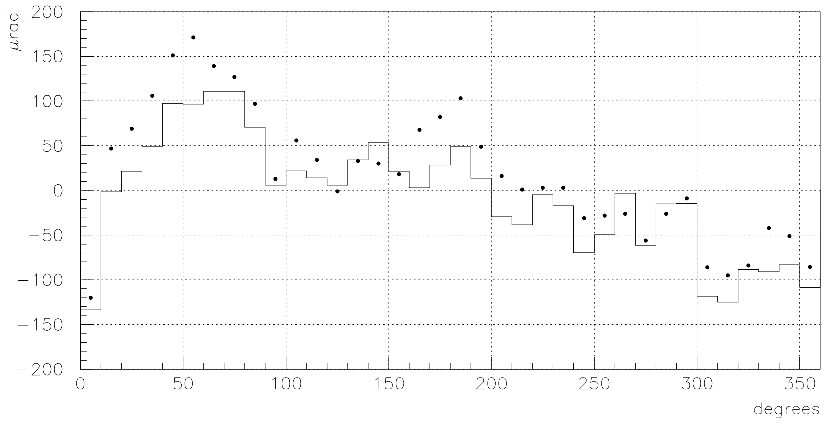


**Figure 5.29**: Average tilt of top and bottom poles (histogram) and radial field (points)

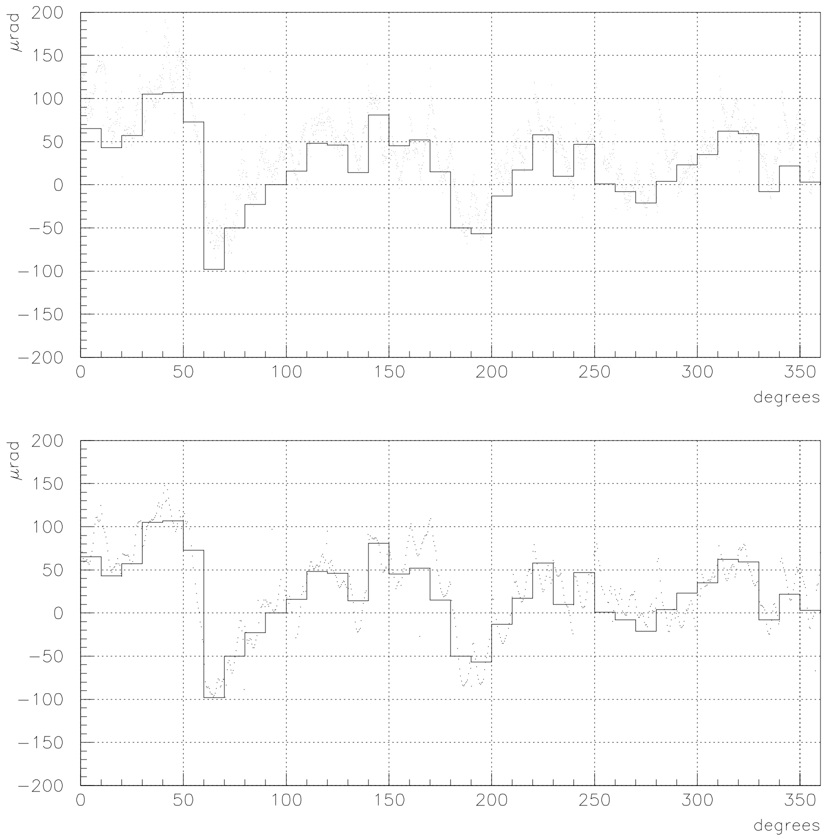


**Figure 5.30**: Relative tilt of top and bottom poles: measured by tilt sensors (histogram), measured by Capacitec sensors (points, top) and evaluated from normal quadrupole field (points, bottom)

Another important measurement made with Hall probes was the measurement of magnetic field in the region of the traceback system (see section 4.12) which occupies the radial region from R = 680 cm to 705 cm and the vertical region from $Z$ = –10 cm to +10 cm, where the magnetic field varies from 1.45 T to $\sim$ 0.2 T. Both vertical and radial components of the field are needed for reconstruction of the electron track. The azimuthal component of the field is assumed to be zero from symmetry.

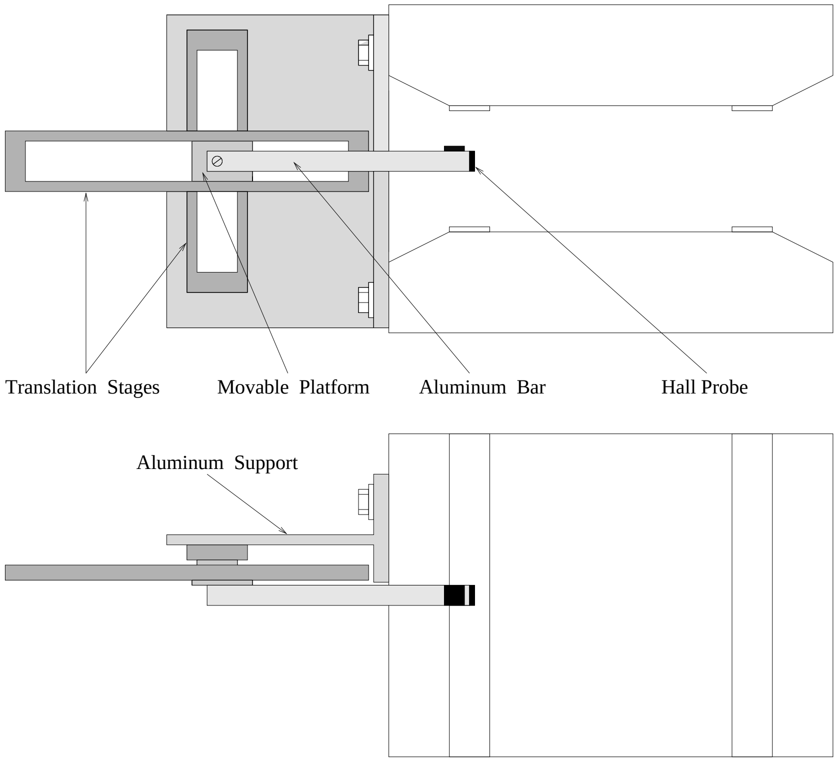


**Figure 5.31**: Apparatus for magnetic field measurements for the electron traceback system

The apparatus used for magnetic field measurements in the traceback region is shown in Figure 5.31. It consists of two Hall probes mounted on a system of two translation stages which in turn are mounted on the rigid aluminum support and the whole assembly is bolted to the top and bottom poles. The Hall probes were oriented so that one of them measured the vertical component of the field and the other measured the radial component. The translation stages provided radial and vertical motion of the probes. Possible misalignments of the Hall probes and translation stages as well as position calibration can be found by comparing the data and calculations.

The results of measurements are shown in Figure 5.32 by points. The smooth lines are fits based on calculations made by W. Meng. Measurements and calculations are in agreement at the $10^{-3}$ level, which is required to reconstruct electron tracks.

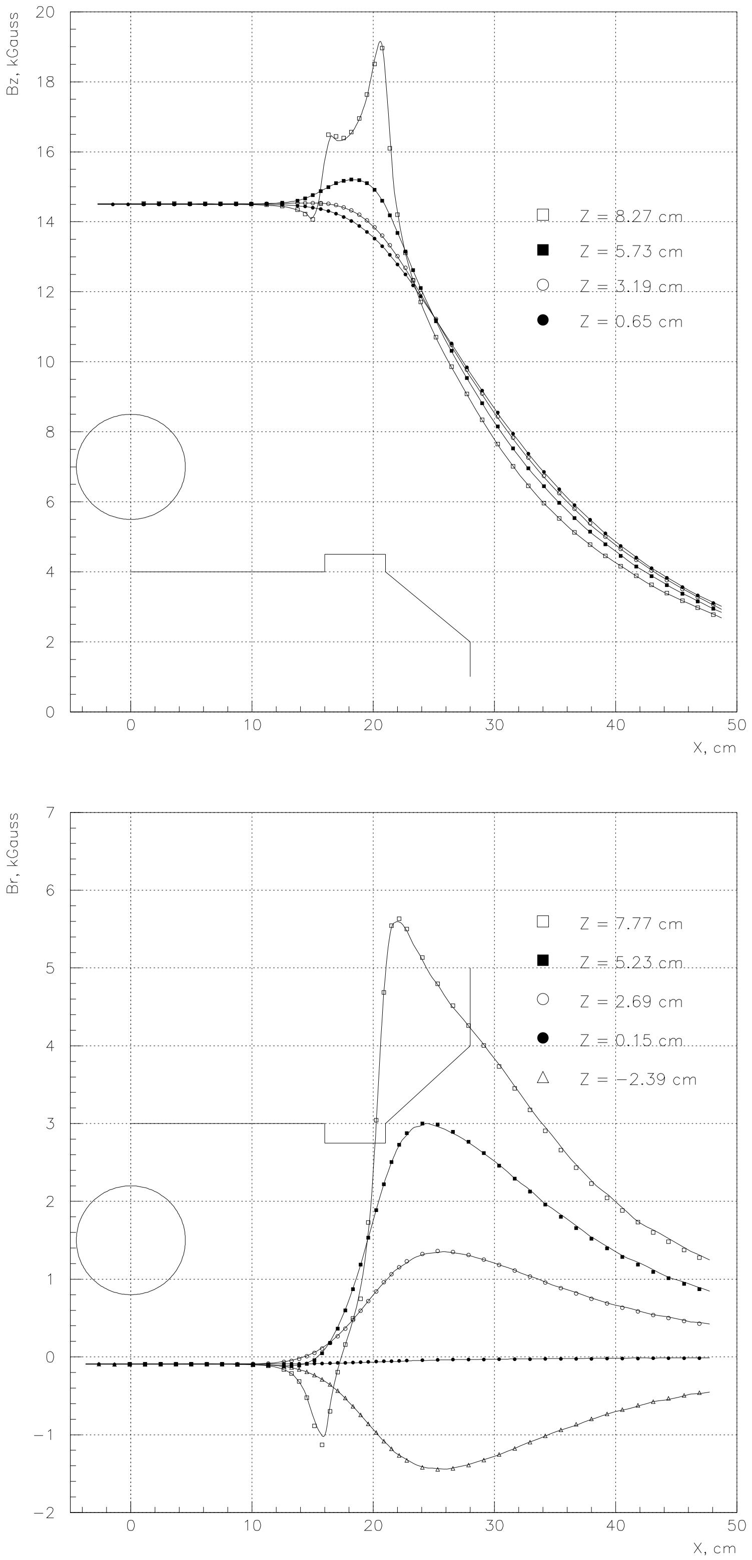


**Figure 5.32**: Magnetic field in the electron traceback region: vertical (top) and horizontal (bottom) components. Muon storage region and pole profile are shown for references.

# Chapter 6

# First Run, April–July 1997

## 6.1 Beam Tune, first (g–2) Oscillations

The AGS began its 1997 proton program on April 1. It was scheduled to run April and May in the fast extracted beam (FEB) mode for a variety of high energy physics experiments, including our muon (g–2) E821. The latter was planned to get one bunch out of 8 per AGS cycle (2.6 seconds), for testing the apparatus and the data acquisition system. The dedicated muon (g–2) run was scheduled for June 1997.

So, in early April 1997 the muon (g–2) experiment started its first run with pion injection. The cryogenic system had been working continuously since February 1997. After several retraining quenches, the inflector was successfully commissioned with the maximum current of 2800 Amp. Vacuum chambers with their electrostatic quadrupoles were installed and tested at a vacuum of $10^{-7}$ Torr. The beam tube trolley system (drive, garage) was installed in the ring and several field maps were taken by the trolley NMR probes both in air and vacuum. The fiber beam monitors and the traceback system were installed. Six calibrated detectors were installed inside the muon storage ring, while the rest were being calibrated in the test beam and expected to be ready soon.

Due to much increased safety requirements at BNL and to technical safety features related to the compatibility of our AGS E821 experiment and RHIC, no AGS beam was obtained until late April. By this time all detector stations had been installed. During late April and May, major efforts were devoted to beam tuning and commissioning the detectors in the real environment of the experiment.

The first beam was delivered to the inflector entrance on April 23, AGS operators extracted one bunch of $\sim 0.6 \cdot 10^{12}$ protons out of 8 in an AGS cycle with other 7 bunches been crashed on the beam stop. In order to tune the beam through the inflector, two scintillating counters were prepared and inserted into the muon storage volume at about

$80^{\circ}$ and $165^{\circ}$ downstream of the inflector exit. With these counters we tuned the beam momentum and found an optimum at $\sim 2\%$ above the expected value with a base width of about 2.5%. Scan of the inflector current revealed a broad maximum from 2800 down to 2760 Amp. We had to take the two scintillating counters out of the ring soon, when we closed the vacuum chamber for pumping. Since then we used calorimeter signals for the beam tuning.

In calorimeter 24, which is about $\sim 340^{\circ}$ downstream of inflector, we saw the signal at the moment of injection and an even larger one 150 nsec later, when the pion beam hit the inflector. With pion injection the pion beam can not survive more than one turn, therefore a bigger second signal in calorimeter 24 means less pion losses in the electrostatic quadrupoles, walls of vacuum chamber, etc. We used the ratio of the first and second signals from the calorimeter 24 as a tool for the beam tuning.

In other calorimeters we saw very large "flash" signals from products of interaction of the pion beam with matter for up to 20 $\mu$sec after the beam injection. The flash was much higher for calorimeters in the first half of the ring, i.e. on detector stations 2 to 11 (see Figure 4.15) which were made of boron doped calorimeters with multialkaline photocathode PMTs, while the others were nonboron/bialkaline stations. We had to set different gating times for calorimeters at different locations in the ring. Later we exchanged two stations and found that both detector location and performance contribute in the magnitude of the flash. The stray magnetic field was found to disturb detector PMTs, so we installed steel plates between the magnet and PMT for additional screening of the magnetic field.

It seemed very reasonable to include number of decay electrons in a set of parameters for the beam optimization. For this purpose four calorimeters from the quiet part of the ring were included in the electron counter, which counted coincidences of signals from any two of four quadrants of the same calorimeter in a visual scaler. Tuning the pion beam momentum, we found a sharp optimum at $P_{magic} + 2.5\%$ instead of "nominal" $P_{magic} + 0.5\%$, in agreement with the earlier tune with the two scintillating counters. Here $P_{magic} = 3.094$ GeV/c is the muon "magic" momentum.

The optimum at higher pion momentum might be explained if the pion beam went through about 20 cm of aluminum along the edge of the inflector and degrade to the design momentum $P_{magic}{+}0.5\%$ at the inflector exit. To test this model we set the beam momentum at $P_{magic}{+}2.0\%$ and scanned the inflector current, trying to move the beam "out of the inflector wall". The scan from 2800 Amp down to 2550 revealed a broad peak at about 2700 Amp with full width at the half maximum (FWHM) $\sim$ 200 Amp. The crucial test of the model would be to raise the current above the inflector maximum 2800 Amp. Alternatively, we could scale down both magnetic field in the muon storage ring and momentum of the pions, such that the trajectory of particles would be the same and we would effectively gain more room to rise the inflector current.

We did scale down the magnetic field by 11.7% and retune the beam line. Using the electron counter we found the optimum at pion momentum $(P_{magic}{+}2.5\%) - 11.7\%$

and fixed the beam line setting. Then we scanned inflector current from 2800 Amp down to 2500 and got a broad peak at 2600 Amp. We didn't see pion beam coming out of inflector wall, so the model failed. The $P_{magic} + 2.5\%$ phenomenon remained not well understood. The most reasonable explanation is that the current–field relations for the beam line magnets changed since installation due to numerous power losses (the Umbrella effect, see section 5.4).

Something important, however, happened when we worked at the beam moment $(P_{magic} + 2.5\%) - 11.7\%$. We never stopped tuning the beam and on their night shift of May 6, Novosibirsk accelerator expert Y. Shatunov with assistance of the author achieved significant improvement in the beam setting. Using the beam line magnets D5 and D6 and opening collimators K3 and K4 (see Figure 4.2), they were tuning the angle at which the pion beam enters the inflector. As a parameter for optimization they used the ratio of the second to first signals from calorimeter 24. Tuning the angle they were able to improve this ratio by a factor of $\sim$5. The new beam line setting was named "Novosibirsk tune".

The next night we came back from the "–11.7%" state to the nominal one. The author with assistance of another Novosibirsk collaborator, V. Druzhinin, set the "Novosibirsk tune" for the nominal state. It was very exciting night shift. We repeated the inflector current scan and got basically same results as before. Using the pitch magnets at the downstream end of the beam line we tuned the vertical angle of the beam entrance to the inflector and found the optimum at the zero angle. Most importantly, with improved beam tuning we collected a lot of data and in the prompt offline analysis we found the (g–2) oscillations for the first time, see Figure 6.1.

At that time the AGS operators extracted 4 out of 8 bunches from every $8^{th}$ AGS cycle and later all 8 bunches. With less bunches going to the beam dump, we could increase the beam intensity per bunch (this is a radiation safety issue) and collect more data per shift.

## 6.2 Detector Pulses

With the first (g–2) oscillations observed during the morning May 8 shift we started offline analysis of collected data. At that stage of the experiment we were optimizing the experimental setup and offline procedures. To reject PMT noise and to select high energy decay positrons we first used an area cut of the WFD pulses (the pulse area corresponds to the energy deposited in the calorimeter). It was, however, soon found by the author and V. Druzhinin that a two dimensional distribution of area versus amplitude of a pulse provides significantly more information and allows better selection of high energy positrons compared to a one dimensional distribution of area or amplitude. Figure 6.2 shows the energy versus amplitude distribution for one of the

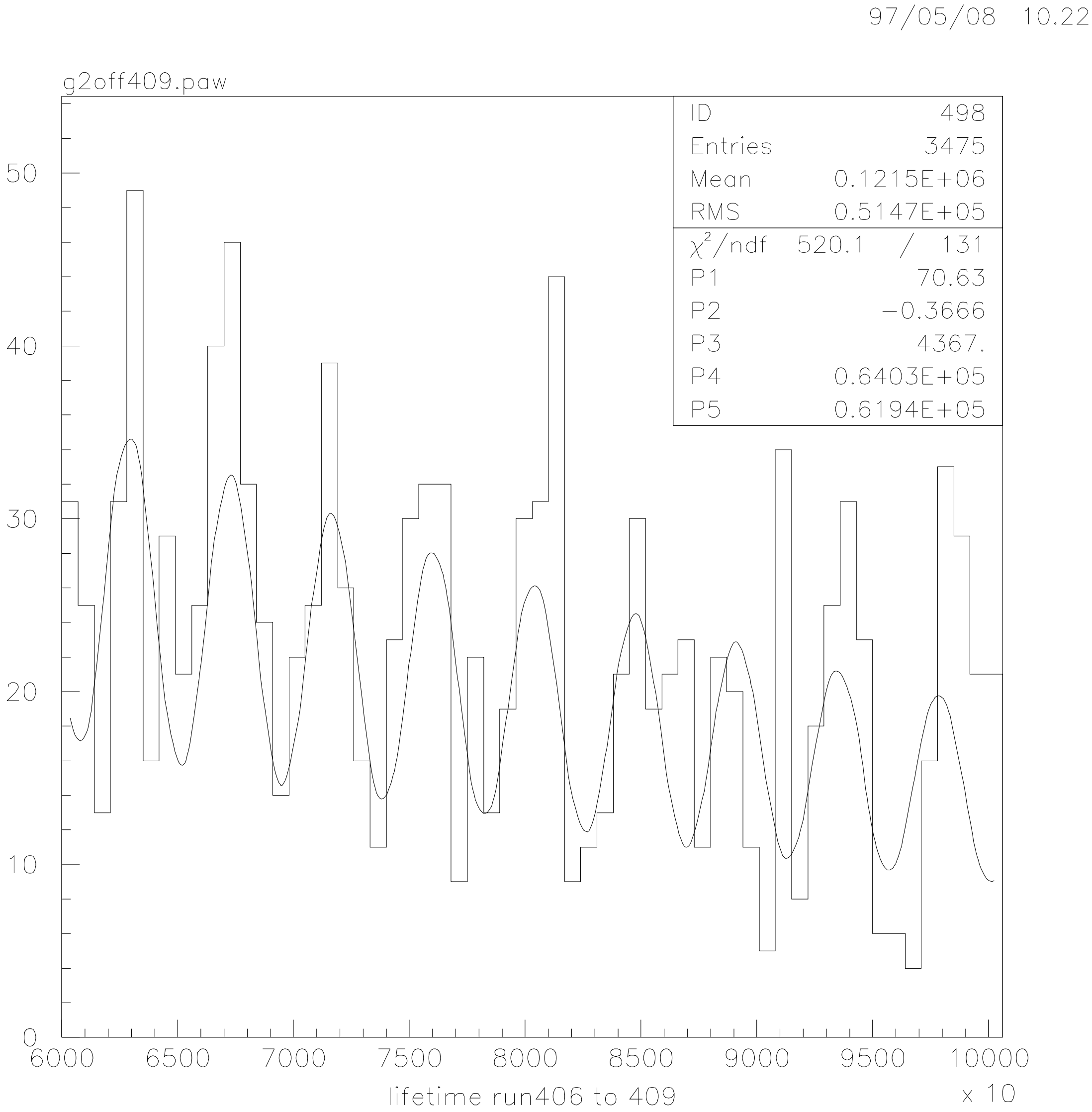


**Figure 6.1**: First g–2 oscillations observed in 1997 run. Horizontal scale is time in nsec.

later runs (#612) with high statistics. There are two clearly separated regions on the plot, above and below the dashed line. The time distribution of events above the line in Figure 6.2 is shown in Figures 6.3 and 6.4. The exponential decay with $\tau \approx 60\,\mu$sec and the (g–2) oscillations are clearly seen. The time distribution of events below the dashed line in Figure 6.2 has no (g–2) oscillations and doesn't follow an exponential decay line, see Figures 6.5 and 6.6. We conclude that we are observing decay positron events above the dashed line in Figure 6.2 and some background below the line. These two can be separated by the two dimensional cut, but the number of background events is much higher than the number of decay positrons and can contaminate the decay positron sample. The background also contributes to filling the detector electronics buffers. For the same amplitude the background events have less area as compared to positron pulses and they are called narrow pulses. The narrow pulses were one of the main concerns in this 1997 run.

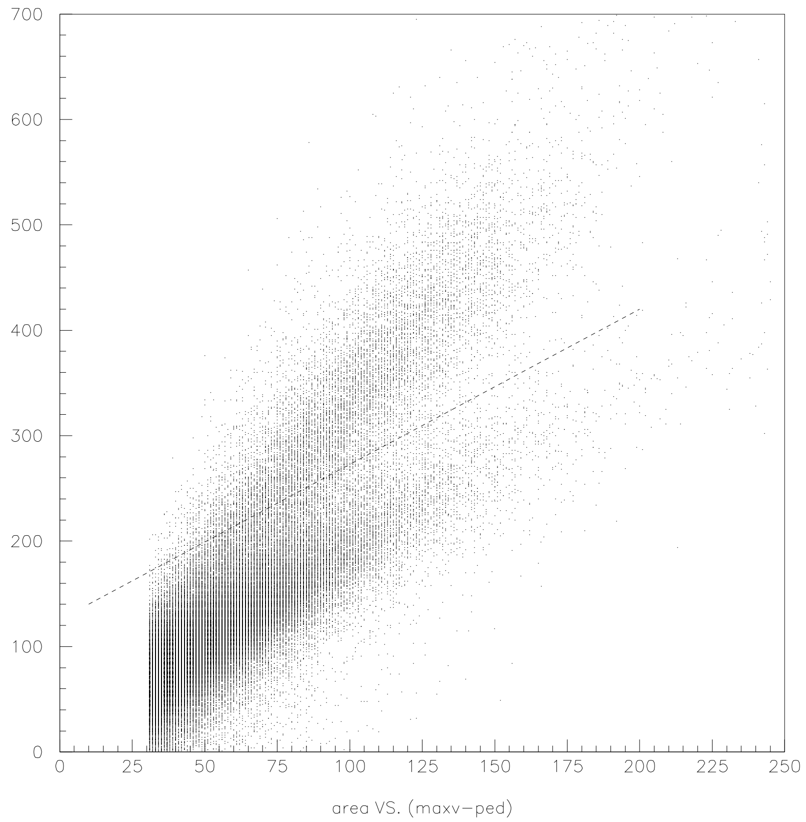


**Figure 6.2**: Energy versus amplitude distribution

A number of tests were made to understand the nature of the narrow pulses and to suppress their number in the data stream. First with a digital scope we verified that the narrow pulses are signals from the calorimeters and are not artifacts of the offline programs. We also found that the narrow pulses from two different quadrants of the

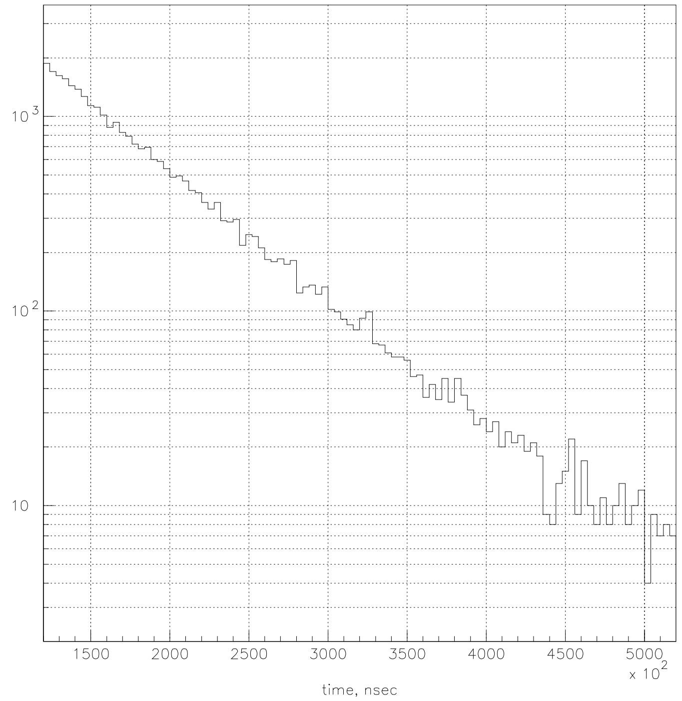


**Figure 6.3**:

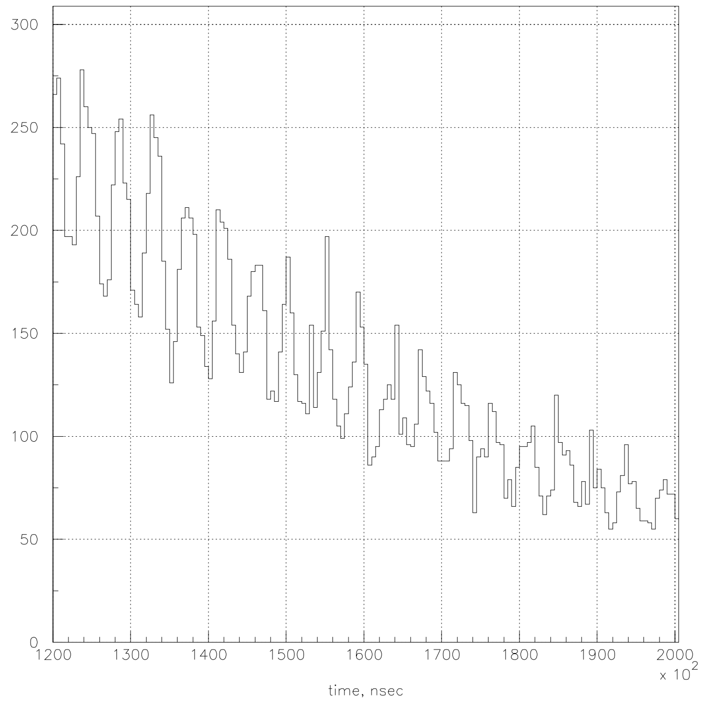


**Figure 6.4**:

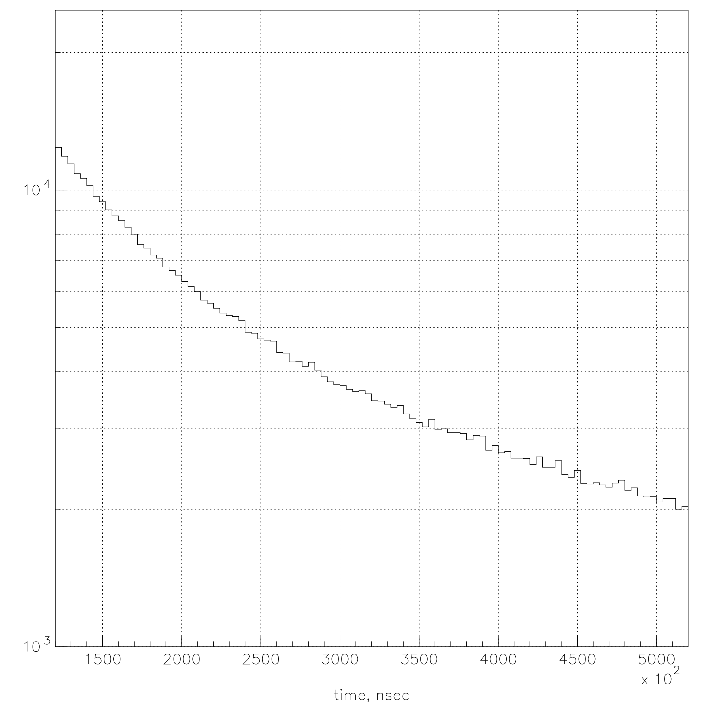


**Figure 6.5**:

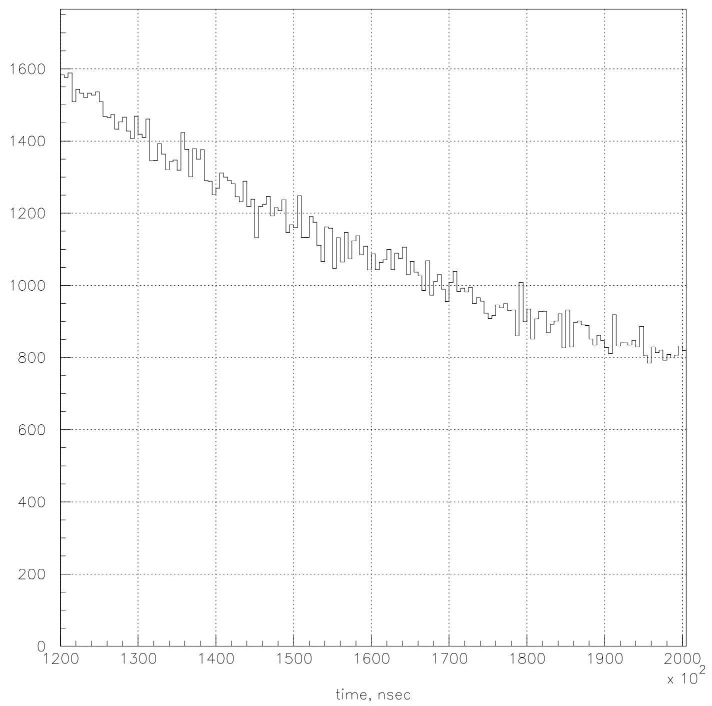


**Figure 6.6**:

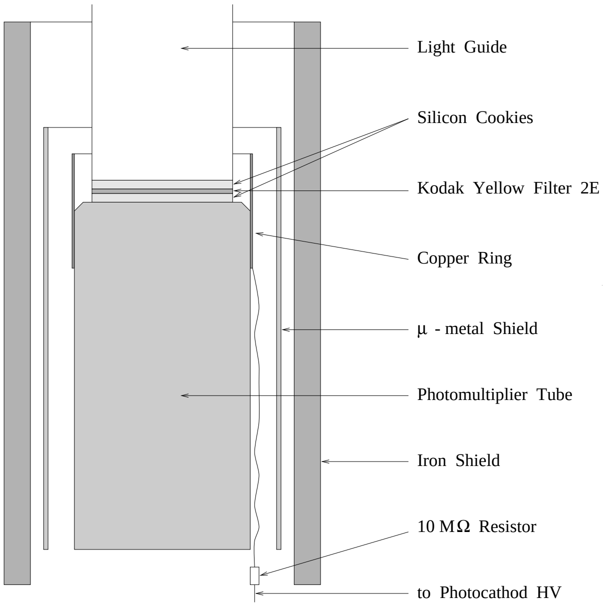


**Figure 6.7**: Scheme of the calorimeter light guide – PMT assembly

same calorimeter are rarely in coincidence, in contrast to the decay positron pulses. The narrow pulses seem to be most prevalent in tubes with a multialkaline photocathode operated above 2 kV, which are located in the first half of the ring, where the flash is high.

Correlations between narrow pulses and the operating condition of PMTs was investigated. Low rate narrow pulses were seen in the tubes even without any light input. The number of such narrow pulses scales linearly with high voltage for both PMTs with either bialkaline or multialkaline photocathode PMTs, which implies that the signal is not passing through the standard dynode chain. Another important observation was that a noise ripple on the HV supply line to the PMT always occurs in time with the narrow pulse. In contrast, no effect was seen on the HV line from an LED pulse. This can be explained by some arcing in the PMT shields. Note that ionization of the air when the beam is in the ring could increase the spark rate and that the shields were not present during the studies in the test beam, when narrow pulses were not observed.

Several tests were done by removing various parts of the tube assembly (Figure 6.7): the $\mu$ – metal shield, the copper ring plus 10 M$\Omega$ resistor assembly, etc. These resulted in changes in the pulse amplitude and frequency but were not reproducible.

Another important test was done with a Ruthenium 106 source placed next to the PMT photocathode. Ru 106 is a beta source with an endpoint of about 3 MeV. It caused narrow 500 mV pulses on a PMT with a high voltage of 2.2 kV. This implies that a low energy electron going through the glass knocks off atomic electrons (secondary emission) which pass into the vacuum and get accelerated down the dynode chain. In the storage ring a possible source of low energy electrons which cause narrow pulses, could be neutron capture in the light guides which produce $\gamma$ rays and then Compton scattered electrons. The neutrons are produced by the injected pions which interact with matter throughout the ring. The narrow pulses in Figure 6.5 have an approximate $1/t^2$ time dependence, which is expected for the neutron capture.

The model discussed above also implies that even more narrow pulses should be triggered by the Cherenkov light from electrons travelling in light guides. The signals should be narrow in time and associated with multialkaline PMTs rather than the bialkaline ones, which are less sensitive to Cherenkov light.

An interesting test was done with one of the calorimeter PMT in the ring. The PMT was optically separated from the light guide. Nevertheless it recorded signals with the same time structure as the other calorimeter tubes, although at a lower rate. This supports the model for narrow pulses arising from neutron capture.

Several different types of neutron shields were tested on the ring:
— plastic (30% of boron) was wrapped around one PMT;
— 3/8 inch of lead was wrapped around another PMT;
— 1 inch paraffin (3% of boron) and a lot of boxes of borax were placed around station 10.
The offline analysis had indicated no significant effect of lead on the narrow pulses, but the shielding around calorimeter 10 led to a factor of 2 reduction in the narrow pulse rate. Hence more shielding material was installed later at other calorimeter stations.

It was useful to compare the calorimeter of the CERN III experiment, where no narrow pulses were observed, with our calorimeter. A CERN III calorimeter consisted of a lead–scintillator sandwich with $\sim$30% of the energy deposition in the scintillator, and a relatively ineffective air light guide. We have lead–scintillating fibers blocks with only 5% energy deposition in the fibers but more efficient acrylic light guides, which we believe is the source of the narrow pulses resulting from the neutron capture. We had a yellow filter installed between the light guide and PMT (see Figure 6.7) in order to homogenize the light from decay positrons as discussed below. The blue component of the light has less absorption in the scintillating fibers and thus positrons hitting the calorimeter farther from the light guide will give less light signal. The yellow filter suppresses the blue component and makes the light signals more uniform, though the total amount of light decreases substantially.

For a test, we removed yellow filters from calorimeter station 11 in order to increase the light signal for a decay positron. The PMT high voltage was decreased and adjusted with an LED to keep the signal for a decay positron at the same level. The offline analysis showed that this suppressed the rate of the narrow pulses by a factor of two. Later we removed the yellow filters from all the boron/multialkaline detector stations.

We shall discuss other aspects of the narrow pulse problem in chapter 7.

## 6.3 AGS Background

With the beginning of the (g–2) dedicated run in June 1997, every AGS cycle was used and hence more statistics became available for the offline analysis and more sophisticated tests could be conducted. A Fourier transformation applied to the measured time distribution of decay positrons showed a significant peak at about 400 kHz which corresponds to a process with a period of 2.5 $\mu$sec. Later we found real "extra" events, mostly at 150 – 250 $\mu$sec after injection, which show a structure with period of 2.5 – 2.7 $\mu$sec. Since this period is close to the revolution time of 2.7 $\mu$sec for a proton bunch in the AGS, we concluded that these extra events are AGS background.

Extensive studies showed that those extra events had higher areas than decay positrons and hence could be distinguished. Soon, however, the author found several long runs for which the AGS background, apart from the 2.7 $\mu$sec period structure, had signals identical to the decay positron events. Figure 6.8 shows a section of the time distribution for selected events for run #883. The sharp 2.7 $\mu$sec peaks are clearly seen together with the (g–2) oscillations with their period of 4.37 $\mu$sec.

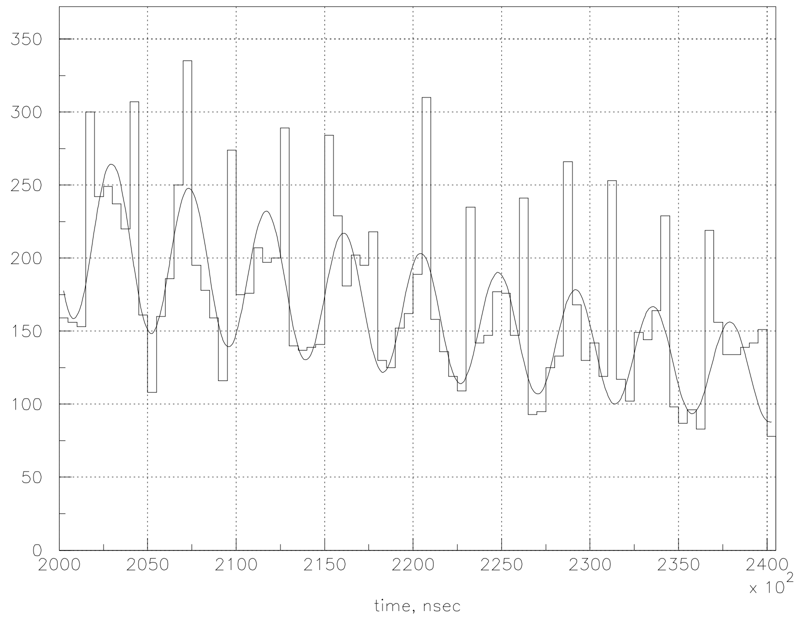


**Figure 6.8**: Fragment of decay positrons time distribution for the run #883

It was necessary to prevent leakage of particles from AGS after the beam extraction and also to monitor the presence of these "flashlets" both online and offline. The author had developed a very sensitive method to monitor the AGS background in the offline analysis. The idea is to put all the data into one AGS period of 2.7 $\mu$sec. The transformation

$$t' = \frac{t}{T_{AGS}} - integer(\frac{t}{T_{AGS}})$$

was applied to the data, where $t$ is the time of the event measured from the beam injection time and $T_{AGS}$ is the AGS period. $t'$ is measured in fractions of the AGS period and varies from 0 to 1. Figure 6.9 shows the result from one of the longest runs (#1041) without AGS background. The (g–2) oscillations average out completely. The exponential decay with time constant $\tau = \gamma \cdot \tau_\mu = 64.4\,\mu$sec appears as a 4% slope, as shown by the solid line. The distribution has a maximum at $t'$=0.15 which corresponds to the start of data taking. For the most of the runs taken in 1997, the statistical accuracy was not sufficient to see this 4% slope.

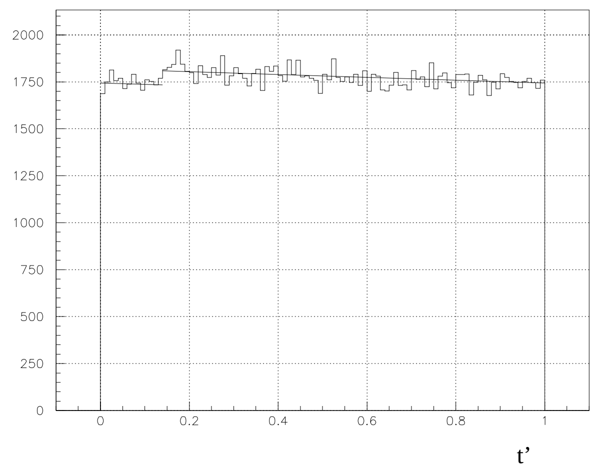


**Figure 6.9**: Distribution of $t'$ for the run #1041

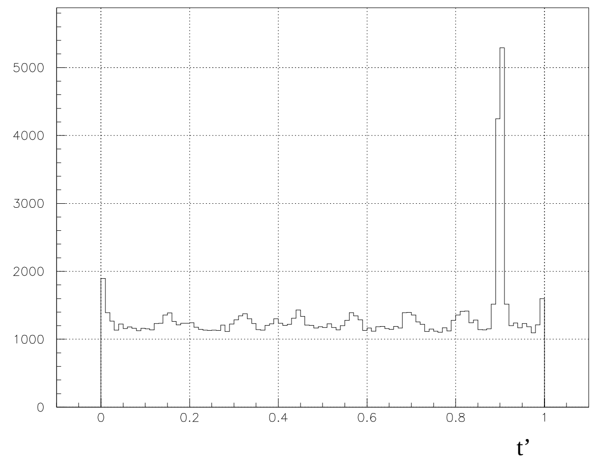


**Figure 6.10**: Distribution of $t'$ for the run #883

The distribution of $t'$ for the run #883 is shown in Figure 6.10. The highest peak at $t' = 0.90$ corresponds to the 2.7 $\mu$sec structure seen in Figure 6.8. Also 7 smaller peaks are clearly seen. All together the 8 peaks correspond to the 8 bunches in the AGS. The distribution in $t'$ is very sensitive to the exact value of the AGS period $T_{AGS}$. Figure 6.11 shows the $t'$ distributions for $T_{AGS} = 2.696$, 2.695, 2.693 and 2.692 $\mu$sec. Obviously, the distribution for $T_{AGS} = 2.694$ $\mu$sec, shown in Figure 6.10, has the sharpest structure. AGS experts confirmed that 2.694 $\mu$sec is really the best estimate for the AGS period.

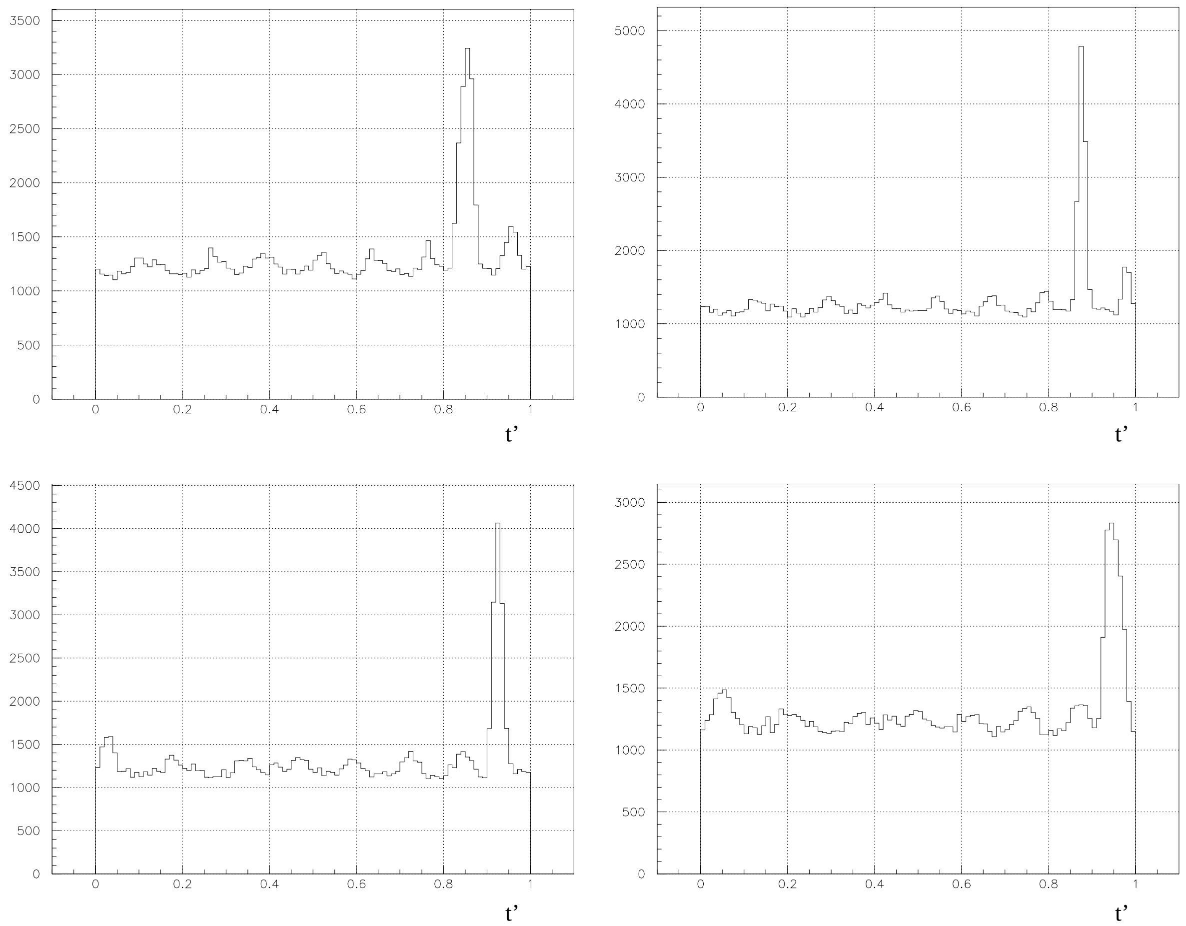


**Figure 6.11**: Distributions of $t'$ for the run #883 for different $T_{AGS}$, from left top clockwise: 2.696 $\mu sec$, 2.695 $\mu sec$, 2.692 $\mu sec$, 2.693 $\mu sec$.

For monitoring the AGS background the method using $t'$ has advantages compared to the Fourier analysis method. Fourier analysis works well for sinewave structures. But for the AGS background shown in Figure 6.8, which looks like a set of equally spaced delta–functions in time, the Fourier analysis would give a similar set of equally spaced delta–functions in a frequency domain, where the statistical analysis is complicated. Furthermore the 8 beam structure can be better understood from analysis of the $t'$ distribution than from the Fourier analysis.

Results of the offline analysis of the run #883 were discussed with AGS experts. The reason for the AGS flashlets was incorrect timing of the extraction magnet pulse so that the AGS beam entered the magnet at the rising edge of the extraction pulse instead of at its peak. The timing was corrected and since then the AGS background was not been a problem.

The analysis of the $t'$ distribution was made for all runs of 1997. Unfortunately, most of the runs were taken with the AGS background and could not be used for precision evaluation of the muon (g–2) frequency. Figure 6.12 shows different runs with a variety of AGS flashlets. For (g–2) analysis we used about 150 runs with correct extraction timing. These runs were taken between June 28 and July 11 and contain approximately $12 \cdot 10^6$ high energy decay positrons. The analysis of these data will be discussed in chapter 7.

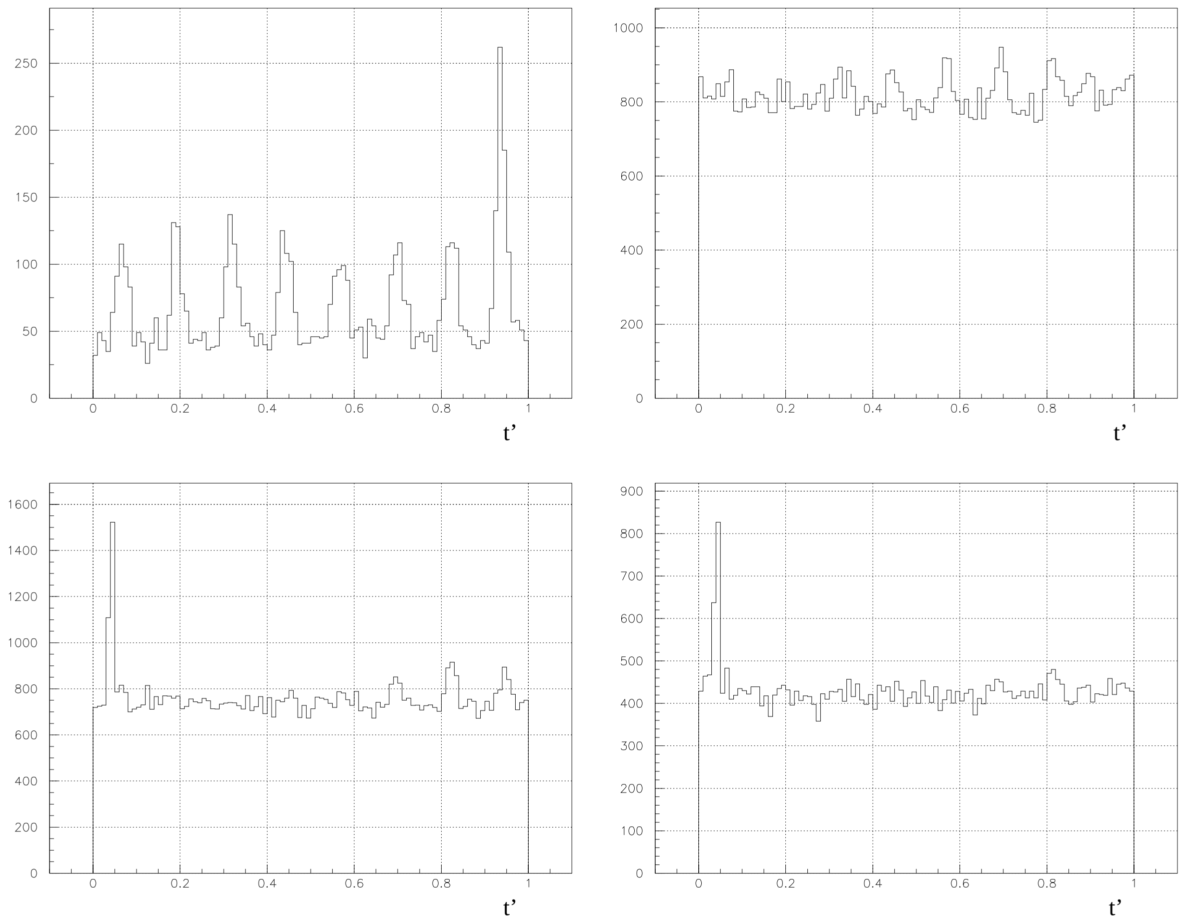


**Figure 6.12**: Distributions of $t'$ for different runs

Simple control of the extraction timing combined with online and offline monitoring using $t'$ distribution was chosen as a solution for the AGS background problem. A more certain method would use a fast shutter magnet, which closes the beam line after extraction, but this would be very expensive.

## 6.4 Magnetic Field Measurements during the Run

### 6.4.1 Beam Tube Trolley

During the run the magnetic field in the muon storage region was measured with 17 NMR probes mounted in the beam tube trolley. The trolley is a vacuum–tight vessel with cylindrical shape and a length of 0.5 m, curved with the same radius as the storage ring. A profile of the trolley is shown in Figure 4.10 in the kicker vacuum chamber environment. Along with NMR probes, the trolley carries a position sensor, electronic modules and temperature and pressure probes. It is filled with air for better heat transfer from electronics to the trolley body.

The trolley drive mechanism pulls the trolley along the ring with an electrical cable. The same cable is used for communication between the trolley and computer in the control room. The trolley rides on rails which help to form the desired electrical quadrupole field, see section 4.9 and Figure 4.14. During data taking the trolley is parked in its garage, located radially inward from the muon storage region. The trolley garage mechanism can move a complete 50 cm section of the rails with trolley on it radially outward (inward) at the beginning (end) of magnetic field measurements. Both trolley drive and trolley garage are parts of the muon vacuum chamber, so field measurement with the beam tube trolley can be done without breaking the vacuum.

During the run the measurements with the beam tube trolley were taken every 24 to 72 hours. Each field map consists of about 6000 readings for each of the 17 NMR probes, i.e. $\sim 10^5$ measurements in total. Between these measurements the drift of magnetic field was monitored by the 366 fixed NMR probes embedded in the walls of the vacuum chamber as shown in Figure 6.13, in 72 azimuthal locations. Fixed probes are calibrated by beam tube trolley probes during each field mapping. At the end of the run the 17 trolley NMR probes were calibrated against a single standard calibration probe, see section 4.4.

More details about beam tube trolley design and operation can be found in [97].

### 6.4.2 Temperature Variations of the Magnetic Field

An extensive study was done of the temperature dependence of the magnetic field in the storage ring [98]. A number of temperature sensors are located on the iron yoke. Three are on the top, bottom and back of each of yoke sections C, D, E, F, G as shown in Figure 6.13 and one at the back of yoke sections A, B, H, I, J, K and L. The temperature of the magnet cryostat box, measured by two sensors was taken as the room temperature. The accuracy of the temperature measurements was about 0.1°C.

Figure 6.14 shows the room temperature and the temperature of some yoke sections during the period from May 8 to July 7, 1997. Due to the large heat capacity of

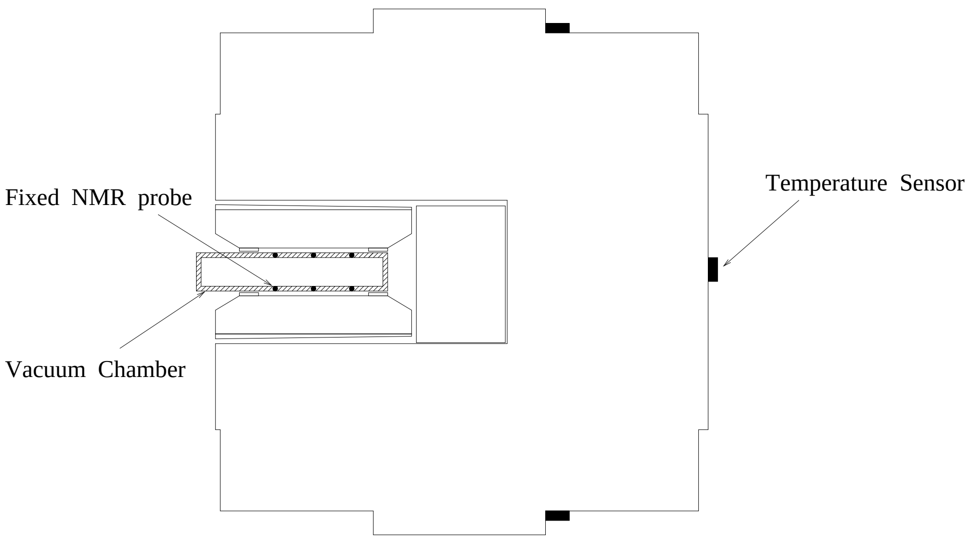


**Figure 6.13**: Location of fixed NMR probes and temperature sensors on the ring.

the iron yoke, day to night temperature variations of the yoke are less than the room temperature variations. For the same reason, the temperature change of the yoke is delayed compared to room temperature. The largest observed rate of change of the yoke temperature was 0.1°C per hour. For all yoke sections the temperature at the top is higher by about 1.2°C than the temperature at the bottom. The yoke sections E and F, which are close to the door, show the largest temperature variations.

The magnetic field monitoring during the run was based on the 366 fixed NMR probes. With 6 (or at some locations 4) NMR probe measurements at each azimuthal location, we can determine the lowest multipoles of the magnetic field: the normal dipole, normal quadrupole and skew quadrupole. Figure 6.15 shows these multipoles as a function of time. As to the correlation of field and temperature, a delay of about 6 hours was observed in the field change compared to the temperature change. Therefore, in Figures 6.16, 6.17 and 6.18 we shifted the temperature data by 6 hours with respect to the NMR data.

Figures 6.16 and 6.17 show the normal dipole and normal quadrupole fields, respectively as functions of temperature. The dipole field changes by about 35 ppm per °C, whereas the quadrupole field does not depend on temperature in a simple way. This is because the quadrupole field depends on the relative tilt of the top and bottom poles, rather than on the gap between them, and hence should depend on the temperature gradients across the yoke. Figure 6.18 shows that the normal quadrupole changes by about 25 ppm per °C/hour and the skew quadrupole changes by about 6 ppm per °C/hour. These temperature changes are quite large and hence the yoke should be thermally insulated.

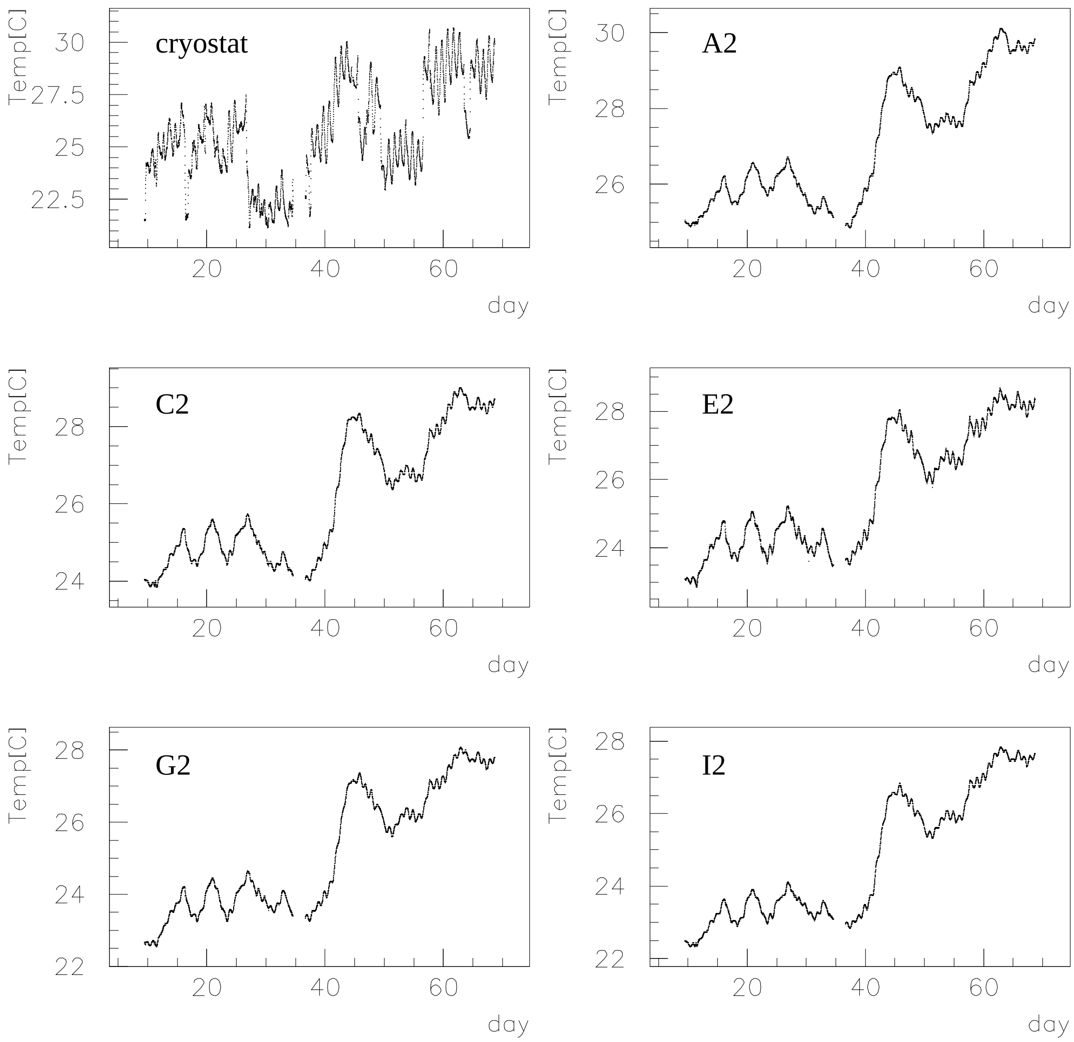


**Figure 6.14**: Temperature of the cryostat and yoke sections A2, C2, E2, G2 and I2 during the run.

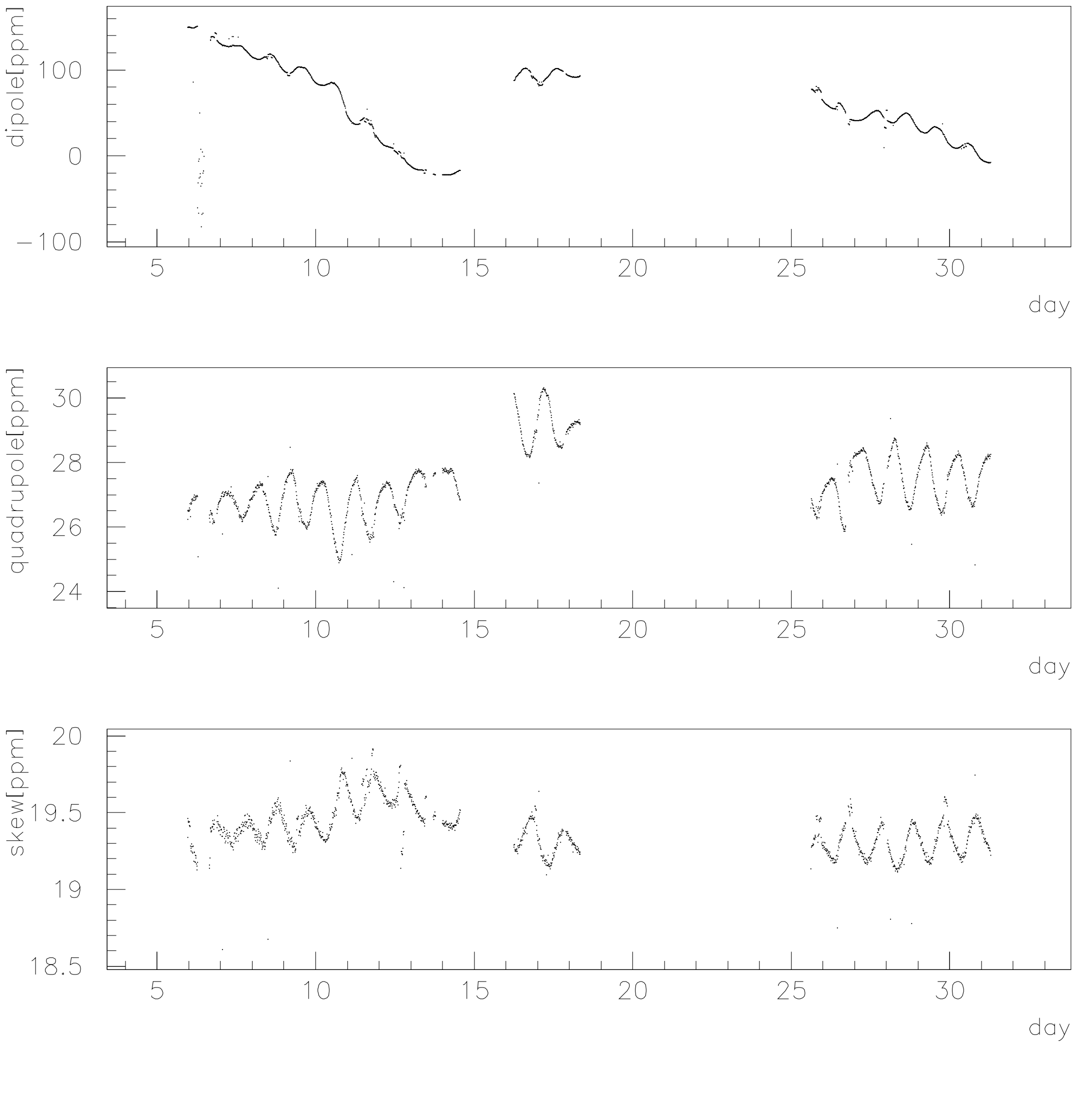


**Figure 6.15**: Dipole, quadrupole and skew quadrupole components of magnetic field during the run.

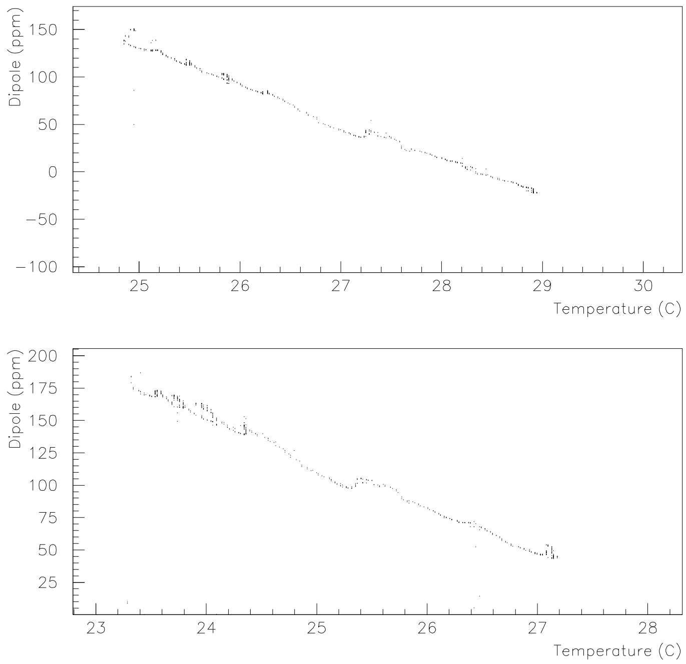


**Figure 6.16**: Temperature dependence of the dipole field at $\Theta = 5°$ (top) and $\Theta = 185°$ (bottom) locations.

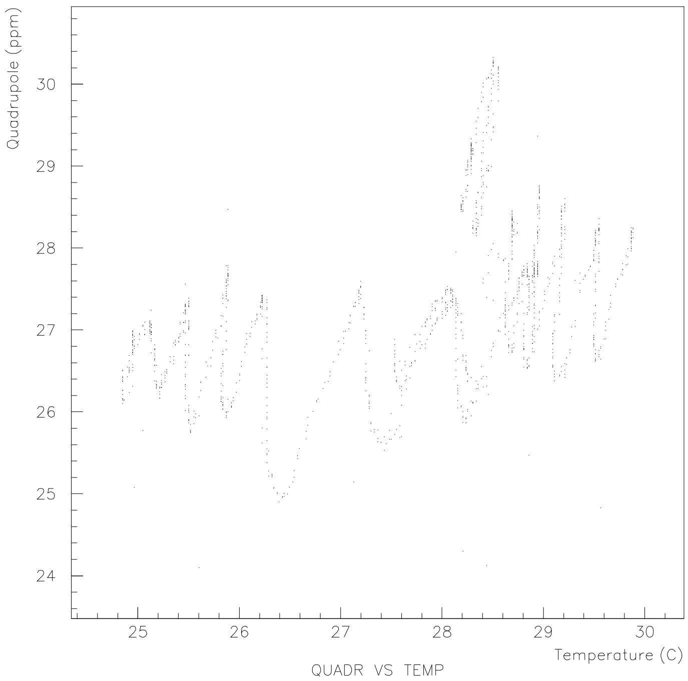


**Figure 6.17**: Temperature dependence of quadrupole field.

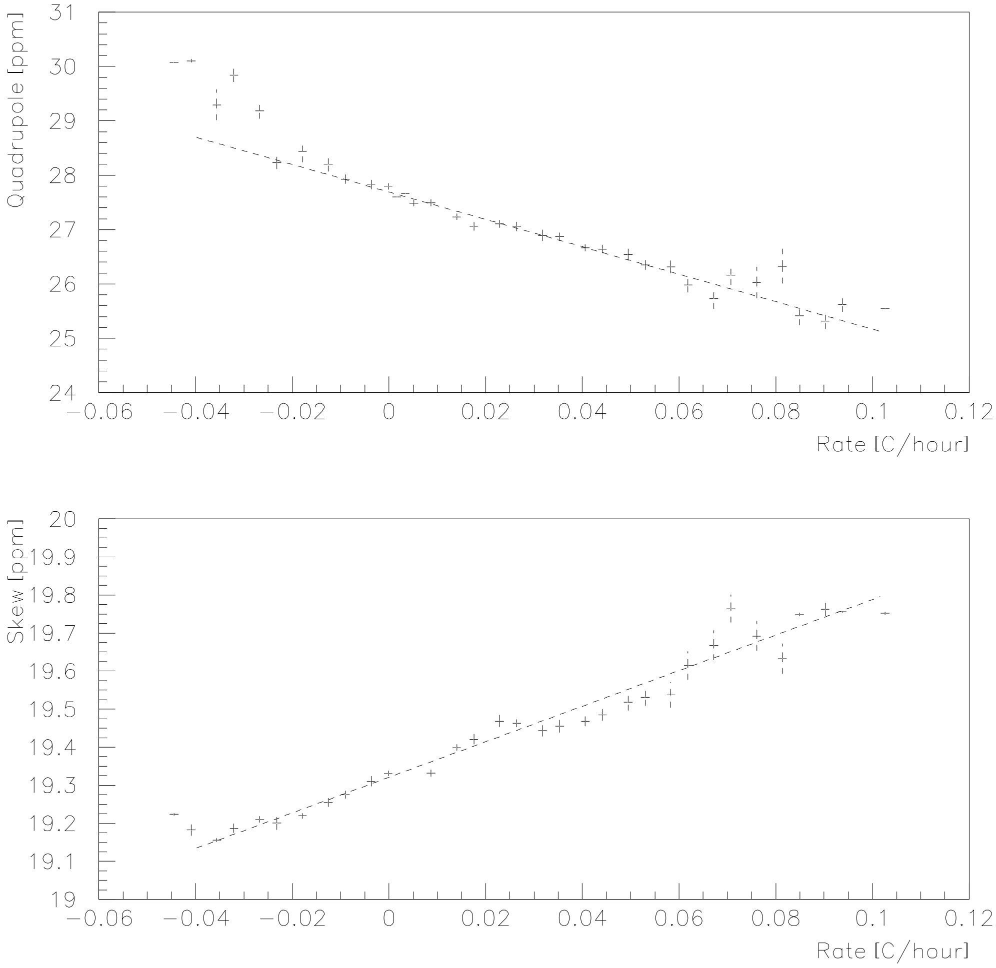


**Figure 6.18**: Normal (top) and skew (bottom) quadrupole fields as functions of rate of temperature change.

## 6.5 Measurements of the Inflector Transmission and Beam Profile

By the end of the run we had
— fixed AGS extraction timing,
— obtained $40 \cdot 10^{12}$ protons on the target per AGS cycle,
— improved online electron counter (see section 6.1),
— collected much data for offline analysis.

It was important to estimate the number of stored muons per $10^{12}$ protons on the target. The crucial parameters are beam composition at the inflector entrance, calibration of the ion chamber upstream of the inflector, the inflector transmission and the muon storage efficiency, i.e. number of stored muons per pion entering the storage ring.

The beam composition was estimated using the CERN III measured beam composition. With a 15 cm long Cu target and a 115.5 m beam line, their beam composition was 65% of pions, 22% of protons, 12.5% of positrons and 0.5% of kaons. We have a Ni target of about the same length and a 173.3 m beam line, which gives beam composition 58% of pions, 27% of protons and 15% of positrons. We neglect the kaon admixture.

To estimate the muon storage efficiency from our beam tracking simulation, the spatial, angular and momentum distributions of the pions at the inflector exit are required. Equivalently we can use the spatial distribution of the beam at the inflector exit and at two other azimuthal locations. The spatial distribution as well as the calibration of the ion chamber and the inflector transmission were measured on the last shift of the run using two different techniques: an activation of aluminum foils placed in the pion beam and a scintillator/photodiode counter [99]. The measurements were done with open vacuum chamber.

For the activation technique foils of 0.003 inch thick high purity aluminum were placed into the beam at various locations around the ring and at the entrance of the inflector. The activation is proportional to the integrated beam exposure. Therefore, a comparison of the foil activities at different azimuthal locations determines the beam intensity as a function of azimuth. Two foils were cut into horizontal and one into vertical strips for beam profile measurements. In addition, a very accurate radial beam profile measurement was done with the scintillator/photodiode device.

Pions and protons interact with $^{27}Al$ and produce several different nuclear fragments, but only two long–lived nuclei $^{18}F$ and $^{24}Na$ with half lives of 1.83 hours ($\beta^+$ decay) and 14.96 hours ($\beta^-$ decay) respectively, were used for our measurements. All foils were exposed to the beam for 12.4 hours. Activation measurements were performed with a closed NaI detector about 20 hours after the exposure. Cross sections for the reactions

$$\pi, p + {}^{27}Al \longrightarrow {}^{24}Na + X$$

and

$$\pi, p + {}^{27}Al \longrightarrow {}^{18}F + X,$$

given in [100], were used for absolute calibration of the ion chamber upstream of the inflector. From the activation of the foil located between the ion chamber and the entrance of the inflector, the calibration constant was obtained $88.3 \pm 17$ ion chamber counts per $10^7$ minimum ionizing particles, in good agreement with the previous AGS calibration value of 80 counts.

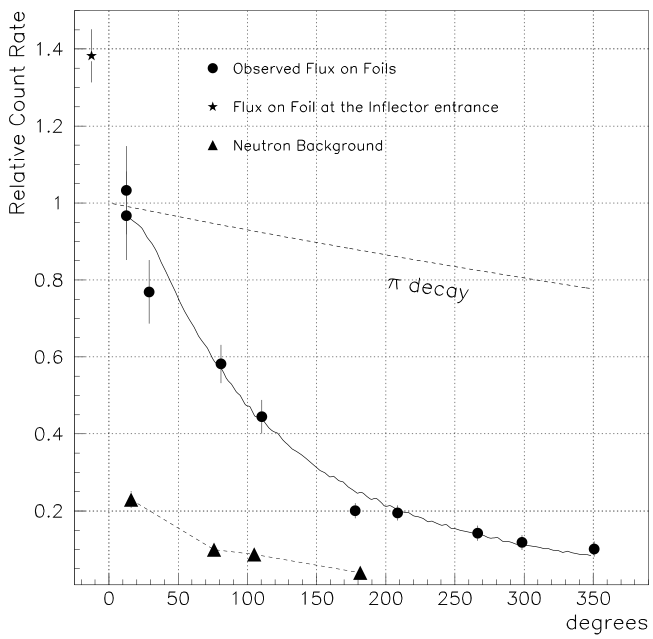


**Figure 6.19**: Pion beam flux as a function of azimuth

The relative activations of the foils as a function of azimuthal position are shown in Figure 6.19 by circles. The background counts (triangles) from additional foils located in the ring but outside the beam were subtracted from the data. The activation of the foil at the inflector entrance is shown by the star. Two foils were located at the inflector cryostat exit, which is 12.5° downstream from the inflector exit. The measurements are in a good agreement with a beam dynamics model (solid line). Using the relative activation values for the foils at the inflector entrance and at the inflector exit (obtained by extrapolation to $\Theta = 0°$), the inflector transmission was calculated to be 0.67 in excellent agreement with the design value.

Three foils were cut into strips to measure the radial (two foils) and vertical (one foil) profiles of the beam. Figures 6.20 and 6.21 show results for the radial and vertical beam profiles at the inflector cryostat exit, $\Theta = 12.5°$. The shadow region in Figure 6.20 indicates the radial position of the inflector cryostat wall. As shown in Figure 6.20, about 20% of the beam comes through the wall, but with the uncertainty of the foil radial position of 0.5 cm, the value could be between 10 and 40%. If pions travel through 16 inches of aluminum in the wall from the inflector exit to the inflector cryostat exit, they lose about 1% of their energy and have an orbit radius decreased by 7 cm. This would cause a distortion of the radial beam profile further downstream.

The measured vertical profile of the beam at the inflector cryostat exit is shown in Figure 6.21 by black circles. It is not compatible with the expected uniform distribution shown by black stars. Better agreement was found by assuming that the beam has a Gaussian distribution of width of $2\sigma = 3.2$ cm and centered 2.4 mm below the midplane (white squares).

The radial beam profile at 155° was measured with the photodiode device shown in Figure 6.22. A plastic scintillator $40 \times 15 \times 11$ mm$^3$ was optically connected to a Hamamatsu photodiode S3590–01 with active area $10 \times 10$ mm$^2$. The scintillator/photodiode assembly was held on an aluminum bar bolted to a movable platform of a translation stage and the whole device was mounted to a vacuum port approximately 155° downstream of the inflector. A stepping motor was used to move the aluminum bar with respect to the translation stage and a simple electro–mechanical position readout was used to control this motion remotely with the relative precision $\sim 0.3$ mm. The absolute precision of radial positioning of the photodiode in the vacuum chamber was estimated to $\sim 2$ mm.

The photodiode signal was measured by a digital scope located in the control room. The signal was normalized to the beam intensity using the signal from the T0 counter upstream of the inflector, which was recorded by another channel of the same digital scope. Each measurement averaged 10 to 20 AGS cycles. We repeated measurements 3 to 5 times at each radial location. The deviations between measurements at the same radial location were typically less than 1%. The results are shown in Figure 6.23. The shoulder of the distribution at small radii is consistent with the observation that 10 – 40% of the beam lost up to 1% of its energy in the inflector partition wall.

The radial profile at 268.5° downstream of the inflector exit, measured with activated foils, is shown in Figure 6.24. It also has a shoulder at small radii consistent with the beam profile measurements at 155° and 12.5°.

The muon storage efficiency, obtained from the measured spatial distributions of the pion beam and beam tracking simulation is in excellent agreement with the design value of $2.6 \cdot 10^{-5}$.

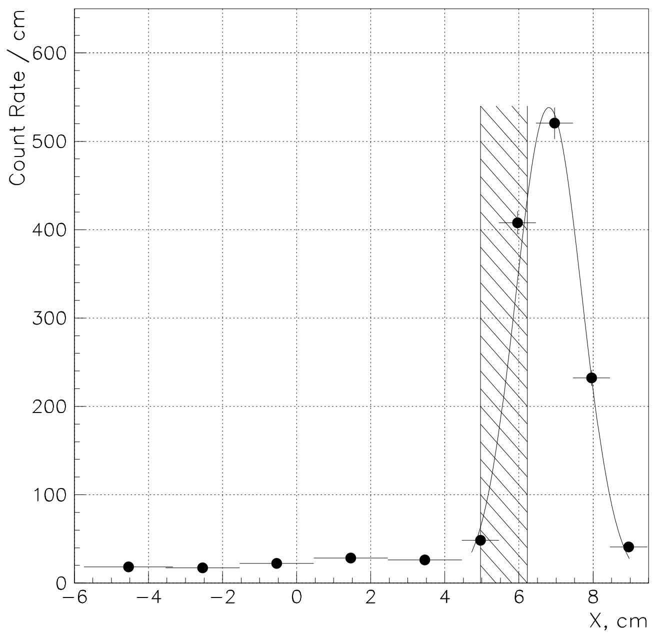


**Figure 6.20**: Radial beam profile at $\Theta = 12.5°$

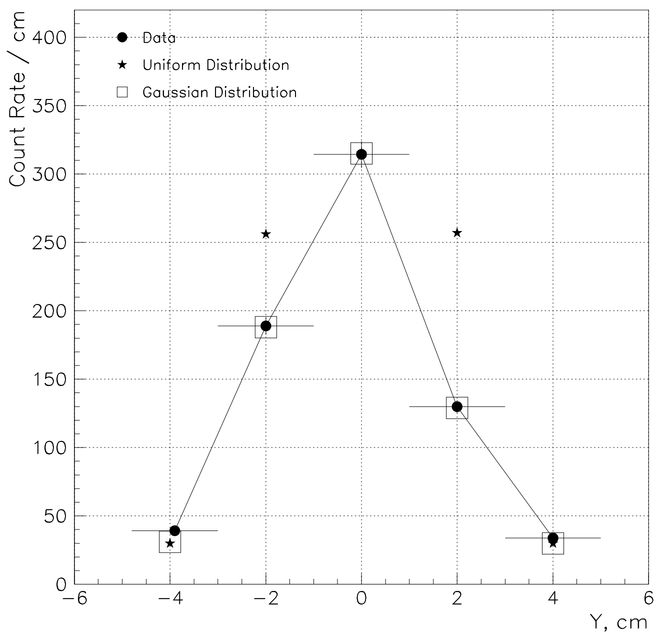


**Figure 6.21**: Vertical beam profile at $\Theta = 12.5°$

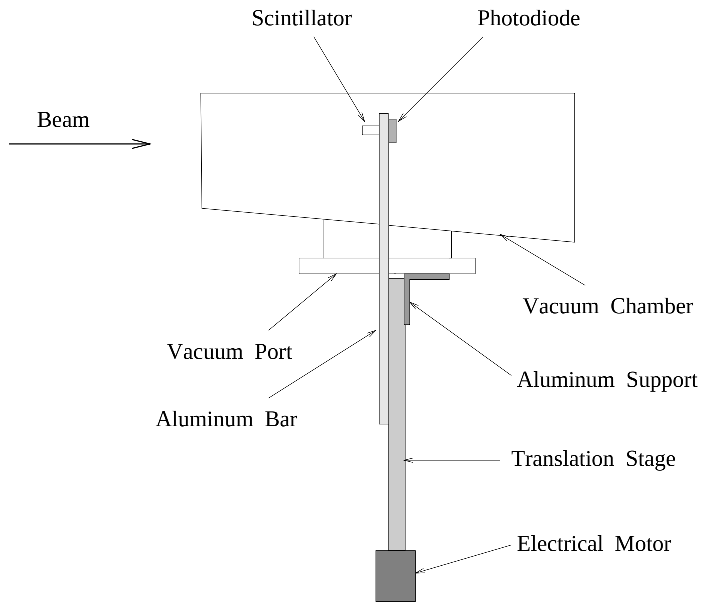


**Figure 6.22**: Scheme of scintillator/photodiode measurements

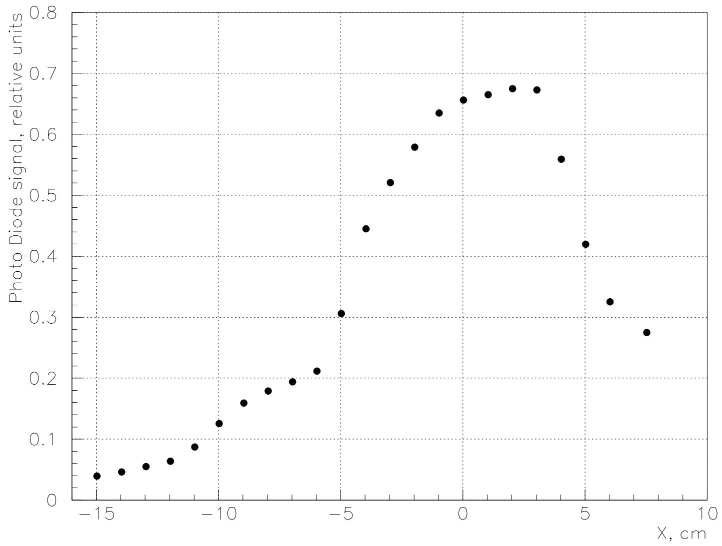


**Figure 6.23**: Radial beam profile at $\Theta = 155°$

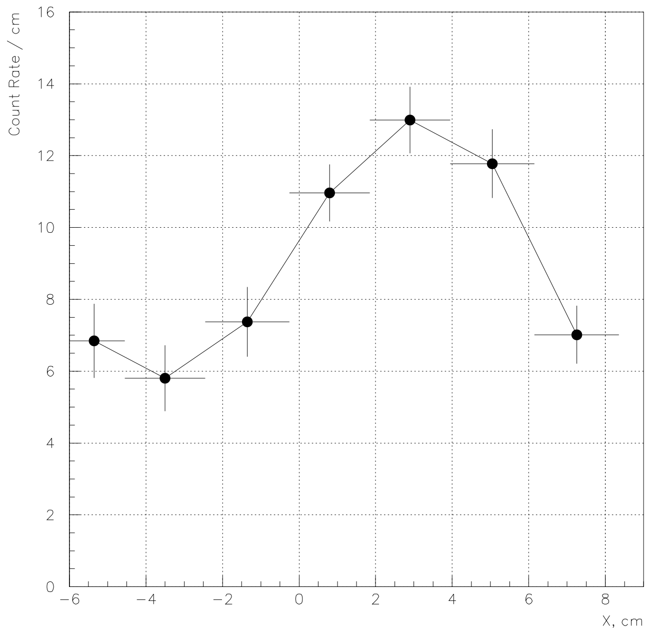


**Figure 6.24**: Radial beam profile at $\Theta = 270°$

# Chapter 7

# Data Analysis

## 7.1 Pulses with Missing Phases

The studies of the narrow pulses started during the run and were continued in the offline analysis of the data. Thirty two WFD samples for each pulse were added to a standard set of NTUPLE pulse parameters for direct analysis of pulse time structure with PAW. Figure 7.1 shows the different types of observed time structures [101]. The analysis immediately revealed the presence of missing phase in some pulses such as in Figure 7.1c. This pulse contains 8 samples of one phase but only 4 samples of the other. Normally, the number of samples of the first and second phases should be equal as shown in Figure 7.1a and 7.1b. The simple pulse finding algorithm called DEFNA sets the end of a pulse at the end of the last non–zero sample. For the pulse in Figure 7.1c, this algorithm will cut out the tail beyond 486.55 $\mu$sec and makes the pulse narrower. Indeed, detailed analysis showed that roughly half of all narrow pulses were decay positron events with missing phase, while others were presumably associated with neutron capture (see section 6.2), like that shown in Figure 7.1b. In other words, there is a substantial fraction of decay positron events which have the missing phase defect and hence fall mixed with narrow pulse background by the simple pulse finding algorithm DEFNA.

Detailed analysis was done in [102] to understand why some pulses have a missing phase. Figure 7.2 shows the triggering scheme used for the 1997 run. The discriminated sum of the analog signals from all 4 PMTs of each calorimeter is fed to a "discriminator" input for the two phases. At the same time, a copy of the analog discriminated sum signal is sent into the pulse stretcher. In the pulse stretcher this signal quickly charges up a 200 pF capacitor, which then slowly discharges. The slowly decaying output signal from the pulse stretcher is compared with a programmable level in the comparator. From the time the discriminated sum signal comes to the triggering circuit until the

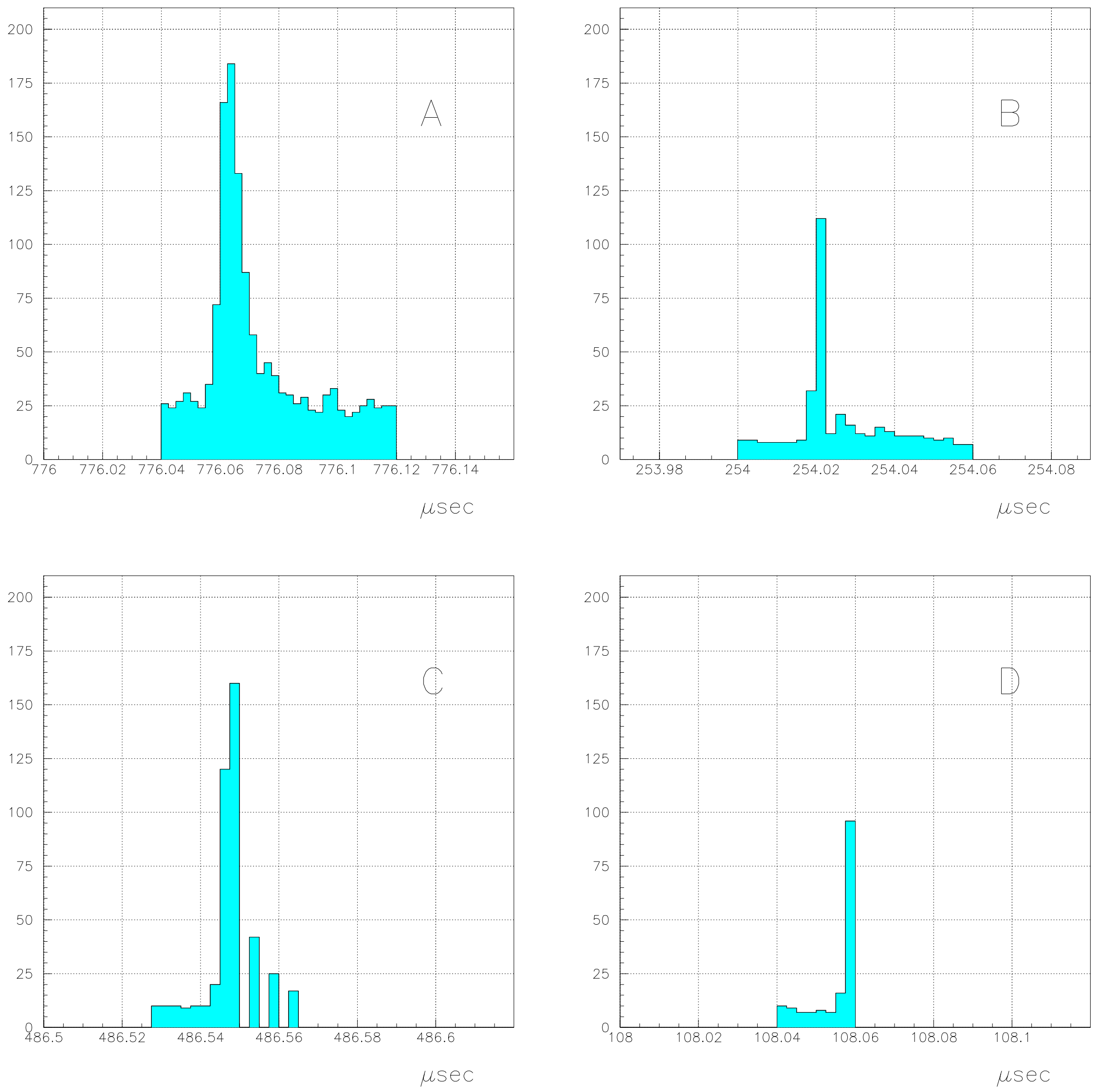


**Figure 7.1**: Time structure of some signals from calorimeter: A – positron event, B – narrow pulse, C – pulse with one missing phase, D – pulse with two missing phases.

output of the pulse stretcher is higher than the programmable level, the signal from the calorimeter is digitized in 20 nsec blocks, with 4 samples of one phase and 4 samples of the other phase. Positron pulses in the data are generally either 20,40, 60 or 80 nsec long. Trouble can arise if the discriminator thresholds are set too high. In this case the pulse may only be over threshold for a short period of time and the stretching circuit may be less effective or not fired at all.

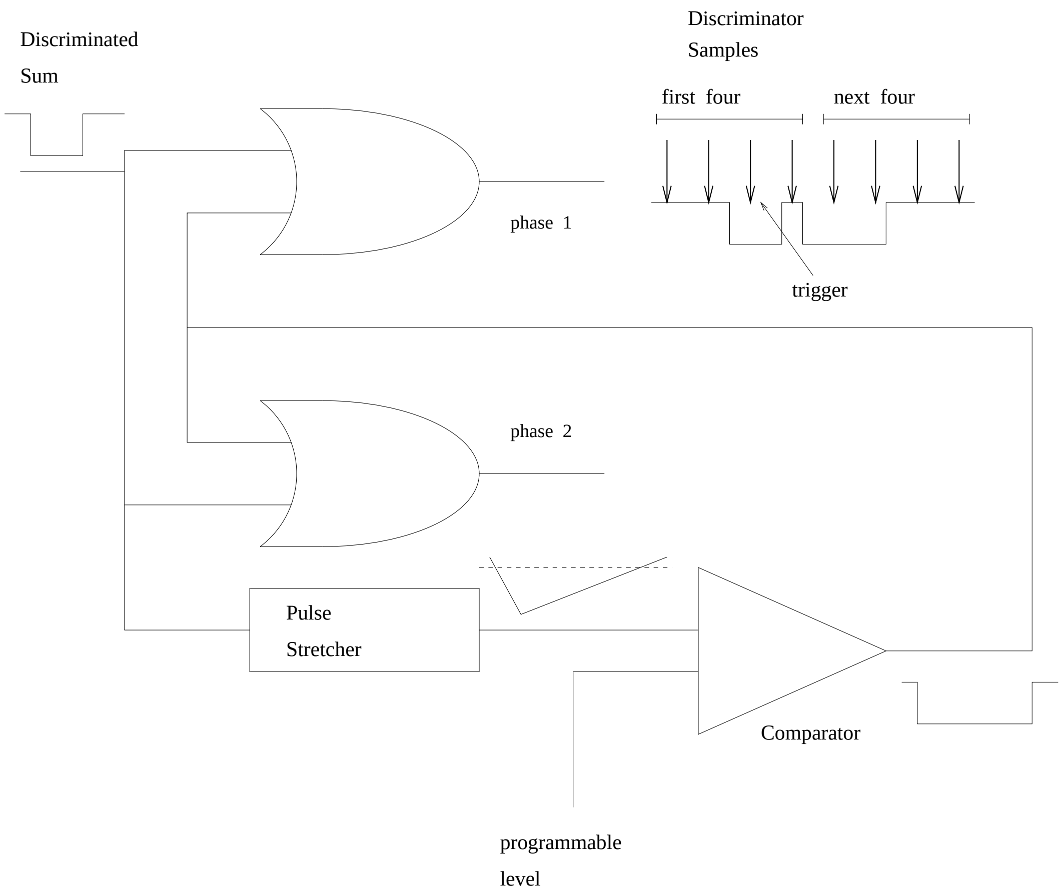


**Figure 7.2**: Triggering scheme for June 1997 run

Several failure modes have been observed. Sometimes the pulse stretching is only long enough to trigger one of the two phases for a second 20 nsec set of samples. These pulses have 12 samples followed by what looks like 4 missing teeth at the end, as in Figure 7.1c. Perhaps the most common failure mode is when only two sets of 4 samples from the two phases are observed as in Figure 7.1d. In this case, the pulse stretching was not triggered. In addition there are other failure modes. We believe that the reason for the large number of missing phases in the 1997 run data was that the discriminator thresholds were raised without a corresponding adjustment of the programmable level of the pulse width comparator.

## 7.2 Pulse Fitting Algorithm

A new pulse finding algorithm FIT, which is less sensitive to the missing phase, was developed. The pulse is fit by some analytic function omitting the missing phase channels. The four parameter function

$$F(t) = P_1 + P_2 \cdot exp\left[-\frac{ln^2\left(1 - \frac{(t-P_3)\cdot\eta}{P_4}\right)}{2\sigma_\circ^2}\right],$$

$$\sigma_\circ = \frac{ln\left(\eta\sqrt{2\,ln\,2} + \sqrt{1+\eta^2\cdot 2\,ln\,2}\right)}{\sqrt{2\,ln\,2}}, \ \eta = -0.4$$

was chosen [103], where the fitting parameters are: pedestal $P_1$, pulse amplitude $P_2$, pulse time $P_3$ and pulse width $P_4$. Figure 7.3 shows the results of the fit to the pulses in Figure 7.1a, 7.1b and 7.1c. The pulse in Figure 7.1d, which has two missing phases, could not be fit unambiguously and was omitted from the final data sample.

The new pulse finding algorithm also provides better selection for decay positron events. Figure 7.4 shows positron selections using 2–dimensional distributions of energy versus amplitude for the DEFNA algorithm and of amplitude versus width for the FIT algorithm. Positron events, selected as shown in Figure 7.4b, were used for further analysis.

## 7.3 Energy Threshold

The muon (g–2) spin precession would manifest itself as a harmonic time variation in the forward–backward asymmetry of decay positrons in the muon rest frame. In the experiment the forward–decay positrons have higher energy with a maximum $E_{max} = 3.096$ GeV while the backward–decay positrons have lower energy with a minimum $E_{min} = 0.97$ MeV. The energy of the positron depends on the direction of the decay positron in the muon rest frame and hence provides information about the muon polarization at the instant of decay.

In practice, an energy threshold is set to select high energy positrons, which come dominantly from the forward decays of muons. The positron counting rate has a time distribution in which the exponential factor for muon decay is modulated by the (g–2) frequency $\omega_a$:

$$N(t) = N_\circ\, e^{-t/\tau}\,[1 + A\,\cos(\omega_a t + \phi)\,].$$

The statistical precision in determining $\omega_a$ is given by:

$$\frac{\delta\omega_a}{\omega_a} = \frac{\sqrt{2}}{\omega_a \tau A\sqrt{N}},$$

where $N$ is the number of detected positrons. While $\omega_a\tau$ is fixed by the muon beam energy and magnetic field, both $A$ and $N$ are functions of the energy threshold $E_{thr}$

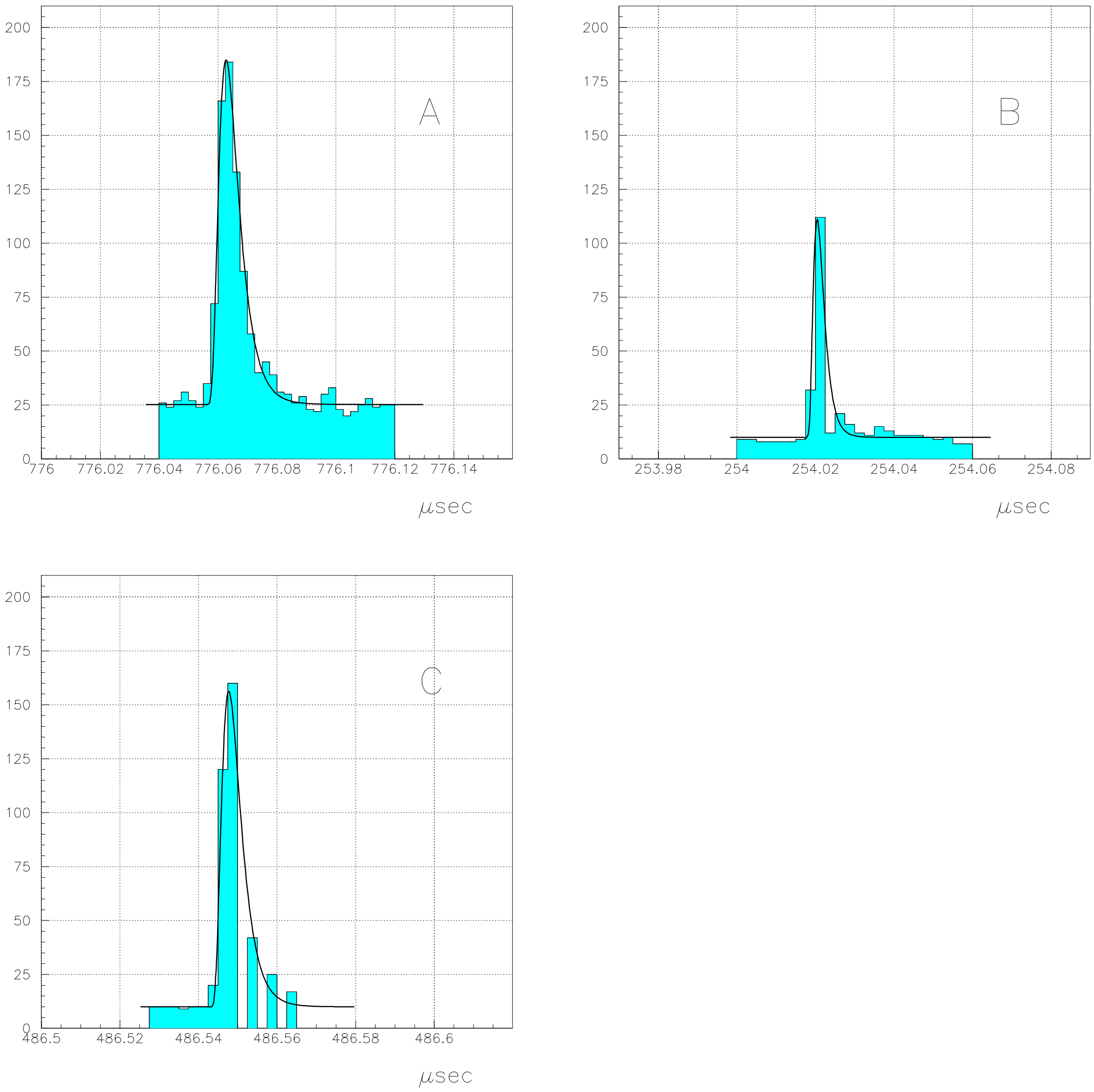


**Figure 7.3**: Fitting pulse shape with 4–parameter function

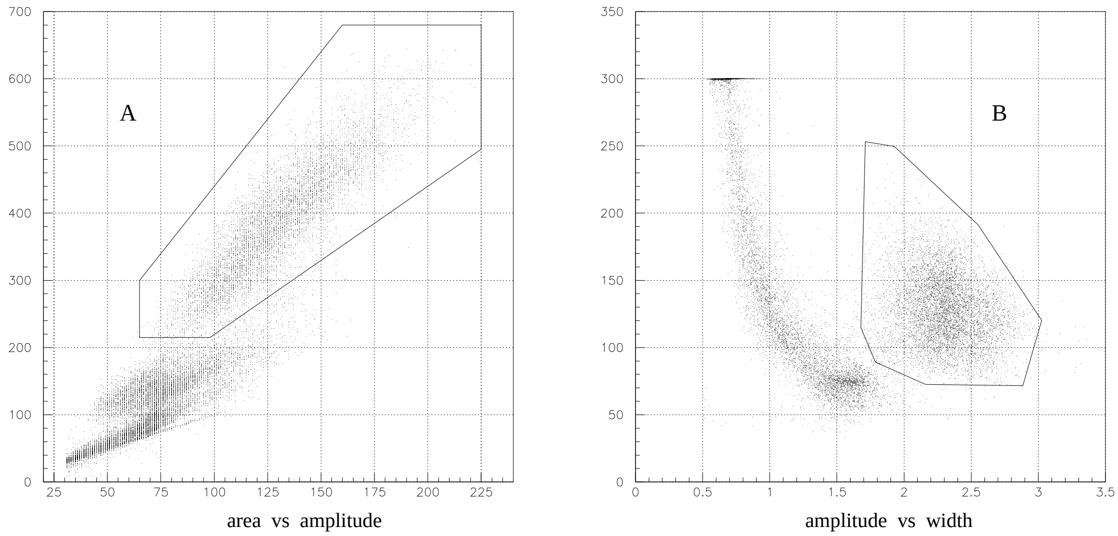


**Figure 7.4**: Positron events selection with DEFNA (A) and FIT (B) algorithms

and the value of $\delta\omega_a/\omega_a$ is made smallest by maximizing $N \cdot A^2$. Figure 7.5 shows the number of positrons $N$ and the asymmetry $A$ as functions of positron energy in the lab frame. Figure 7.6 shows same $N$ and $A$ and the product $N \cdot A^2$ as a functions of energy threshold $E_{thr}$. One can see that the optimal $E_{thr}$, which maximizes $N \cdot A^2$, is about 0.6 of $E_{max}$.

In practice, each detector has its own gain and hence the energy scale, $E_{max}$ must be determined for each detector individually. Figure 7.7 shows the amplitude distribution of positrons for one detector. The solid line is a plot of $N/N_{max}$ from Figure 7.5, scaled in both vertical and horizontal directions to fit the right slope of the amplitude distribution. The line meets the axis at the amplitude $\approx 183$, which corresponds to the $E_{max}$ for this detector.

## 7.4 Fitting (g–2) Oscillations

As was mentioned in section 6.3, about 150 runs of data were collected between June 28 and July 11 in $\sim 150$ hours of running. All were free from AGS background and were used for the final (g–2) analysis. Since gating, pedestal, background and gain were different for different detectors, we determined $\omega_a$ from each detector separately and then averaged the results. For some detectors, the data had to be further divided due to the presence or absence of yellow filters (see section 6.2) or due to different gating times. Hence some 50 groups of data were analysed separately.

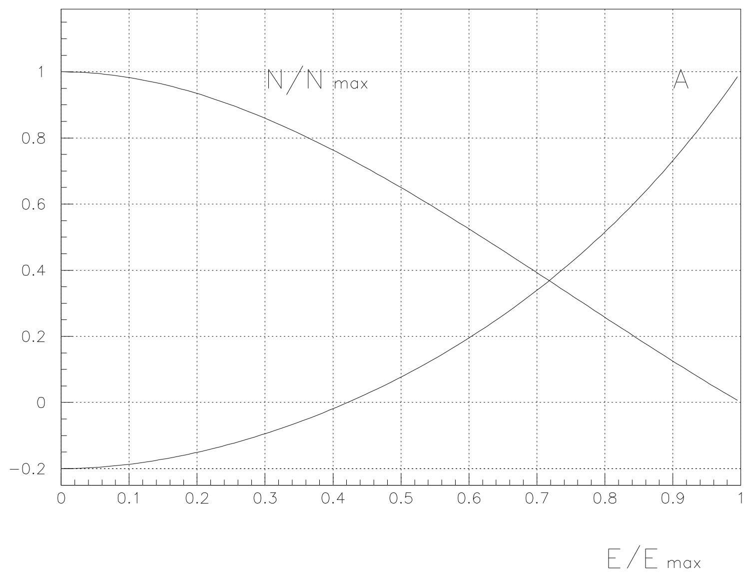


**Figure 7.5**: Number of decay positrons and asymmetry as a function of positron energy

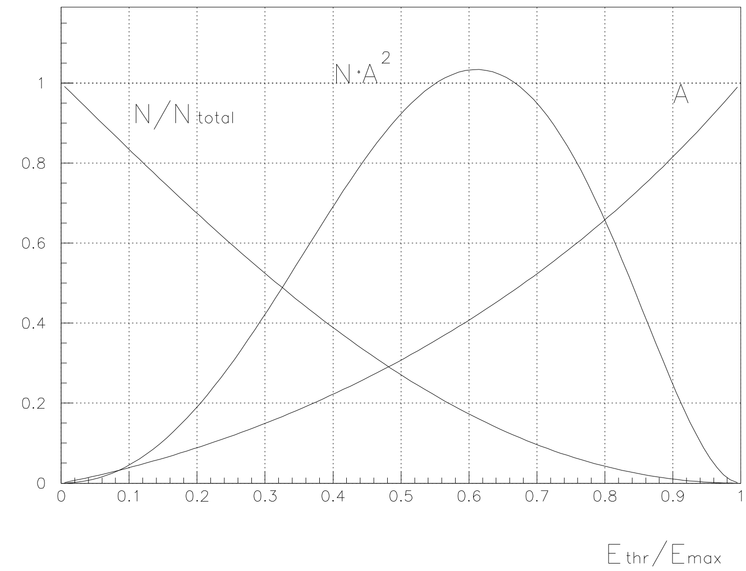


**Figure 7.6**: Number of decay positrons, asymmetry and $N \cdot A^2$ (in relative units) as a function of energy threshold

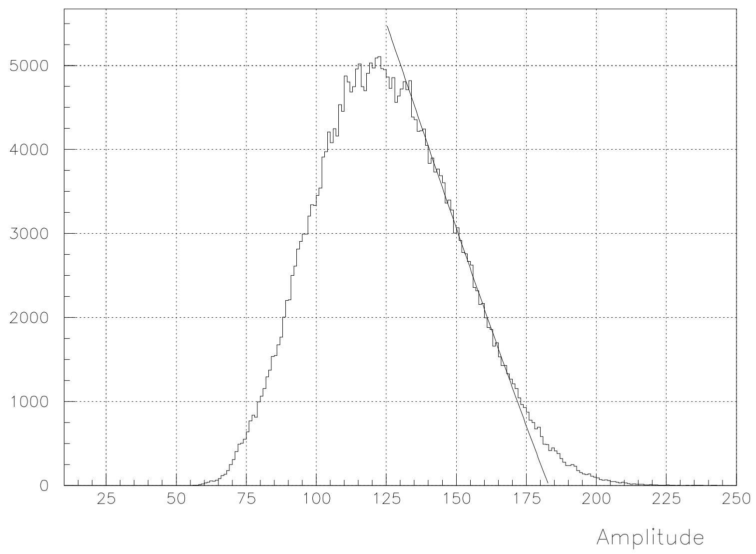


**Figure 7.7**: Amplitude distribution of decay positrons for single detector

Figure 7.8 shows the time distribution of positrons with energy $E > 0.6 \cdot E_{max}$ for one of the detectors. The data contain a number of runs with the different gating times of 30, 40 and 50 $\mu$sec after injection. The (g–2) oscillations are clearly seen modulating the exponential decay. However the data reveal significant deviations from the simple exponential at $t < 120$ $\mu$sec, which correlates with the high pedestal of the PMT signal (see Figure 7.9) caused by the flash.

To fit the data in Figure 7.8 with the 5–parameter function

$$N(t) = N_\circ \, e^{-t/\tau} \, [1 + A \, \cos(\omega_a t + \phi) \, ],$$

one must eliminate data for $t < \sim 120$ $\mu$sec. The confidence level (C.L.) of a 5–parameter fit as a function of the starting time of the fit is shown in Figure 7.10. With the time cut at 120 $\mu$sec the C.L. of the fit is 4%, which is reasonably good. Note, however, that we have thus eliminated about 2/3 of our data. It seems worthwhile to add a few more parameters to the fitting function in order to include more data, especially at earlier times.

The 8–parameter function

$$N(t) = \frac{N_\circ \, e^{-t/\tau}}{t^\alpha} \, [1 + (A_\circ + A_1 t) \, \cos(\omega_a t + \phi) \, ] + C,$$

was chosen to take into account the triggering inefficiency of the WFD due to missing adjustment. Because the comparator level in the trigger was too high, positrons with lower energy often miss one or even two sets of the WFD samples, and hence are lost, see section 7.1. At earlier times, however, the pedestal of the PMT signal is relatively high

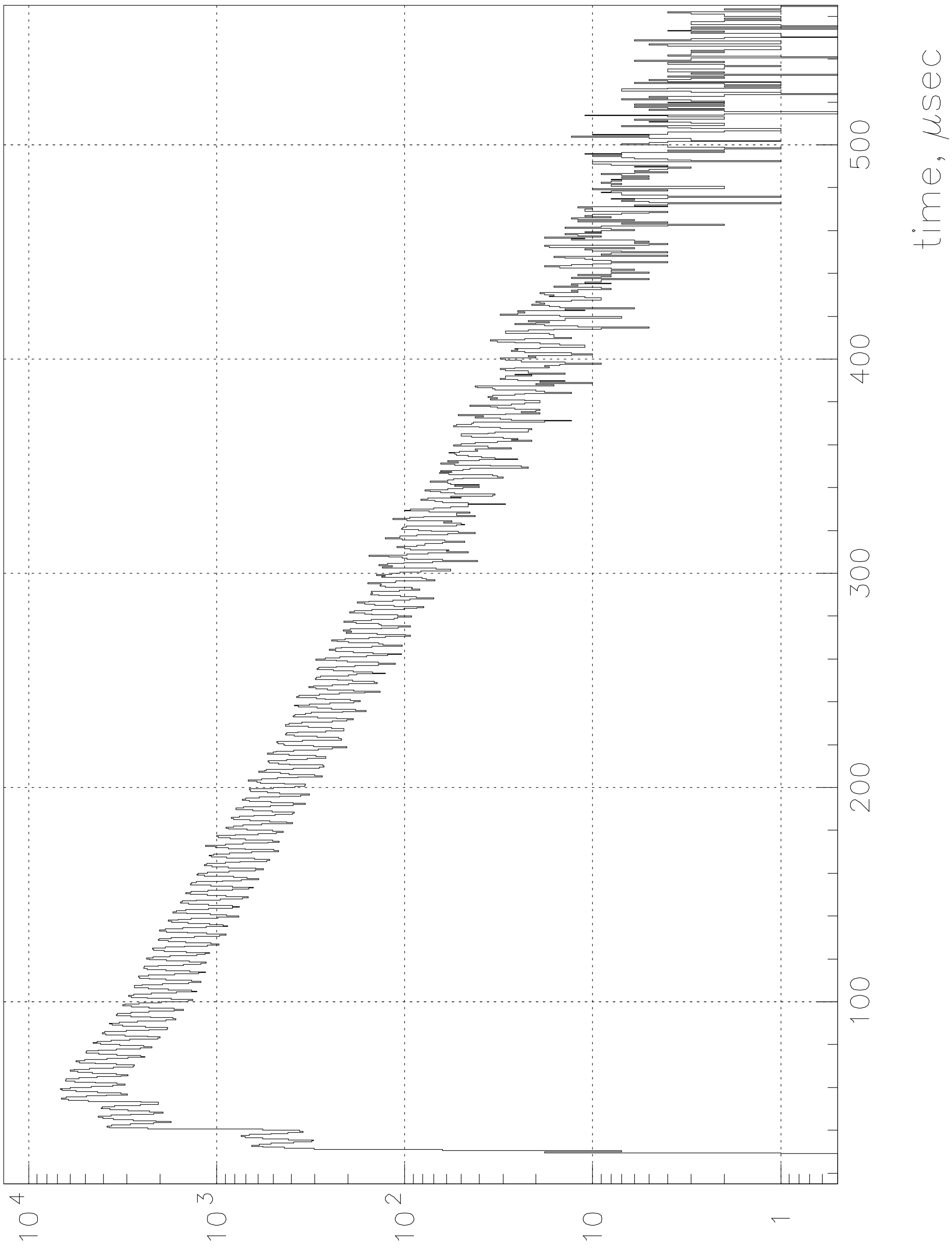


**Figure 7.8**: Time distribution of decay positrons

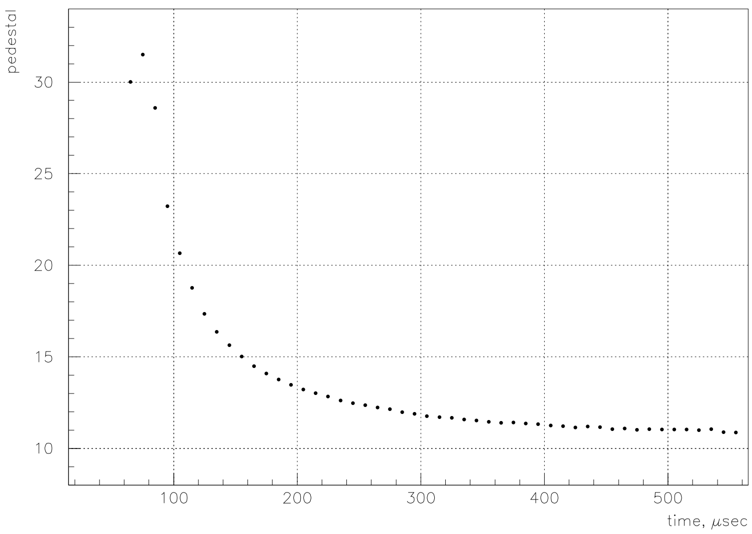


**Figure 7.9**: Pedestal versus time from injection

and the total amplitude (i.e. signal + pedestal) of a low energy pulse is higher than at the later time, and hence the overall efficiency of triggering on decay positrons of a given energy is higher at early times than at late times. The dependence of the efficiency on time is much stronger for low energy positrons particularly at early times. This causes deviations from the exponential decay function and a change in the energy spectrum of the detected positrons, and hence the asymmetry $A$, from early to late times. Selection of high energy positrons with $E > 0.6 \cdot E_{max}$ and $t > \sim 100$ $\mu$sec significantly removes the dependence of the efficiency on time. The residual dependence can be fit with the 8–parameter function. The factor $t^{-\alpha}$ modifies the exponential baseline, and $(A_\circ + A_1 t)$ expresses the time dependence of the asymmetry. An additional term $C$ represents a possible constant background.

Use of 5– and 8–parameter fits is essentially the same approach as taken in the CERN II and CERN III experiments. A completely different approach for analysis of the data was proposed by Y. Orlov [104] and implemented by J. Kindem [105]. This method takes the positron time distribution

$$f(t) = N_\circ(t)\, e^{-t/\tau}\, [1 + A(t)\, \cos(\omega_a t + \phi)\, ] + C(t),$$

in which $N_\circ(t)$, $A(t)$ and $C(t)$ are smooth functions, and defines the shifted functions

$$f^+(t) = f(t + \frac{1}{2}T_\omega), \qquad f^-(t) = f(t - \frac{1}{2}T_\omega),$$

where $T_\omega = 2\pi/\omega_a$ is the period of the (g–2) oscillations. Then the ratio $R(t)$ is

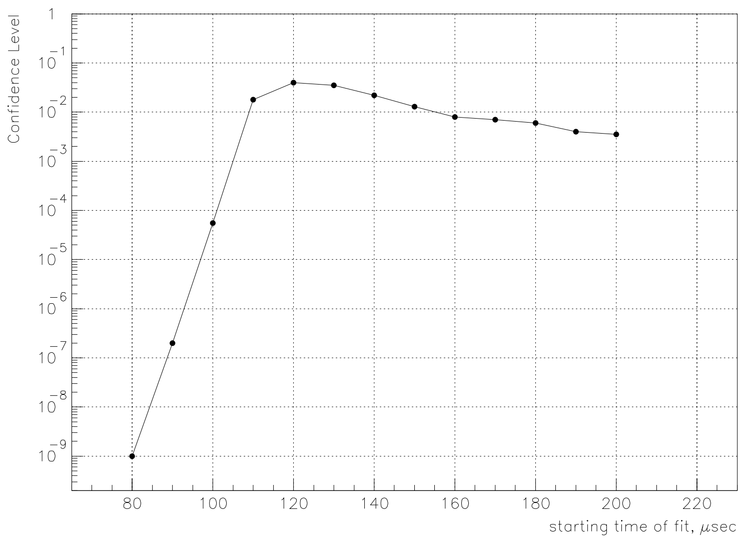


**Figure 7.10**: Confidence level of 5–parameter fit as a function of starting time

defined:

$$R(t) = \frac{f^+ + f^- - 2f}{f^+ + f^- + 2f} = A(t)\,\cos(\omega_a t + \phi)\,\left[1 + \frac{C(t)}{N_\circ(t)\,e^{-t/\tau}}\right]^{-1}.$$

For relatively small background $C(t)$, $R(t) = A(t)\,\cos(\omega_a t + \phi)$ and does not depend on $N_\circ(t)$, provided it is a smooth function. Thus, this method is less sensitive to the effects of WFD inefficiency.

For the Orlov–Kindem method the data were split into four groups, one part for $f^+$, one for $f^-$ and two for $f$. Then the distribution $R(t)$ was plotted and fit by the simple cosine wave $A(t)\cdot\cos(\omega_a t + \phi)$. Early to late time variation of the asymmetry was approximated by a linear term: $A(t) = A_\circ + A_1 t$, as for the 8–parameter fit. Figure 7.11 shows an $R(t)$ plot for one of the detectors (crosses), fit by the function $(A_\circ + A_1 t)\cdot\cos(\omega_a t + \phi)$.

## 7.5 Evaluation of $a_\mu$

A precise measurement of $a_\mu$ requires precise measurements of two quantities, the precession frequency $\omega_a$ and the magnetic field $B$:

$$a_\mu = \frac{mc}{eB}\,\omega_a.$$

The magnetic field is measured by a proton resonance frequency $\omega_p$ and hence $a_\mu$ can be found from the ratio of muon and proton spin precession frequencies in the same

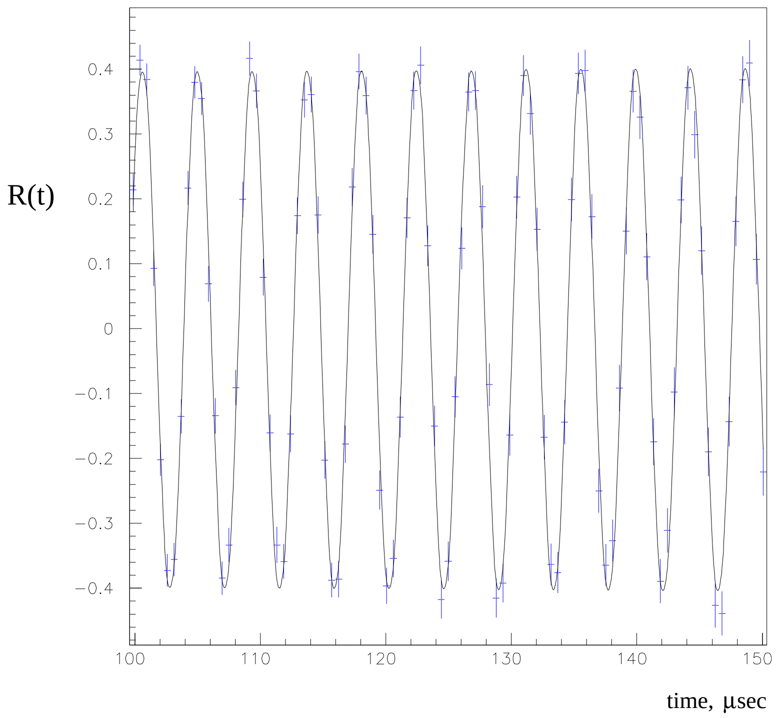


**Figure 7.11**: Ratio R(t) as a function of time from injection

magnetic field:

$$\frac{\omega_s}{\omega_p} = \frac{1+a_\mu}{a_\mu}\,\frac{\omega_a}{\omega_p} = \frac{\mu_\mu B/\hbar}{\mu_p B/\hbar} = \frac{\mu_\mu}{\mu_p},$$

where $\mu_\mu/\mu_p$ is a ratio of muon and proton magnetic moments, which has been measured with a precision of 0.15 ppm:

$$\frac{\mu_\mu}{\mu_p} = 3.183\,345\,47(47)\ \ (0.15\,ppm)\ [3].$$

The anomalous gyromagnetic ratio of muon can be evaluated using $\mu_\mu/\mu_p$, the muon (g–2) precession frequency $\omega_a$ and the proton resonance frequency $\omega_p$:

$$a_\mu = \frac{\omega_a/\omega_p}{\mu_\mu/\mu_p - \omega_a/\omega_p}\ .$$

During the run, the magnetic field was measured 2–3 times every week by 17 NMR probes mounted on the beam trolley and was permanently monitored by the system of fixed NMR probes. Figure 7.12 shows the average frequency of a group of selected fixed NMR probes as a function of run number, for data used in the offline analysis. Fixed NMR probes were calibrated by beam trolley data. There were 6 beam trolley measurements taken between data taking runs useful for offline analysis.

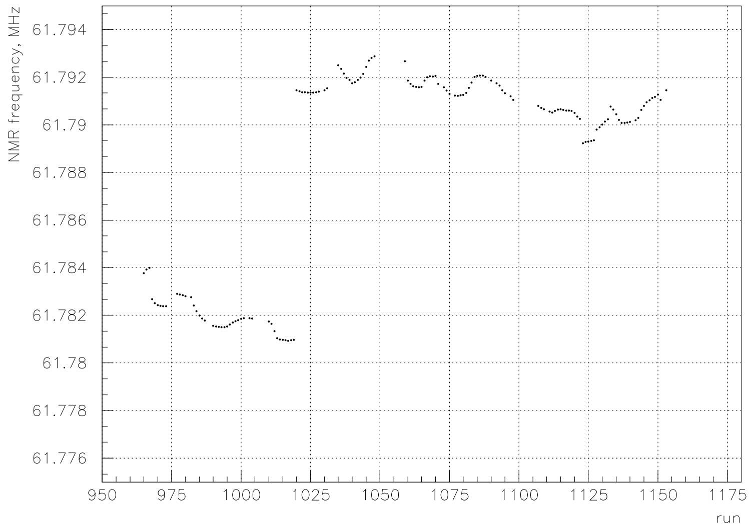


**Figure 7.12**: Frequency of fixed NMR probes.

The NMR frequency as a function of run number, shown in Figure 7.12, has a jump of about 10 kHz (160 ppm), which corresponds to the magnet quench caused by an accidental energy extraction. Otherwise, the frequency changes smoothly with a $\sim$ 2 kHz (30 ppm) drift over all the runs. Data before and after the quench were treated separately and the residual magnetic field variations were corrected by changing the time scale of (g–2) oscillations by a factor of $\omega_p(run)/\omega_p(average)$ on a run–by–run base.

Using the muon tracking code [106], each 3–dimensional magnetic field map was averaged over muon phase space distribution. The fast rotation signal from the initial time structure of the injected beam was useful to provide information on the radial distribution of stored muons as shown in Figure 7.13, where the comparison with a phase–space distribution is also presented. Knowledge of the muon distribution is important since it is the magnetic field weighted by the muon distribution $\langle B \rangle$, which is required to evaluate $a_\mu$.

The vertical distribution of muons in the storage ring was studied by applying current in the surface correction coils (see section 5.5) to add a small radial magnetic field. This moved the beam up and down and thus changed the efficiency for muon storage in the ring. It was found that the stored muon beam filled the vertical phase space, but that the distribution was about 1 mm higher than midplane due to the known radial magnetic field in the ring, see section 5.6.

The three methods of data analysis described in section 7.4 were all used and gave consistent results for $a_\mu$. For the final result we chose the 8–parameter fit which is less sensitive to the choice of the starting time of the fit and gives slightly smaller statistical

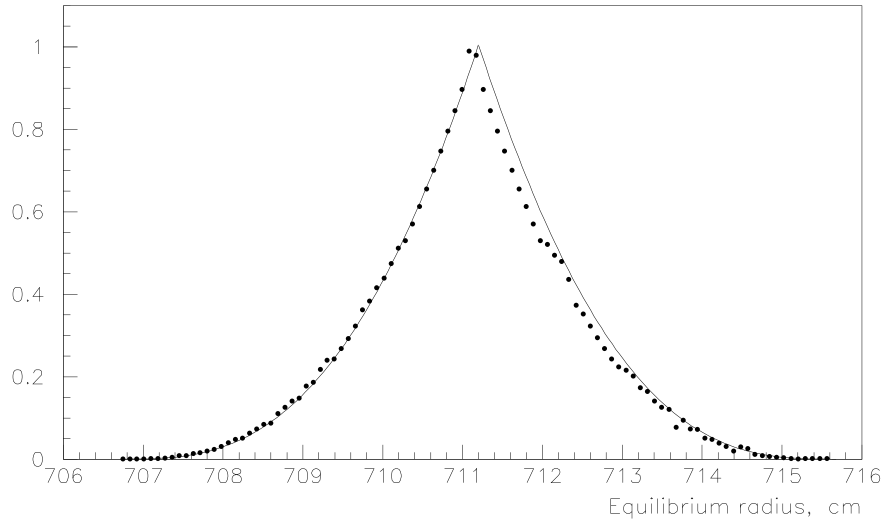


**Figure 7.13**: Distribution of equilibrium radii of stored muons. Solid line is a phase–space distribution.

error. The result is

$$a_{\mu^+} = 116\ 592\ 500(1520) \times 10^{-11}\ (13.0\ ppm).$$

The quoted uncertainty is the statistical error of 12.7 ppm in $\omega_a$ obtained from the fit, summed in quadrature with a systematic error of 2.9 ppm, see section 7.6.

## 7.6 Analysis of Systematic Errors

The systematic errors for the 1997 run are listed in Table 7.1. The error associated with the limited knowledge of the magnetic field was estimated at 1.0 ppm. It includes:
— Azimuthal variations of the magnetic field and accuracy of trolley position.
The magnetic field was measured for each trolley run at $\sim 10^5$ points. Azimuthal field variations were about 300 ppm which in view of the limited precision of the beam trolley azimuthal positioning ($\sim$ 2 cm) introduced an error of 0.3 ppm in $\langle B \rangle$.
— Magnetic field variations with temperature.
As was shown in section 6.4, the dipole component of the field changes with temperature by 35 ppm per °C and the quadrupole components change with temperature gradients by 25 ppm per °C/hour (normal quadrupole) and 6 ppm per °C/hour (skew quadrupole). These variations were monitored by a system of fixed NMR probes and temperature sensors. Still, residual effects can shift $\langle B \rangle$ by $\sim$ 0.5 ppm for the dipole and by $< 0.2$ ppm for the quadrupole components of the field.
— Systematic errors in the absolute calibration of the beam trolley NMR probes (see

**Table 7.1**: Systematic errors in ppm.

| Systematic effect | error (ppm) |
|---|---|
| Magnetic field | 1.0 |
| Muon distribution and $\langle B \rangle$ | 0.9 |
| WFD energy threshold | 1.5 |
| Muon losses | 0.2 |
| Timing shifts | 0.1 |
| Pitch and E field corrections | 0.05 |
| Fitting start time | 2.0 |
| Binning effects | 0.2 |
| Total systematic error | 2.9 |

section 4.5) at the level of 0.5 ppm.
— Magnetic field distortion by the inflector.
The magnetic field varies by about 300 ppm over the short distance in the inflector region. Several NMR probes, mounted on the beam tube trolley radially utmost, failed to work in such a high magnetic field gradient. The magnetic field at the inflector region was measured with modified NMR probes after the 1997 run and these data were incorporated in the magnetic field maps. The systematic error associated with this magnetic field distortion by the inflector was estimated by 0.5 ppm.

Other sources of systematic errors are:
— Limited knowledge of the muon distribution.
The azimuthally averaged magnetic field varies over the muon storage region by about 20 ppm (peak–to–peak), see Table 5.2 and Figure 7.14. Our limited knowledge of the muon distribution can change $\langle B \rangle$ by up to 0.9 ppm.
— WFD triggering scheme inefficiency.
As was discussed in sections 7.1 and 7.4, the inefficiency in the WFD triggering scheme together with the high pedestal at early times leads to variation with time in the trigger efficiency for decay positrons and distortion of the positron energy spectrum. Since higher energy positrons have a longer drift time in the storage ring before hitting the calorimeters, this distortion shifts the average phase of the (g–2) oscillations forward at later times, which is equivalent to lowering $\omega_a$. The effect was studied by Monte–Carlo simulation and found to be less than 1.5 ppm.
— Muon losses.
The average polarization of the stored muons can depend slightly on their momentum and hence on the average radius. If losses were large for muons stored at large average radii, then the average phase of the stored muons could change with time. This effect was estimated to be less than 0.2 ppm on the value of $\omega_a$.

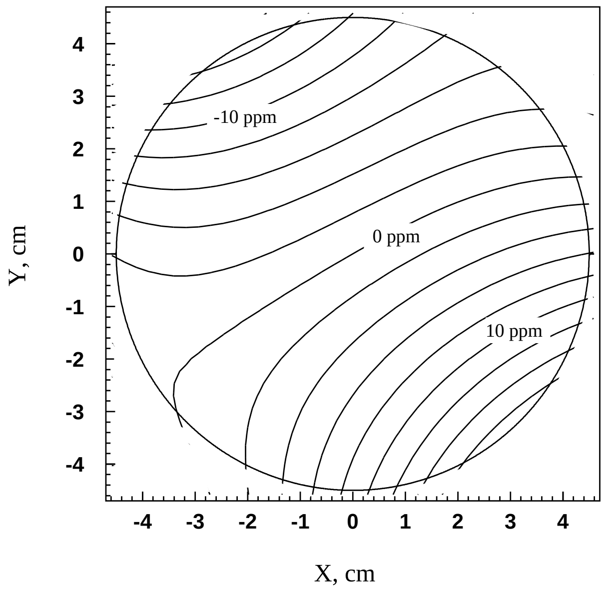


**Figure 7.14**: Magnetic field averaged azimuthally over the muon storage region.

— Time shifts of PMT signals.
Due to the flash after injection, the rate of PMT signals changes dramatically from early to late time. This rate variation could change some parameters of the PMT circuit, in particular the transit time. This effect was studied with calibration laser pulses, which were mixed with real decay positron signals on each detector at several well defined times. Early–to–late timing shifts over the first 200 $\mu$sec were on average less than 20 psec and hence systematic error associated with this effect is less than 0.1 ppm.
— Start time of the fit.
The baseline of (g–2) oscillations deviates significantly from simple exponential at early times. Fitting the experimental time distribution with an analytical function, we clearly saw oscillations and a drift in $\omega_a$ as a function of start time of the fit. This effect was also seen in the CERN III experiment. We had to choose the start time late enough to keep this effect reasonably small. The residual systematic error was estimated to be $\sim 2$ ppm.
— Pitch correction.
This is a correction to spin motion for muons due to vertical betatron oscillations in the vertical direction. The theory of the pitch correction was given by F. Farley [107]. For the BNL muon (g–2) storage ring it was calculated to be $+0.4 \pm 0.05$ ppm. Another correction is due to residual effect of electric field on $\omega_a$, see formula 1.2. For our ring with $\delta p/p = \pm 0.5\%$, the electric field correction is $+0.69$ ppm. Both these corrections were applied for our final result in section 7.5.

Summing all these errors in quadratures gives the total systematic error of 2.9 ppm.

# Chapter 8

# Conclusion

The first "engineering" run of the BNL (g–2) experiment using pion injection gives the following result for the anomalous gyromagnetic ratio of muon:

$$a_{\mu^+} = 116\ 592\ 500(1520) \times 10^{-11}\ (13.0\ ppm).$$

This should be compared with the most accurate previous measurement at CERN for $\mu^+$ and $\mu^-$:

$$a_{\mu^+} = 116\ 591\ 000(1100) \times 10^{-11}\ (9.4\ ppm),$$

$$a_{\mu^-} = 116\ 593\ 700(1200) \times 10^{-11}\ (10.3\ ppm)$$

and for $\mu^+$, $\mu^-$ combined:

$$a_{\mu} = 116\ 592\ 300(840) \times 10^{-11}\ (7.2\ ppm).$$

All these results are shown in Figure 8.1 with the current theoretical value (see Chapter 1 and section 2.1):

$$a_{\mu} = 116\ 591\ 628(77) \times 10^{-11}\ (0.66\ ppm).$$

The differences are:

$$a_{\mu^+}(BNL) - a_{\mu^+}(CERN\ III) = 1500(1880) \times 10^{-11},$$

$$a_{\mu^+}(BNL) - a_{\mu^-}(CERN\ III) = -1200(1940) \times 10^{-11},$$

$$a_{\mu^+}(BNL) - a_{\mu}(CERN\ III) = 200(1740) \times 10^{-11},$$

$$a_{\mu^+}(BNL) - a_{\mu}(theory) = 870(1530) \times 10^{-11}.$$

Our result is comparable in precision with the CERN III experiment and consistent within one standard deviation with both the CERN III result and the theoretical value. A paper with the first result of our expriment is submitted to *Physical Review Letters* and reprinted in Appendix I.

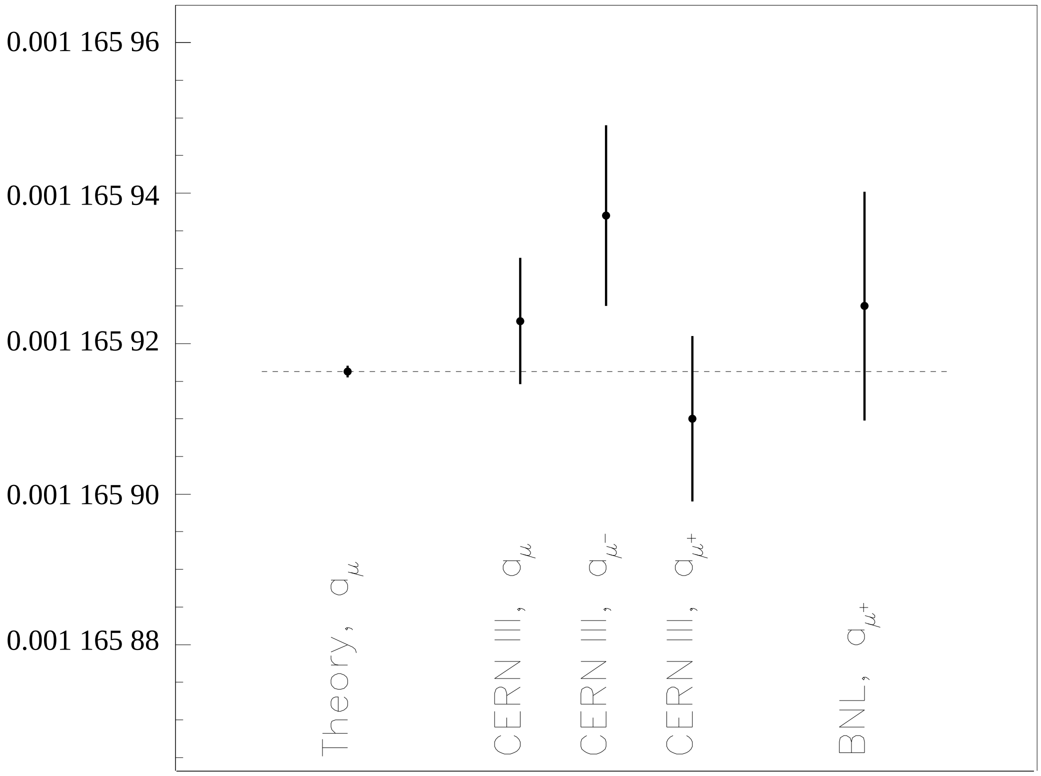


**Figure 8.1**:

The next run of BNL (g–2) experiment is scheduled on August 1998 and January 1999 and has a goal to reach precision in $a_\mu$ of about 1 ppm. The major improvements that should allow us to do so are:

(1) Implementation of direct muon injection with commissioning of the muon kicker. This would increase number of stored muons and reduce the background due to pion flash.

(2) Improved magnetic field homogeneity, stability and control by:

— Static iron shimming with Rose shims and aluminum/iron sandwiches (see section 5.5) both on the pole–to–pole base;

— Dynamic corrections with surface coils;

— Improved shimming and measurements in the inflector region;

— Thermal insulation of the yoke;

— Implementation of the NMR signal feedback to the power supply;

(3) Improved secondary beam diagnostics with:

— Cherenkov threshold counters for $e$, $\mu$, $\pi$ and for $p$ just upstream of the inflector;

— Pair of photodiode counters up– and downstream of the inflector for optimization of the inflector transmission;

— Improved scintillating fiber monitor and scintillator/photodiode systems for the beam profile measurement inside the storage region;

(4) Measurement of stored muon distribution with electron traceback chambers and with muon loss counters.

(5) Optimization of the calorimeter detectors and the waveform digitizer operation, full use of front scintillating detectors and position sensitive detectors.

With all the above improvements tested and tuned in the 1998–1999 run, we plan to achieve an overall error of 0.35 ppm for $a_{\mu^+}$ and $a_{\mu^-}$ in 2000–2001. By that time we expect the precision of $a_\mu(theory)$ to be improved to the same or better value due to number of experiments measuring $a_\mu(hadrons)$ in Novosibirsk, Beijing, Frascatti and Cornell.

# Appendix I

Submitted to *Physical Review Letters*

# Appendix II

# Bibliography


[1] J. Bailey et al., Nucl. Phys. **B150**, 1(1979).

[2] F. J. M. Farley and E. Picasso in *Quantum Electrodynamics*, (Direction in High Energy Physics Vol.7) T. Kinoshita ed., World Scientific, 1990, p.479.

[3] Particle Data Group, Eur. Phys. J. **C3**, 1(1998).

[4] T. Kinoshita and W. J. Marciano in *Quantum Electrodynamics*, (Direction in High Energy Physics Vol.7) T. Kinoshita ed., World Scientific, 1990, p.419.

[5] M. Hayakawa and T. Kinoshita, Phys. Rev. **D57**, 465 (1998).

[6] S. Eidelman and F. Jegerlehner, Z. Phys. **C67**, 585 (1995).

[7] M. Davier and A. Hocker, Phys. Lett. **B419**, 419 (1998);
R. Alemany, M. Davier and A. Hocker, Eur. Phys. J. **C2**, 123 (1998).

[8] B. Krause, Phys. Lett. **B390**, 392 (1997).

[9] A. Czrnecki, B. Krause and W. Marciano, Phys. Rev. Lett. **76**, 3267 (1996).

[10] Design Report of BNL experiment E821, 1995.

[11] BNL E821 experiment proposal, 1985.

[12] V. W. Hughes in *A gift of prophesy*, E. C. G. Sudarshan ed., World Scientific, 1994, p.222.

[13] R. S. Van Dyck Jr., P. B. Schwinberg and H. D. Dehmelt, Phys. REv. Lett. **59**, 26 (1987).

[14] A. Jeffery et al., Conf. on Precision Electromagnetic Measurements, Braunschweig, Germany, 1996.

[15] V. W. Hughes and T. Kinoshita, Submitted to Rev. of Mod. Phys. Special Centenary Issue, March 1999.

[16] T. Kinoshita, B. Nizic and Y. Okamoto, Phys. Rev. **D41**, 593 (1990);
T. Kinishita, Phys. Rev. **D47**, 5013 (1993);
M. Samuel and G. Li, Phys. Rev. **D44**, 3935 (1991); **D48**, 1879(E) (1993);
S. Laporta and E. Remiddi, Phys. Lett. **B301**, 440 (1992);
S. Laporta, Phys. Lett. **B312**, 495 (1993);
S. Karshenboim, Yad. Fiz **56**, 252 (1993) [Phys. At. Nucl. Transl. of Yad. Fiz. **56**, 857 (1993)].
T. Kinoshita, Phys. Rev. Lett. **75**, 4728 (1995)

[17] D. H. Brown and W. A. Worstell, Phys. Rev. **D54**, 3237 (1996).

[18] J. Gronberg et al., Phys. Rev. **D57**, 33 (1998)

[19] K. Fujikawa, B. W. Lee and A. I. Sanda, Phys. Rev. **D6**, 2923 (1972);
R. Jackiw and S. Weinberg, Phys. Rev. **D5**, 2396 (1972);
G. Altarelli, N. Cabibbo and L. Maiani, Phys. Lett. **B40**, 415 (1972);
I. Bars and M. Yoshimura, Phys. Rev. **D6**, 374 (1972);
W. A. Bardeen, R. Gastmans and B. E. Lautrup, Nucl. Phys. **B46**, 319 (1972).

[20] T. V. Kukhto, E. A. Kuraev, A. Schiller and Z. K. Silagadze, Nucl. Phys. **B371**, 567 (1992).

[21] J. J. Aubert et al., Phys. Rev. Lett. **33**, 1404 (1974);
J. –E. Augustin et al., Phys. Rev. Lett. **33**, 1406 (1974).

[22] G. Arnison et al., Phys. Lett. **122B**, 103 (1983);
G. Arnison et al., Phys. Lett. **126B**, 398 (1983).

[23] F. Abe et al., Phys. Rev. Lett. **74**, 2626 (1995);
S. Abachi et al., Phys. Rev. Lett. **74**, 2632 (1995).

[24] V. A. Novikov et al., Mod. Phys. Lett. **A9**, 2641 (1994).

[25] J. C. Pati and A. Salam, Phys. Rev. Lett. **31**, 275 (1973);
H. M. Georgi and S. L. Glashow, Phys. Rev. Lett. **32**, 438 (1974).

[26] J. P. Leveille, Nucl. Phys. **B137**, 63 (1978).

[27] Yu. A. Gol'fand and E. P. Likhman, JETP Lett. **13**, 323 (1971);
D. V. Volkov and V. P. Akulov, JETP Lett. **16**, 438 (1972);
J. Weiss and B. Zumino, Nucl. Phys. **B70**, 34 (1974).

[28] T. Moroi, Phys. Rev. **D53**, 6565 (1996).

[29] U. Chattopadhyay, P. Nath, Phys. Rev. **D53**, 1648 (1996).

[30] W. Buchmuller and D. Wyler, Phys. Lett. **B177**, 377 (1986);
J. C. Pati and A. Salam, Phys. Rev. **D10**, 275 (1974).

[31] O. Shanker, Nucl. Phys. **B204**, 375 (1982); **B206**, 253 (1982).

[32] H1 Collaboratiion, I. Abt et al., Nucl. Phys. **B396**, 3 (1993); Z. Phys. **C64**, 545 (1994);
ZEUS Collaboration, M. Derrick et al., Phys. Lett. **B396**, 173 (1993).

[33] CDF Collaboration, F. Abe et al., Phys. Rev. **D48**, 3939 (1993); Phys. Rev. Lett. **75**, 1012 (1995).

[34] D0 Collaboration, S. Abachi et al., Report No. hep-ex/9507002, unpublished.

[35] G. Bhaattacharyya, J. Ellis and K. Sridhar, Phys. Lett. **B336**, 100 (1994); **B338**, 522(E) (1994).

[36] G. Couture and H. Konig, Phys. Rev. **D53**, 555 (1996).

[37] P. Mery et al., Z. Phys. **C46**, 229 (1990)

[38] B. Lautrup, A. Peterman and E. de Rafael, Phys. Rep. **3**, 193 (1972).

[39] L. M. Barkov et al., Nucl. Phys. **B256**, 365 (1985).

[40] L. M. Barkov et al., JETP Lett. **46**, 165 (1987);
A. I. Shekhtman, Ph.D. thesis, BINP, Novosibirsk, Russia, 1987.

[41] L. M. Barkov et al., Preprint BINP 89–15, Novosibirsk, Russia, unpublished.

[42] G. V. Anikin et al., Preprint BINP 83–85, unpublished.

[43] L. M. Barkov et al., Sov. J. Nucl. Phys. **47**, 248 (1988).

[44] L. M. Barkov et al., Nucl. Instr. and Meth. **204**, 379 (1983).

[45] D. H. Brown and W. A. Worstell, g–2 technical note #220, unpublished.

[46] G. A. Aksenov et al., BINP Preprint 85–118, Novosibirsk, Russia, unpublished;
E. V. Anashkin et al., IGFA Instr. Bul. 5 (1988);
V. M. Aulchenko et al., Nucl. Instr. and Meth. **A252**, 299 (1986);
E. V. Anashkin et al., Nucl. Instr. and Meth. **A323**, 178 (1992);
L. M. Barkov et al., Proc. of 5th Int. Conf. on Instr. for Coll. Beam Phys., Novosibirsk, Russia, 1990;
B. A. Shwartz et al., Proc. of 5th Int. Conf. on Instr. for Coll. Beam Phys., Novosibirsk, 1990;
E. V. Anashkin et al., Nucl. Instr. and Meth. **A265**, 137 (1988);

E. V. Anashkin et al., BINP Preprint 88–43, unpublished;
G. A. Aksenov et al., Proc. of the Int. Conf. on Comp. in High Energy Phys., Annecy, France, 1992.

[47] R. R. Akhmetshin et al., Phys. Lett. **B364**, 199 (1995).

[48] R. R. Akhmetshin et al., Phys. Lett. **B398**, 423 (1997).

[49] D. Bisello et al., Phys. Lett. **B220**, 321 (1989).

[50] L. M. Barkov et al., Sov. J. Nucl. Phys. **40**, 286 (1994).

[51] S. R. Amendolia et al., Phys. Lett. **B138**, 454 (1984).

[52] I. B. Vasserman et al., Sov. J. Nucl. Phys. **33**, 709 (1981).

[53] A. Quenzer et al., Phys. Lett. **B76**, 512 (1978).

[54] B. Esposito et al., Phys. Lett **B67**, 229 (1977).

[55] G. Cosme et al., Preprint LAL 1287, Orsay, France, 1976, unpublished.

[56] D. Bellini et al., Lett. Nuov. Cim. **14**, 418 (1975).

[57] G. Barbiellini et al., Lett. Nuov. Cim. **6**, 557 (1973).

[58] A. Antonelli et al., Z. Phys. **C56**, 15 (1992).

[59] S. I. Dolinsky et al., Phys. Rep. **202**, 99 (1991).

[60] A. Cordier et al., Nucl. Phys **B172**, 13 (1980).

[61] D. Bisello et al., Z. Phys. **C39**, 13 (1998).

[62] L. M. Kurdadze et al., Preprint BINP 82–97, Novosibirsk, Russia, 1982, unpublished.

[63] F. Mane et al., Phys. Lett. **B99**, 261 (1981).

[64] Preprint LAL 90–35, Orsay, France, 1990, unpublished.

[65] A. Cordier et al., Phys. Lett. **B109**, 129 (1982).

[66] L. M. Kurdadze et al., Preprint BINP 79–69, Novosibirsk, Russia, unpublished.

[67] L. M. Kurdadze et al., JEPT Lett. **43**, 643 (1986).

[68] A. Cordier et al., Phys. Lett. **B106**, 155 (1981).

[69] D. Bisello et al., Phys. Lett. **B107**, 145 (1981).

[70] C. Bacci et al., Nucl. Phys. **B184**, 31 (1981).

[71] I. B. Logashenko, Proceedings of the 7th Int. Conf. on Hadron Spectroscopy (HADRON 97), BNL, NY, 1997.

[72] C. M. G. Lattes et al., Nature **159**, 694 (1947); **160**, 453, 486 (1947).

[73] G. Charpak et al., Nuovo Cimento **37**, 1241 (1965).

[74] A. Petermann, Helv. Phys. Acta **30**, 407 (1957).

[75] D. T. Wilkinson and H. R. Crane, Phys. Rev. **130**, 852(1963);
W.H.Louisell, R. W. Pidd and H. R. Crane, Phys. Rev. **94**, 7 (1954)

[76] C. M. Sommerfield, Phys. Rev. **107**, 328 (1957);
H. Suura and K. Wichmann, Phys. Rev. **105**, 1930 (1957).

[77] J. Bailey et al., Phys. Lett. **B28**, 287 (1968);
J. Bailey et al., Nuovo Cimento **A9**, 369 (1972).

[78] V. W. Hughes and G. T. Danby, Proceedings of the Conf. on Intersections Between Particle and Nuclear Physics, R. E. Mischke ed., Americal Institute of Physics, NY, 1984.

[79] M. Tanaka and Y. Y. Lee, IEEE Part. Accel. Conf., 1993
W. W. MacKay et al., 5th Europian Part. Accel. Conf., 1996
M. Tanaka and Y. Y. Lee, IEEE Part. Accel. Conf., 1991
M. Blaskiewicz et al., IEEE Part. Accel. Conf., 1996

[80] H. Brown, private communication.

[81] E. R. Cohen and B. N. Taylor, Rev. Mod. Phys. **59**, 1121 (1987).

[82] F. Bloch, Phys. Rev. **70**, 460 (1946).

[83] R. Prigl, Ph.D. thesis, University of Heidelberg, 1994.

[84] R. Prigl et al., Nucl. Instr. Meth. **A374**, 118 (1996).

[85] X. Fei, V. W. Hughes and R. Prigl, Nucl. Instr. Meth. **A394**, 349 (1997).

[86] W. D. Phillips, W. E. Cooke and D. Klepper, Metrologia **13**, 179 (1977).

[87] B. W. Petley and R. W. Donaldson, Metrologia **20**, 81 (1984).

[88] F. Krienen, W. Meng and D. Loomba, Nucl. Instr. Meth. **A283**, 5 (1989).

[89] Y. K. Semertzidis et al., g–2 technical note # 168, unpublished.

[90] Y. K. Semertzidis, g–2 technical note # 247, unpublished.

[91] F. Combley and E. Picasso, Phys. Rep. **C14**, 1 (1974).

[92] S. Sedykh et al., Proceedings of the 7th Int. Conf. on Calorimetry in High Energy Physics (CALOR 97), Tuscon, AZ, 1997.

[93] J. Miller, R. Carey, E. Hawk, g–2 technical note # 247, unpublished.

[94] M. Green, g–2 technical note # 159, unpublished.

[95] K. Halbach, Nucl. Instr. and Meth. **107**, 529 (1973).

[96] B. Turk, Nucl. Instr. and Meth. **95**, 205 (1971).

[97] A. Grossmann, Ph.D. thesis, University of Heidelberg, 1998.

[98] H. Deng, g–2 technical note # 291, unpublished.

[99] P. Debevec et al., g–2 technical note # 298, unpublished.

[100] J. Cumming, Ann. Rev. of Nucl. Sci. **12**, 261 (1963);
B. J. Dropesky et al., Phys. Rev. **C32**, 1305 (1985);
Landolf–Börnstein, New Series, Springer Verlag (1996) 285;
A. M. Poskanzer and L. P. Remsberg, Phys. Rev. **B779**, 134 (1964).

[101] E. P. Solodov, g–2 technical note # 293, unpublished.

[102] R. Carey, g–2 technical note # 301, unpublished.

[103] I. B. Logashenko, g–2 technical note #299, unpublished.

[104] Y. F. Orlov, private communication.

[105] J. Kindem, Ph.D. thesis, University of Minnesota, 1998.

[106] E. Efstathiadis, B. L. Roberts and Y. K. Sermertzidis, g–2 technical note # 283, unpublished.

[107] F. J. M. Farley, Phys. Lett. **42B**, (1972) 66.